Multi-electron dynamics investigated with strong-field tunnelling and XUV photoionization.

Nemeth, Gregory Richard Alexander James

Swansea University
Prifysgol Abertawe

Multi-electron dynamics investigated with strong-field tunnelling and XUV photoionization

Gregory Richard Alexander James Nemeth

Department of Physics
Swansea University

Submitted to Swansea University in fulfilment of the requirements for the Degree of Doctor of Philosophy

2011

To the memory of Dr. Colin J. Evans, Emeritus Professor of Physics. His daughter, Louise – one of my first music teachers – was delighted that I was considering applying to Swansea University, since this would potentially give me the opportunity to meet and study under her father, with whom she felt I shared many similarities – in our approaches to science and to life. As an undergraduate, Dr. Evans was assigned to be my Personal Tutor, and chance would lead me to follow in some of his academic footsteps as a postgraduate. In my many shared conversations with him, whether about science, computers, music, radio, or our attachment to the university, Louise's intuitions were proven.

"We meet at a college noted for knowledge, in a city noted for progress, in a State noted for strength, and we stand in need of all three, for we meet in an hour of change and challenge, in a decade of hope and fear, in an age of both knowledge and ignorance."

— *President John F. Kennedy*

"If I have seen further it is by standing on the shoulders of giants."

— *Isaac Newton*

Contents

Abstract

Tunnel ionization initiated by intense ultrashort laser pulses is highly nonlinear with intensity. Few-cycle pulses can therefore be used to control electron dynamics on subfemtosecond timescales. Experimental measurements of xenon ionization by a temporally-shaped pulse are compared to modern tunnel theory, modified to allow the time-dependent population of multiple energy levels. A temporal asymmetry is seen in the experiment, the behaviour of which is best-matched by the model when multiple degenerate $5p$ and $5s$ energy levels are allowed to tunnel directly to the continuum. This is the first observation of this phenomenon.

A similar pump-probe measurement is conducted using krypton and a combination of extreme-ultraviolet (XUV) and near-infrared (NIR) pulses. Individual XUV harmonics are selected using a state-of-the-art monochromator. If NIR follows XUV, satellite states populated by $4s$ or $4p$ photoionization by the XUV are tunnel ionized by the NIR to Kr^{2+}. Vice versa, much less Kr^{2+} is produced, resulting in a step in the ion yield as a function of pump-probe delay. From this, the contributions of $4s$ and $4p$ photoionization to the overall ion yield can be elucidated, with application to specific population of core or valence electronic states.

Finally, beam propagation along a few-cycle NIR beamline is modelled, demonstrating the effects of diffraction due to hard-edged and annular optics typically used to minimise material dispersion. Optical configurations predicted to give longer interaction lengths and improved phase-matching are found, with implications for high-harmonic generation and attosecond pulse generation. The model's usefulness as a tool for beamline design and optimisation is discussed, with relevance to the experiments described.

Declarations and Statements

This work has not previously been accepted in substance for any degree and is not being concurrently submitted in candidature for any degree.

Signed ..... (candidate)

Date .....

This thesis is the result of my own investigations, except where otherwise stated. Other sources are acknowledged by citations giving explicit references. A bibliography is appended.

Signed ..... (candidate)

Date .....

I hereby give consent for my thesis, if accepted, to be available for photocopying and for inter-library loan, and for the title and summary to be made available to outside organisations.

Signed ..... (candidate)

Date .....

Acknowledgements

I would like to thank:
My supervisor, Dr. William Bryan, and all of the lecturing and support staff at Swansea University Physics department who – through my undergraduate and postgraduate education – have all made this work possible. Special thanks go to David Payne for computing support.

My office-mates Mark Round, Jim Rafferty, Robert Rickman, Jonathan Lloyd, Omar Al-Hartomy, Jérôme Gaillard and Ross Stanley, with Ross's tea- and coffee-making particularly recognised and appreciated.

The members of the QUB–UCL–Swansea experimental collaboration I've had the pleasure of meeting and working with, particularly Chris Calvert, Raymond King, John Alexander, Orla Kelly, Jason Greenwood, Ian Williams, and Roy Newell.

The staff at Astra Artemis, STFC Rutherford Appleton Laboratory, particularly Emma Springate, Chris Froud, Cephise Cacho and Edmond Turcu.

All of the researchers, lecturers and postdoctoral students I've enjoyed sharing lunch and ideas with, whether at Swansea, at RAL, or at conferences.

My family and friends for their continual support and encouragement, particularly my parents for innumerable lifts in the 'Nemethmobile'.

Financial support from the Engineering and Physical Sciences Research Council (EPSRC) and the Science and Technology Facilities Council (STFC) is gratefully acknowledged.

List of Tables

List of Figures

Chapter 1

Introduction

Intense laser pulses can generate electric fields strong enough to suppress the Coulomb potential of atoms, triggering tunnel and multiphoton ionization. Few-cycle pulses can control the outgoing electron motion, which can lead to the generation of attosecond pulses, and the probing of time-resolved multielectron dynamics on timescales approaching the atomic unit of time (24 attoseconds).

This chapter reviews the development of modern strong field photoionization theory, including electron recollision processes, the generation of high-harmonics by recombination, and landmark experiments.

1.1 Strong-field photoionization

An electron may be removed from an atom in a strong field by multiphoton ionization (MPI) and tunnel ionization (TI). In MPI, several photons are required to be absorbed in order for an electron to transition to the continuum, which has a high probability of occuring in an intense laser focus due to the high photon flux. The atom is able to nonlinearly absorb multiple quanta, thus allowing electron ejection. Where the field is strong enough to distort the Coulomb potential of the atom ($I > 10^{14}$ W/cm^2), the electron can tunnel through the

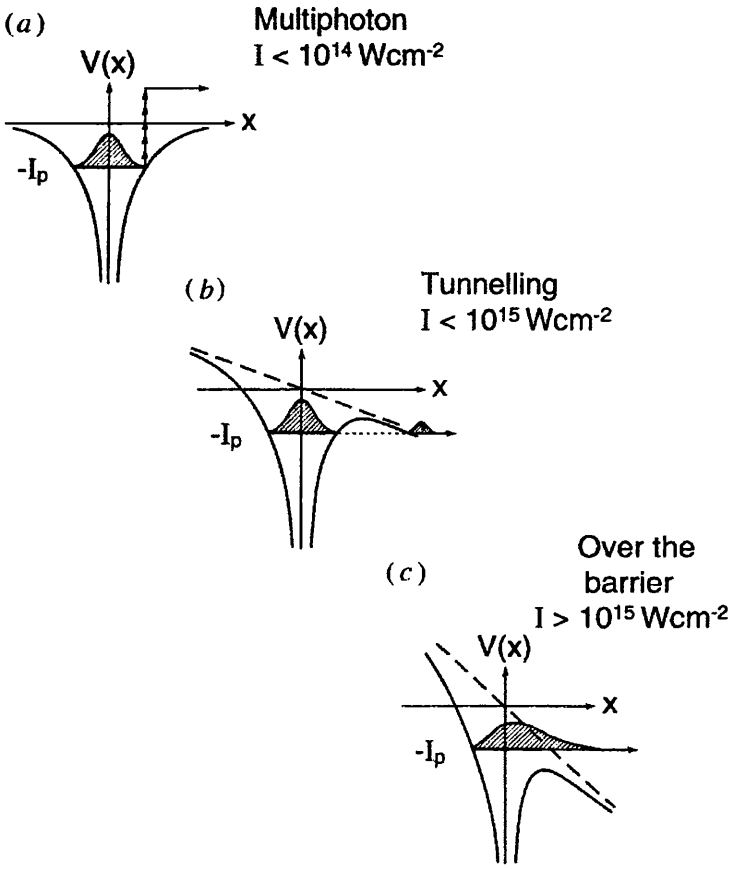

Figure 1.1: Strong-field ionization mechanisms and approximate intensity regimes: (a) MPI, (b) TI, (c) OBI. Reproduced from [1].

modified Coulomb barrier directly into the continuum. Over-the-barrier ionization (OBI) occurs when the field is strong enough to completely suppress the barrier ($I > 10^{15}$ W/cm^2), and the probability of ionization is therefore unity. Figure 1.1 illustrates the shape of the modified Coulomb potential for each of these processes.

In 1965, the theory of Keldysh [2] related the mechanisms of nonlinear photoionization to a strong-field oscillating electromagnetic wave. Where the photon energy is far from resonance with an excited state or ionization threshold, the theory can be applied to ionization in an intense laser pulse.

Keldysh also defined the adiabaticity parameter (or Keldysh parameter), γ, as [2]

$$\gamma = \frac{\omega_L}{\omega_t} = \frac{\tau_t}{\tau_L} \tag{1.1}$$

i.e. the ratio of tunnelling time through the Coulomb potential barrier (τ_t) to the wave period of the applied electric field (τ_L), in atomic units ($h = m_e = e = 1$). ω_t and ω_L are the corresponding frequencies of the tunnelling and applied electric field respectively, also in atomic units.

The Keldysh parameter can also be expressed in terms of the energy of a free electron in an oscillating field, also known as the ponderomotive potential, U_p [3,4]

$$\gamma = \omega_L \sqrt{\frac{2I_p}{I}} = \sqrt{\frac{I_p}{2U_p}} \tag{1.2}$$

where I the intensity, I_p the ionization potential or binding energy of the electron, ω_L the frequency of the laser field, all in atomic units, and

$$U_p = \frac{\varepsilon^2}{4\omega_L^2} \qquad \text{(in a.u.)} \tag{1.3}$$

$$U_p = 9.33 \times 10^{-14} I\lambda^2 \quad \text{(in eV)} \tag{1.4}$$

is the ponderomotive energy of the electron due to the laser field, where ε is the amplitude of the induced electric field and ω_L the laser frequency, both in atomic units, I the intensity in W/cm^2, and λ is the wavelength in μm.

If $\tau_L \ll \tau_t$, multiphoton absorption dominates and tunnel ionization is suppressed, since the electron does not have sufficient time to tunnel through the barrier during half the laser cycle. The rate of MPI is given by [1]

$$\Gamma_{\text{MPI}} = \sigma_N I^N \tag{1.5}$$

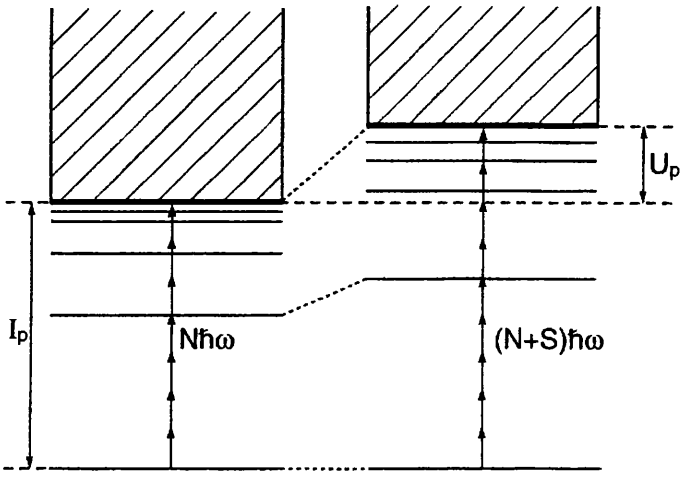

Figure 1.2: The ponderomotive potential U_p results in an energy-level shift, affecting the outer levels most, raising the ionization potential, I_p, to I_p+U_p. $N+S$ photons are therefore required to ionize via MPI. Reproduced from [1].

where σ_N is the N-photon photoabsorption cross-section, and I is the laser intensity. Where $\tau_L \gg \tau_t$, there is a high probability of tunnel ionization. This can dominate over MPI, since in a strong electric field, the influence of the ponderomotive potential results in the ionization potential being raised, actively reducing the MPI probability, as illustrated in Figure 1.2.

The Keldysh parameter is often used as an indicator of the dominant ionization process in intense laser-matter interactions, with $\gamma \gg 1$ signifying MPI-dominance, and $\gamma \ll 1$ signifying TI-dominance. For intermediate $\gamma \sim 1$, both processes influence the ionization rate. The use of γ as a general quantifier of strong-field ionization behaviour has recently been criticised by Reiss [4], being strictly applicable only over a small wavelength range. This is demonstrated in Figure 1.3. Many strong-field ionization experiments are conducted at wavelengths of ~800 nm, where $\gamma = 10$ corresponds to an intensity of $\sim 10^{12}$ W/cm^2 (predominantly MPI), and $\gamma = 0.1$ to an intensity of $\sim 10^{16}$ W/cm^2 (predominantly TI/OBI). However, at ~5 nm for example, γ implies that TI and MPI take place in a high-intensity regime (mid-10^{16} to mid-10^{20} W/cm^2), where the

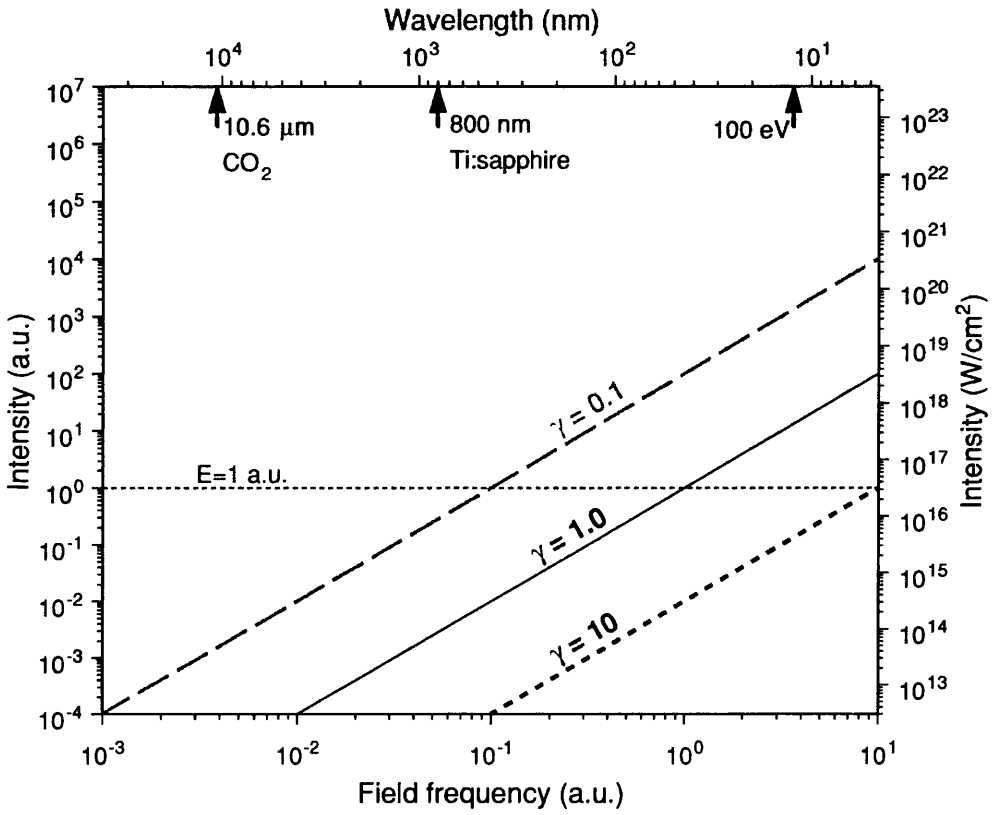

Figure 1.3: The Keldysh parameter for ground-state hydrogen, γ, plotted as a function of intensity and laser period for $\gamma = 0.1$ ('TI-dominant'), 1 ('TI and MPI') and 10 ('MPI-dominant'). This interpretation is strictly only applicable to a narrow wavelength range in the vicinity of 800 nm. Reproduced from [4].

energy of a single photon (272 eV) is far in excess of the ionization potential of hydrogen at 13.6 eV. The photon energy is so large as to eject core electrons, causing significant excitation (as will be covered in more detail in Chapter 6). This is very unlike the situation at $\sim$ 800nm, where ionization is expected to proceed by removal of the outer valence electrons. Reiss therefore argues that ionization mechanisms cannot be reliably described using the same parameter, γ, for all wavelengths.

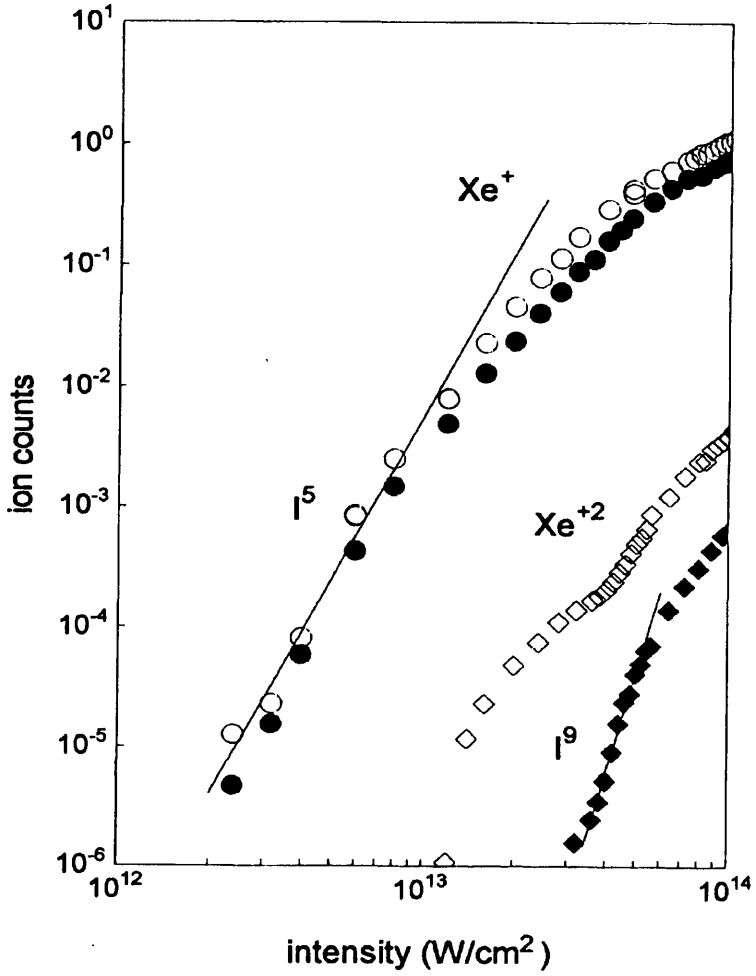

Figure 1.4: Singly-charged (circles) and doubly-charged (diamonds) xenon ion yields produced by a 527 nm, 50 ps laser pulse, for linear- (open markers) and circular-polarization (filled markers). Reproduced from [5].

Figure 1.4 shows ionization yields for xenon in a 50 ps, 527 nm laser pulse. When $\log(\Gamma_{\mathrm{MPI}})$ is plotted, the gradient of the ion yield in the MPI regime is N, the number of photons required. As the intensity increases, and therefore γ decreases, the MPI contribution to the overall yield is actively reduced as described previously, and the signal results from a mixture of MPI and TI behaviour.

The Schrödinger equation for atomic systems cannot be solved exactly in a direct fashion. Keldysh's approach treated the tunnelling electron using the

Gordon-Volkov wavefunction [6, 7] describing the interaction of a free electron with a plane-wave field, which can be solved exactly. However, Keldysh neglected the effect of the Coulomb potential. After tunnelling into the continuum, the outgoing electron may remain in the vicinity of the parent ion, in which case the continuum electron wavefunction deviates from the Volkov plane wave [8]. The Coulomb effects cannot therefore be neglected. For multiply-charged ions, considering the Coulomb potential becomes increasingly important, as its influence on the outgoing electron will strengthen with successive charge states. Perry *et al.* [9] studied multiple ionization of argon, krypton and xenon at 586 nm for $\gamma = 1.5$ - 4, comparing their results to the full version of Keldysh's original formulation. They conclude that the discrepancy between their experimental results and Keldysh theory, which becomes larger with increasing charge state, is due to the exclusion of Coulomb potential effects.

In 1966–67, Perelomov, Popov and Terent'ev (PPT) [10–12] developed Keldysh's tunnelling rate calculations by including corrections to the tunnelling rate due to the effects of the Coulomb potential. This resulted in the successful prediction of ionization rates for $\gamma \leq 3$ - 4 [3, 13].

In 1986, Ammosov, Delone and Kraĭnov (ADK) [14] used [10] as a starting point, deriving tunnel ionization rates for complex atoms in arbitrary states. Popov [15] identifies the ADK theory as a special case of the generalized PPT formula. ADK can dramatically underestimate the yield in the MPI regime [13], but is found to converge with the generalized PPT formula for $\gamma < 0.5$ [16]. Therefore, since ADK features a significantly less complex Coulomb correction factor, its ease of implementation and integration has led to it often being used as a comparison for experimental data [17, 18].

Alternative treatments by Reiss [19] in 1980 and Szoke [9] in 1988 are based on the Keldysh-Faisal-Reiss (KFR) formulation of S-matrix theory [2, 19, 20]. These

theories were found to make reasonable qualitative predictions of the variation of tunnel rate with intensity, but there is a significant quantitative offset in comparison to experimental data [13,21] since they also do not include the influence of the Coulomb potential on the outgoing electron.

A large number of investigations of atomic tunnel ionization occurred during the 1990s, using ADK theory for comparison. Auguste *et al.* [22] used linearly- and circularly-polarized 1053 nm, 1 ps pulses to produce ion yield data for multiply-charged helium, neon, argon and xenon over a peak intensity range 10^{13}–10^{18} W/cm^2. For circular polarization, results were found to be satisfactorily described by ADK theory. However, for linear polarization, discrepancies emerged at low intensities. With improved sensitivity, subsequent experiments such as those by Walker *et al.* [5,18] and Larochelle *et al.* [17] were able to resolve these discrepancies as distinctive 'knee' structures, which were proportional to the experimental and theoretical yields of the previous charge states (see Figures 1.7 and 1.8 in Section 1.2).

In 2005, the intense-field many-body S-matrix theory (IMST) of Becker and Faisal [23] took into account the Coulomb interaction, laser interaction and intermediate states of the ionizing atom using a flexible *ab initio* approach; it was also not limited to a single active electron. IMST successfully reproduced the characteristic knee in the ionization yield for linear polarization. The predictions of the IMST are compared to helium data from Walker *et al.* [18] in Figure 1.5. Becker and Faisal were able to provide evidence that the 'knee' was a result of recollision ionization, whereby electrons removed from the atom in a linearly-polarized field are driven back towards the parent ion, which may cause additional ionization by removal of another electron when it collides with the core. However, in a circularly-polarized case, the electron is driven on a path where it is unlikely to

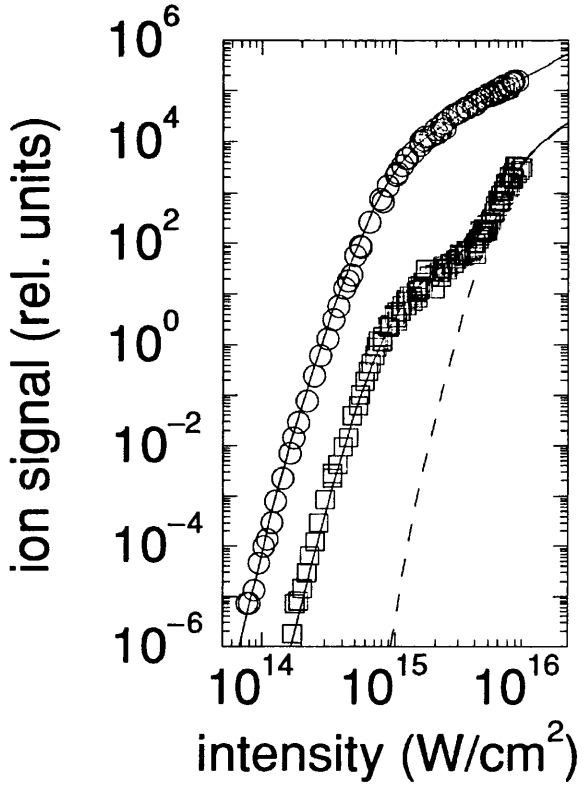

Figure 1.5: IMST predictions of intensity-dependent He ionization yields at 780 nm (solid lines) by Becker and Faisal [23], compared to data from Walker *et al.* [18] for singly-ionized (circles) and doubly-ionized helium (squares). The dotted line shows the IMST prediction for sequential ionization only. Reproduced from [23].

recollide; the 'knee' is therefore suppressed. Recollision will be discussed in more detail in Section 1.2.

Other *ab initio* techniques include the R-matrix methods of Lysaght *et al.* [24–26], where the Schrödinger equation is solved for multielectron atoms interacting with ultrashort pulses of ultraviolet wavelengths. The atom is split into two regions: an inner region considering all interactions between the electrons and the laser field; and an outer region considering only long-range effects on the outgoing electron. The method is in good agreement with ADK theory at

high intensities, and has resulted in successful predictions of electron momentum distributions.

Modern laser technology now allows for the production of few-cycle pulses (FCPs) [27–34]. Some of the techniques used to produce ultrashort pulses will be described in more detail in Chapter 2. FCPs provide opportunities to rigorously test atomic ionization theory. However, most models previously described [2,9–12,14,19] calculate cycle-averaged rates, and assume adiabatic tunnelling, which is inappropriate in a situation where the ionization dynamics can vary significantly between cycles, as occurs in intense FCPs.

In 2001, Yudin and Ivanov [3] derived expressions for nonadiabatic instantaneous ionization rates for arbitrary γ, with applicability to FCPs. The Yudin and Ivanov theory takes the general form [3]

$$\Gamma(t) = N(t)\exp\Big(-\frac{\varepsilon^2 f^2(t)}{\omega_L^3}\Phi(\gamma(t),\theta(t))\Big) \tag{1.6}$$

where $N(t)$ is the pre-exponential factor, ε is the electric field amplitude, $f(t)$ the envelope of the electric field, ω_L the laser period, and $\Phi(\gamma(t),\theta(t))$ a function which depends on the time-varying Keldysh parameter $\gamma(t)$ and the phase $\theta(t)$ of the oscillating laser field. This theory will be discussed in more detail and modified in Chapter 4.

1.2 Recollision and high-harmonic generation

Recollision is now known to be the dominant mechanism by which nonsequential atomic ionization takes place. The outgoing electron from an MPI or TI event is still in the vicinity of the parent ion and remains under the influence of the laser field. In some cases, the electron which is removed from the atom during one half

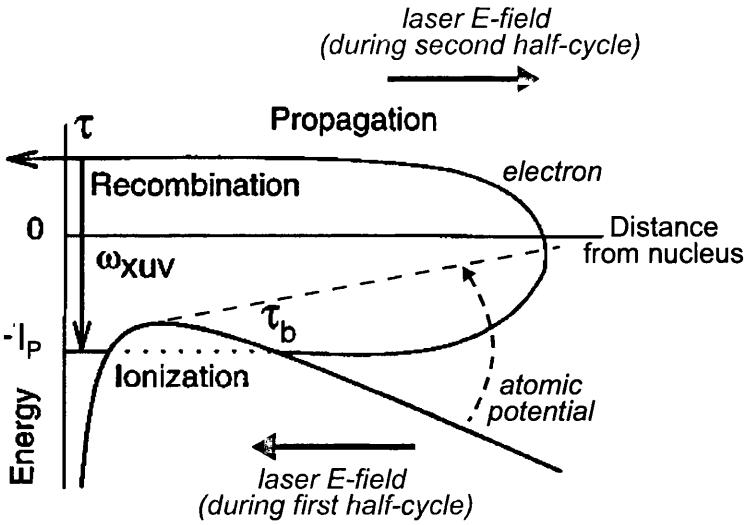

Figure 1.6: Illustration of Corkum's three-step model (ionization, propagation, recombination) of recollision ionization [35]. Starting at zero electric field, the magnitude of the electric field increases, reaches a maximum $\frac{1}{4}$-cycle later, and decreases again to zero after another $\frac{1}{4}$-cycle. The electric field distorts the atomic potential (maximally $\frac{1}{4}$-cycle after zero field), allowing an electron to tunnel through the suppressed Coulomb barrier, which appears in the continuum at time τ_b. Depending on the electric field magnitude at the point of release, it is initially driven away from the ion, then back towards it when the field direction reverses, having gained energy as a result of the ponderomotive potential. The returning electron can now recollide with the core, or recombine at time τ releasing a high-energy XUV photon, ω_{XUV}. Adapted from [36].

of the laser period can be driven back towards the atom within the same cycle when the field direction reverses, recolliding with the ionic core.

Corkum [35] explains this with a purely classical 'simple-man's' or three-step model, as illustrated in Figure 1.6. The electron is removed from the atom or ion, then driven away from the ion by the laser field. For a linearly-polarized pulse, the electron is driven back towards the parent ion with increased kinetic energy when the field direction reverses, where it either recollides or recombines with the core. In recollision, the free electron impacts on the core and causes further ionization by removal of an additional electron. In recombination, the electron gives up its excess kinetic energy as a high-energy photon. The probability of either process

occurring decreases with decreasing ellipticity, with a minimum probability for circular polarization, since the increased angular momentum drives the electron on a helical trajectory which takes it further from the core with each cycle.

Except for IMST, the tunnelling theories summarised in Section 1.1 describe sequential ionization, assuming a single active electron (SAE) interacts with the laser field for each charge state. For circular polarization, experimental data is relatively well-described, but see Section 1.3 on multielectron effects for a more detailed discussion. For linear polarization, additional contributions to the ion yield are observed for multiply-charged ions and found to be proportional to the behaviour of previous charge states. Figure 1.7 shows the comparison of ADK tunnel theory and experimental data for doubly-ionized neon. Figure 1.8 shows a similar comparison for multiple charge states of xenon.

There were three proposed mechanisms for nonsequential ionization. Fittinghoff *et al.* [39] proposed 'shake-off', whereby the atomic configuration rearranges due to the removal of an electron, resulting in another electron being promoted to the continuum. Corkum [35] suggested recollision as described previously. A third possibility of collective multielectron tunnelling was also proposed by Eichmann *et al.* [40]. The IMST [23, 41] indicated recollision was the best description for the process, successfully describing experimental results from [18] for several ions, as shown in Figure 1.5. In 2000–1, conclusive experimental proof of recollision as the dominant mechanism came from cold-target recoil-ion momentum spectroscopy (COLTRIMS), which gave a complete kinematical understanding of the electron-ion system following ionization. For photoionization experiments, COLTRIMS [42] crosses an intense laser focus with a carefully-prepared supersonic gas jet target. Figure 1.9 illustrates a typical supersonic expansion: a gas at pressure P_0 accelerates due to the decreasing area of the nozzle and the pressure difference between P_0 and the background pressure, P_b. If

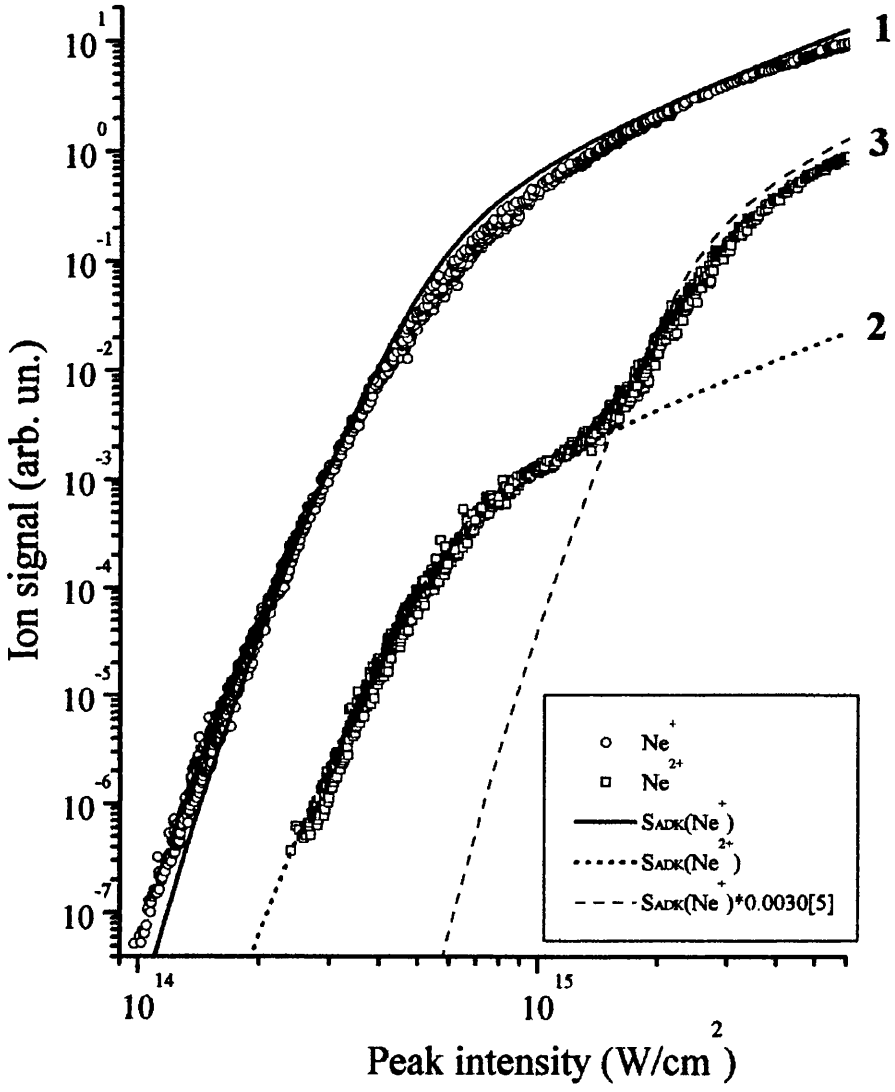

Figure 1.7: Ne^+ (open circles) and Ne^{2+} yields (open squares) for an 800 nm, 200 fs laser pulse. The solid line (1) and dotted line (3) are the sequential ADK predictions [14], dotted line (2) has been scaled to fit the data and is proportional to (1). Reproduced from [17].

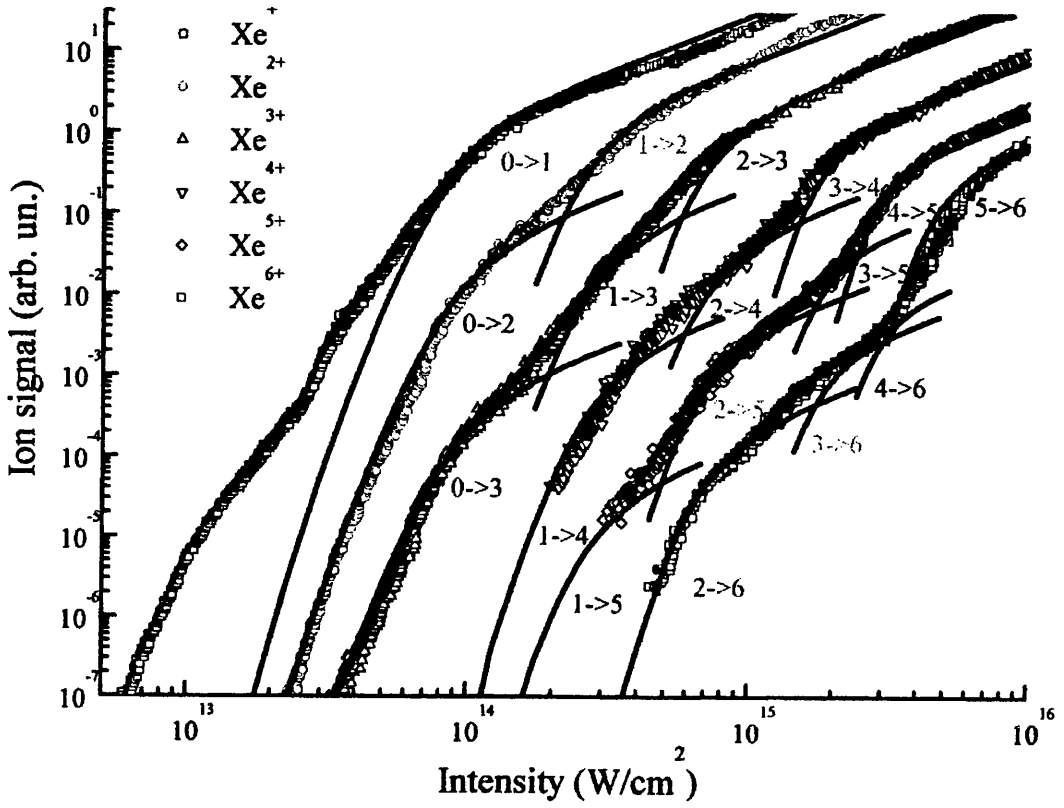

Figure 1.8: Multiple ionization of xenon using an 800 nm, 200 fs laser pulse. Experimental results of Larochelle *et al.* [17] are compared to ADK theory [14] which (for nonsequential ionization) have been scaled vertically to fit the data. The ionization channels leading to each feature in the ion signal are labelled according to the form $i \rightarrow j$, where i and j correspond to the charge state of the ion (equivalent to $Xe^{i+} \rightarrow Xe^{j+}$). Reproduced from [17].

$(P_0/P_b) \gtrsim 2.1$, the pressure at the exit becomes independent of P_b. Without the constriction of the nozzle, the gas expands supersonically. The internal energy of the gas is converted to the increasing flow velocity in the 'zone of silence' identified in Figure 1.9, up to a terminal velocity which depends on the atomic/molecular weight and the initial temperature. As a consequence, the temperature of the jet decreases with distance from the nozzle, as shown in Figure 1.10 [37]. The recoil energy of the ions during ionization can therefore be significantly lower than the kinetic energy at room temperature. Using well-characterised electric and magnetic fields, the ions and electrons are guided towards position-sensitive detectors.

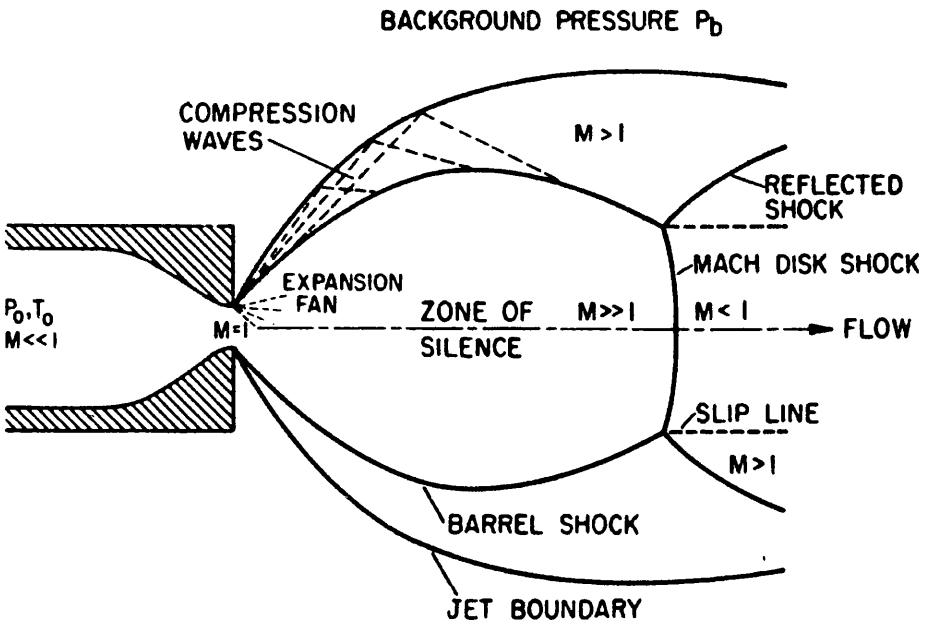

Figure 1.9: Illustration of a supersonic jet expansion for a gas at initial pressure P_0 and temperature T_0. M is the Mach number, indicating the speed of the gas ($M = 1$ is the speed of sound). Ion beams for COLTRIMS are extracted from the 'zone of silence'. Reproduced from [37].

From the impact position and time-of-flight, the momenta of the electrons and ions can be uniquely calculated. The detection efficiency of each individual ion or electron may be near 100%, but in coincidence measurements there will be a significant number of 'false coincidences', where electrons and ions arrive at the detector at the same time but did not originate from the same atom. Additionally, depending on the intensities used and the tunnelling dynamics investigated, the ion count rate may be low ($\sim$ 10%). In tunnelling, the electron and ion momenta are expected to be equal, but in opposite direction, thereby providing a method by which the background of false coincidences can be removed from the results. Figure 1.11 shows the argon electron-ion coincidences for a 220 fs, 800 nm laser pulse with a peak intensity of 3.8×10^{14} W/cm^2. True coincidences are expected to lie along the antidiagonal of the plot.

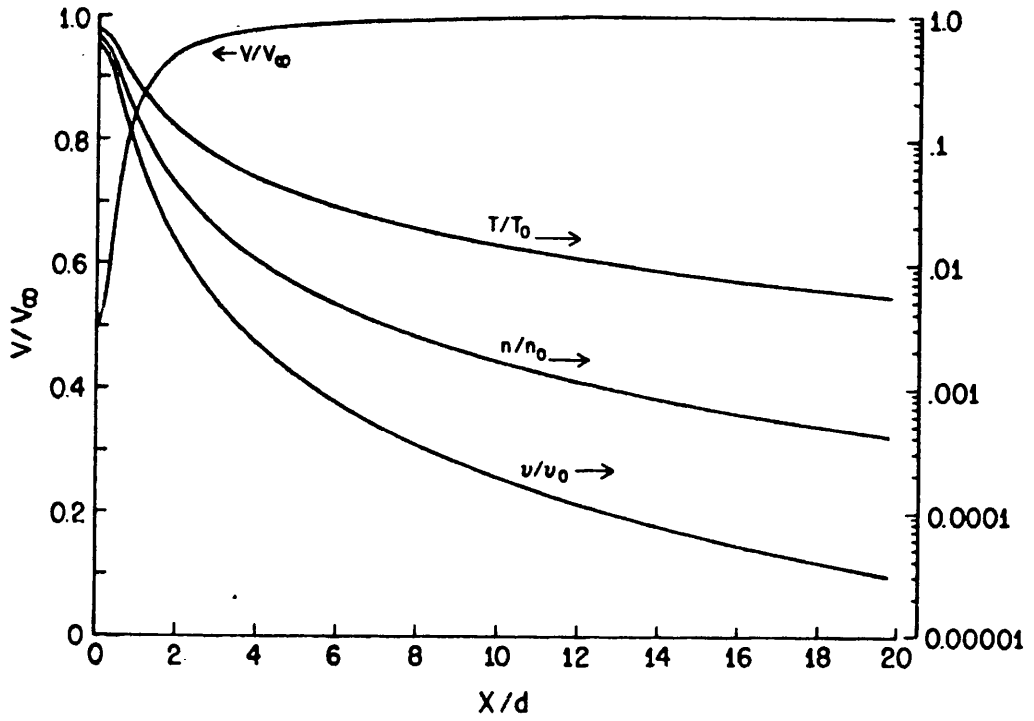

Figure 1.10: Properties of an ideal atomic gas as a function of distance from nozzle (in nozzle diameters) in a supersonic expansion. V = velocity, V_∞ = terminal velocity, T = temperature, n = density and ν = collision frequency. T_0, n_0, ν_0 denote the values of the same quantities in the region behind the nozzle throat and exit. Reproduced from [37].

In the shake-off and collective tunnelling scenarios, the electrons were predicted to have a distribution centred around zero momentum, being released near-simultaneously at maximum field strength. In the case of recollision however, there is a significant time delay between the release of the first electron and the release of one or more subsequent electrons on recolliding with the parent ion. As recollision predominantly occurs at a zero of the electric field, this results in a large final drift momentum and momentum transfer between the electrons. A double-peaked structure appears in the direction parallel to the polarization direction for multiply-charged ions [41,43], in stark contrast to the single-peak for the singly-charged ion. Figures 1.12 and 1.13 show the electron momentum results

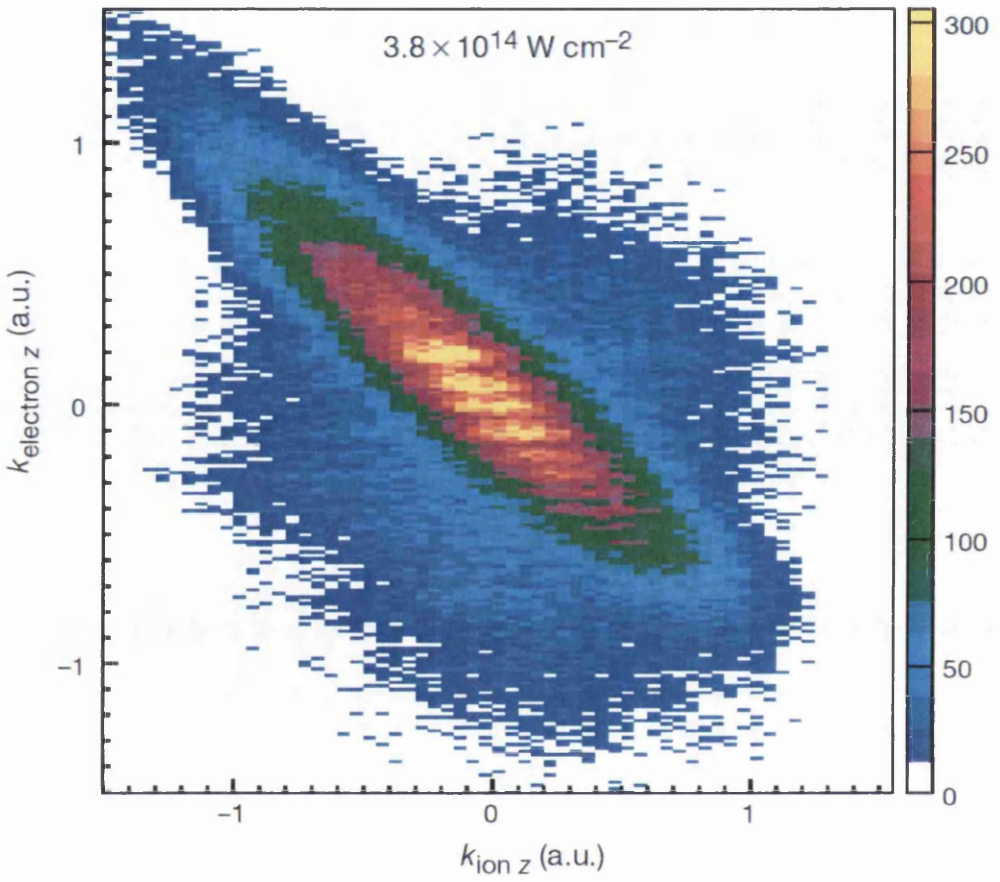

Figure 1.11: COLTRIMS electron-ion coincidence measurement for argon ionization in a 220 fs, 800 nm pulse with a peak intensity of 3.8×10^{14} W/cm^2. Momenta are recorded along the laser polarization axis. Reproduced from [38].

obtained for singly- and multiply-charged neon electron momentum distributions from [41].

Figure 1.14 shows the momentum correlation of the electrons released when Ar^{2+} is produced by a 220 fs, 800 nm laser pulse. At 3.8×10^{14} W/cm^2, a substantial contribution to the nonsequential ion yield is expected, and this corresponds to a strong correlation for non-zero electron momenta. The peaks lie along the direction labelled k_z^+, indicating the electron momenta are dominated by the

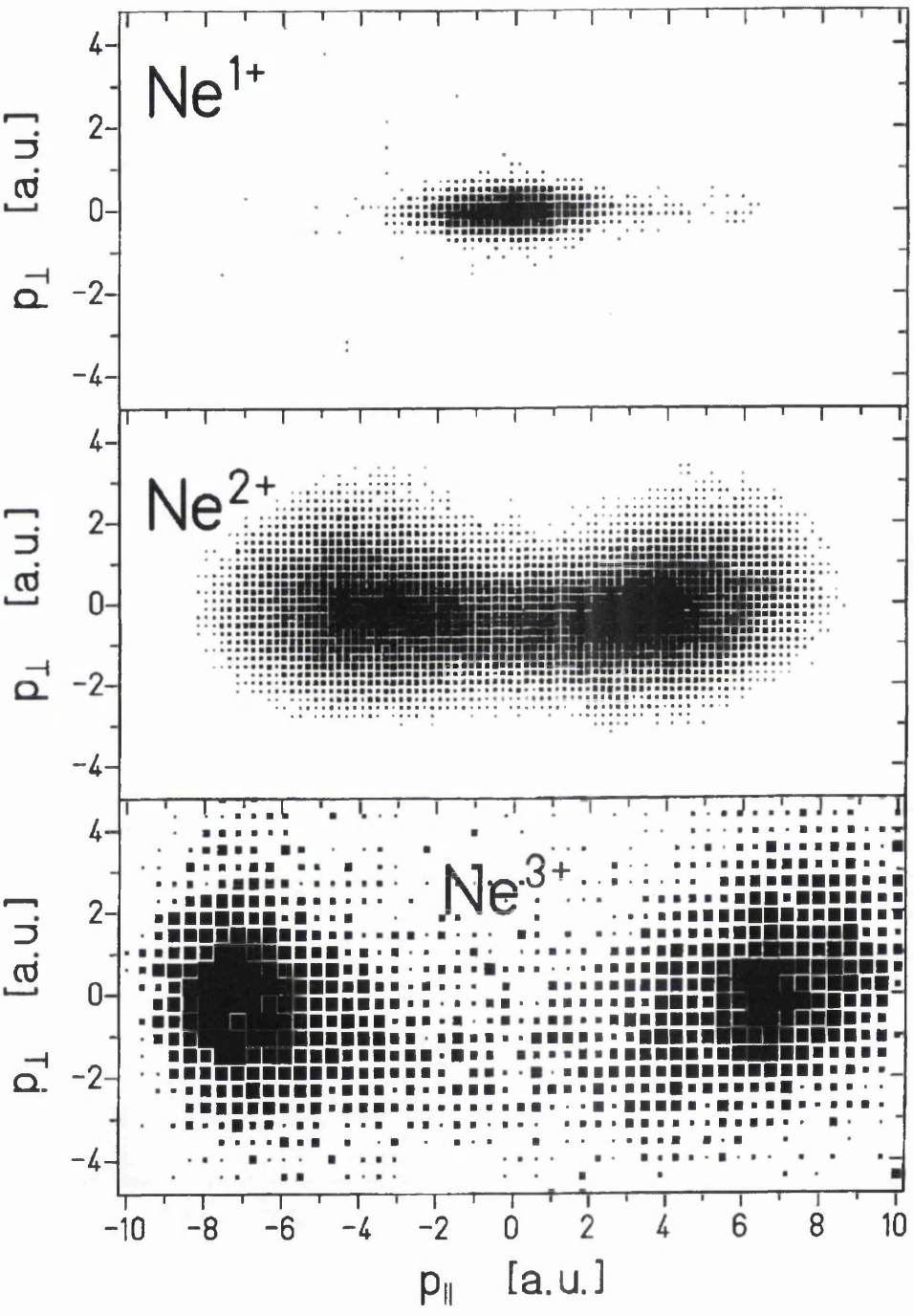

Figure 1.12: Two-dimensional COLTRIMS measurements for Ne using 30 fs, 795 nm laser pulses. Reproduced from [41].

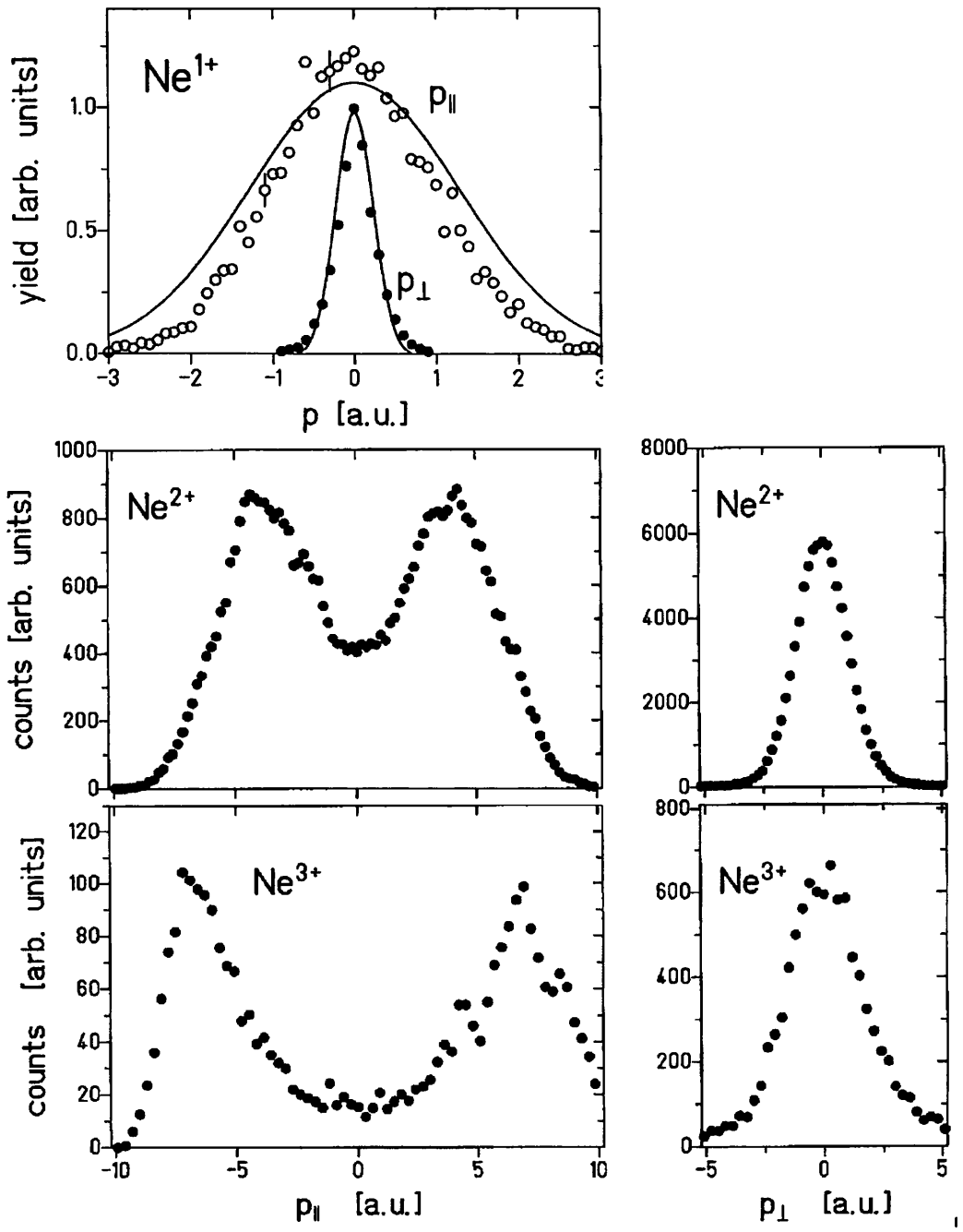

Figure 1.13: Projections of the COLTRIMS measurements from Figure 1.12 onto the axis parallel ($p_\parallel$) and perpendicular ($p_\perp$) to the polarization direction. The distinctive double-peak in the $p_\parallel$-direction for Ne^{2+} and Ne^{3+} is due to recollision. Reproduced from [41].

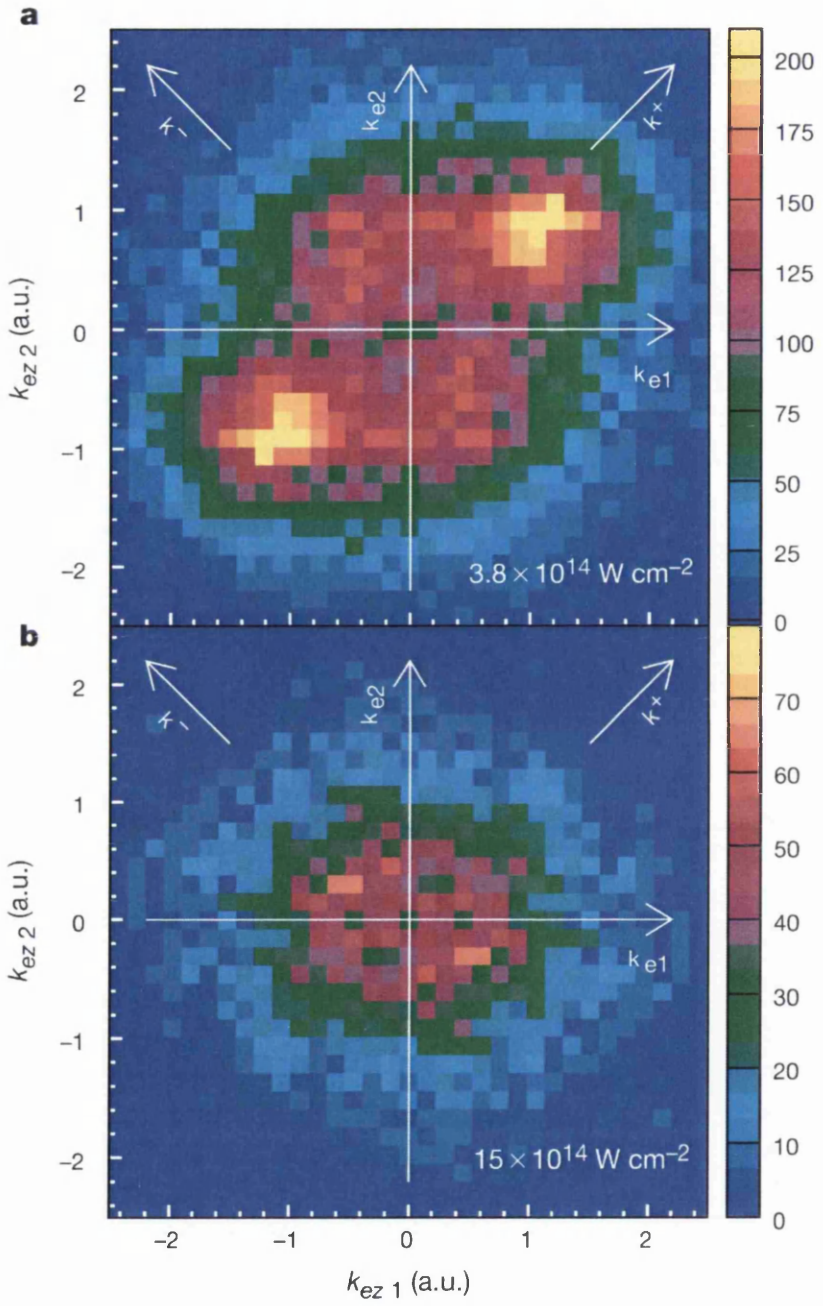

Figure 1.14: COLTRIMS electron-electron correlation measurement (a) for a peak intensity of 3.8×10^{14} W/cm^2, where nonsequential ionization is significant, and (b) 15×10^{14} W/cm^2, where sequential ionization is dominant. Reproduced from [38].

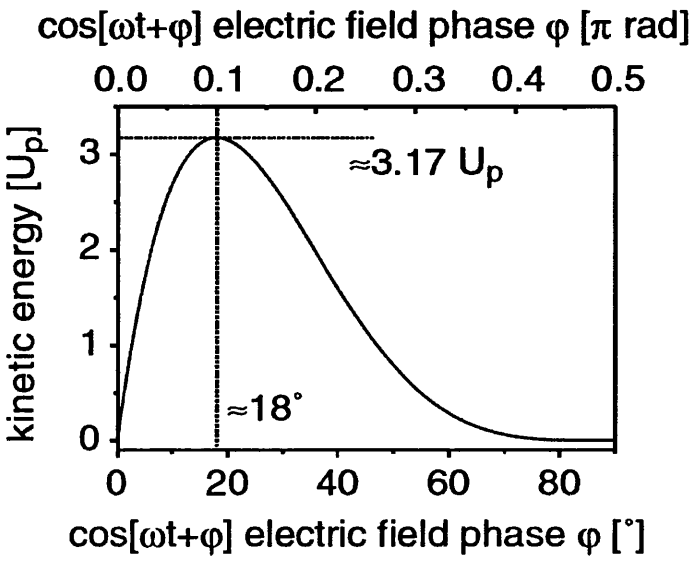

Figure 1.15: Kinetic energy gained by the electron as a result of the ponderomotive potential, U_p, as a function of the phase φ of the laser pulse at which the electron is released into the continuum. Reproduced from [44].

driving laser field and not by electron-electron repulsion (which would result in a wider distribution in the k_z^- direction). At a higher intensity, 15×10^{14} W/cm^2, the strong correlation is lost, corresponding to sequential ionization becoming dominant.

The energy gained by the recolliding electrons depends on the point at which tunnel ionization takes place in relation to the phase of the laser radiation, reaching a maximum at the classical 'cut-off' at [45]

$$E_c = \hbar\omega_c \sim I_p + 3.17U_p \tag{1.7}$$

A graph of this dependence is shown in Figure 1.15.

The probability of the electron recolliding with the core depends on the ellipticity, ε, of the laser field. For increasing ellipticity, the electron is driven on an increasingly helical trajectory, making a re-encounter with the core unlikely,

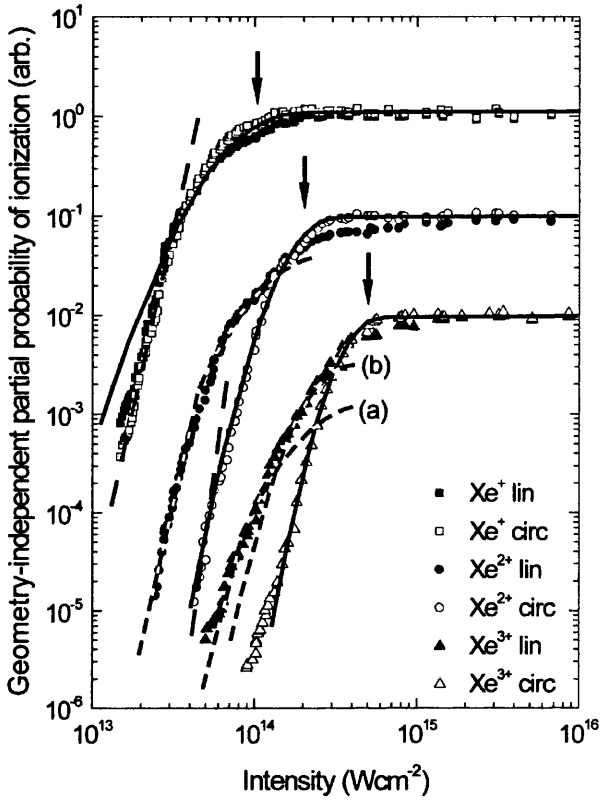

Figure 1.16: Experimental xenon ionization probabilities for a 50 fs, 790 nm linearly- (filled markers) and circularly-polarized (open markers) laser pulse. (solid line) ADK tunnelling theory, (long dashed line) MPI prediction, (short dashed line) ADK of previous charge states, scaled to the data to show proportionality of extra contribution to the linear yield due to recollision. The deconvolution procedure does not work above saturation, therefore the recovered probabilities flatten. Reproduced from [46].

with the probability minimised for circular polarization $\varepsilon = 1$. An example of recollision suppression in xenon is shown in Figure 1.16.

When the electron recombines with the ionic core, rather than resulting in the ejection of another electron, it releases the energy gained as a high-energy photon. This process is exploited in high-harmonic generation (HHG) [45, 47]. Typically an intense linearly-polarized NIR drive pulse is focused into a gas jet [48–55],

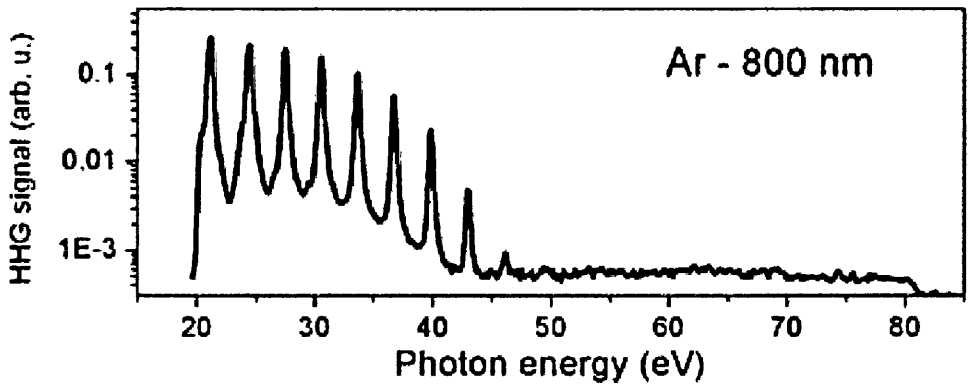

Figure 1.17: Argon HHG spectrum produced by an 800 nm, 30 fs laser pulse, focused to a peak intensity of $\sim 10^{14}$ W/cm^2 in an argon gas jet. The peaks correspond to odd harmonics of the fundamental drive laser frequency. Reproduced from [56].

resulting in the generation and collinear propagation of the fundamental NIR and odd harmonics up to XUV wavelengths.

XUV radiation is typically produced only at odd harmonics of the driving laser frequency, since most HH-generating media possess inversion symmetry. Odd harmonics are produced up to the cut-off given by Equation (1.7). An example HHG spectra is given in Figure 1.17 for argon using an 800 nm drive laser.

The phase at which ionization occurs also determines the trajectory followed by the outgoing electron. Not all trajectories will result in recollision or recombination, even for a linearly-polarized pulse. The classical trajectories are modelled in Figure 1.18, and the trajectory with maximum recollision energy corresponds with Figure 1.15 ($\varphi \sim 20°$). This means that the highest harmonics will be emitted as a pulse train, producing a subfemtosecond or attosecond burst of XUV radiation every half-cycle near the zeroes in the electric field, peaking when the electron is released at $\varphi \sim 18°, 198°$.

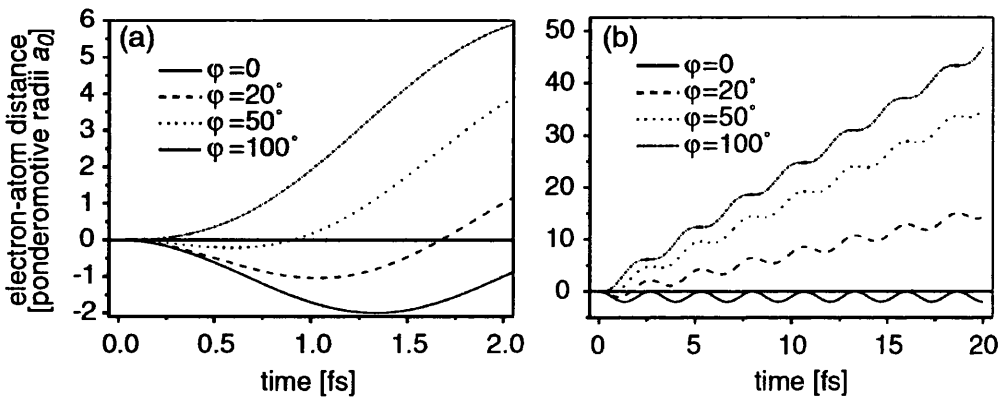

Figure 1.18: Electron trajectories as a function of phase φ at which the electron is released into the continuum. Only some trajectories result in the recollision. Reproduced from [44].

The macroscopic effects of focusing the driving laser into the target gas can limit the harmonic yield [36] through absorption, dephasing and (at high intensities) defocusing. HH photons may be absorbed by the gas target itself, due to core excitation. Additionally, for any laser focus, the wavefront phase will not be uniform over the entire focal volume. As such, HHG will occur at different phases throughout the interaction volume of the drive laser and gas jet. Changes to the spatial profile can improve this phase-matching [47,57]. There will also be nonlinear distortions to the focus caused by the generated plasma.

The geometric effects of propagation through a typical attosecond beamline on the wavefront phase and focal volume intensity distribution are covered in [58], which will be discussed in Chapter 6.

1.3 Multielectron effects

The tunnel theory described in Section 1.1 assumes that the outermost electron is removed from the atom without affecting the remaining ion core. As a result, this ignores the possibilities of excitation of the core due to the outgoing electron, and direct tunnelling of electrons other than the highest-lying.

Inspired by [40], Zon *et al.* [59] developed the ADK theory [14] to include nonsequential tunnelling of N equivalent electrons, e.g. $N = 6$ in the outer $5p$ shell of ground-state xenon. This multielectron tunnel ionization (METI) theory was further developed by Kornev *et al.* [60] to include the effects of core excitation, where the outgoing electron results in the population of excited states through shake-up (inelastic tunnelling). The output of the Kornev model is shown and compared to ADK [14] theory in Figure 1.19.

In many experiments [17, 22], the ion yield from the full signal producing volume is recorded. As the intensity increases, and therefore γ decreases, the yield changes from MPI-dominant behaviour (gradient N, where N is the number of photons required for MPI) to a mixture of MPI and TI (gradient $\neq N$), and OBI where the yield is said to be saturated. At this point, for a Gaussian focus the gradient is $\frac{3}{2}$ [62], dominated by the increase in the signal-producing volume with increasing intensity. This is illustrated in Figure 1.20. For any comparisons, the full focal volume must be reintroduced to the tunnel theory. Focal averaging of both the theory and experimental data therefore obscures the saturation point and tunnelling behaviour, which would make a conclusive comparison of METI and non-METI theory with experimental data difficult.

Varying the intensity in the full-volume case requires the laser power to be adjusted or the beam to be attenuated, which reduces the count rate dramatically. Additionally, the focal geometry and/or temporal characteristics of the

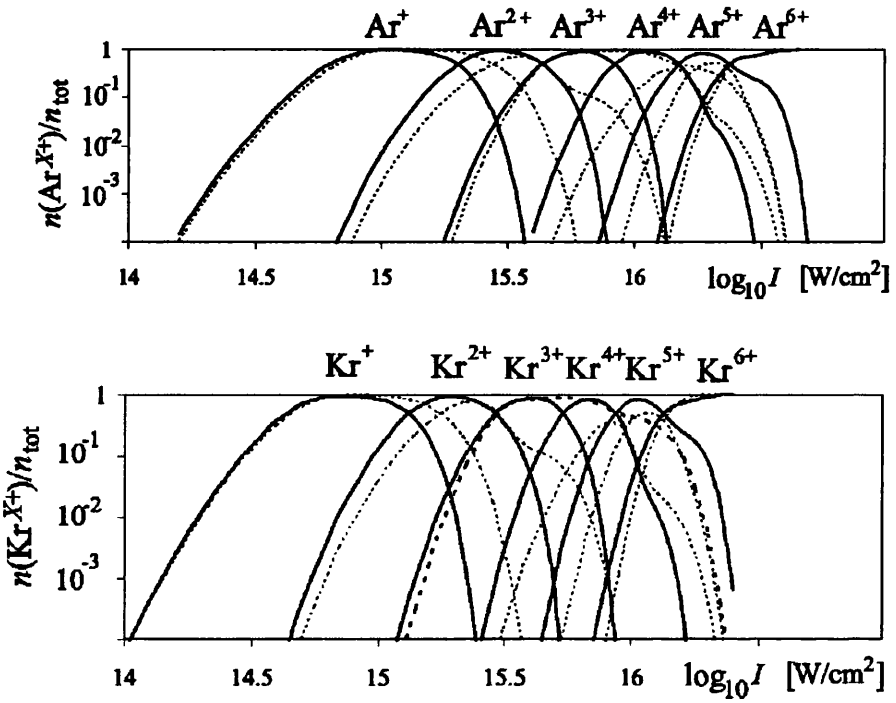

Figure 1.19: Comparison of the intensity-dependent ionization probabilities predicted by the METI (solid lines) and ground-state-only models (dotted lines) by Kornev *et al.* [60] for argon and krypton ionized by an 800nm, 50 fs circularly-polarized pulse. The ground-state-only models exclude the core excitation ionization channels, and are therefore equivalent to the predictions of sequential ADK theory [10, 14, 61]. Reproduced from [60].

laser pulses may be affected, especially if additional material is introduced in order to attenuate the beam. In 1996–8, Van Woerkum and coworkers [63–65] proposed and utilised a scheme to avoid these undesirable effects and circumvent the need for focal averaging, by keeping the focal conditions constant and scanning the signal-producing volume using a thin slit or aperture. This technique is known as intensity-selective scanning (ISS), since for a slit width/aperture diameter $\Delta z < z_R$, where z_R is the Rayleigh length of a Gaussian focus, the variation of the signal in z can be assumed to be small. An illustration of the difference between full-volume and ISS techniques is shown in Figure 1.21; in ISS, low-intensity

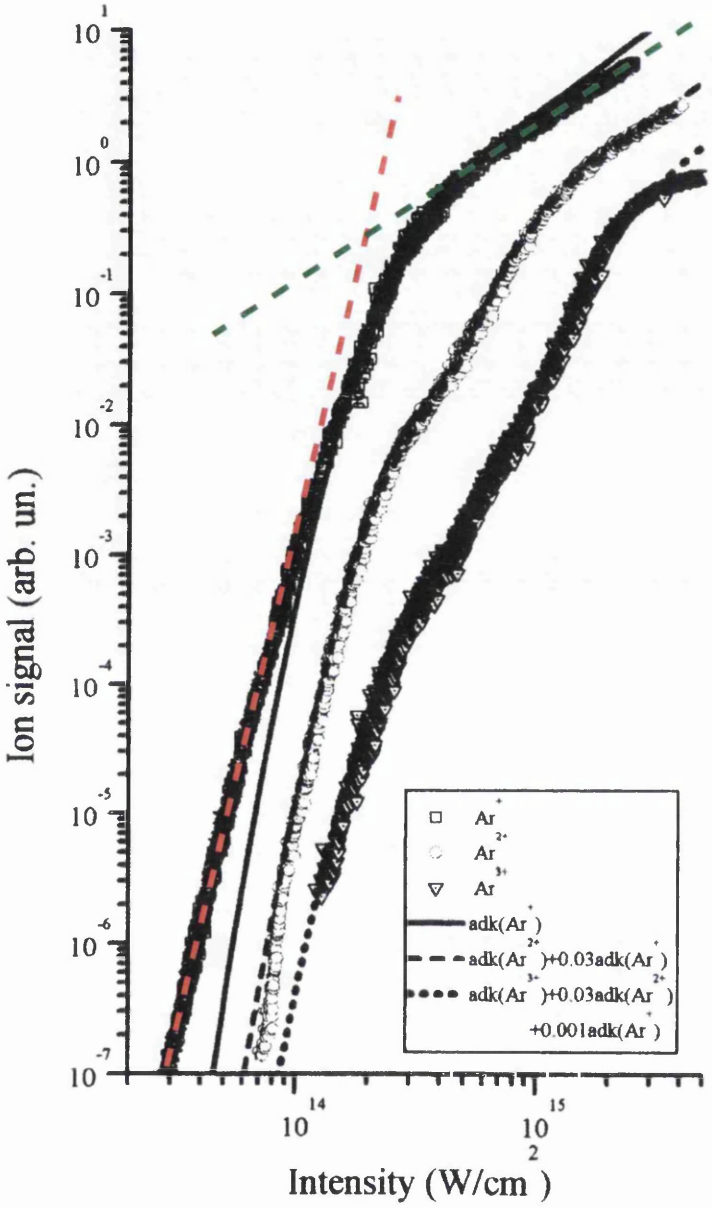

Figure 1.20: Argon ionization yields for an 800 nm, 200 fs pulse. The MPI contribution (red dotted line) has a gradient of ~9, indicating a 9-photon process. Above saturation, the gradient is $\frac{3}{2}$ (green dotted line) due to the expansion of the Gaussian focal volume with increasing intensity. Adapted from [17].

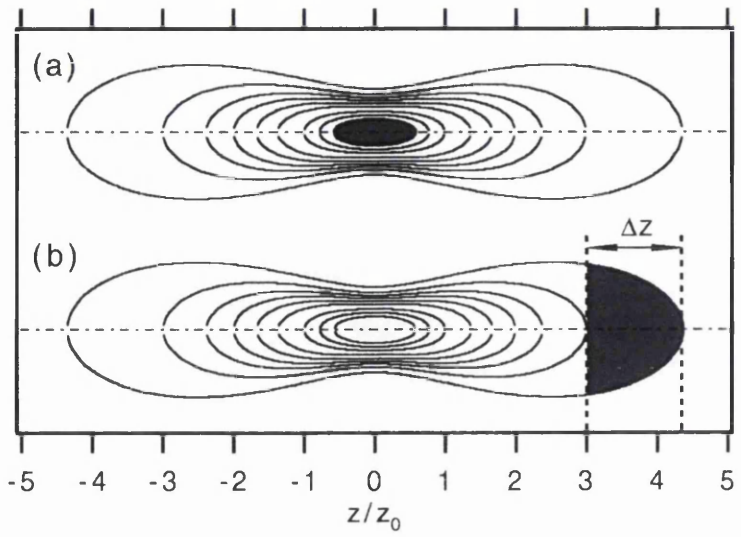

Figure 1.21: Section of the focal volume which dominates the detected signal in the (a) full-volume and (b) ISS case, where the detected volume is limited by a slit of width Δz. Reproduced from [64].

behaviour can be selected so as not to be dominated by high-intensity signal closer to the centre of the focus.

In the full-volume case, the detected signal is effectively a convolution of the ionization probabilities and the entire three-dimensional focal geometry. In 1998, Walker *et al.* [65] introduced the deconvolution technique, enabling the extraction of the ionization probabilities directly from experimental data. Using ISS for the condition $\Delta z < z_R$, the signal is reduced to a convolution of the ionization probabilities and the on-axis intensity distribution, $I_{\mathrm{ax}}(z)$, such that

$$P(I_{\mathrm{ax}}(z)) \propto \left(\frac{I_{\mathrm{ax}}(z)}{dI_{\mathrm{ax}}(z)/dz} \right) \frac{d}{dz} \left[I_{\mathrm{ax}}(z) S(z) \right] \tag{1.8}$$

where P is the ionization probability, $I_{\mathrm{ax}}(z)$ is the on-axis intensity representative of the slice through the signal-producing volume, S is the ion signal i.e. the integrated ion yield in this case, and z is the axial position of the detector with respect to the geometric focus. The deconvolution procedure was adapted for a

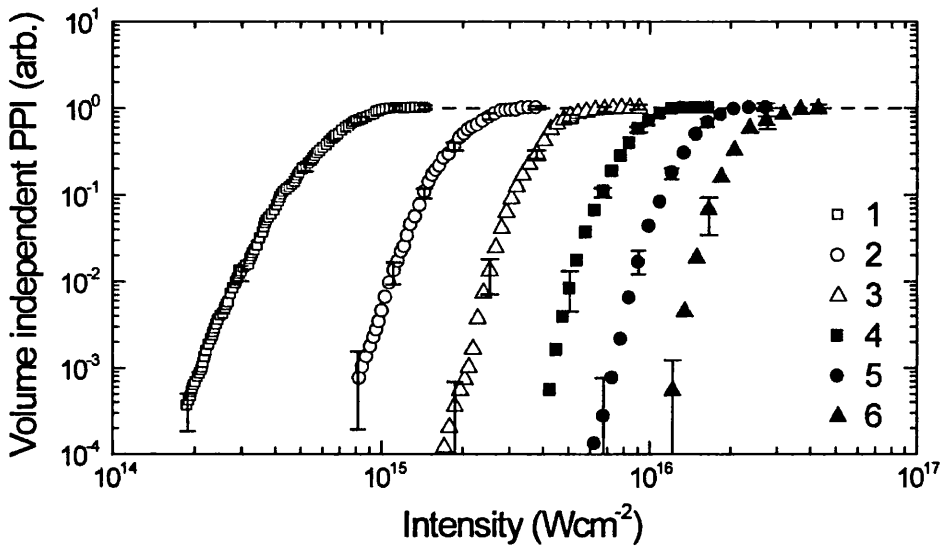

Figure 1.22: Deconvoluted ISS ionization probabilities for argon generated by a 790 nm, 50 fs laser pulse. The numbers in the key refer to the charge state ('1' for Ar^+, '2' for Ar^{2+} etc.). Reproduced from [66].

non-Gaussian focus by Bryan *et al.* [46] in 2006, in order to take into account the effects of diffraction in the beamline. An example of deconvoluted ISS results is shown in Figure 1.22.

Bryan *et al.* compared the ISS-deconvoluted recollision-free yields of argon [66] and krypton [67] to the predictions of Kornev *et al.* [60] and ADK [14] theory, finding them to be in superior agreement when METI and core excitation were taken into account, as shown in Figures 1.23 and 1.24, supporting the importance of considering multi-electron dynamics.

In contrast to the excitation previously described, it is also possible for electrons to directly tunnel from lower-lying orbitals. Though the probability of this process is low, in some cases it is not negligible. Akagi *et al.* [68] provided experimental COLTRIMS evidence for direct tunnel ionization from the highest-occupied molecular orbital (HOMO) and a lower-lying orbital (HOMO-1) for hydrogen chloride (HCl), with $I_p = 12.747$ and 16.265 eV respectively, comparing

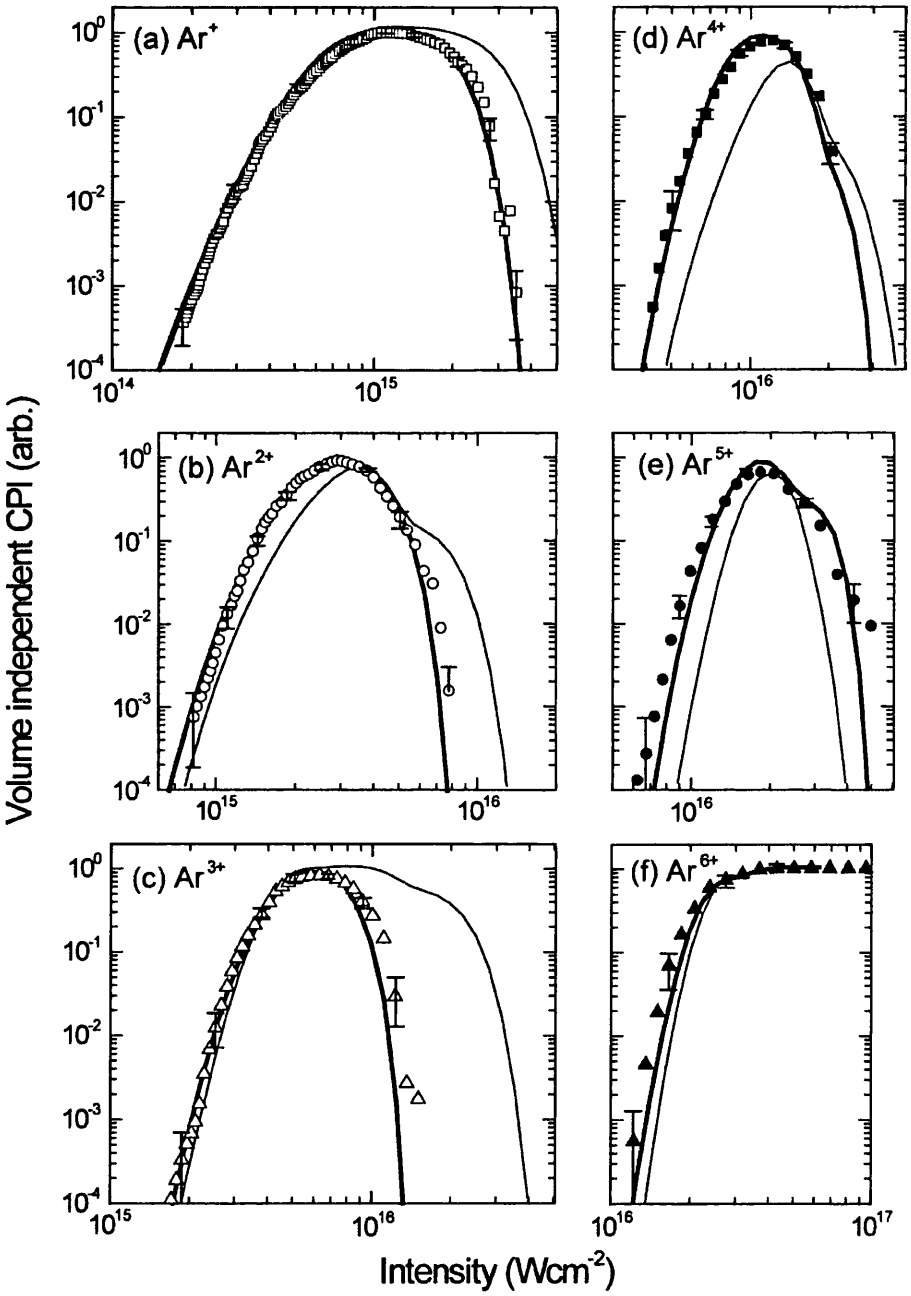

Figure 1.23: Ar^+ (open squares), Ar^{2+} (filled squares), Ar^{3+} (open circles), Ar^{4+} (filled circles), Ar^{5+} (open triangles) and Ar^{6+} experimental ion yields (filled triangles) measured by Bryan *et al.* [66] are compared to the METI (thick solid line) and ground-state-only ADK theory (thin solid line) as modelled by Kornev *et al.* [60]. Reproduced from [66].

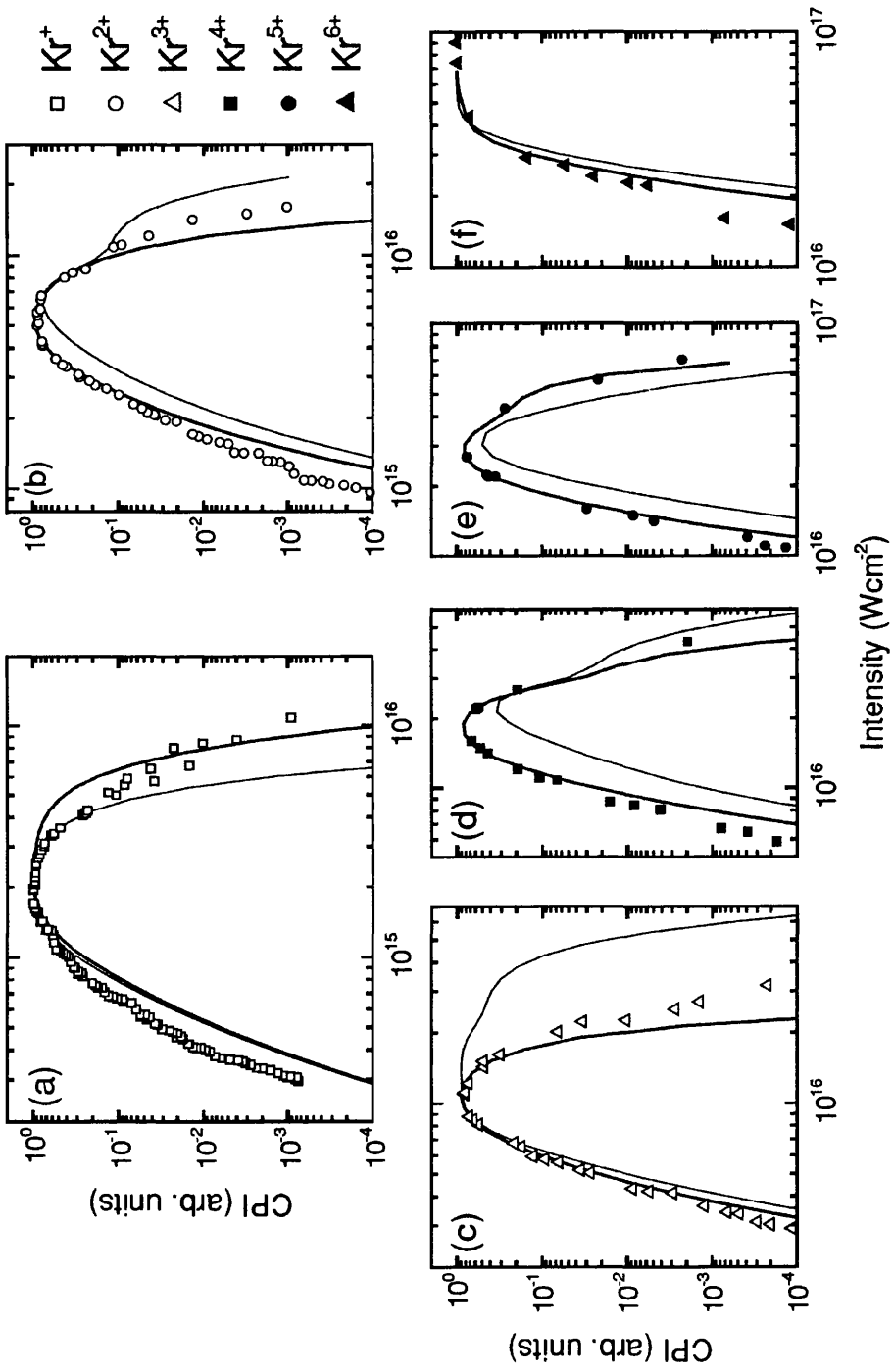

Figure 1.24: Krypton experimental ion yields measured by Bryan *et al.* [67] are compared to the METI (thick solid line) and ground-state-only ADK theory (thin solid line) as modelled by Kornev *et al.* [60]. Reproduced from [67].

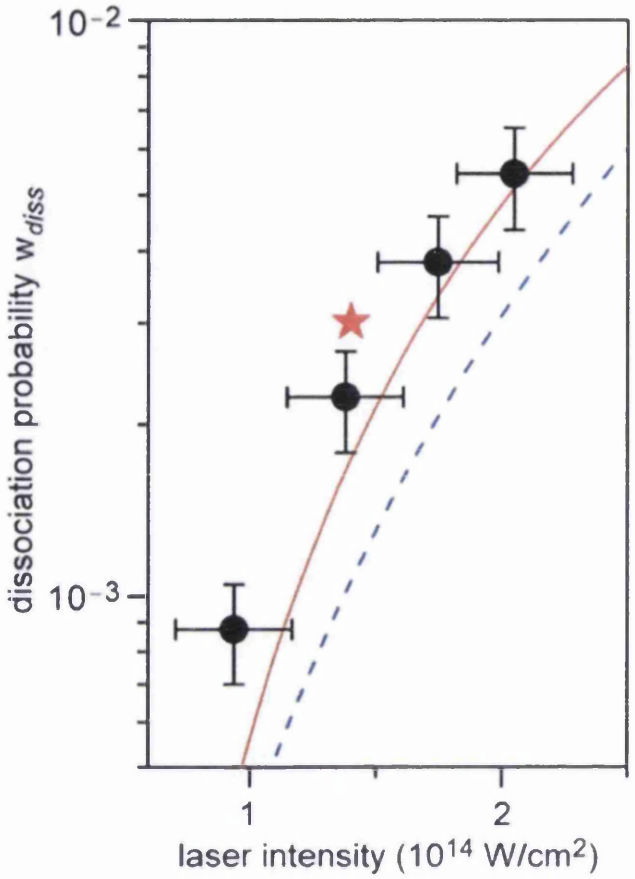

Figure 1.25: Ratio of measured dissociation probability from two different orbitals, $\Gamma_{\mathrm{HOMO}}/\Gamma_{\mathrm{HOMO\text{-}1}}$, following ionization from HOMO and HOMO-1 respectively (filled circles) is plotted and compared to ADK theory for the same process (red solid line) and for bond softening (black dotted line). Reproduced from [68].

their results to *ab initio* simulations. Circular polarization was used to suppress recollision. In this case, electron-ion coindicence measurements were used to spatially distinguish the yields from the HOMO and HOMO-1. The ratio of the dissociation probabilities following removal of an electron from the two levels, $\Gamma_{\mathrm{HOMO}}/\Gamma_{\mathrm{HOMO\text{-}1}}$ was calculated and compared to an ADK model for dissociation due to ionization from the two orbitals, and dissociation via bond softening, the results of which are shown in Figure 1.25. The data is found to be best described by the former, within error.

In 2011, Shiner *et al.* [69] have shown experimental evidence of collective multi-electron dynamics influencing high-harmonic generation in xenon. They observe a contribution to the high-harmonic spectrum due to the $4d$ orbital, despite the direct tunnel ionization yield being negligible compared to the outermost $5p$ orbital. Measured photoionization cross-sections are compared to a model based on the strong-field approximation (SFA) and found to be in agreement. The authors attribute the results to inelastic scattering resulting in the population of an excited state as illustrated in Figure 1.26. This is similar to to the excitation mechanism described by [59] in the recollision-free case.

The modelling of tunnel ionization in the present work is described in Chapter 4, where direct tunnel ionization is allowed from multiple levels in the xenon atom. This is in contrast to [60], as lower-lying electrons are assumed to tunnel directly to the continuum without interacting with the remaining bound electrons, albeit with a lower probability of ionization due to the increased ionization potential for states above the ground-state ionization threshold.

1.4 Conclusion

Multiphoton and tunnel ionization processes have been discussed, with landmark experimental and theoretical work reviewed. Experimental results for multiple ionization yields confirm the existence of excitation due to inelastic tunnelling. The characterisation of multielectron dynamics in atoms will lead to a better understanding of more complex systems, such as molecules, clusters and other nanoscale targets, and solids, where electron correlation effects become increasingly important. Recollision processes and therefore the generation of correlated electrons can be controlled using carrier envelope phase (CEP) stabilised FCPs, enabling the control and optimization of high-harmonic generation, leading to the production of attosecond pulses.

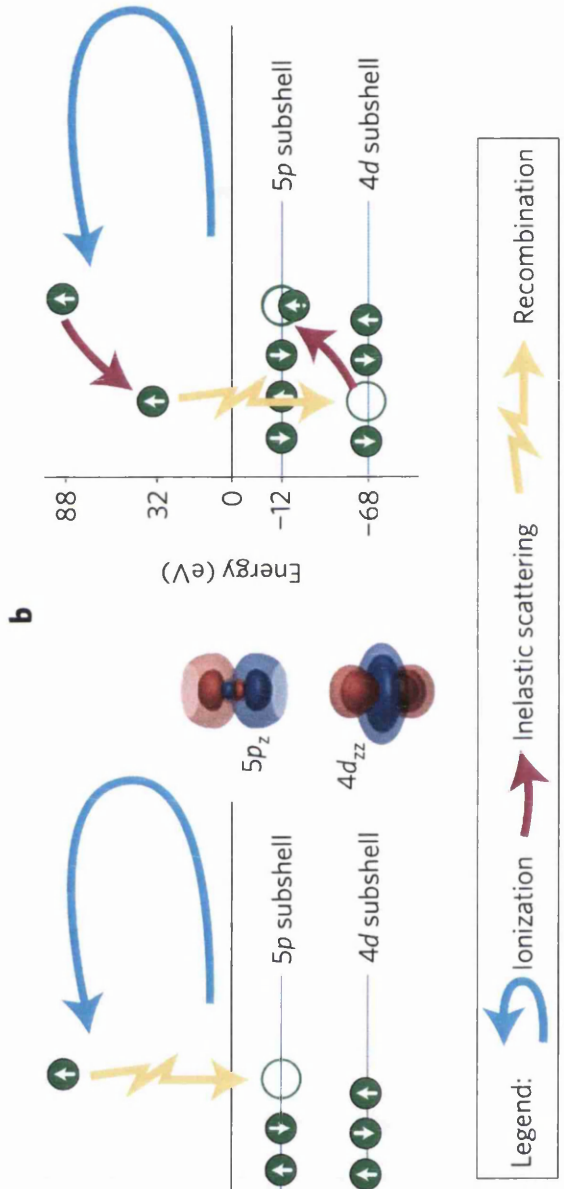

Figure 1.26: Recombination process (a) without and (b) with inelastic scattering, causing promotion of a $4d$ electron to the $5p$ orbital, populating an excited state. Reproduced from [69].

Chapter 2

Ultrashort intense laser pulse generation and characterisation

This chapter describes the production of ultrashort (<100 fs) near-infrared (NIR) pulses in laser oscillators, the temporal compression techniques used to approach the single-cycle limit (~2.7 fs) and amplification techniques to produce very high intensity (> 10^{14} W/cm^2) pulses capable of significantly distorting the Coulomb potential of atoms and molecules. The interaction of intense many-cycle pulses with matter results in tunnel and multiphoton ionization processes. With intense few-cycle pulses (~10 fs), tunnelling becomes dominant, hence can be resolved.

2.1 Generation

2.1.1 Oscillators

A laser oscillator comprises the gain medium – in this case titanium-doped sapphire (Ti:Al_2O_3, or Ti:S) – within a resonant optical cavity. The electronic energy levels of the titanium ions are strongly coupled to the vibrational energy levels of the sapphire crystal structure, splitting the degeneracy of the titanium energy

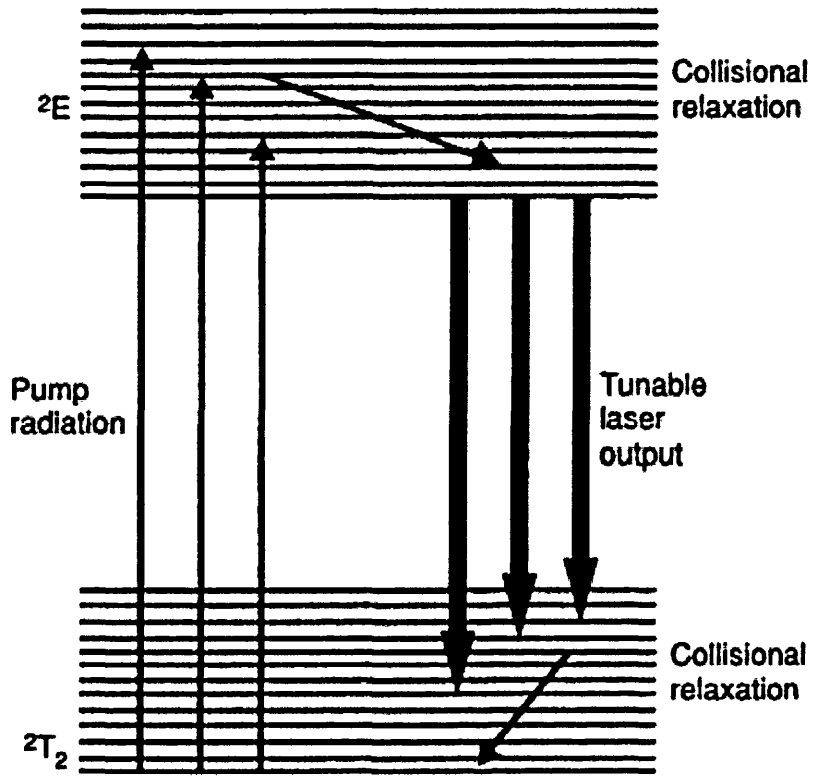

Figure 2.1: Schematic of four-level laser operation in a Ti:S crystal, showing the pump, lasing (tunable laser output) and non-radiative (collisional relaxation) transitions. Reproduced from [70].

levels and effectively creating a four-level system (as illustrated in Figure 2.1) with broad-bandwidth absorption (450 – 600 nm) and lasing (600 – 1000 nm), as shown in Figure 2.2. A pump laser creates a population inversion by promoting electrons from the $^2T_2$ ground state to the ^2E excited states. These decay rapidly via non-radiative vibronic relaxation to the lowest-energy ^2E state. Spontaneous or stimulated emission occurs for the lasing transition $^2E \longrightarrow ^2 T_2$, and the population inversion between the lowest ^2E and the non-ground-state $^2T_2$ levels maintained by their rapid relaxation to the $^2T_2$ ground state [70–72].

Ti:S is typically pumped using frequency-doubled infrared lasers: Nd:$Y_3Al_5O_{12}$ (neodymium-doped yttrium aluminium garnet, or Nd:YAG),

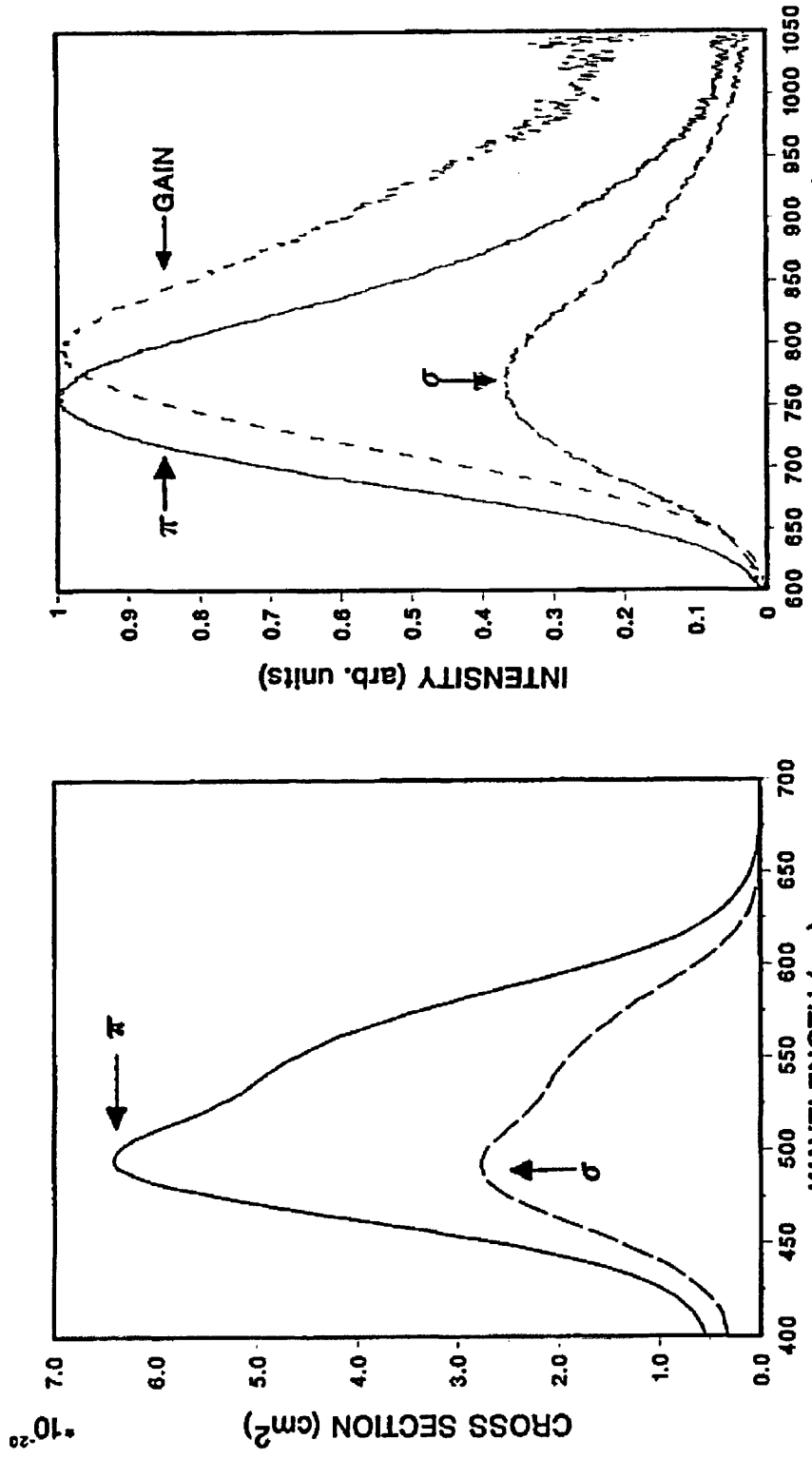

Figure 2.2: Ti:S absorption *(left)* and emission *(right)* spectra for π- and σ-polarization. Reproduced from [71].

Nd:YVO_4 (neodymium-doped yttrium vanadate) at 532 nm; and Nd:$YLiF_4$ (neodymium-doped yttrium lithium fluoride, or Nd:YLF) at 527 nm, which are near the absorption peak at ~500 nm.

The optical cavity comprises high-reflectivity mirrors at each end. As such, standing waves are formed when the reflected waves are in phase. The cavity supports standing waves, or modes with frequency spacing:

$$\Delta\nu = \frac{c}{2L} \tag{2.1}$$

where L is the cavity length, typically ~1 – 2 m. Though the cavity in principle supports n modes of frequency $\nu = \frac{nc}{2L}$, only modes within the gain bandwidth and reflectivity response of the mirrors will be amplified in the oscillator, typically resulting in a gain bandwidth for a Ti:S oscillator of 700 – 900 nm centred at ~780 nm.

2.1.2 Q-switching

High-intensity pulses with duration ~ns can be produced by allowing the quality of the resonant cavity – or Q-factor – to be modified [73]. In practice, this can be achieved by reducing the reflectivity of one of the mirrors, using a mechanical or electronic shutter within the cavity. By continuing to pump the gain medium in an optical cavity with a low Q-factor, stimulated emission is suppressed, allowing the population inversion to build to its maximum level. If the same cavity is quickly switched so that it has a high Q-factor, the maximal population inversion results in maximum gain, resulting in a 'giant' pulse (with ~GW peak power).

Typically, a Pockels cell between two polarizers is used as a fast electro-optic shutter (switching time ~ns). The first polarizer is aligned to the laser polarization, and the second at 90°. The Pockels cell consists of a crystal with a

birefringence that depends linearly on the voltage applied, and is set up to rotate the incoming polarization by 0° (no voltage) or 90° (voltage applied), thereby allowing or preventing the laser light from passing through the shutter. This is known as active Q-switching. Alternatively, the process can be achieved passively at regular intervals using media with intensity- and therefore time-varying gain such as saturable absorbers, which are made from materials which have an intensity-dependent absorption such as absorbant-doped material or semiconductors.

2.1.3 Mode-locking

When a laser output is continuous-wave (cw), each cavity mode oscillates with a random phase with respect to the next, resulting in an almost-continuous output, fluctuating slightly due to the random occurrence of phase matching between modes. If the gain of the oscillator is modulated to coincide with the round-trip time $t = \frac{2L}{c}$ of the optical cavity, several modes can be locked together in phase, and the laser produces a series of pulses regularly spaced in time.

Saturable absorbers can be used to modulate the cavity in such a way. Alternatively, the properties of the gain medium can be exploited in a technique known as self-modelocking (SML) or Kerr lens modelocking [74], where the nonlinearities in the gain medium itself act to suppress the gain. The Kerr effect is an intensity-dependent contribution to the refractive index of certain media, so that the refractive index becomes

$$n = n_0 + n_2 I \tag{2.2}$$

where n_2 is 3×10^{-16} cm^2/W for Ti:S. Two phenomena occur as a result: the variation of refractive index across the spatial intensity distribution of the beam

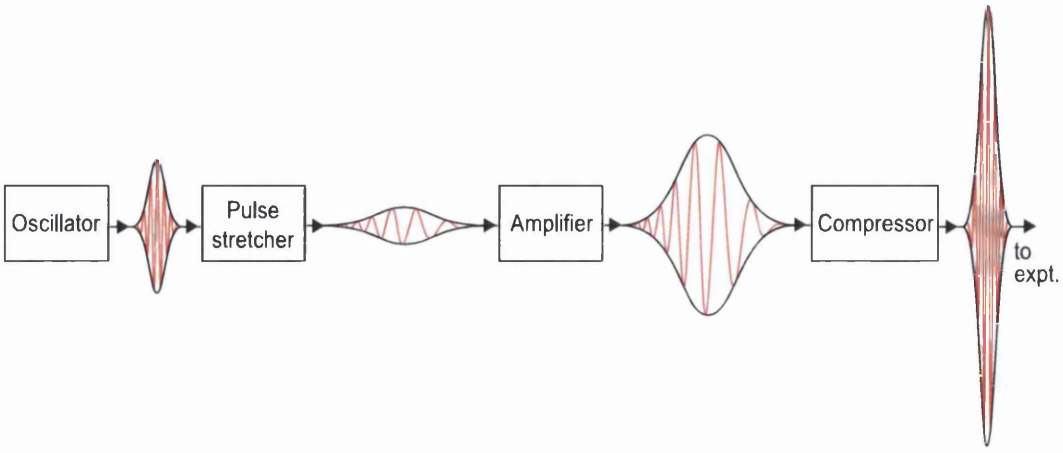

Figure 2.3: Illustration of chirped-pulse amplification (CPA). A pulse stretcher introduces chirp to spread the peak power over the spectrum of the pulse, allowing it to be amplified without exceeding the damage threshold of the amplifier crystal. A compressor restores the original pulse duration by removing the chirp imposed by the stretcher.

creates a lensing or self-focusing of the beam; the pulse also experiences self-phase modulation (SPM), which increases material dispersion.

In principle, in mode-locked operation the oscillator can produce near-bandwidth-limited few-cycle pulses. However, as the pulse energy is typically of the order of nJ, focused intensities can only reach up to 10^{14} W/cm^2. These intensities would just be capable of single ionization by tunnelling, but higher charge states would not be generated.

2.1.4 Chirped-pulse amplification (CPA)

Direct amplification of the pulses from the oscillator would result in nonlinear effects developing further along the beam line (e.g. in subsequent gain media), degrading the beam quality and, in the worst case, resulting in damage due to heating. To circumvent this, a technique known as chirped-pulse amplification (CPA) is employed, as illustrated in Figure 2.3. A pulse stretcher – consisting of a pair of prisms or diffraction gratings – uses angular dispersion to impose a

wavelength-dependent path length and therefore a wavelength-dependent temporal delay. On passing through the pulse stretcher, fs-duration pulses from the oscillator are typically stretched to ~ns. The peak power is also significantly reduced, which allows for larger amounts of amplification without exceeding the damage threshold of the gain medium. Following amplification, a pulse compressor – also consisting of a grating or prism pair – can be used to restore the original pulse duration after amplification, recompressing the pulse by introducing the opposite dispersion to that introduced by the amplification stage.

Ideally, the resultant frequency variation with time will remain linear, in which case the pulse is said to be chirped. However, higher-order time-dependent dispersion is possible and likely. Additional dispersion control optics (e.g. prisms) may be employed to try to compensate for these higher-order dispersive effects, or in the case of a prism compressor the angularly dispersive elements themselves can be adjusted to minimise dispersion.

2.1.5 Chirped mirrors

An alternative method of dispersion compensation is to use multilayer dielectric chirped mirrors (see Figure 2.4), which reflect light at different depths depending on the incident wavelength. The idea of dispersion removal using a wavelength-dependent path length is similar in principle to the operation of the grating or prism compressor, but the chirped mirrors are much more accommodating of wider bandwidth pulses and significantly easier to align. Since each mirror is fabricated to add or remove a fixed amount of dispersion, several mirrors are typically used in series to compensate for dispersive effects introduced intentionally (e.g. spectral broadening for few-cycle pulse generation) or unintentionally (e.g. dispersion in air) along the beam path.

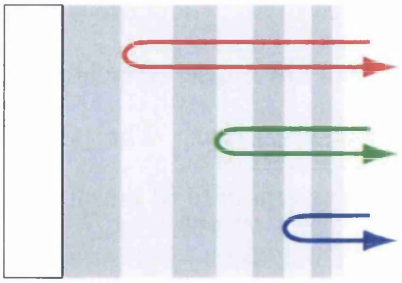

Figure 2.4: Multilayer chirped mirror. Assuming the incident pulse is positively chirped as shown, longer wavelength components (red) penetrate to a greater depth than shorter wavelengths (blue), and as such traverse a longer path length. This delays the longer wavelength components and temporally compresses the pulse.

2.1.6 FemtoLasers 30 fs 1 kHz NIR laser system

The FemtoLasers system shown in Figure 2.5 comprises a Ti:S oscillator, pumped with a frequency-doubled diode-pumped Nd:YVO_4 laser (Coherent Verdi) at 532 nm. Chirped mirrors within the oscillator cavity minimize dispersion; the resulting pulses are 12 fs, >4 nJ, 75 MHz repetition rate with a bandwidth of 750 – 850 nm. A Pockels Cell reduces the repetition rate to 1 kHz. These pulses are stretched to ~20 ps in a 10 cm long SF57 glass block, and pass through an acousto-optic programmable dispersive filter (Fastlite Dazzler), which uses a measurement of the spectral phase to generate an inverse filter, in principle flattening the spectral phase. The pulse then enters a Ti:S amplifier (FemtoLasers Femtopower CompactPro), pumped with a continuous-wave frequency-doubled diode-pumped Nd:YLF laser (Thales JADE) at 532 nm, producing pulses of around ~20 fs in duration. The Ti:S amplifier crystal is housed within a vacuum chamber, and Peltier-cooled to -20°C. After recompression using two fused silica prism pairs, the resultant pulses are ~30 fs pulses with a bandwidth of ~40 nm, which reach a peak energy of ~0.8 mJ.

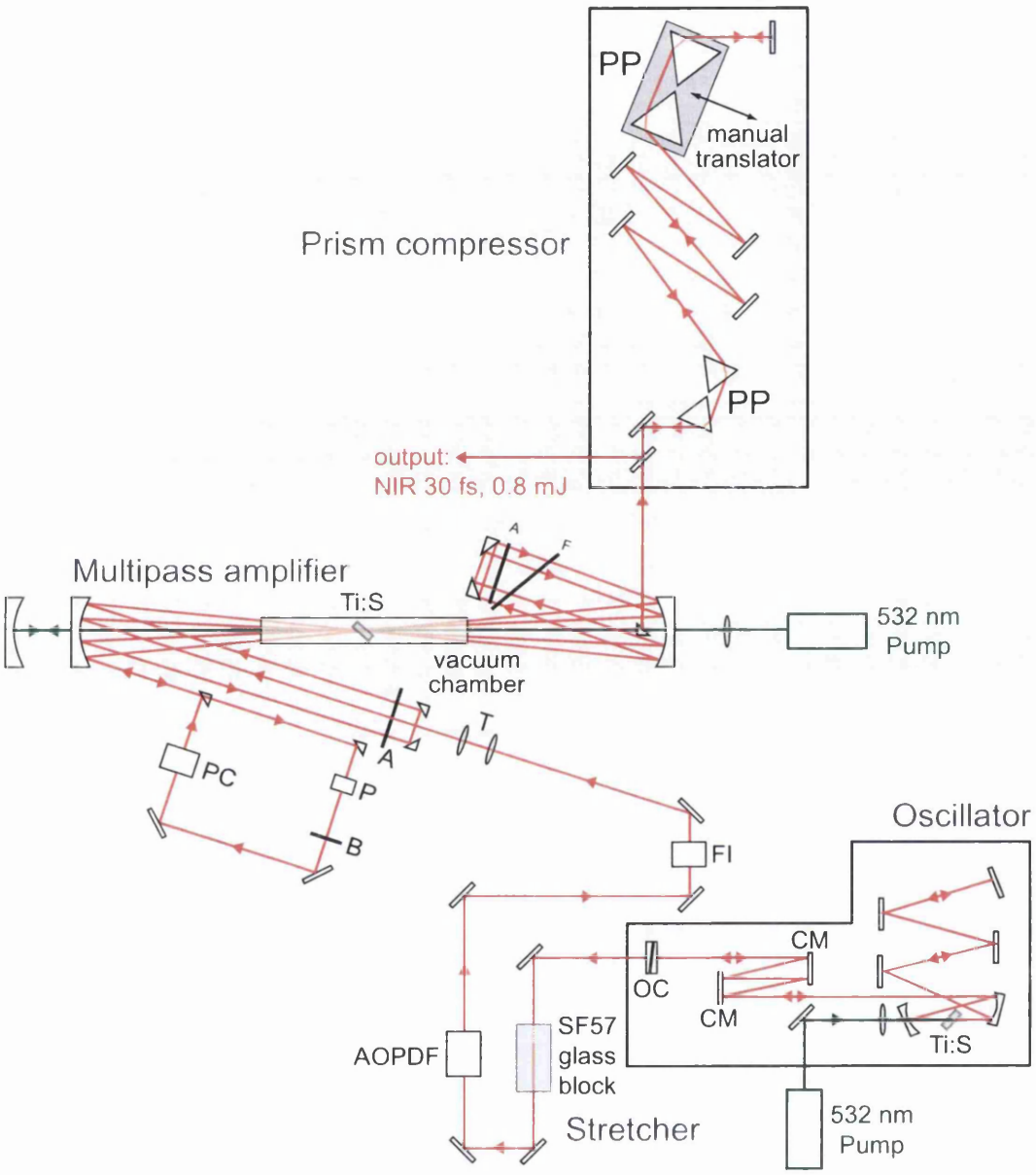

Figure 2.5: FemtoLasers laser system overview. The system comprises a Ti:S oscillator and multipass Ti:S amplifier (Femtopower CompactPro), producing ~30 fs, ~0.8 mJ NIR pulses with a bandwidth of ~40 nm after recompression as described in the text. The separation between the second prism pair (PP) in the prism compressor can be adjusted to optimise dispersion removal. AOPDF = acousto-optic programmable dispersive filter (Dazzler), FI = Faraday Isolator, T = demagnifying telescope, P = polarizer, B = Berek polarization compensator, PC = Pockels Cell, A = apertures, F = filter, PP = prism pair, OC = output coupler, CM = chirped mirror.

2.1.7 KMLabs RedDragon 30 fs NIR laser system

The RedDragon laser system shown in Figure 2.6 comprises a centre-wavelength-adjustable (700 – 900 nm) Ti:S oscillator (KMLabs Griffin) pumped by a 532 nm diode laser running at 5.6 W (Coherent Verdi), producing ~6 nJ pulses of <10 fs duration with a bandwidth of 55 – 60 nm. Chirped mirrors are used in the oscillator to minimize dispersion. The pulse then passes through two cryogenically-cooled mechanically-isolated Ti:S multipass amplifier stages. The first stage is pumped by a 527 nm diode-pumped Nd:YLF laser (Photonics Industries DM30) running at ~28 W, and the second by two similar pump lasers (Photonics Industries DM30 and DM40) with a combined maximum power of 70 W. The pulses are then recompressed using a grating pair to a duration of <30 fs.

With the first amplifier in operation, output pulses are 1.2 – 1.5 mJ. With both amplifiers, the maximum pulse energy increases to 14 mJ, with a 1 kHz repetition rate, centred at 785 nm with a bandwidth of ~40 nm.

2.1.8 Hollow fibre compression

In order to generate few-cycle pulses approaching the transform-limit, additional bandwidth is required. The minimum achievable pulse duration or transform-limited pulse depends ultimately on the time-bandwidth product (TBWP)

$$\Delta\nu\Delta\tau = c_B \tag{2.3}$$

where $\Delta\nu$ is the bandwidth, $\Delta\tau$ is the pulse duration, and c_B is a constant which depends on the temporal pulse shape. Assuming the pulse could be made approximately Gaussian in time after dispersion compensation (for a Gaussian, $c_B = 0.441$), the minimum achievable duration for the pulse spectrum in

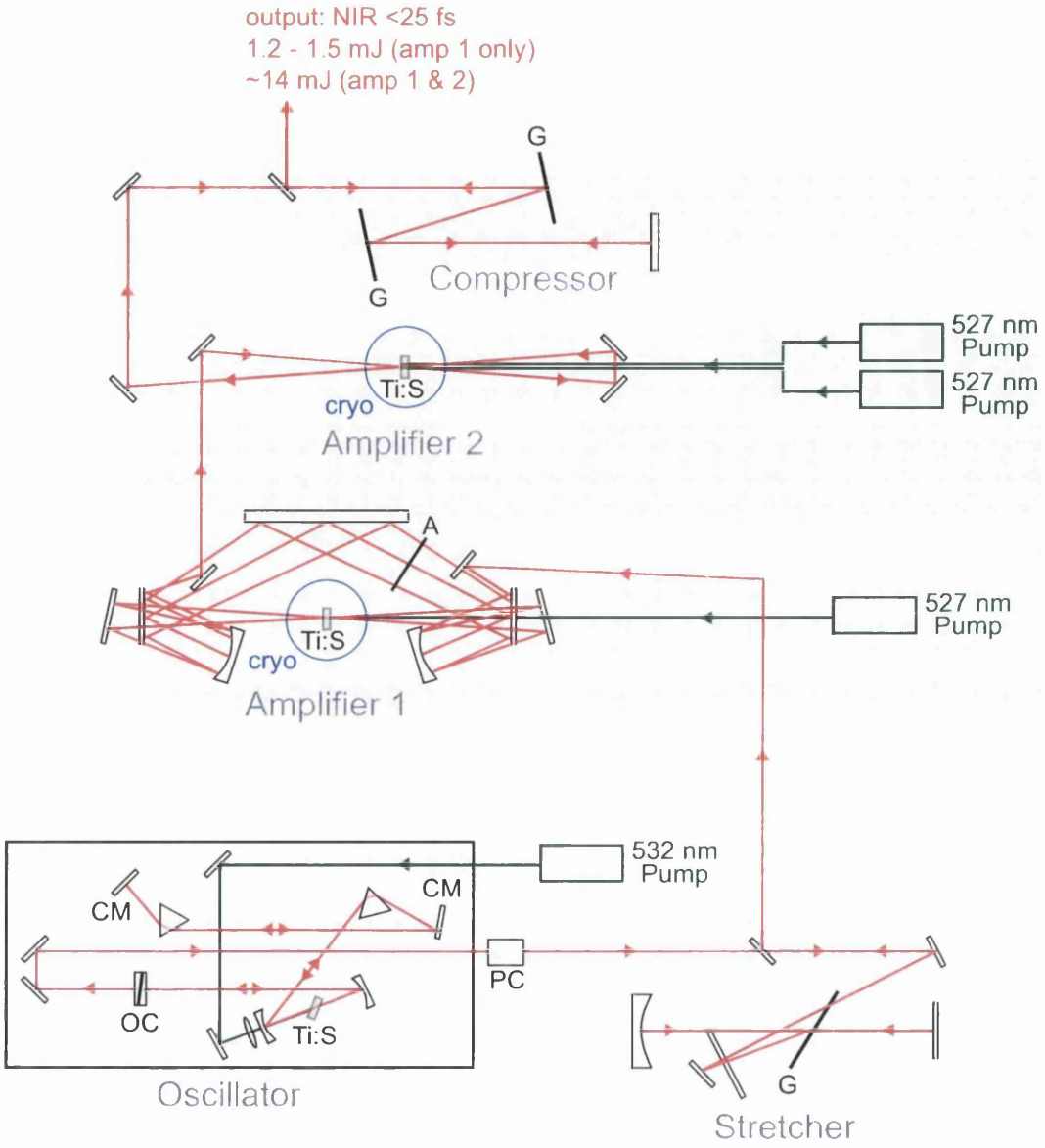

Figure 2.6: KMLabs RedDragon laser system overview. The laser comprises a Ti:S oscillator (KMLabs Griffin), grating stretcher, first-stage amplification (KMLabs Dragon), second-stage amplification and a grating compressor, producing NIR output pulses of <25 fs, ~40 nm bandwidth and an energy of 1.2 – 1.5 mJ (amplifier 1 only) or 14 mJ (amplifiers 1 & 2), as described in the text. G = gratings, PC = Pockels cell. The pulse exiting the grating stretcher enters a 14-pass amplifier ring (some passes omitted for clarity). A set of apertures (A) only allows the most intense central part of the beam on each pass to proceed to the next pass. The Ti:S crystals in both amplification stages are cryogenically cooled (cryo) to 50 – 80 K, preventing thermal lensing and damage due to heat buildup. The grating compressor compensates for linear and second-order dispersion; the angle of the final grating can be adjusted to optimise the dispersion compensation.

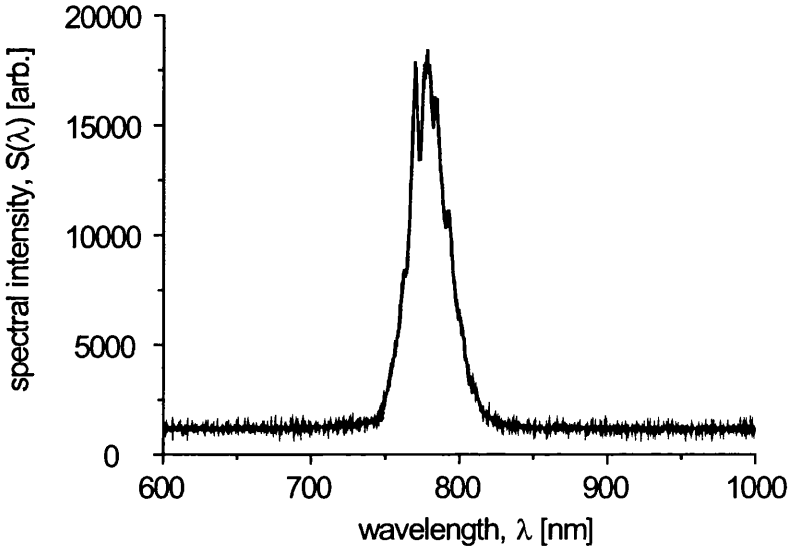

Figure 2.7: Typical measured spectrum from the laser system described in Section 2.1.7, with a bandwidth of ~40 nm.

Figure 2.7 (bandwidth ~40 nm) would be ~24 fs. For few-cycle NIR pulses, a single cycle is $2\frac{2}{3}$ fs at 800 nm, hence ~10 fs and shorter pulses are desirable.

The phenomenon of self-phase modulation (SPM) may be exploited in a gas-filled hollow fibre [31] to broaden the pulse spectrum; the fibre acts as a waveguide and therefore increases the interaction length of the laser with the broadening medium. The optical Kerr effect results in an intensity- and therefore time-dependent nonlinear change to the refractive index, so the propagating pulse affects its own phase- and therefore frequency-shifts. Assuming a positively-chirped input pulse the leading edge shifts to lower frequencies (longer wavelengths) and the trailing edge to higher frequencies (shorter wavelengths), as shown in Figure 2.8. Using a differentially-pumped hollow fibre, shown in Figure 2.9, broadening is improved and becomes tunable by adjusting the pressure. Typical spectra obtained before and after the fibre are shown in Figure 2.10, demonstrating a bandwidth of ~140 nm is achievable, enabling near-transform-limited (~ 8 – 12 fs) pulses to be produced after recompression using e.g. chirped

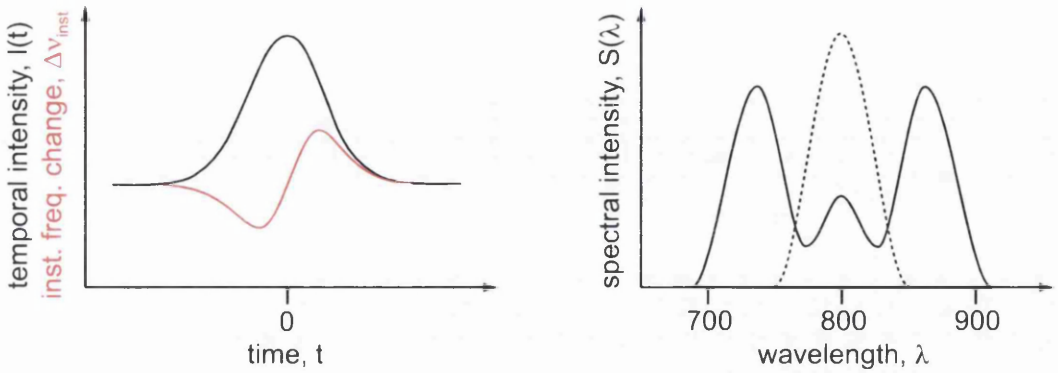

Figure 2.8: Illustration of self-phase modulation (SPM). *(left)* The Kerr effect in the gas-filled hollow fibre results in an intensity- and therefore time-varying refractive index. As a result, the front of the pulse experiences a decrease in frequency (increase in wavelength) whilst the back of the pulse experiences an increase (decrease in wavelength). *(right)* The input pulse (dotted line) is spectrally broadened by SPM (solid line). The spectrum therefore has a distinctive broadening pattern centred at the input pulse centre wavelength.

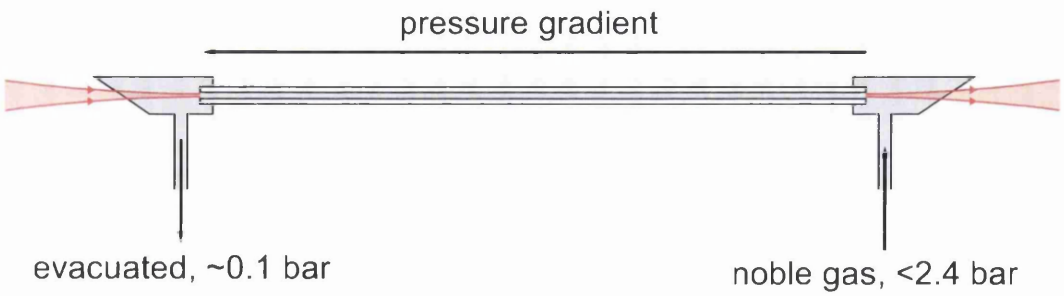

Figure 2.9: Differentially-pumped gas-filled hollow fibre. The end pieces are attached to the fibre and have Brewster windows at the outer faces. The laser pulses enter at the evacuated end of the fibre; this reduces the chances of ionization which would at best reduce the power transmitted to the fibre entrance, and at worst temporally distort the pulse. SPM due to the nonlinear interaction with the noble gas spectrally broadens the pulse along the length of the fibre as demonstrated in Figure 2.8. The pressure gradient, maintained by the differential pumping, enhances the effect of SPM compared to a static-filled hollow fibre, as detailed in [31].

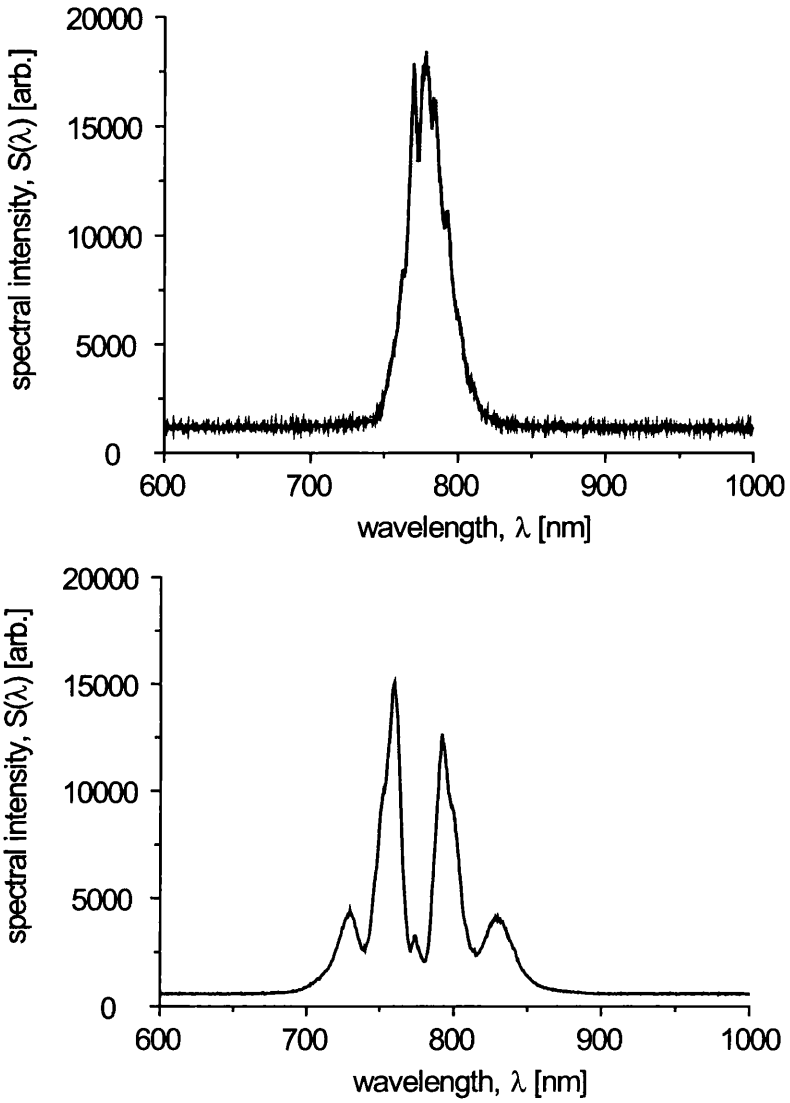

Figure 2.10: Typical measured spectra from the laser system described in Section 2.1.7 before *(top)* and after hollow fibre compression *(bottom)*. The spectrum before the fibre has a FWHM of ~40 nm, centred at ~785 nm. After broadening in a 75 cm differentially-pumped hollow fibre (see Figure 2.9), with ~1.6 bar of argon at the high-pressure end, the spectrum is still centred at ~785 nm but has a bandwidth nearer ~140 nm. The new wavelengths generated by SPM are not necessarily in phase, the resulting interference creating structure in the sidebands (in contrast to the smooth sidebands illustrated in Figure 2.8).

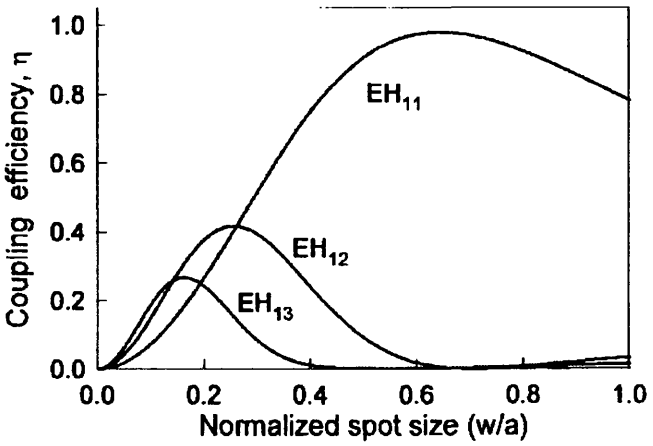

Figure 2.11: Overlap functions for the first three $l = 1$ fibre modes. The coupling between a Gaussian input beam and the EH_{11} mode of the fibre reaches a peak when the input beam waist is 0.65 times the fibre inner radius, a. Reproduced from [30].

mirrors to compensate for the additional dispersion incurred due to the fibre (the transform limit is ~7 fs).

Assuming the input beam profile can be considered to be approximately Gaussian, the overlap between the input beam and the fibre modes is given by the overlap function [30]

$$\eta = \frac{4[\int r J_0(u_{lm} r/a) \exp(-r^2/w^2)\, dr]^2}{[w^2 \int r J_0^2(u_{lm} r/a)\, dr]} \tag{2.4}$$

where η is the coupling efficiency, a is the hollow fibre inner radius, u_{lm} is the root of the equation $J_0(u_{lm}) = 0$ and is 2.405 for the EH_{11} mode, and w is the beam waist ($1/e^2$ radius). The Gaussian beam profile at the input results from the fundamental TEM_{00} (transverse electromagnetic) mode output expected from the laser oscillator, where the electric and magnetic fields only have components which are transverse to the beam propagation direction. The EH_{11} fundamental mode supported by the fibre is a hybrid mode, where the electric field also has

an axial component, since the beam propagates by grazing incidence reflections from the fibre wall [30, 75–77].

Figure 2.11 shows the coupling efficiency (given by Equation (2.4) for the first three $l = 1$ modes vs. normalized spot size at the fibre entrance. The optimum coupling efficiency ($\sim$ 98%) is achieved by coupling to the EH_{11} mode, which requires the input beam radius to be 0.65 times the fibre inner radius. However, the coupling efficiency is expected to be 90% even if the input beam radius is between 0.49 and 0.84 times the fibre radius.

Experimentally, such high coupling efficiency is difficult to achieve. The input pulse profile is not necessarily Gaussian, resulting in the excitation of higher fibre modes. There will also be deviations of the 'real' fibre as compared to an ideal one; due to the manufacturing process the core is unlikely to be perfectly circular nor the fibre perfectly straight along its length. The fibre may also bend due to external stresses such as may be caused by the mountings used, which will result in losses. Ionization may also occur within the gas-filled fibre core, despite attempting to minimize this effect using differential pumping. There is also the possibility of thermal damage to the end of the fibre, which will gradually reduce the coupling efficiency throughout the fibre's lifetime. The combination of all these effects results in a typical experimental energy throughput of 50 – 60%, after optimizing the fibre angle and position with respect to the focus at the input to produce a predominantly single-mode (EH_{11}) output.

2.2 Metrology

In order to fully characterise an ultrashort pulse, either the temporal intensity and phase, or the spectral intensity and phase are required. Pulse spectra are easily and readily measurable, but temporal characterisation is more difficult, since the

only diagnostic tool capable of measuring the pulse on ultrashort timescales is the pulse itself.

This chapter describes two methods which are commonly used to characterise ultrashort pulses: the autocorrelator, which has significant limitations for pulses much shorter than ~30 fs; and its successor, frequency-resolved optical gating (FROG) which is capable of uniquely characterising shorter few-cycle pulses by extracting information from a simultaneous measurement of the pulse in the spectral and temporal domains, i.e. a spectrogram.

2.2.1 Autocorrelator

Autocorrelation involves overlapping a pulse with a delayed copy in a nonlinear crystal, producing the autocorrelation signal

$$A(\tau) = \int_{-\infty}^{\infty} I(t)I(t-\tau)dt \tag{2.5}$$

where τ is the relative delay between the two copies of the pulse.

A 50:50 pellicle beamsplitter splits the pulse to be measured. In order to achieve single-shot measurement of the pulse duration, rather than changing the pulse delay by mechanically changing the path length of one of the arms with respect to the other, the two beam paths are made to cross at a small angle in a slice of Type I β-BaB_2O_4 (β-barium-borate, or BBO) crystal, as shown in Figure 2.12. This produces a spatial distribution of second-harmonic intensity, which is essentially a mapping of the delay τ. A CCD camera (Sony) images the second-harmonic signal. The pulse shape is assumed and deconvolved from the measured autocorrelation, and the full-width half-maximum (FWHM) determined to give a measurement of the pulse duration.

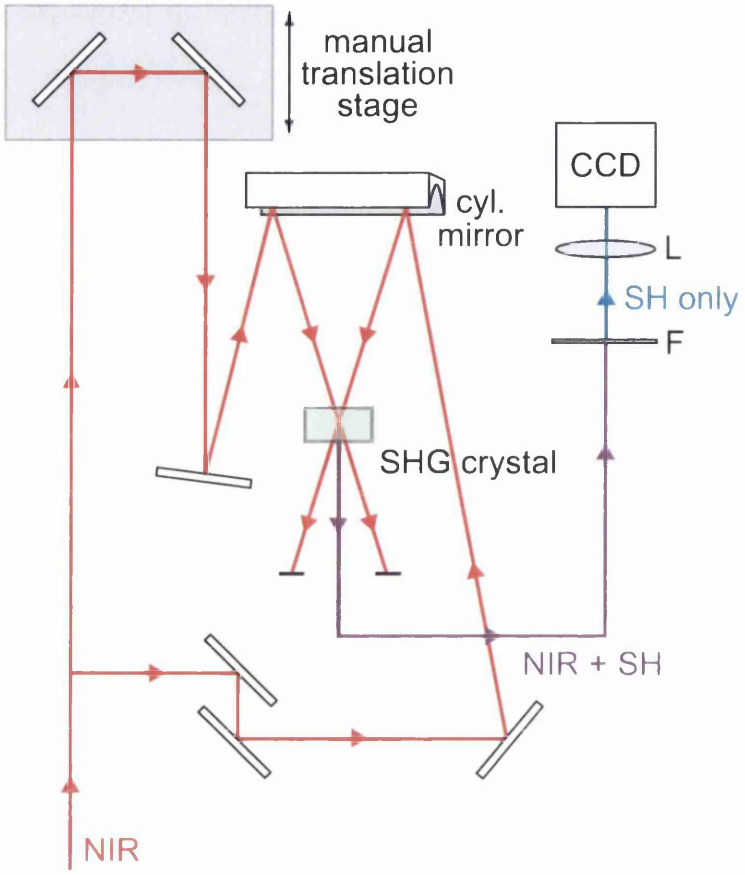

Figure 2.12: Second-harmonic autocorrelator. The near-infrared (NIR) input pulse is split equally using a 50:50 pellicle beamsplitter (BS), with the two copies of the pulse following different paths which cross at a small angle in a piece of BBO crystal. The manual translation stage can be adjusted until the temporal overlap of the two pulses occurs within the crystal. The second-harmonic (SH) signal produced is filtered (F) to remove the NIR, and the SH focused onto a CCD, with the image i.e. autocorrelation trace being transferred to a PC.

Autocorrelation is limited to measuring the pulse duration, and cannot give any information about the temporal or spectral phase. It also requires the pulse shape to be known or assumed. For >30 fs pulses, a measurement of the pulse spectrum allows the expected pulse shape to be inferred, and a successful autocorrelation measurement can be made assuming the pulse has a flat spectral phase i.e. dispersion has been successfully compensated. However, for shorter pulses, higher-order dispersion is more likely to remain in the pulse despite (or because

of lower-order) dispersion compensation. Unless the effects of these multiple orders of dispersion are accurately quantified and included in the assumed pulse shape, the autocorrelation becomes ambiguous and unreliable [78]. Dispersion information cannot be reliably inferred from the spectrum either, since there is no one-to-one mapping of spectrum and autocorrelation.

2.2.2 Frequency-resolved optical gating (FROG)

Frequency-resolved optical gating (FROG) [79] temporally- and spectrally-resolves the pulse in order to retrieve the information that autocorrelation cannot. Moreover, as FROG simultaneously measures the pulse temporally and spectrally, a unique solution can be found for the temporal pulse shape, and the temporal/spectral phase can be determined.

SHG-FROG (a variant of FROG) overlaps the pulse to be measured and a delayed copy in a second-harmonic crystal such as BBO, producing a spatial mapping of τ as with the autocorrelator, but the second-harmonic signal is then spectrally resolved by e.g. passing it through a diffraction grating, as shown in Figure 2.13. This produces a spectrogram of the form

$$\Sigma_g(\omega, t) \equiv \left| \int_{-\infty}^{\infty} E(t)\, g(t-\tau)\, exp(-i\omega t)\, dt \right|^2 \tag{2.6}$$

where $E(t)$ is the pulse electric field, and $g(t-\tau)$ is the gating function, which in this case is a copy of the pulse $E(t)$ itself, delayed by τ. The resulting spectrogram is recorded using a CCD camera (AVT Pike), an example of which can be seen in Figure 2.14.

A proprietary algorithm is used to recover the temporal intensity envelope $I(t)$ and phase $\phi(t)$ from the measured spectrograms, as well as the spectral intensity $S(\lambda)$ and phase $\varphi(\lambda)$. Figure 2.15 shows the output of this algorithm

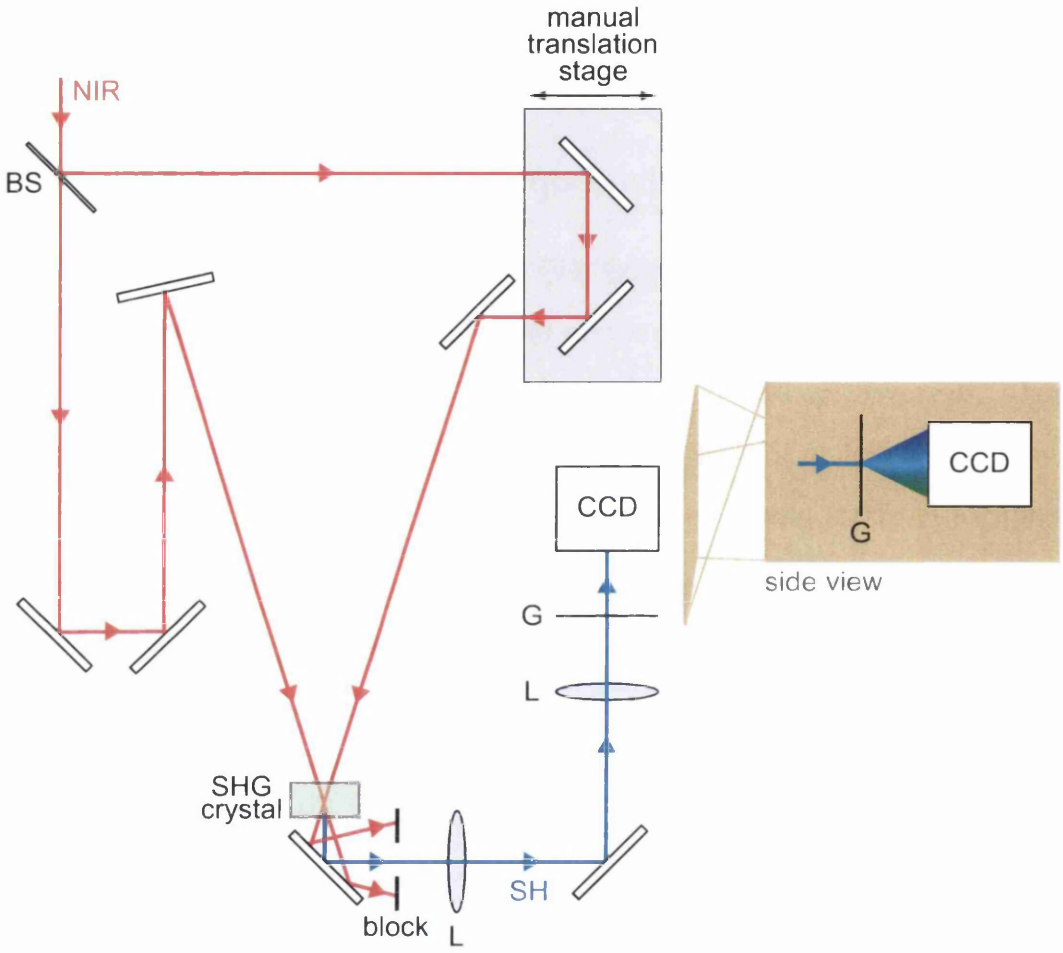

Figure 2.13: SHG-FROG. The input pulse is split equally by a 50:50 thin glass beamsplitter. The two copies of the pulse cross at a small angle in the SHG crystal as with the autocorrelator in Figure 2.12, but in this case the second-harmonic (SH) signal is focused onto a transmission diffraction grating (G). The resulting spectrogram (an example of which can be seen in Figure 2.14), with delay τ in the x-direction, and wavelength λ in the y-direction (illustrated by 'side view') is recorded by a CCD and transferred to a PC.

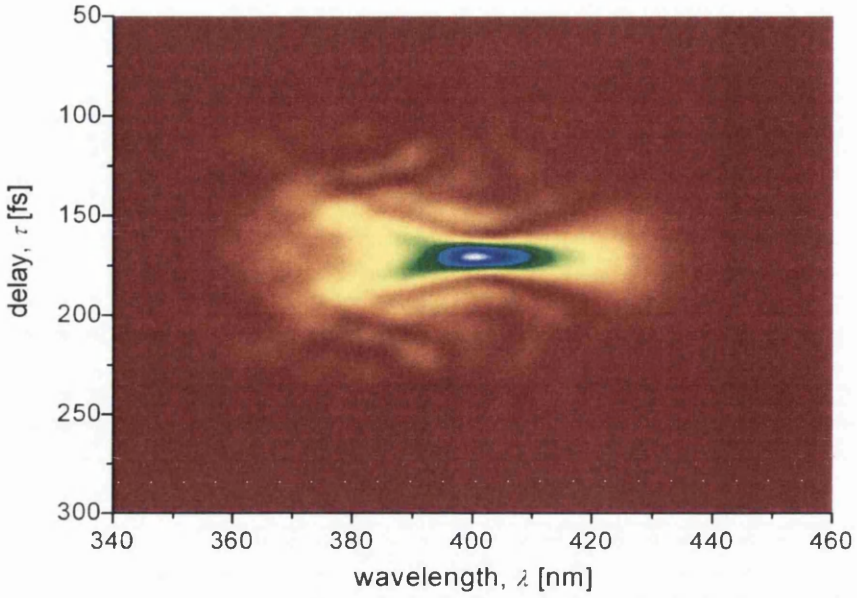

Figure 2.14: Typical measured SHG-FROG spectrogram for a ~12 fs pulse. The 'ripples' at lower wavelength and large delay are due to higher-order dispersion.

for the spectrogram shown in Figure 2.14. From the recovered $I(t)$ and $\phi(t)$, it is possible to reconstruct the complete pulse electric field, using the equation

$$E(t) = \tfrac{1}{2}\sqrt{I(t)}\, exp\big(i(\omega_0 t - \phi(t)\big) + c.c. \tag{2.7}$$

where ω_0 is the centre frequency, and *c.c.* is the complex conjugate of the first term.

2.3 Conclusion

Intense ultrashort pulse production, amplification and dispersion compensation have been discussed, and the layout of the beamlines used for the experiments in Chapters 5 and 6 detailed. The retrieved pulse characteristics from FROG are

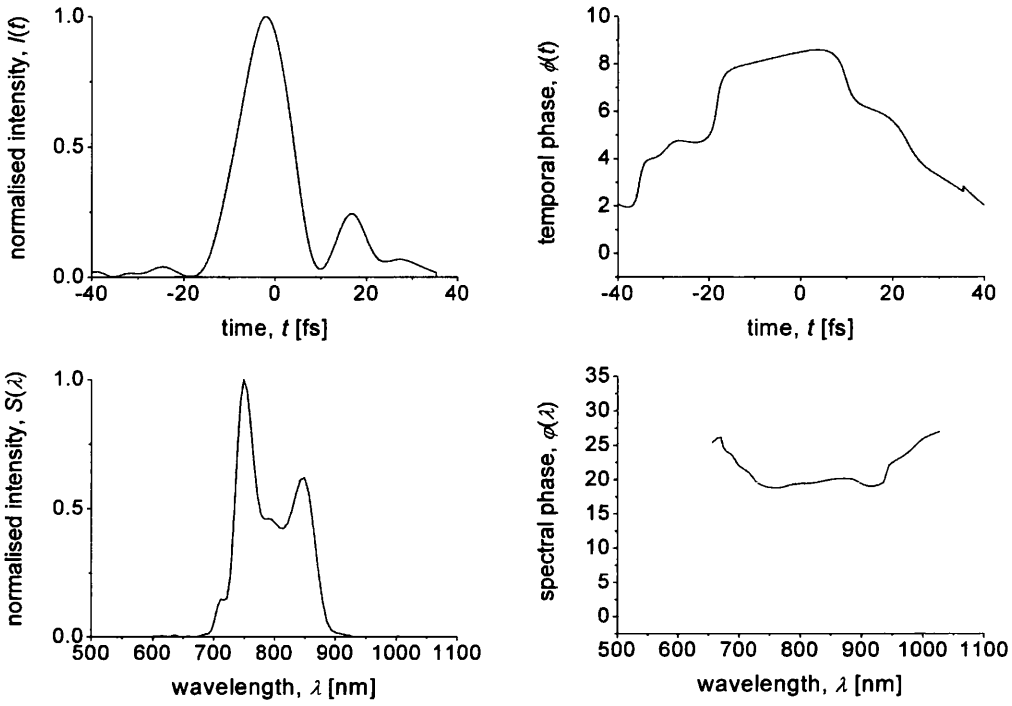

Figure 2.15: FROG retrieval, showing the normalised temporal and spectral intensity and phase for the spectrogram in Figure 2.14

shown, and form the basis of the pulse electric field reconstructions discussed in Chapter 4.

Chapter 3

Experimental techniques

This chapter describes the use of time-of-flight mass spectrometry to detect and distinguish the ions produced by the interaction of an ultrashort intense laser pulse with atoms. Interferometric techniques are also described which allow for pump-probe studies, or modifications to the temporal intensity profile of the incoming pulses.

3.1 Time-of-flight mass spectrometer

Figure 3.1 shows the ultra-high vacuum (UHV) tank, which houses the ion time-of-flight mass spectrometer (TOFMS) and focusing optic. The pressure in the tank is monitored using a combined Pirani/Bayard-Alpert ionization gauge (Pfeiffer PBR 260), with a range of $5 \times 10^{-10} - 1000$ mbar. A turbo pump (Pfeiffer Vacuum TPU 450H), with a pumping rate of 450 l/s backed by an oil-free diaphragm pump (Pfeiffer MD 4T) typically reduces the measured base pressure of the tank to $\sim 10^{-9}$ mbar.

Laser pulses enter through an AR-coated 3 mm thick fused silica window, and are reflectively focused by an $f = 50$ mm spherical mirror. The mirror is mounted on an XYZ manual translation stage with the manipulators on the tank

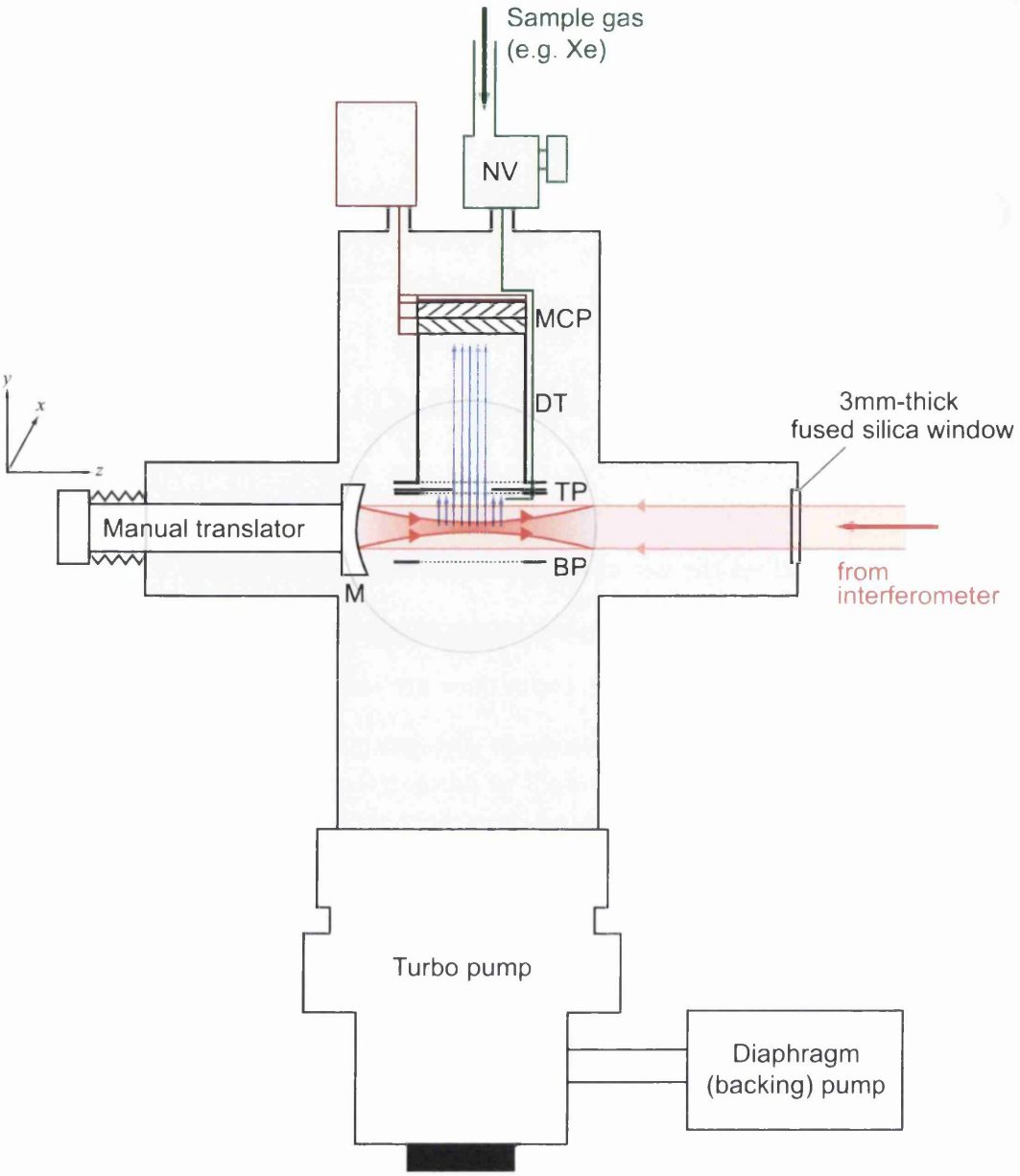

Figure 3.1: Schematic of the time-of-flight mass spectrometer (TOFMS). The diaphragm and turbo pumps maintain ultra-high vacuum (UHV) in the interaction region, and the needle valve (NV) controllably introduces the sample gas. NV = needle valve, BP = bottom plate, TP = top plate, DT = drift tube, MCP = microchannel plate detector stack, M = focusing mirror. Ions produced at the laser focus (represented by blue arrows) are accelerated by the electric field produced between BP and TP. The ions enter DT through a 250 μm aperture, encountering a field-free region where they separate according to their charge-to-mass ratio, and are detected by the MCPs.

exterior, with 0.01 mm resolution in x and y, and 0.1 mm resolution in z. After temporarily placing a fluorescent card with a pinhole at the entrance window, the laser can be aligned to the tank by adjusting the translation stage until the centres of the pinhole, the incoming beam and back-reflected beam are coincident.

The target gas enters the tank via a needle valve, which controls the flow rate. A 1 mm diameter capillary tube connected to the needle valve channels the target gas to the focal region, where it is delivered as an effusive gas jet ~1 cm from the focus. The needle valve is adjusted so that the tank pressure is increased to $\sim 10^{-7}$ mbar, corresponding to a target density (for xenon) of $\sim 10^{9}$ cm^{-3}.

Target ions produced at the laser focus, under the influence of an external electric field, will experience an acceleration which depends on their mass and charge. The ion time-of-flight mass spectrometer illustrated in Figure 3.1 is used to detect and distinguish ions by their mass-to-charge ratio. By applying voltages to the top plate (TP), bottom plate (BP) and drift tube (DT), each of which are electrically insulated from each other, three independent electric field regions may be generated: an accelerating 'source' region (between BP and TP), a second accelerating region (between TP and DT), and a field-free drift region (within DT). Typically, equal voltages of opposite polarity are applied to TP and BP respectively, introducing a constant electric field over the source region. In the current work, the spectrometer is set up to detect positive ions, i.e. BP has a positive voltage applied, and all accelerating voltages (TP, DT and at the detector) are negative. The specific voltages applied, and the ratios between them, will depend on the mode of operation required.

Spatial mode The voltage applied to TP and DT are set equal, reducing the spectrometer to a simple two-stage case: a source region (between BP and TP) and a field-free drift region (TP and DT). Ions are accelerated in the source region, then separate in time according to their mass-to-charge ratio in the drift

region. Assuming the ions have zero initial momentum at the point of ionization, they follow a straight trajectory throughout, and the expected flight-time is given by [80]

$$t = (2s + D)\sqrt{\frac{m}{2neEs}} \tag{3.1}$$

where m is the mass of the sample atom, n is the charge state, e is the elementary charge, E is the magnitude of the electric field in the acceleration region, s is the distance between the point of origin of the ion and the end of the acceleration region, and D the length of the drift region.

Wiley-McLaren mode The source region is split into two stages: one between BP and TP, and the other between TP and DT. The ions no longer follow straight trajectories, but undergo spatial lensing due to the increased electric field curvature [80–83], as illustrated in Figure 3.2. A ratio of voltages is found which allows all ions of a particular mass-to-charge ratio are made to arrive at the detector at the same time, wherever they are generated within the laser focus. The mass resolution of the spectrometer is therefore increased, at the expense of spatial resolution. Additionally, in studies where the initial kinetic energy is not negligible and is to be measured, the Wiley-McLaren mode gives greater energy resolution, e.g. in the case of photodissociation and Coulomb explosion in molecules, as reviewed in [84].

At the end of the drift tube, a high-voltage grid accelerates the ions towards the detector, and rejects any electrons which may have travelled through the drift tube. The detector is illustrated in Figure 3.3, and consists of a pair of impedance-matched Philips G25-25DT/13 microchannel plates (MCP), each with diameter 25 mm, 2 mm thick with 25 μm diameter pores at 13° bias angle. These are mounted in a chevron configuration to reduce electron backscattering. Ions striking the first MCP produces a cascade of electrons which drift towards the

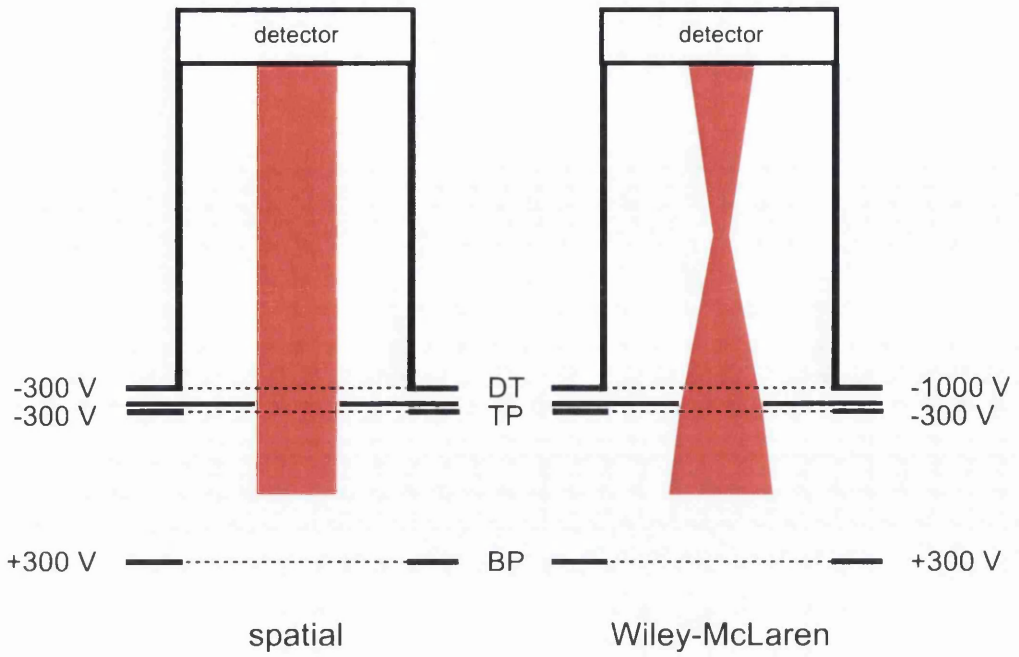

Figure 3.2: Illustration of spatial lensing. In spatial mode, the field line curvature is negligible, and the ions follow a straight trajectory. In the Wiley-McLaren mode, the field line curvature is significantly higher, particularly in the presence of the aperture, resulting in an electrostatic lens between the source and the detector, and a spatial focusing of the ions in the drift tube.

second MCP, producing another cascade. By this point, the gain is $\sim 10^7$. These electrons are driven towards the anode, where they are collected and conducted to ground via a known resistance. The resulting brief increase in the potential difference between the anode and ground produces a pulse of duration ~2 ns.

3.2 Data collection

The pulses produced by the MCP are passed through a fast pre-amplifier (EG&G ORTEC VT120A), with a gain of 200 and response time ~1 ns. The amplified pulses are then detected using a 40 gigasamples/s, 2.5 GHz bandwidth digital phosphor oscilloscope (Tektronix DPO7254). At this point, the pulses are measured to be ~a few ns, spreading as a result of the filtering circuit between

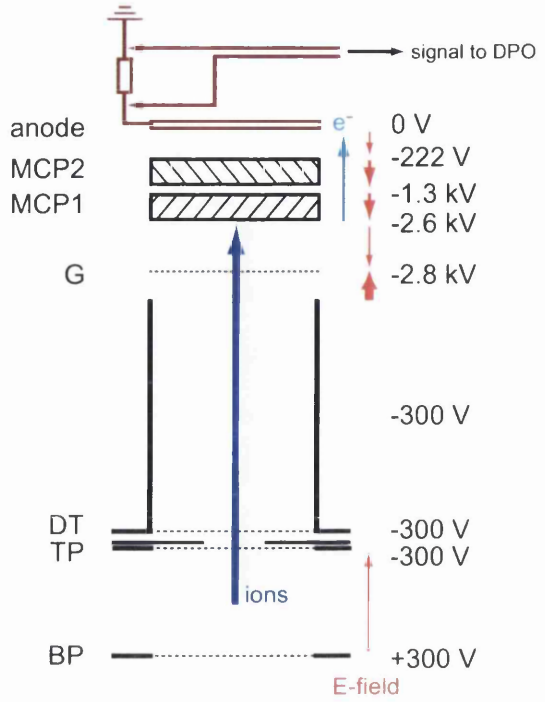

Figure 3.3: Illustration of TOFMS, highlighting the detector stack and electronics. Typical applied voltages are shown for spatial mode operation with a xenon target. G = acceleration grid, MCP = microchannel plate, BP = bottom plate, TP = top plate, DT = drift tube. The red arrows represent the direction and magnitude of the electric fields, and the direction of travel of ions and electrons (e^-) are shown.

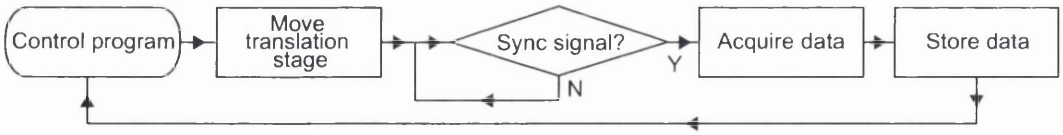

Figure 3.4: Flowchart of the procedure followed by the oscilloscope.

the MCP anode and the signal output of the detector electronics. The timebase is adjusted according to the minimum measurable pulse.

The DPO simultaneously runs the data collection, storage and processing software under LabVIEW, as well as communicating with a motion controller (Newport MM4005) via RS-232 and ASCII commands to automate the pump-probe delay and temporal pulse shaping described later. The oscilloscope behaviour for

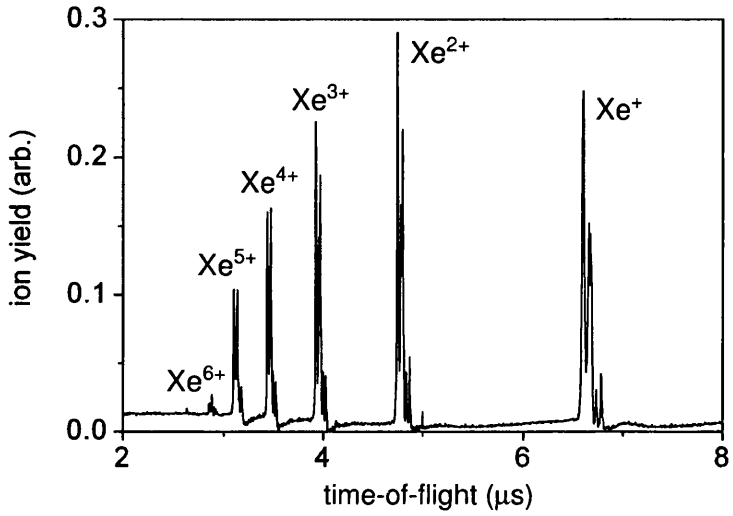

Figure 3.5: Typical time-of-flight spectrum for xenon, timebase 4 ns. Xe^{+} to Xe^{6+} charge states are visible (higher charge states appear earlier than lower charge states), with the five most abundant isotopes (^{129}Xe,^{131}Xe,^{132}Xe,^{134}Xe,^{136}Xe) detected. The mass resolution, $\frac{m}{\Delta m} \simeq 120$ (average Xe mass = 131.29 amu, from average isotope mass weighted by natural abundance [85]).

the experiments described in Chapters 5 and 6 is summarised in Figure 3.4. A photodiode samples the incoming laser pulses, utilising mirror leakage or back-reflection, and triggers the oscilloscope to be synchronised with each laser pulse.

A typical time-of-flight spectrum for xenon using spatial mode is shown in Figure 3.5. The velocity of each ion on leaving the acceleration region increases with increasing charge state; as such, the highest detected charge state (Xe^{7+}, at ~2.6 μs) arrives at the detector first, and the lowest charge state last (Xe^{+}, at ~6.7 μs). The total time-of-flight for each ion is predominantly determined by its charge, but the mass dependence can be resolved in the structure of each charge state peak, with the subpeaks corresponding to the arrival times of the different isotopes. Using the time-of-flight spectrum, the position of the focus with respect to the TOF aperture can be fine-tuned by maximising the amplitude

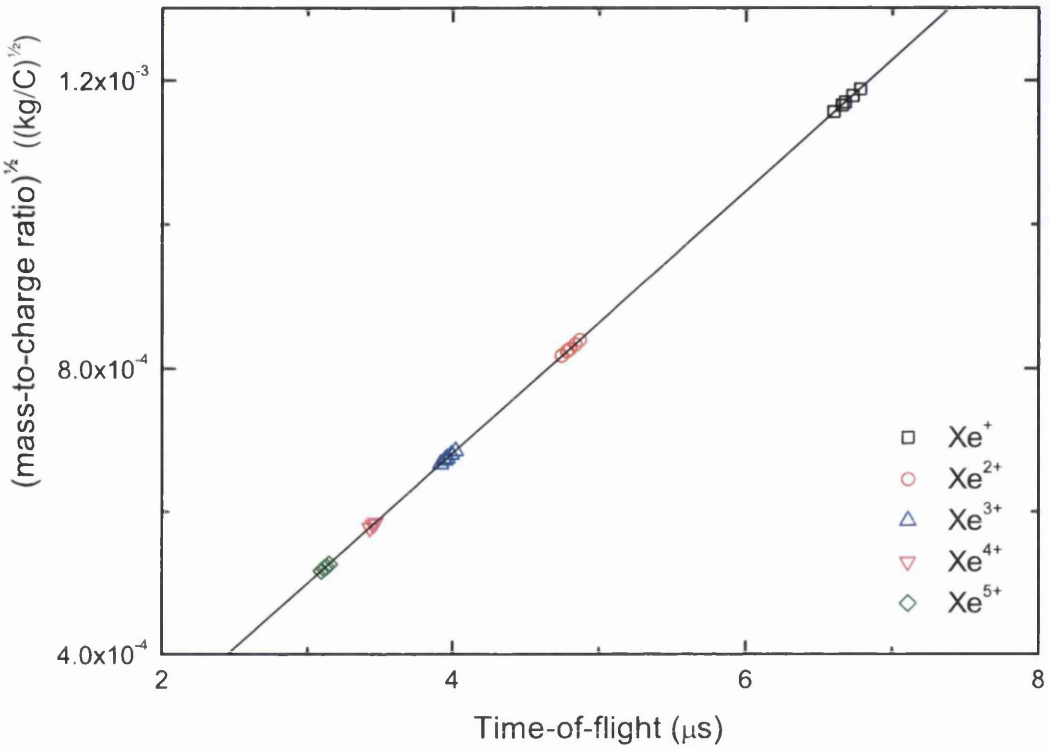

Figure 3.6: Xenon time-of-flight ion yield peaks plotted as a function of the square-root of their mass-to-charge ratio. Charge states are well-separated in time. The multiple data for each charge state correspond to the several isotopes of xenon present. The linear fit shown confirms the relationship expected from Equation (3.1).

of the highest charge state peaks, which are only generated over a small volume of the focal region.

Equation (3.1) predicts a linear relationship between the square root of the mass-to-charge ratio and the time-of-flight, which is verified in Figure 3.6 for the flight times, identified masses and charges in Figure 3.5.

3.3 Interferometric techniques

In order to investigate the temporal behaviour of ionization processes, an interferometer is used to create co-propagating identical copies of a pulse separated in time. The Mach-Zehnder interferometer layout is shown in Figure 3.7. The pulse

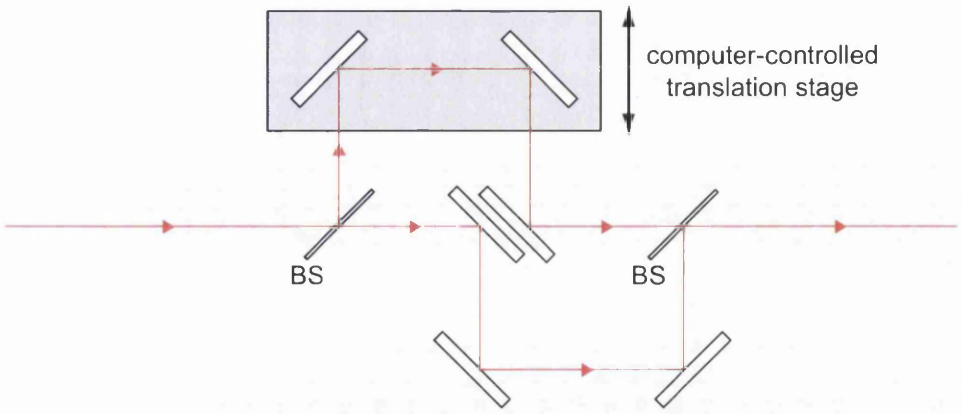

Figure 3.7: Mach-Zehnder interferometer, with a computer-controlled motorised translation stage in the variable arm. BS = thin beamsplitter.

is split at the input beamsplitter, and each copy traverses one of the interferometer arms. One arm has a fixed length; the other can be varied using a translation stage, which is controlled by the DPO via the Newport MM4005. A difference in path length corresponds to a difference in the time taken for each pulse copy to arrive at the output beamsplitter, where the beam paths recombine.

In order for time-dependent studies to be successful, the interferometer needs to be spatially well-aligned over the range of translation of the variable arm, with the overlap verified initially visually, then with a CCD. Near the temporal overlap, the spatial overlap can be fine-tuned using interference fringes as a guide. Typically, a path variation of less than a fringe (~30 nm, beam diameter 10 mm, distance 9 m) is acceptable, corresponding to ~0.1 fs.

A coarse determination of the temporal overlap position will be determined from the beam path length. The autocorrelator described in Section 2.2 is then used for a more accurate determination. Near temporal overlap, three peaks will be seen in the autocorrelation signal, which correspond to four temporal overlaps, the origin of which are illustrated in Figure 3.8. Temporal overlap is achieved where all peaks are superimposed.

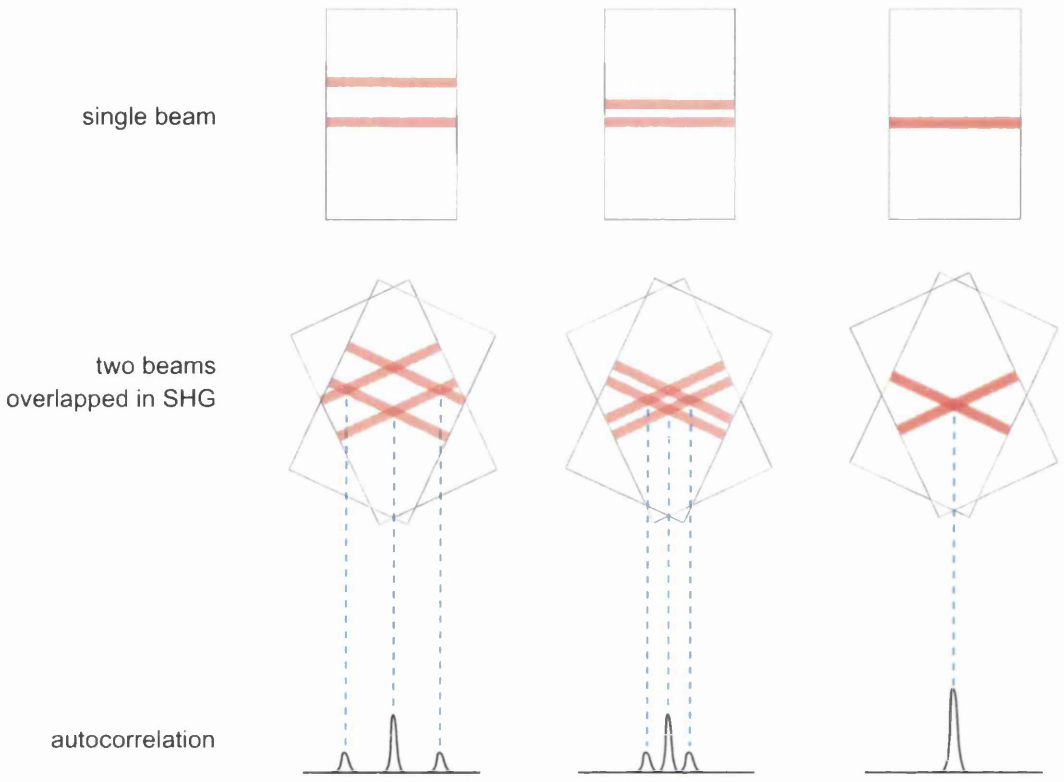

Figure 3.8: Measuring temporal overlap using an autocorrelator. The illustration shows two beams overlapped at a small angle (exaggerated in the figure for clarity) in a SHG crystal as illustrated in Figure 2.12. An autocorrelation signal is produced wherever the pulses overlap spatially and temporally within the crystal.

The translation stage in the variable arm of the Mach-Zehnder interferometer is comprised of a 25 mm long high-resolution translation stage (Newport M-MFN25CC), which may be mounted on a 25 cm long motorised translation stage (Newport ILS250CCL) to facilitate coarse adjustment of the beam path length. The small stage has a minimum increment of $\sim \frac{1}{6}$ fs (0.055 μm), repeatability of 1 fs (0.3 μm) and a stability of <300 as. The larger stage has a minimum increment of $\sim 3\frac{1}{3}$ fs (1 μm), repeatability of 1.5 μm, and a range of ~800 ps.

The optical cycle of NIR (wavelength ~800 nm) is ~2.7 fs. In order to resolve subcycle behaviour, a resolution of at least one half-cycle is required. Once the

approximate position of temporal overlap is found, the delay between the two pulses can be varied with ~0.3 fs resolution (twice the translation stage resolution, as the beam path length increases by $2\Delta z$ for every change Δz in stage position), which corresponds to $\frac{1}{8}$-cycle resolution as used in the experiment.

For pump-probe studies, e.g. the XUV-NIR experiment described in Chapter 6, either or both stages may be used in combination, with the smaller stage providing subcycle resolution if required.

With overlapped NIR-NIR pulses of the same polarization, the interferometer may be used for temporal pulse shaping, as modelled in Chapter 4 and used in the experiment described in Chapter 5. Superposition of the electric fields of the two pulses results in constructive and destructive interference, changing the temporal intensity profile of the pulse. Depending on the beamsplitters chosen, an unequal energy splitting can be used, enabling the weaker pulse to modify the shape of the stronger pulse without complete destructive or constructive interference occuring at temporal overlap.

The carrier envelope phase (CEP) of the pulses are not locked for the laser systems described in Section 2.1.6 and 2.1.7. However, the two copies of the pulse traversing the interferometer maintain the same relative CEP. The beamsplitters are thin to minimise material dispersion, and each pulse experiences the same amount of material dispersion, i.e. (aside from the mirrors) each pulse experiences one reflection from, and one transmission through a beamsplitter at 45°.

3.4 Polarization control

In order to transform the initially linearly-polarized pulses to circular polarization (as used in Chapter 5), a broadband achromatic quarter-waveplate (FemtoLasers OA229) is used, with a 14.5 mm clear aperture. The QWP consists of alternating

layers of quartz (SiO_2) and magnesium fluoride (MgF_2) crystals. The retardation is 0.25 ± 0.007 over the range 650 – 950 nm. The pulse propagation through the QWP is modelled in Section 4.1.1.

3.5 Conclusion

The detection of ions produced at the laser focus by TOFMS is thoroughly discussed, as well as the apparatus for temporal pulse shaping and polarization control. The TOF spectra obtained as a function of mirror position and pulse shape are processed and analysed in Chapter 5.

Chapter 4

Tunnel ionization and spatiotemporal pulse modelling

This chapter describes the spatial and temporal modelling of pulse propagation through the NIR beamline used for the experiments in Chapter 5, incorporating temporal pulse shaping. The nonadiabatic tunnel theory of Yudin and Ivanov described in Chapter 1 is used in a modified form to incorporate multielectron effects, and used to generate ionization probabilities for comparison to the data in Chapter 5. The beamline and tunnelling models are then combined in order to predict the three-dimensional ion distributions over the focal region.

4.1 Pulse propagation

In order to generate laser intensities required for most strong-field processes, it is typically necessary to produce a laser focus. Gaussian optics are commonly assumed to sufficiently describe the focal geometry. However, as a consequence of the processes leading to ultrashort pulse generation described in Chapter 2, and diffraction due to beam transport optics over propagation distances of a few metres as discussed in Chapter 7, the resultant beam profile may differ signif-

icantly from a Gaussian. In these cases, more rigorous predictions of the focal geometry are required in order to derive meaningful results from experimental data, particularly where strong-field physics at the focus is spatially resolved.

It is convenient to describe an optical system mathematically as a matrix, which is a combination of individual matrices describing optical components. Typical experimental setups are radially-symmetric, and it is fair to assume that the paraxial condition is maintained, i.e. that all rays lie near to, and form a small angle with respect to the axis of propagation. The optical matrices are therefore simplified by the paraxial approximation [75] to give

$$T = \begin{pmatrix} 1 & d \\ 0 & 1 \end{pmatrix} \quad L = \begin{pmatrix} 1 & 0 \\ -\frac{1}{f} & 1 \end{pmatrix} \quad R = \begin{pmatrix} 1 & 0 \\ 0 & \frac{n_1}{n_2} \end{pmatrix} \tag{4.1}$$

where T is a free-space translation, L is a thin lens or spherical mirror (with $\frac{1}{f} = \frac{2}{\mathrm{ROC}}$, where f is the focal length and ROC is the radius of curvature), and R is refraction at an index boundary (n_1 and n_2 are the refractive indices before and after the boundary respectively). Each component matrix describes the effect on a paraxial ray $\binom{r}{\theta}$, with r and θ being the displacement and angle with respect to the propagation axis respectively.

Ray-tracing can provide useful information such as approximate changes in beam size, if the initial size is known, and positions of geometric foci. In itself, this method cannot yield changes to beam profile. However, it can be combined with diffraction equations which predict the complex electric field distribution at an output plane from a given input plane. A generalized form of the Huygens-Fresnel diffraction equation for cylindrically-symmetric coordinates, derived from

the work of Collins [86], is given as

$$U_2(r_2,\phi,z) = \frac{-i}{\lambda B}\int_0^{2\pi}\int_0^{a} U_1(r_1,\theta,z=0)\exp(ikS)r_1 dr_1 d\theta \tag{4.2}$$

where

$$S = Z' + \frac{1}{B}(Ar_1^2 - 2r_1r_2\cos(\phi-\theta) + Dr_2^2)$$

is a function describing the distance between any two points on the input and output planes, z is the axial position, λ is the wavelength, $k = \frac{2\pi}{\lambda}$ is the wavenumber, and A, B, D are elements of the paraxial system matrix $M = \left(\begin{smallmatrix} A & B \\ C & D \end{smallmatrix}\right)$ describing the optical system between the two planes. M is constructed by multiplying together the necessary component matrices T, L and R for each section of the beamline, giving

$$M_{in\to1} = L_1T_1 = \begin{pmatrix} 1 & d_1 \\ -\frac{1}{f_1} & 1-\frac{d_1}{f_1} \end{pmatrix} \qquad M_{1\to2} = T_2 = \begin{pmatrix} 1 & d_2 \\ 0 & 1 \end{pmatrix}$$
$$M_{2\to3} = T_3 = \begin{pmatrix} 1 & (d_3) \\ 0 & 1 \end{pmatrix} \qquad M_{3\to4} = T_4L_2 = \begin{pmatrix} 1-\frac{z}{f_2} & z \\ -\frac{1}{f_2} & 1 \end{pmatrix} \tag{4.3}$$

where $M_{in\to1}$ is the matrix describing the section between the hollow fibre exit plane, $U_in(r_in)$ on Figure 4.1, and the collimating mirror plane, $U_1(r_1)$; $M_{1\to2}$ the matrix between the collimating mirror and the quarter-wave plate (QWP), $U_2(r_2)$; $M_{2\to3}$ between the QWP plane and the focusing mirror plane $U_3(r_3)$; and $M_{3\to4}$ between the focusing mirror and the plane $U_4(r_4,z)$ within the focal region at a chosen axial position, z. f_1 and f_2 are the focal lengths of the collimating mirror and focusing mirror respectively. In the model described in this chapter, $d_1 = 1$ m, $d_2 = 6$ m, $d_3 = 2.6$ m, $f_1 = 1$ m, and $f_2 = 50$ mm.

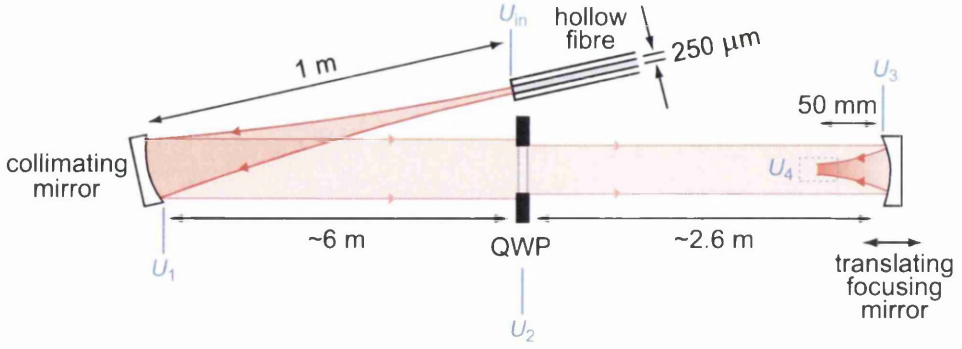

Figure 4.1: Beamline modelling. The Huygens-Fresnel integral (Equation (7.1)) is solved numerically at each of the planes U_1 to U_4, with the propagation between planes modelled using matrices, as described in the text. QWP = quarter-wave plate. Distances and angles have been exaggerated for diagrammatical purposes.

The input and output planes are separated by a total axial distance Z', and co-ordinates (r_1, θ) and (r_2, ϕ) define points on the input and output planes respectively.

Using the laser resonator condition [87]

$$\int_0^{2\pi} \exp[i(\frac{kr_1r_2}{X}\cos[\theta-\phi]-l\theta)]d\theta = 2\pi i^l \exp(-il\phi)J_l(\frac{kr_1r_2}{X}) \tag{4.4}$$

and expanding Equation (4.2), the electric field at the output plane is given by

$$U(r_2,z) = -\frac{2\pi i}{\lambda B}\exp(ik(Z'+\frac{Dr_2^2}{2B}))\int_0^a U_1(r_1,z=0)\exp(Gr_1^2)J_0(Hr_1)r_1dr_1 \tag{4.5}$$

where $G = ikA/2B$ and $H = kr_2/B$.

The optical setup used in Chapter 5 has been modelled as illustrated in Figure 4.1. A Gaussian beam profile is assumed to be optimally coupled at the input end of the hollow fibre described in Section 2.1.8, such that the output consists predominantly of the EH_{11} fundamental Bessel mode [30, 88, 89] of the

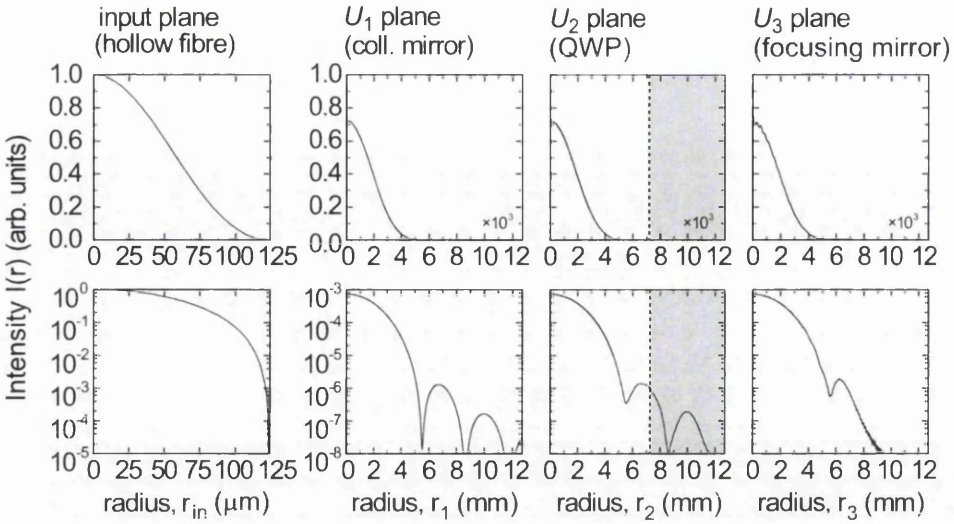

Figure 4.2: Solutions to the Huygens-Fresnel equation at the exit of the hollow fibre (U_{in}), collimating mirror (U_1), quarter-wave plate (U_2) and focusing mirror (U_3), as labelled in Figure 4.1. Normalised intensity, I/I_0 is plotted as a function of radius, r, where I_0 is the peak intensity at the input plane. The grey region in $U_2(r)$ represents the truncation due to the QWP having a clear aperture of 7.25 mm.

form

$$U(r_1) = J_0(2.405r_1/a_1) \tag{4.6}$$

which is a zeroth-order Bessel function of the first kind truncated at the first root, and $a_1 = 125$ μm is the radius of the hollow fibre.

Figure 4.2 shows the solutions of the Huygens-Fresnel (H-F) at the hollow fibre exit, collimating mirror, quarter-wave plate (QWP) and focusing mirror. The beam profile at the output of the hollow fibre forms the input plane for the first stage of the model. The hard edge at the fibre exit causes diffraction, as can be seen in the solution of the H-F at plane U_1. The beam is truncated by the 1" (25.4 mm) diameter collimating mirror, and this is used as the input to the H-F for the second stage of propagation. The QWP converts the initially linearly-polarized light to circular polarization, but also causes further diffraction (14.5 mm-diameter clear aperture). The H-F is evaluated at the QWP after

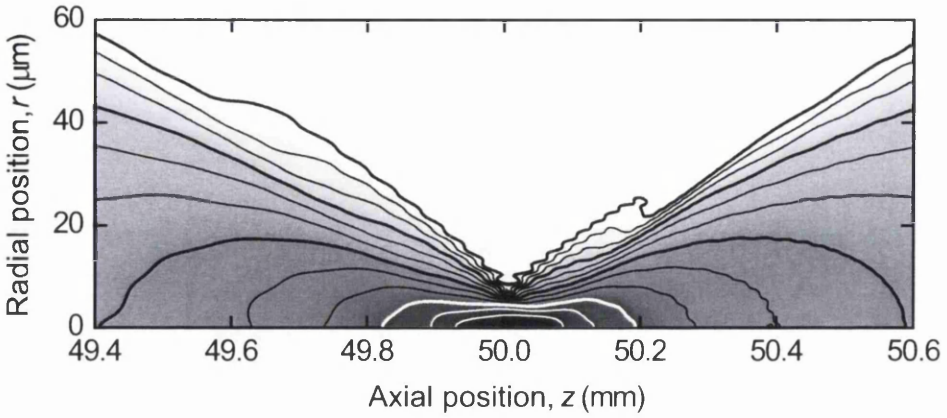

Figure 4.3: Huygens-Fresnel intensity solution in the focal region, $U_4(r_4, z)$ in Figure 4.1, after propagation through the model beamline in the same figure. Thick contours are plotted at each order of magnitude change in intensity, with thin contours for every $\frac{1}{3}$-order. The contour colour change is for clarity only.

truncation (U_2), which propagates towards the 1" diameter focusing mirror, where U_3 is evaluated. In Chapter 5, the focusing mirror is housed within the time-of-flight mass spectrometer (TOFMS) described in Section 3.1. Since the focusing mirror can be translated with respect to the detector, the H-F at $U_4(r, z)$ is evaluated for a range of axial positions, z.

Figure 4.3 shows a radial slice through the full three-dimensional axisymmetric focal region. The effects of diffraction can be seen as oscillations in the contours, most clearly between z =49.4 – 49.7, 50.2 – 50.4 mm for $r \leq 20$ μm. There is also an asymmetry either side of the expected geometric focus at $z = 50$ mm. The peak intensity is offset 40 μm downstream of the geometric focus, and there are asymmetric lobes for intensities between three and four orders below the peak intensity, extending to $z = 49.6$ mm on one side of the geometric focus, and to $z = 50.2$ mm on the other.

Using the procedures described, the full three-dimensional focal volume (in x, y and z) can be modelled numerically. However, a fixed volume element size sufficient to accurately represent the small (in r) structured intensity distribution

at low z will result in an unnecessarily high-resolution representation of the large (in r) smooth distribution at high z, resulting in an inefficient use of computer processing time. An adaptive grid has therefore been adopted, where only Δz is fixed, and $\Delta x, \Delta y$ vary according to the half-width half-maximum (HWHM) in r for each Δz. The calculation time for a section of the focal volume between z = 49–50 mm using an adaptive grid in (x, y), with a minimum step size $\Delta x = \Delta y \sim 0.3$ μm and maximum $\Delta x = \Delta y \sim 5$ μm took $\sim$ 15 minutes, compared to $\sim 3\frac{1}{2}$ hours with a fixed $\Delta x = \Delta y = 0.5$ μm.

Histograms demonstrating the variation in intensity distribution with the axial position, z, as a series of slices through the full three-dimensional volume are plotted in Figure 4.4 for $I_{\text{peak}} = 10^{17}$ W/cm^2, calculated over a volume of 125 μm $\times$ 125 μm $\times$ 5 μm for each z-slice. $\Delta x, \Delta y$ varies between 0.15 – 2 μm, and $\Delta z = 5$ μm is fixed. At 49.0 mm, no volume elements are above $I = 1.4 \times 10^{15}$ W/cm^2, and most are below 3.2×10^{14} W/cm^2. As z increases up to 50 mm, the on-axis peak intensity increases and the radial intensity profile narrows, i.e. the volume decreases and occupies a wider range of intensities, which is reflected in the histograms. At 49.6 mm, secondary peaks appear, corresponding to the diffraction structure in the beam reaching higher intensities. At 50 mm, there are two maxima in the histogram. The peak intensity is 10^{17} W/cm^2, but the volume above 7.5×10^{16} W/cm^2 is at least ten times smaller than the volume contributing to the intensity range 6.7×10^{16} – 7.5×10^{16} W/cm^2. Above $z = 50$ mm, the volume begins to increase and the intensity range occupied decreases.

4.1.1 Temporal effects and polarization

The modelling described in Section 4.1 considers only the spatial effects of beam propagation. For the experiments in Chapter 5, circularly-polarized pulses are

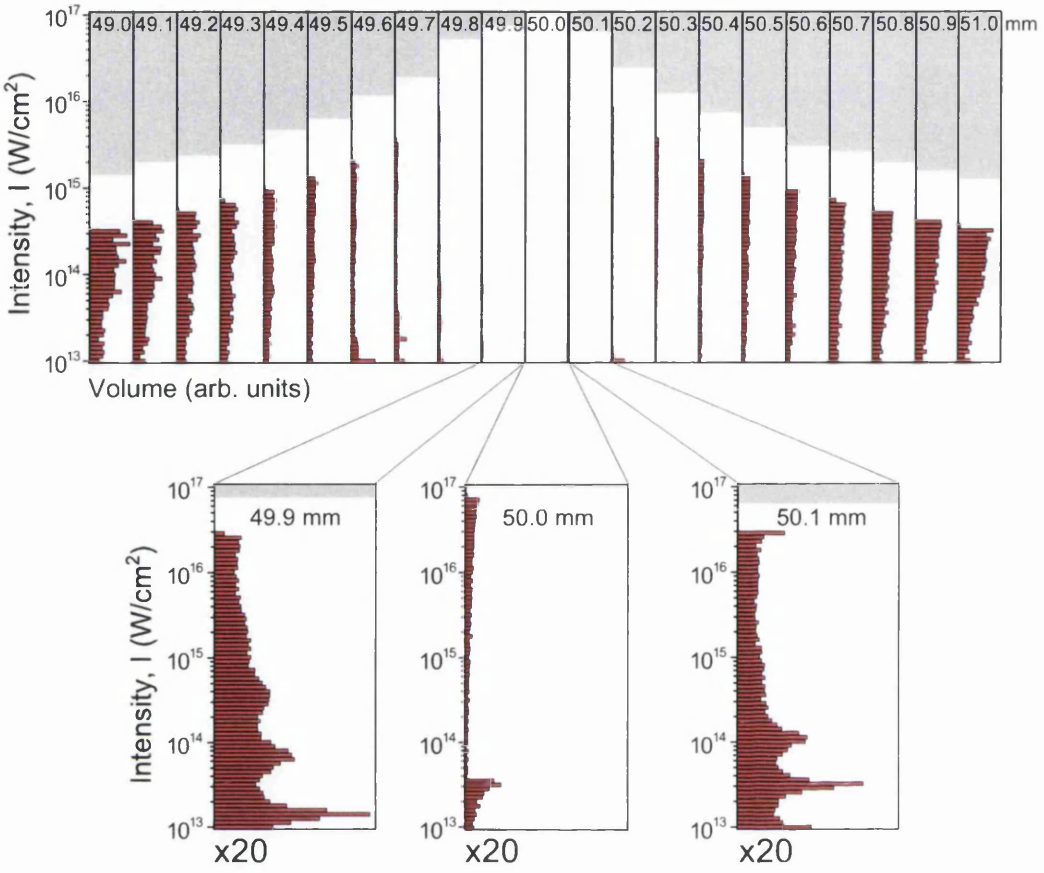

Figure 4.4: Histograms of the full three-dimensional intensity distribution, at the z-positions labelled, for a peak intensity of 10^{17} W/cm^2. The volume scale for all histograms has been normalized to the height of the highest bar at $z = 49.0$ mm for clarity. The grey filled areas indicate regions which are above the peak intensity for that particular z. The intensity bin width is $10^{0.05}$ W/cm^2.

used to suppress recollision ionization (which is discussed in Chapter 1). To transform the initially linearly-polarized pulses from the laser to circular polarization, a QWP is used (Section 3.4). Apart from the entrance window of the TOFMS, the QWP is the only transmissive optic in the NIR-NIR beamline after the hollow fibre (Figure 5.1). Any material in the beam path will result in temporal dispersion of the laser pulse.

Section 2.2.2 describes the FROG technique used to measure the pulse electric field envelope and phase as a function of time, enabling the retrieval of the

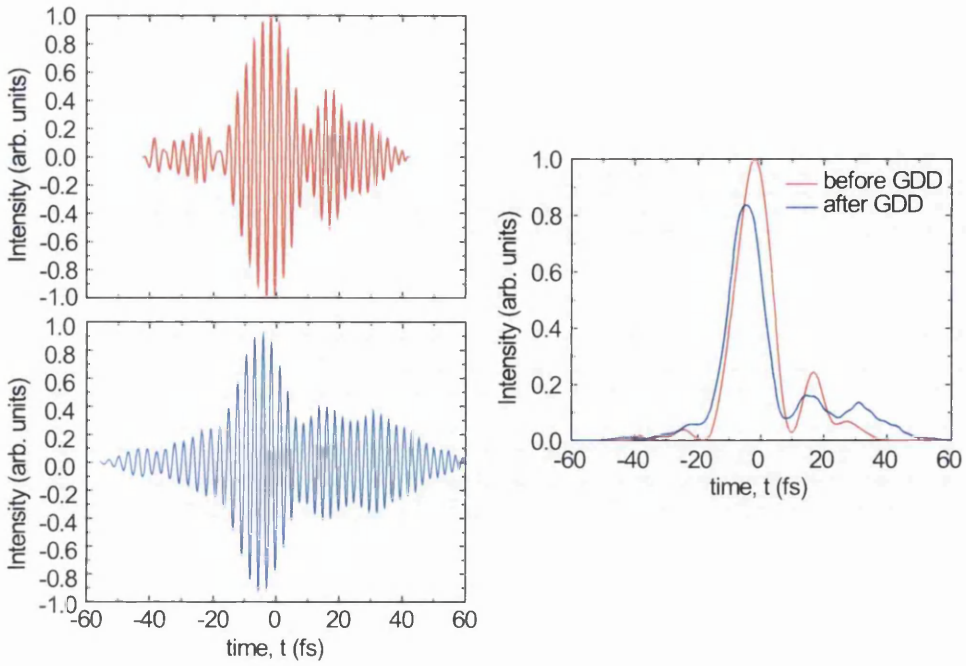

Figure 4.5: *(left)* Measured pulse electric field before the QWP (red), and modelled pulse electric field after the QWP (blue), incorporating the effects of additional group-delay dispersion (GDD). *(right)* Corresponding pulse intensity envelopes before and after QWP.

temporal intensity and reconstruction of the pulse electric field. The FROG measurement already takes into account the propagation through the TOFMS entrance window, with a glass plate of the same thickness positioned in front of the FROG. The group-delay dispersion (GDD) due to propagation through the air is also included, since the beam paths to the FROG and the TOFMS entrance window are equivalent. However, the measurement does not take into account the GDD the pulse acquires due to the QWP, since the circularly-polarized pulses are reduced in intensity, below the FROG's detection threshold. The pulse propagation through the QWP must therefore be modelled to determine the resultant pulse shape.

Since the waveplate retardation is approximately constant over a large spectral range (650 – 950 nm), it is reasonable to consider the effects of material dispersion

and the change in polarization separately. The linearly-polarized pulse electric field is Fourier-transformed. In the frequency domain, the GDD then corresponds to the φ_2 term in the Taylor expansion of the spectral phase

$$\varphi(\omega) = \varphi_0 + \varphi_1(\omega - \omega_0) + \varphi_2\frac{(\omega - \omega_0)^2}{2!} + \ldots \tag{4.7}$$

where φ_1 is the group delay, ω the frequency and ω_0 the centre frequency of the laser field. By analogy with Equation (4.7), the additional spectral phase incurred due to the waveplate is therefore given by

$$\varphi_{\mathrm{QWP}} = \varphi_{\mathrm{GDD}}\frac{(\omega - \omega_0)^2}{2!} \tag{4.8}$$

where φ_{GDD}, is the QWP GDD taken from [90]. φ_{QWP} is then added to the spectral phase of the pulse. The inverse Fourier transform of the pulse then yields the resulting linearly-polarized pulse in the time domain. Figure 4.5 shows the pulse electric field and intensity envelope before and after the inclusion of the QWP GDD. Even though a temporal spreading of the pulse is expected, the full-width half-maximum of the main peak has been retained ($\sim$13 fs). However, the minimum at -20 fs has largely disappeared, and the temporal structure above $\sim$8 fs is significantly distorted.

Figure 4.6 illustrates the modelling of the conversion of the linearly-polarized pulse to circular polarization. The pulse electric field (with GDD) is decomposed into two orthogonal components at 45° to the initial pulse, one component is retarded by $\lambda/4$, and the magnitude of the resultant electric field vector taken as the output electric field from the QWP. The resultant intensity is the square of the electric field magnitude, as shown in Figure 4.7. The small subcycle ripples in intensity are as a result of the propagation through the waveplate: the retardation

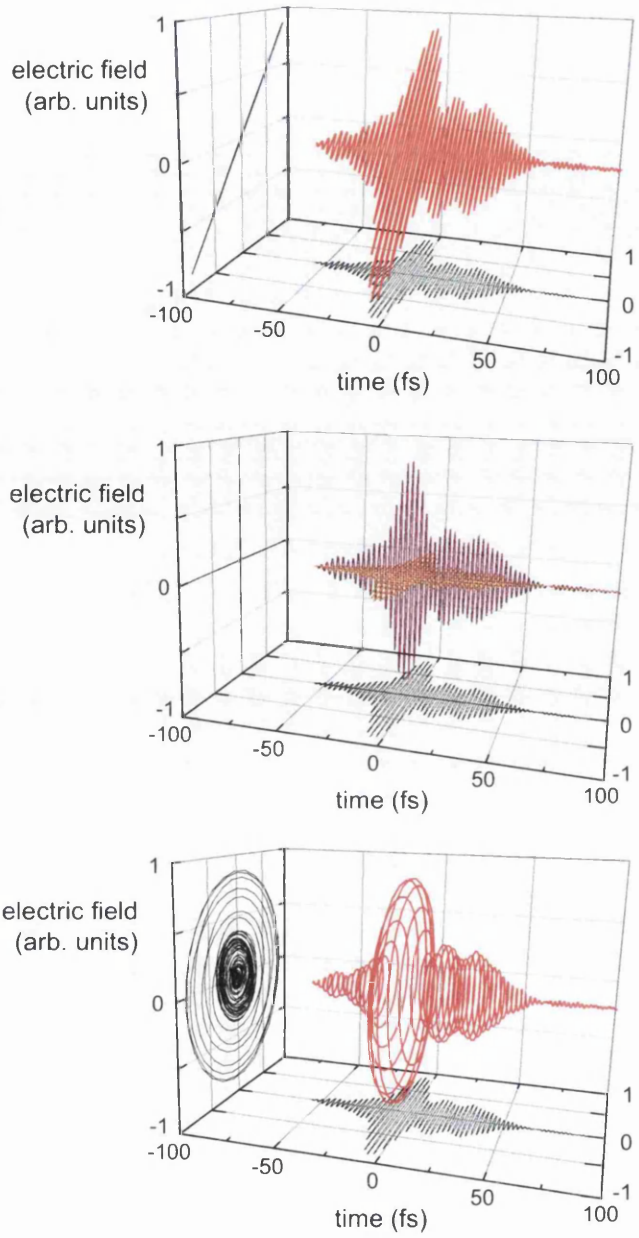

Figure 4.6: Electric field as a function of time, transformed from linear to circular polarization using the method described in Section 4.1.1. For each of the three frames, the left and bottom faces show a projection (black lines) of the three-dimensional plot (coloured lines); the projection on the rear face is omitted for clarity but would be similar to the bottom face. The initial linearly-polarized pulse *(top frame)* is decomposed into two equal-amplitude orthogonal components *(middle frame)* which combine to give the same resultant at each time, t. One of the components is retarded by $\lambda/4$, and the new resultant of the two electric field components calculated *(bottom frame)*, giving the circularly-polarized pulse.

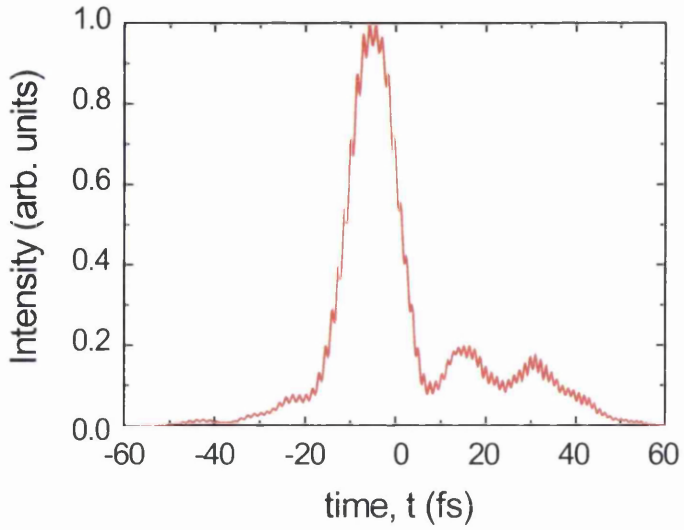

Figure 4.7: Modelled temporal intensity profile of the pulse following inclusion of QWP GDD as shown in Figure 4.5, and transformation from linear to circular polarization as shown in Figure 4.6.

of one of the polarization components by $\lambda/4$ is equivalent to temporally delaying it by $\frac{2}{3}$ fs with respect to the other, resulting in an offset in the intensity envelopes.

4.2 Multielectron tunnelling

The tunnel theory of Yudin and Ivanov [3] discussed in Chapter 1.3 is used to predict the instantaneous ionization rate as a function of intensity. For circularly-polarized pulses, the rate is given by

$$\Gamma_{circ}(t) = N(t)\exp\Big(-\frac{\varepsilon^2 f^2(t)}{\omega_L^3}\Phi_{circ}(\gamma(t))\Big) \tag{4.9}$$

where

$$\Phi_{circ}(\gamma) = (\gamma^2+2)\cosh^{-1}\Big(1+\frac{\gamma^2}{2}\Big) - 2\gamma\sqrt{1+\frac{\gamma^2}{4}}$$

ε is the peak electric field amplitude, $f(t)$ the electric field envelope, ω_L is the frequency of the laser field, and $\gamma(t)$ is the time-dependent Keldysh parameter,

all in atomic units. The pre-exponential factor, $N(t)$, is given by [3]

$$N(t) = A_{n^*,l^*} B_{l,|m|} \left(\frac{3\kappa}{\gamma^3}\right)^{1/2} C I_p \left(\frac{2(2I_p)^{3/2}}{\varepsilon f(t)}\right)^{2n^*-|m|-1} \tag{4.10}$$

where $C \simeq 1$ for tunnelling, I_p the ionization potential, and

$$A_{n^*,l^*} = \frac{2^{2n^*}}{n^*\Gamma(n^*+l^*+1)\Gamma(n^*-l^*)}$$

$$B_{l,|m|} = \frac{(2l+1)(l+|m|)!}{2^{|m|}|m|!(l-|m|)}$$

$$\kappa = \ln(\gamma + \sqrt{\gamma^2+1}) - \frac{\gamma}{\sqrt{\gamma^2+1}}$$

where $\Gamma(x)$ is the mathematical Gamma function, n, l, m are quantum numbers, and n^* and $l^* = n^* - 1$ the effective quantum numbers, where

$$n^* = n - \delta_l = \frac{Z}{\sqrt{2I_p}}$$

δ_l is the quantum defect [91], Z is the core charge, and I_p the ionization potential (in a.u.). The effective quantum numbers include the quantum defect in order to compensate for the core electrons not completely screening the nuclear charge, since the valence electron orbitals can penetrate the core.

Section 1.3 of the review describes the possibility of excitation during the process of ionization, since discrepancies exist between experimental results and ground-state-only models. Agreement between theory and experiment is improved when multiple levels are included, and population transfer occurs, possibly due to shake-up excitation caused by the rapid removal of the outgoing electron [60, 66]. Additionally, in molecular studies [68], contributions from the

highest-lying (highest occupied molecular orbital, or HOMO) and a lower-lying energy level (HOMO-1) have been experimentally-resolved, and matched to models which consider the possibility of direct tunnelling of the lower-lying electrons.

Inspired by [68], some of the modelling described in this section allows tunnel ionization between several/all initial and final states resulting from the sequential removal of electrons from outer- ($5p$) or inner-valence ($5s$) orbitals. The direct removal of lower-lying electrons therefore creates population in several states without any transfer of population taking place between the states via excitation. Each pathway between initial and final states has a probability, which for any particular intensity, orbital will depend on the ionization potential, I_p, determined from the difference in energy between initial and final states.

Spectroscopic data [92] provides the inner- ($5s$) and outer-valence ($5p$) electron configurations and corresponding energy levels for the model, which are listed in Table 4.1, and plotted as a Grotrian diagram in Figure 4.8. There are three possible final energy levels for Xe^+, nine for Xe^{2+}, and thirteen for Xe^{3+}. Figure 4.9 gives illustrative examples of the different ionization pathways possible as a result of including all energy levels. Additionally, each level has $2J+1$ degenerate states with the same energy.

This leads to the two models considered in this chapter. In one model (non-degenerate model), the degeneracy does not affect the rate of ionization between initial and final states. In the other model (degenerate model), the degeneracy of the final state is included, assuming all degenerate states can be reached with the same probability. The degenerate model therefore assumes the rate Γ_{ij} is equal for $m = -1, 0, 1$, whereas Equation (4.10) predicts a lower ionization rate for $m = \pm 1$ compared to $m = 0$.

Table 4.2 summarises the number of $5p^{-n}$ and $5s^{-n}$ levels in each charge state for the degenerate and nondegenerate models.

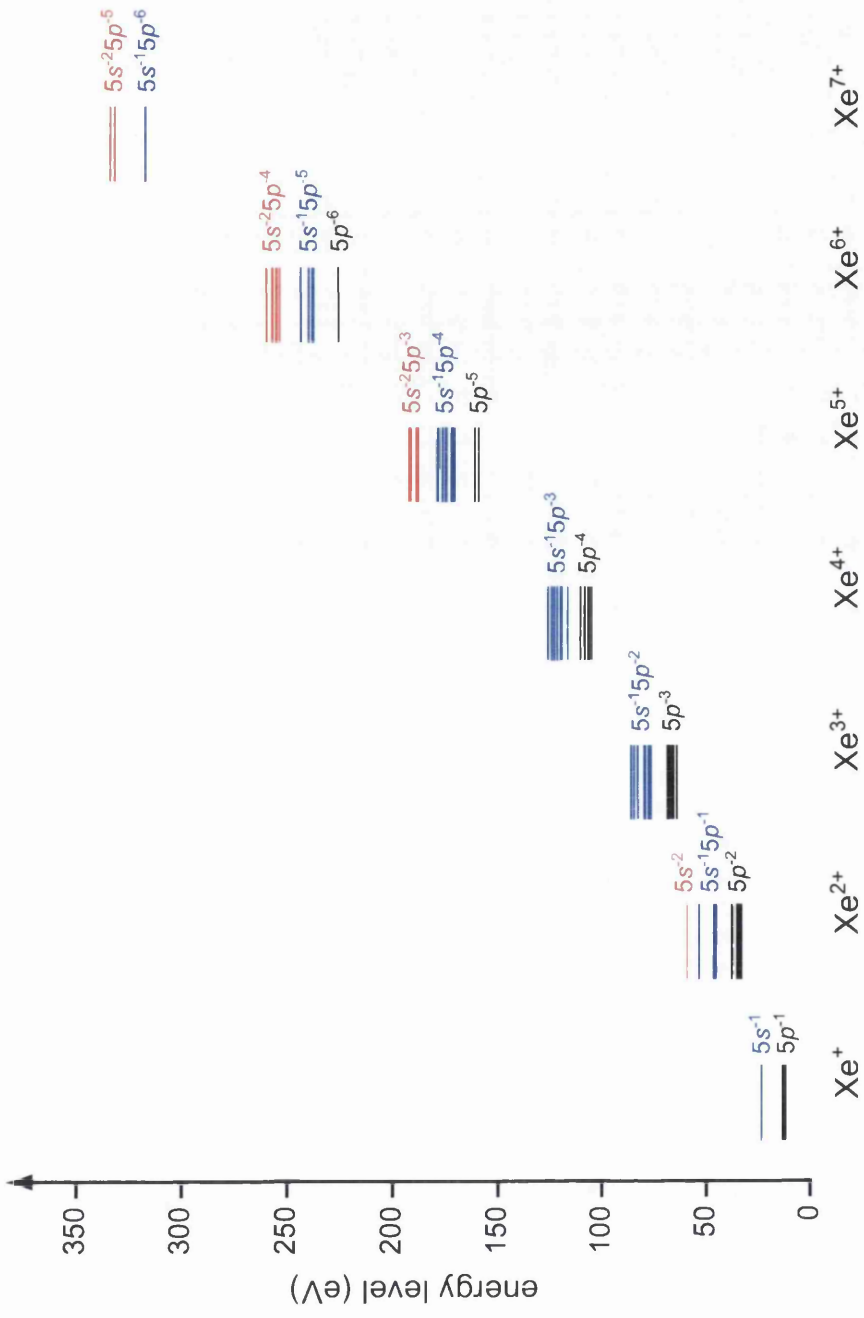

Figure 4.8: Grotrian diagram of xenon energy levels, plotted using data from NIST [92] as listed in Table 4.1. (black) $5p$-electron removal only, (blue) one $5s$-electron removed, (red) two $5s$-electrons removed. There is no NIST data for the $5s^{-2}5p^{-1}$ and $5s^{-2}5p^{-2}$ levels, hence they are assumed to be energetically unfavourable, and have been omitted.

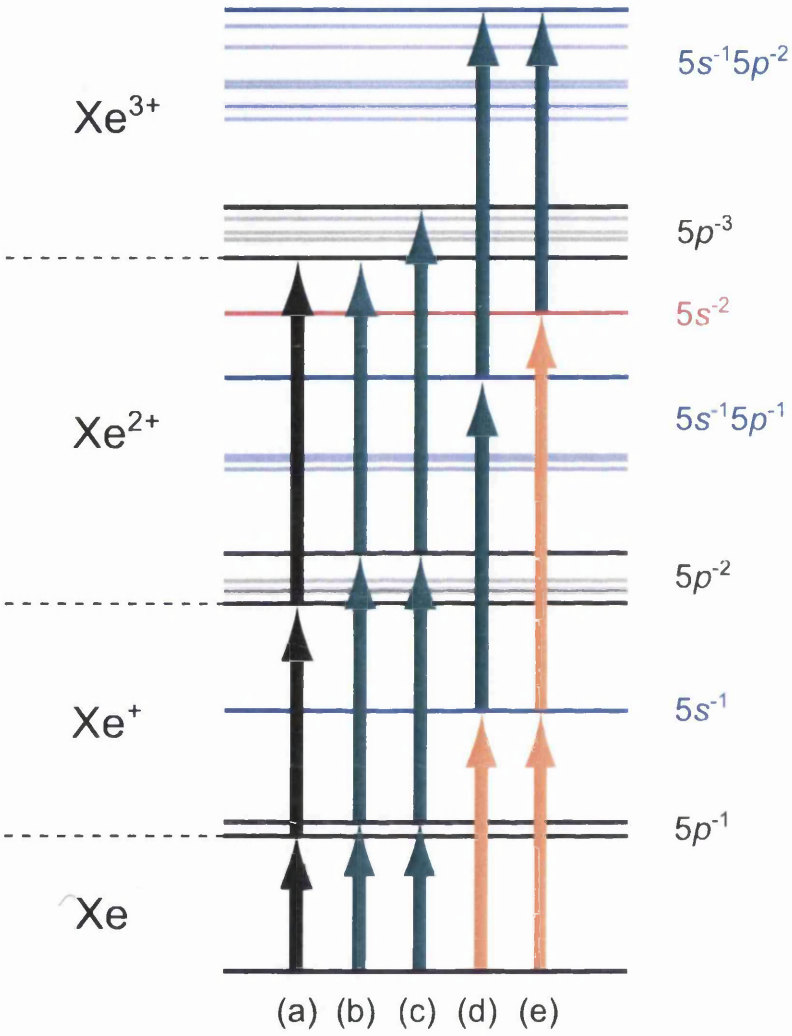

Figure 4.9: Illustration of allowed ionization pathways in Xe, up to Xe^{3+}: (a) ionization proceeds via the ground states only, via $5p$-electron removal, leaving the Xe^{3+} ion in the ground state; (b) removal of lower-lying $5p$ electrons is allowed, enabling an alternative ionization pathway for population of the Xe^{3+} ground state; (c) as before, but with population of a higher-energy Xe^{3+} state; (d & e) additional pathways enabled by allowing removal of $5s$ electrons.

For each energy level, the data are converted to a set of ionization pathways, labelled by the required change in the number of s or p electrons, Δs and Δp respectively, and I_p. Two versions of the model are used: the first includes only the ground, or lowest-energy level for each ion, only allowing a single ionization pathway for each charge state; the second includes all $5s$ and $5p$ levels.

In order to convert ionization rate to ionization probability, the kinetic model used by Perry *et al.* [9] is adopted, whereby the evolution of the populations in each energy level can be described by a set of first-order coupled ordinary differential equations of the form

$$\frac{dn_j}{dt} = \sum_{i=0}^{i<j} \Gamma_{ij} n_i(t) - \sum_{k=j+1}^{k_{\text{tot}}} \Gamma_{jk} n_j(t) \tag{4.11}$$

where $n_i(t)$ is the number of ions in energy level i, and Γ_{ij} is the ionization rate for the production of ions in level j from level i, with k_{tot} being the total number of energy levels included in the model.

Equation (4.11) is adapted for discrete-timestep calculation as

$$n_j(t + \Delta t) = n_j(t) + \sum_{i=0}^{i<j} \Gamma_{ij}(t) n_i(t) \Delta t - \sum_{k=j+1}^{k_{\text{tot}}} \Gamma_{jk}(t) n_j(t) \Delta t \tag{4.12}$$

The electric field term in Γ_{ij}, $\varepsilon f(t)$, is taken from the output of the modelling described in Section 4.1.1. The quantities n^*, l^*, l, m and I_p are determined from the spectroscopic data, resulting in the rate $\Gamma_{ij}(t)$ becoming a function of intensity only, where the intensity is defined as $I(t) = \varepsilon^2 f^2(t)$. For sequential ionization, $\Gamma_{ij} = 0$ for $j > i + 1$. By scaling the peak intensity of the input pulse, the remaining non-zero values of $\Gamma_{ij}(t)$ are calculated, and Equation (4.12) solved for subsequent Δt.

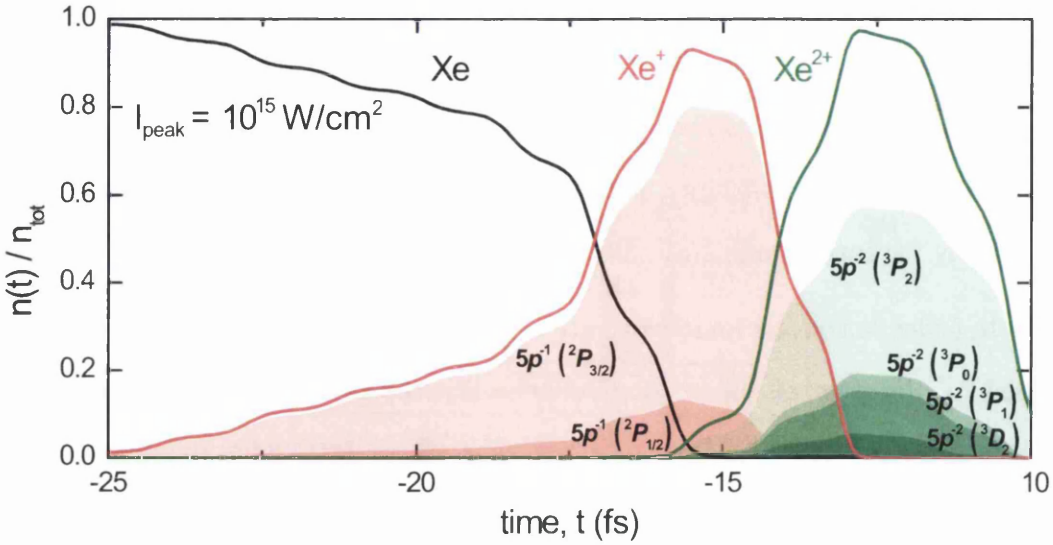

Figure 4.10: Populations of multiple energy states of Xe ions as a function of time. The solid lines denote the total population of each charge state; the shaded regions represent the contribution to the total population of each labelled state (full list of states given in Table 4.1).

Figures 4.10 and 4.11 show the results of an application of Equation (4.12), using the $I(t)$ plotted in Figure 4.7 with a timestep size $\delta t = 0.1$ fs. At this resolution, the error in $n(t)/n_{\text{tot}}$ is 0.001%. Figure 4.10 includes all of the energy levels shown in Figure 4.8 and listed in Table 4.1 without degeneracy included; Figure 4.10 includes the same levels with the degeneracies listed in Table 4.1.

The population in non-ground-state energy levels is significant. For example, in Figure 4.10: at the peak in Xe^+ yield at -15.5 fs, ~86.9% of the population is in the ground state ($^2P_{3/2}$), with the remaining 13.9% in the higher-energy ($^2P_{1/2}$) state. At the peak in Xe^{2+} at -12.8 fs, ~99.8% of the population is spread across four levels ($^3P_2$,$^3P_0$,$^3P_1$,$^1D_2$), with 58.5% in the ground state, 19.8%, 15.8% and 5.7% in the other three states respectively.

The $n_i(t)$ values for each included energy level are grouped and added together according to charge state. Figures 4.12 and 4.13 show $n(t)/n_{\text{tot}}$ and $n(\tau)/n_{\text{tot}}$ for the nondegenerate and degenerate models respectively, for a range of peak

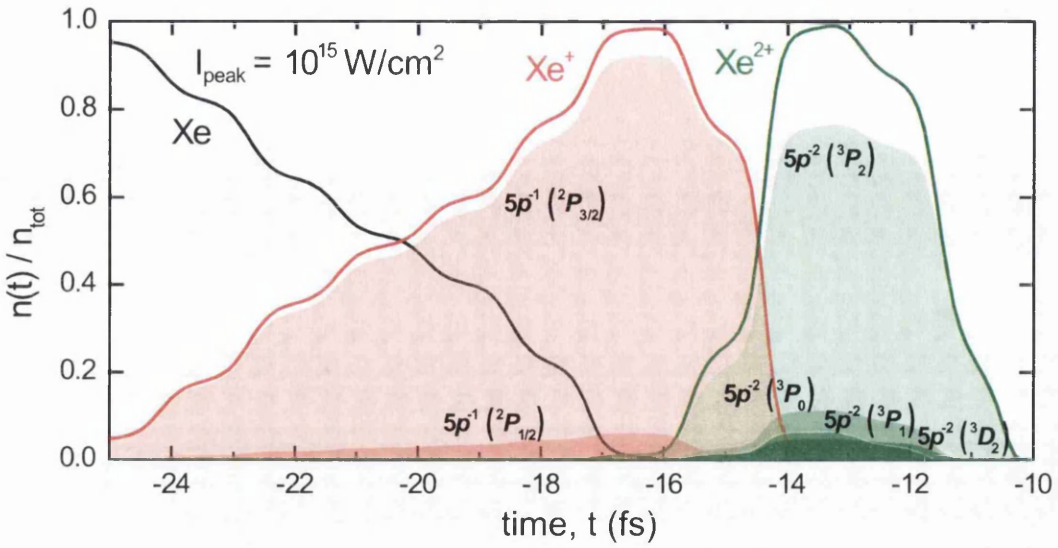

Figure 4.11: Populations of multiple energy states including degenerate states of Xe ions as a function of time. The solid lines denote the total population of each charge state; the shaded regions represent the contribution to the total population of each labelled state (full list of states given in Table 4.1).

intensities, I_{peak}, for charge states up to Xe^{3+}. In all models, nearly all of the ionization is completed in the leading edge of the pulse, between $t = -20$ and -5 fs. However, the peak region of the pulse from around $t = -10$ to 0 fs appears to have the greatest influence on the distribution of population in the highest charge states, since it is here that the largest difference is seen between the ground-state and multiple-state models. Note the peak intensity is positioned at around -5 fs in the figure.

There is also a consistent difference in the degenerate and nondegenerate models over a large range of peak intensities. The leading-edge gradient of $n(t)/n_{\text{tot}}$ is generally steeper in the degenerate case. Also, at $I_{\text{peak}} = 3.2 \times 10^{14}, 5 \times 10^{14}$ and 6.3×10^{14} W/cm^2, it can be seen that the Xe^+ population has a higher peak which persists for a longer duration in the degenerate than the nondegenerate case. At $I_{\text{peak}} = 10^{15}$ W/cm^2, the Xe^+ population begins to be influenced by the weaker part of the leading edge of the pulse, between $t = -30$ and -18 fs. The

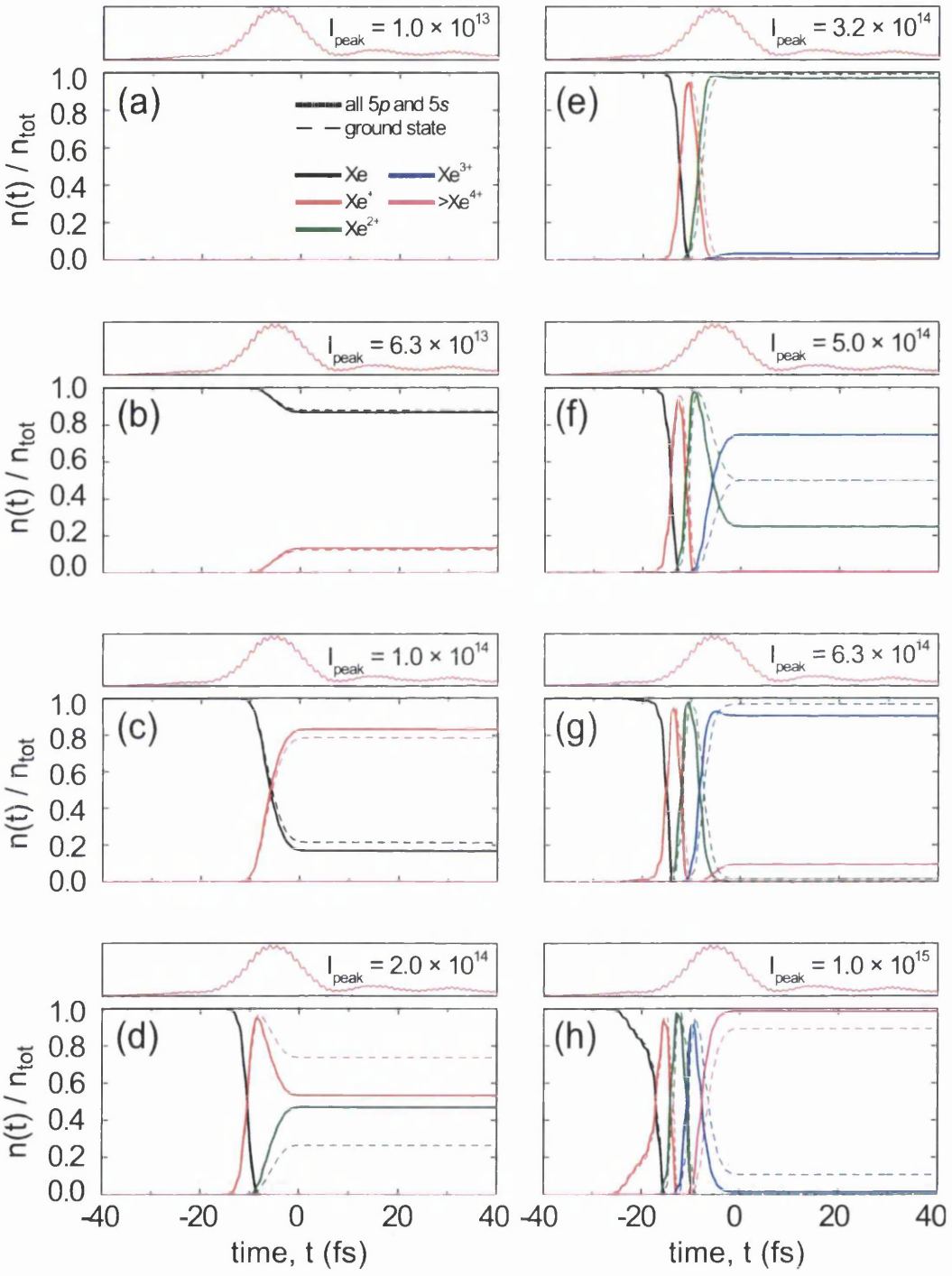

Figure 4.12: Normalized charge state populations, $n(t)/n_{\mathrm{tot}}$, as a function of time for a range of peak intensities, I_{peak}, with no degeneracy considered. The subfigures (a)–(h) are arranged in order of increasing I_{peak}. The temporal intensity profile of the pulse (from Figure 4.7) is also shown above each plot for visual comparison.

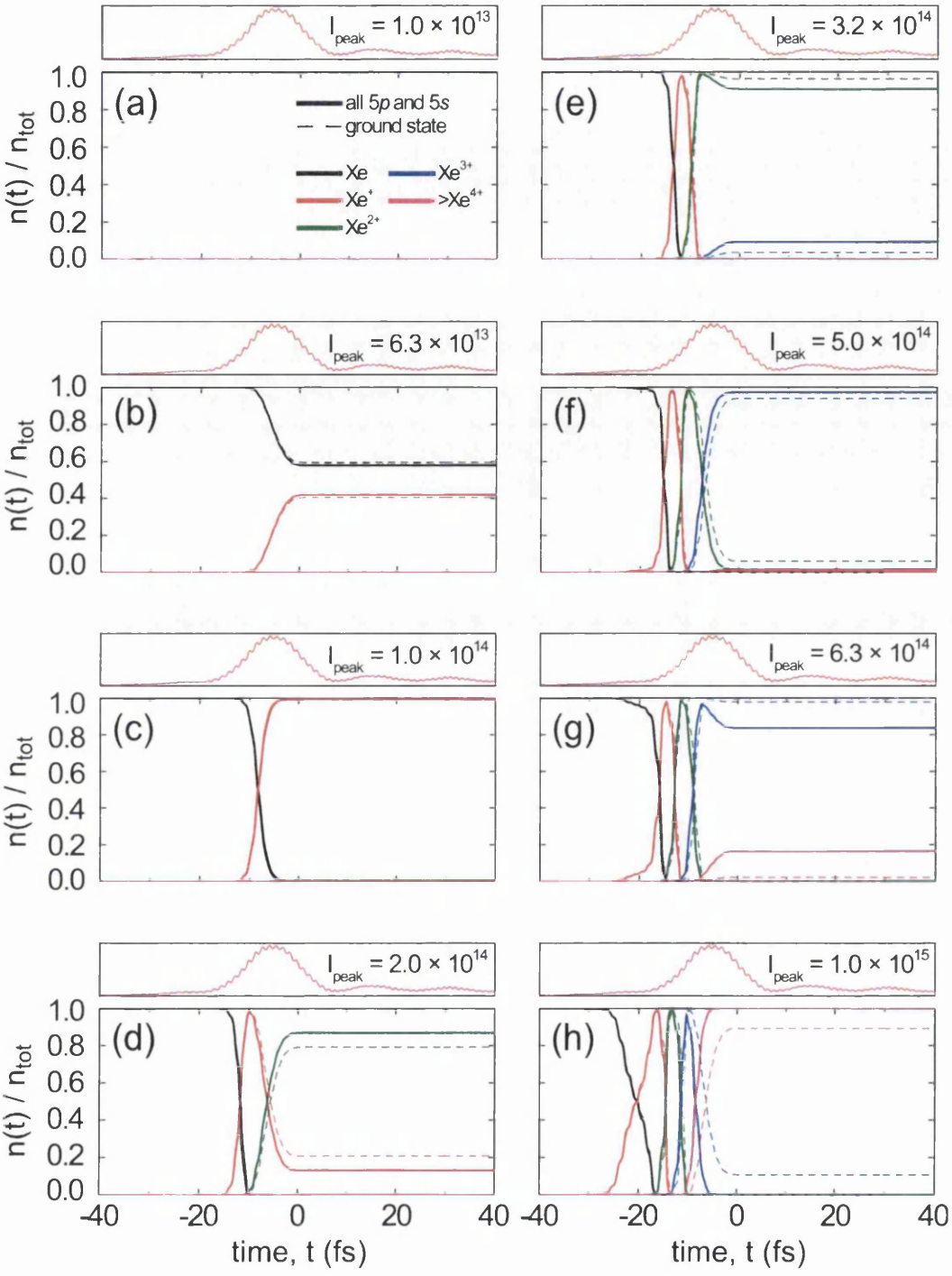

Figure 4.13: Normalized charge state populations including degenerate states, $n(t)/n_{\mathrm{tot}}$, as a function of time for a range of peak intensities, I_{peak}. The subfigures (a) (h) are arranged in order of increasing I_{peak}. The temporal intensity profile of the pulse (from Figure 4.7) is also shown above each plot for visual comparison.

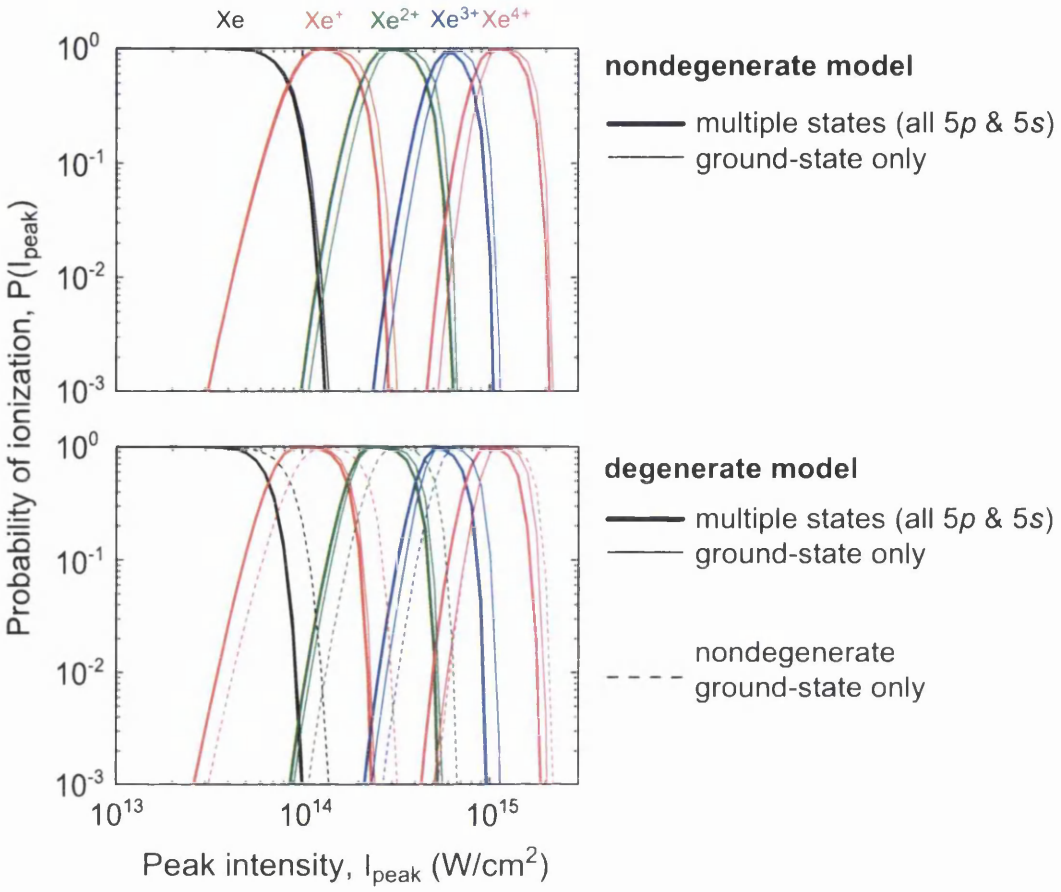

Figure 4.14: Probability of ionization vs. peak intensity for all models: *(top)* nondegenerate ground-state and multiple-state model (all $5p$ and $5s$), *(bottom)* ground-state and multiple-state model including degenerate energy levels.

leading edge of $n(t)/n_{\text{tot}}$ for Xe^+ again has a steeper gradient in the degenerate than the nondegenerate case, and also has a different shape.

The normalized population, $n(\tau)/n_{\text{tot}}$, of each charge state at the end of the pulse (duration τ) is equivalent to the ionization probability, P. In Figure 4.14, $P(I_{\text{peak}})$ for a range of peak intensities I_{peak} are plotted for all models. From Figures 4.10 and 4.11, the predicted Xe^+ yield is expected to be similar in both the ground-state and multiple-state models for the nondegenerate and degenerate cases respectively. This is the case up to $\sim 1.3 \times 10^{14}$ W/cm^2, after which point the differences between all models are clear. The inclusion of additional

ionization pathways as illustrated in Figure 4.9 generally results in the ionization probability curves shifting to lower intensities for charge states above Xe^+, with the magnitude of the shift increasing with increasing charge state. The inclusion of degenerate levels results in a shift to lower intensities for all charge states, with nearly constant magnitude for each charge state except for Xe^{4+} in the ground-state model, where the degeneracy of the ground state is 1, and the probabilities as a function of intensity nearly overlap, being indistinguishable in the figure between $P = 0.1$ to 1.

The magnitude of the differences between the multiple-state and ground-state models also has a distinct behaviour with increasing charge state in the nondegenerate and degenerate models. In the nondegenerate case, there is a large difference between Xe^{2+} in the multiple-state and ground-state models, which increases slightly with increasing charge state, whereas in the degenerate case there is a small difference for Xe^{2+} and Xe^{3+}, followed by a large difference for Xe^{4+} in the multiple-state and ground-state curves.

There is also a shape change due to the inclusion of the degenerate energy levels, with the probability near saturation having a flatter peak, and slightly steeper gradient up to saturation in the degenerate case.

The ionization probabilities in Figure 4.14 can be used in conjunction with the full beamline modelling described in Section 4.1 to generate full three-dimensional predictions of the signal-producing volumes. Figure 4.15 shows radial slices through the full 3D model for the nondegenerate ground-state only predictions, where the probability of ionization at each point in the axisymmetric focal volume shown in Figure 4.3 is calculated and plotted as a function of the radius, r, and axial position, z. The nonlinear dependence of probability picks out the spatial structure of the intensity distribution, with the effects of diffraction causing oscillations in the probability as a function of (r, z). The offset in the peak intensity

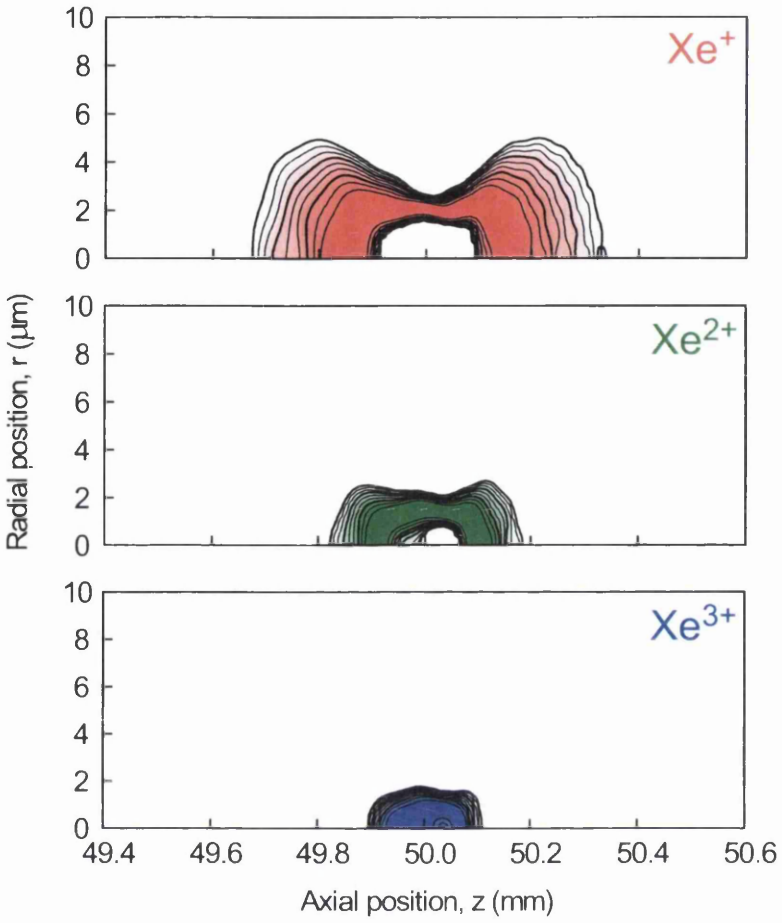

Figure 4.15: Radial slice through the full signal-producing volume modelled using the nondegenerate ground-state only predictions shown in Figure 4.14 for the focal intensity distribution shown in Figure 4.3. The peak intensity is 10^{15} W/cm^2. Thick contours denote an order of magnitude in probability; the thin contours are at every $\frac{1}{3}$-order.

from the geometric focus, as well as the asymmetry of the intensity distribution in z is seen to have an increasing effect with increasing charge state, with the extent of the Xe^{3+} significantly greater upstream of the geometric focus ($z < 50$mm) compared to downstream ($z > 50$mm).

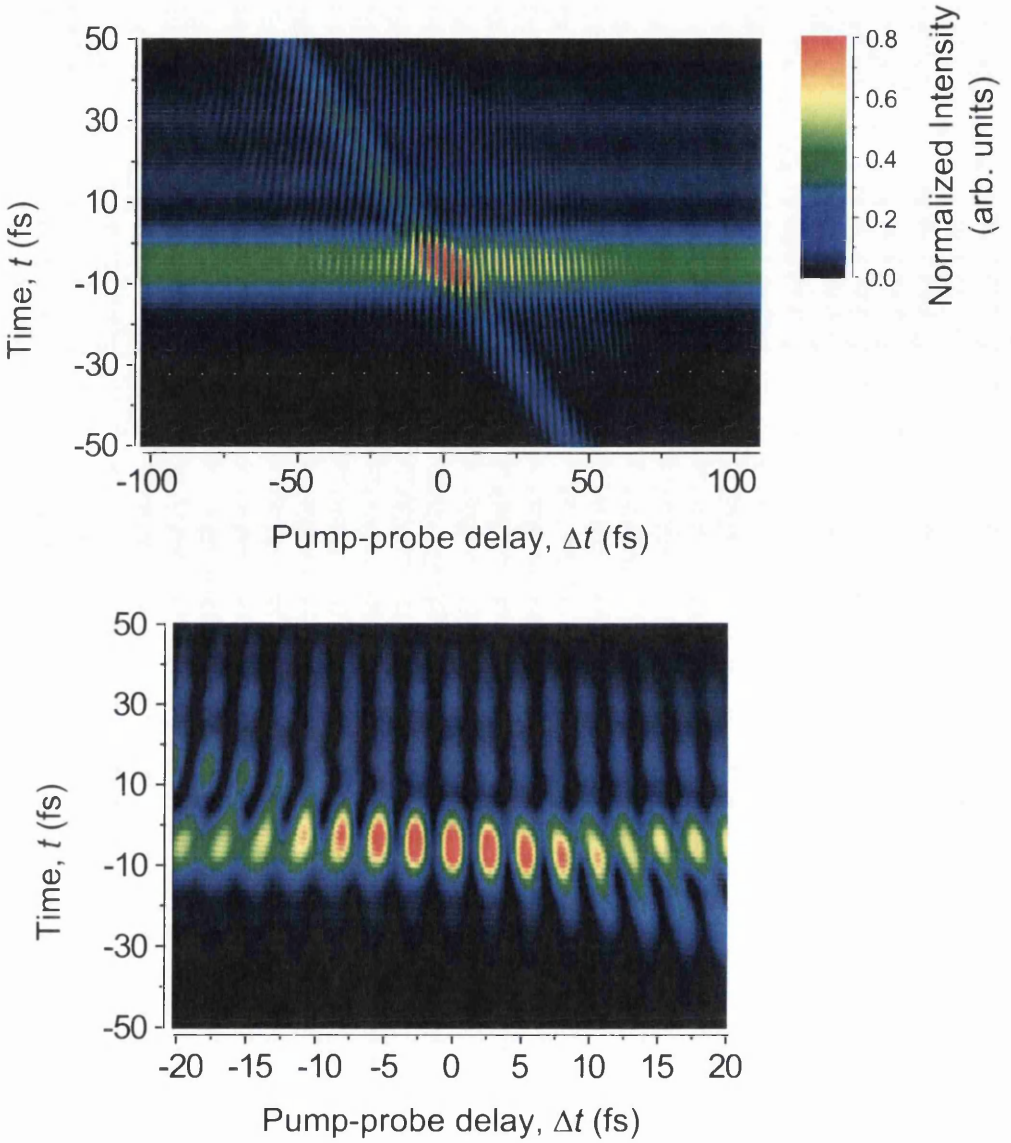

Figure 4.16: Temporal pulse shaping: *(top)* intensity profile after propagation through the interferometer and QWP as described in the text, *(bottom)* enlarged section for $\Delta t = -20$ to $+20$ fs.

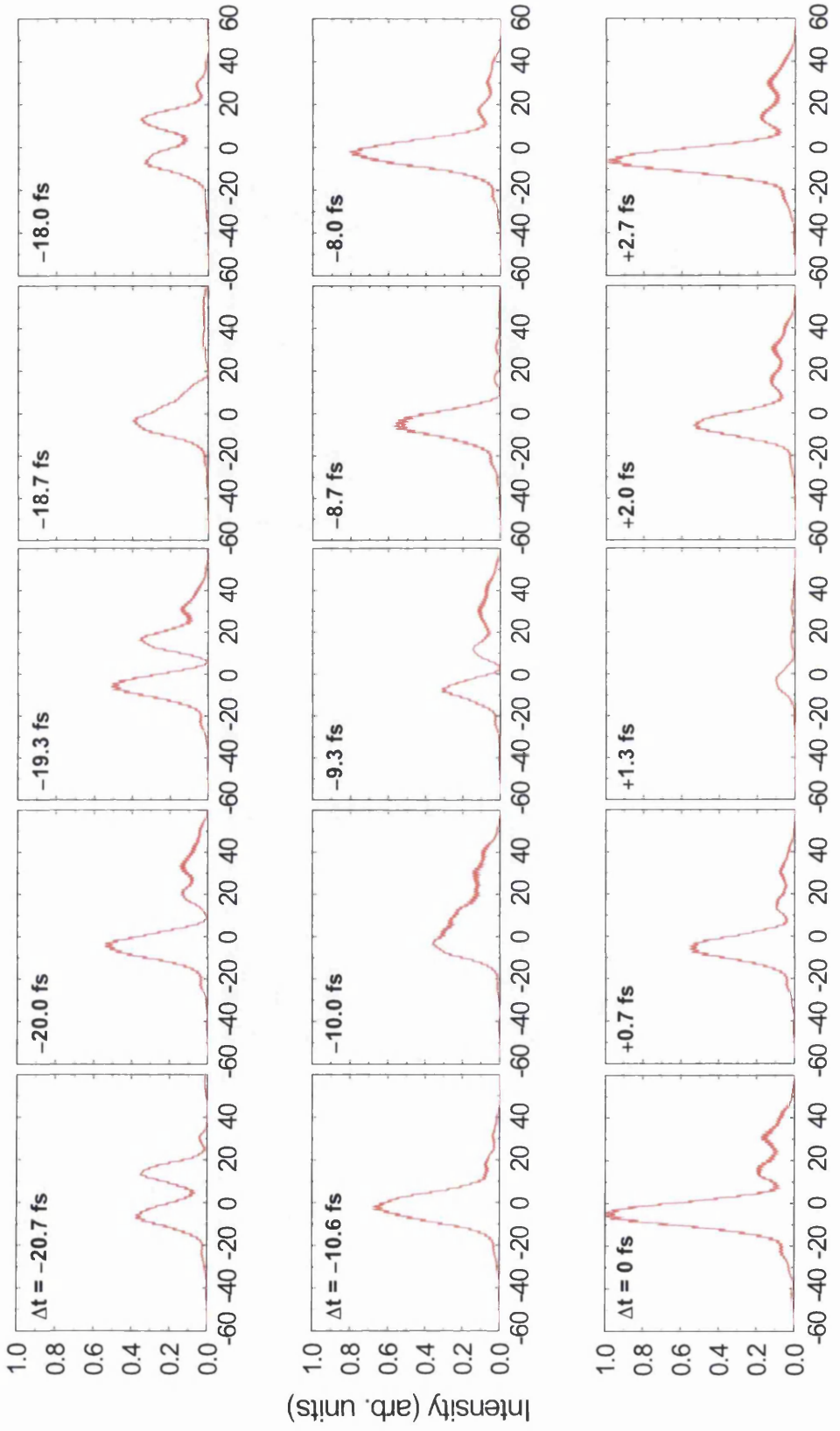
Δt = -20.7 fs
-20.0 fs
-19.3 fs
-18.7 fs
-18.0 fs
Δt = -10.6 fs
-10.0 fs
-9.3 fs
-8.7 fs
-8.0 fs
Δt = 0 fs
+0.7 fs
+1.3 fs
+2.0 fs
+2.7 fs
Intensity (arb. units)
1.0
0.8
0.6
0.4
0.2
0.0
-60 -40 -20 0 20 40 60

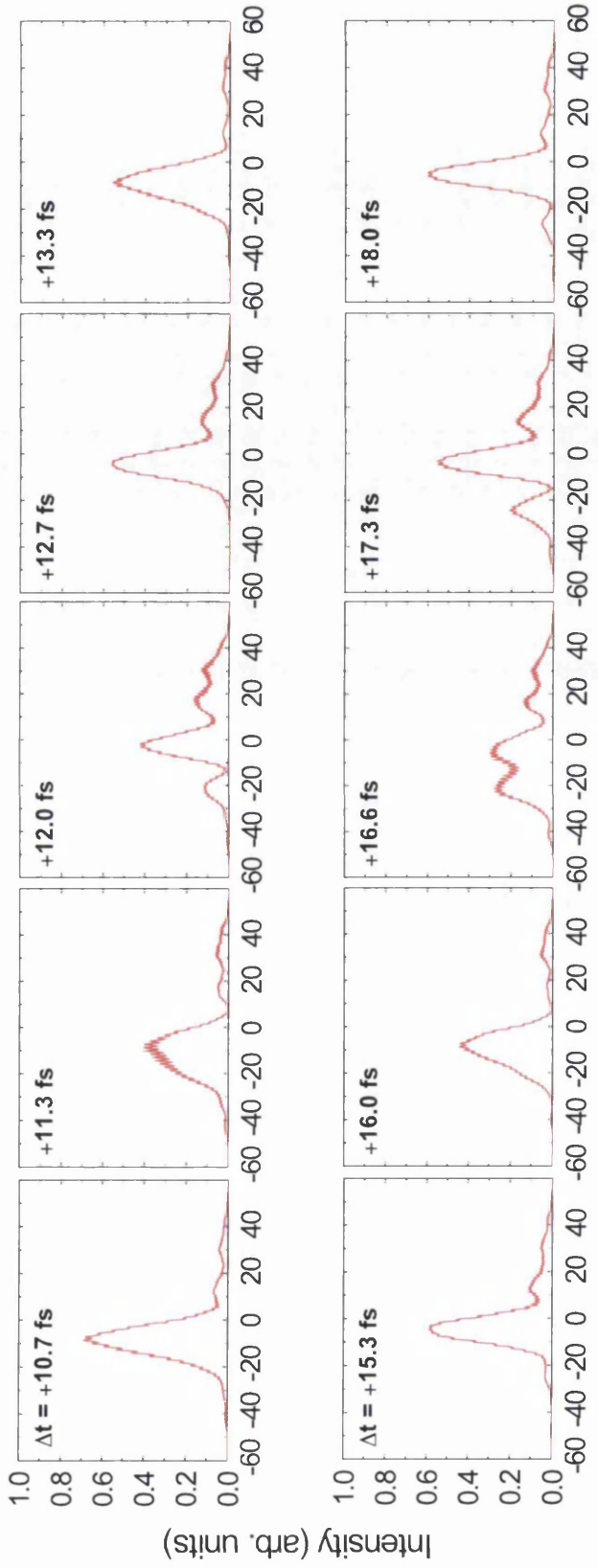

Figure 4.17: Pulse temporal intensity profiles, with QWP GDD included as described in Section 4.1.1, at selected Δt values.

4.3 Temporal pulse shaping

The interferometer described in Section 3.3 is used to temporally shape the linearly-polarized pulse before the QWP. For the work described in Chapter 5, the beamsplitters in the interferometer are chosen to produce two copies of the pulse with an unequal energy splitting (4:1 ratio). As a result, the numerical modelling of the interferometer output pulses begins with two copies of the reconstructed electric field from the FROG measurements (Section 2.2.2) scaled to a corresponding energy ratio of 4:1. The maxima of the pulse envelopes are offset by a variable delay Δt, and the electric fields added. The pulses are then transformed from linear- to circular-polarization using the modelling described in Section 4.1.1, including dispersion due to the QWP GDD.

Figure 4.16 shows the temporal pulse shape following propagation through the interferometer and QWP. Interference is not seen over the whole range of Δt, since there is no data for the electric field for $\Delta t < -60$ fs or $\Delta t > +80$ fs. The maximum intensity occurs at temporal overlap ($\Delta t = 0$). Due to the 4:1 energy splitting, the resulting pulse never undergoes complete destructive interference, but near temporal overlap the difference between maximum and minimum intensity is around an order of magnitude. The asymmetry in the single-pulse electric field also results in an asymmetry in the pulse shapes produced on either side of temporal overlap. At Δt below around -12.5 fs, two distinct peaks are formed, whereas above $+5$ fs the leading edge of the pulse is modified.

Figure 4.17 shows the temporal pulse profiles from Figure 4.16 at selected Δt. Each row in the figure samples a different Δt region, and the slices in each row demonstrate the variation of the pulse profile in this region, over a Δt range corresponding to a single cycle of the laser period. For $\Delta t = 0$ to $+2.7$ fs, the peak intensity variation is at its largest, but the temporal profile changes very

little. This is in stark contrast to the other cycles selected. $\Delta t = +13.3, +16.0$ and $+11.3$ fs are examples of modification of the leading edge of the pulse with increasing magnitude. At $\Delta t = -18.7$ and -10.0 fs, the trailing edge is modified, substantially in the latter case. At $\Delta t = -20.7$ and -18.0 fs, two strong peaks of almost equal intensity, but differing duration are created. In other cases, e.g. $\Delta t = -19.3, +12.0, +16.6$ and $+17.3$ fs, the pulse shape becomes quite complex, with a variety of peak shapes. The nature of the temporal variation of the pulses is expected to have implications for tunnel ionization, which will be discussed further in Chapter 5.

4.4 Conclusion

Modern tunnel theory has been modified to consider the possibility of additional ionization pathways, by allowing direct tunnelling of electrons from energy levels higher than the ground state. The differences between the models are highlighted as a function of time and intensity. The realistic modelling of the spatial propagation of the pulse through the beamline has produced a structured, asymmetric focus. The temporal effects of the polarization control and pulse shaping are also considered, with a diversity of pulse shapes generated as the overlap between the pulses in each interferometer arm changes as a function of the delay, Δt. The pulse shape has important implications for the time-dependent populations of multiple electronic energy levels, as discussed in Chapter 5.

charge state			$2J+1$	energy (eV)
Xe	$5p^6$	$(^1S_0)$	1	0.000000
Xe^+	$5p^5$	$(^2P_{3/2})$	4	12.129843
		$(^2P_{1/2})$	2	13.436266
	$5s5p^6$	$(^2S_{1/2})$	2	23.396763
Xe^{2+}	$5s^25p^4$	$(^3P_2)$	5	33.104843
		$(^3P_0)$	1	34.112843
		$(^3P_1)$	3	34.319143
		$(^1D_2)$	5	35.224815
		$(^1S_0)$	1	37.581037
	$5s5p^5$	$(^3P^\circ_2)$	5	45.287833
		$(^3P^\circ_1)$	3	45.945662
		$(^3P^\circ_0)$	1	46.536517
		$(^1P^\circ_1)$	3	53.379665
	$5p^6$	$(^1S_0)$	1	59.247838
Xe^{3+}	$5s^25p^3$	$(^4S^\circ_{3/2})$	4	64.150443
		$(^2D^\circ_{3/2})$	4	65.795343
		$(^2D^\circ_{5/2})$	6	66.321493
		$(^2P^\circ_{1/2})$	2	67.626513
		$(^2P^\circ_{3/2})$	4	68.570433
	$5s5p^4$	$(^4P_{5/2})$	6	76.507143
		$(^4P_{3/2})$	4	77.407233
		$(^4P_{1/2})$	2	77.696263
		$(^2D_{3/2})$	4	79.267703
		$(^2D_{5/2})$	6	79.707323
		$(^2S_{1/2})$	2	82.839483
		$(^2P_{3/2})$	4	84.731233
		$(^2P_{1/2})$	2	86.213563
Xe^{4+}	$5s^25p^2$	$(^3P_0)$	1	105.065243
		$(^3P_1)$	3	106.217243
		$(^3P_2)$	5	106.816733
		$(^1D_2)$	5	108.587783
		$(^1S_0)$	1	110.578873
	$5s5p^3$	$(^5S^\circ_2)$	5	116.494443
		$(^3D^\circ_1)$	1	119.358923
		$(^3D^\circ_2)$	5	119.459433
		$(^3D^\circ_3)$	7	119.933303
		$(^3P^\circ_0)$	1	121.610293
		$(^3P^\circ_1)$	3	121.750443
		$(^3P^\circ_2)$	5	121.766253
		$(^1D^\circ_2)$	5	123.143003
		$(^3S^\circ_1)$	3	124.347033
		$(^1P^\circ_1)$	3	126.101963

Table 4.1: Energy level data from NIST [92]. Electronic configurations are given in the form nl^N, where n is the principal quantum number, l is the angular momentum quantum number, and N the number of electrons in the subshell l. The term symbols (given in brackets) are in the form $^{2S+1}L_J$, where S is the total spin quantum number, L is the total orbital quantum number, and J is the total angular momentum quantum number. $^\circ$ denotes an odd-parity term. The degeneracy of each state is $2J + 1$.

charge state	$5p^{-n}$	$5s^{-1}5p^{1-n}$	$5s^{-2}5p^{2-n}$
Xe^{+}	2	1	0
Xe^{2+}	5	4	1
Xe^{3+}	5	8	0
Xe^{4+}	5	10	0

charge state	$5p^{-n}$	$5s^{-1}5p^{1-n}$	$5s^{-2}5p^{2-n}$
Xe^{+}	6	2	0
Xe^{2+}	15	13	1
Xe^{3+}	20	30	0
Xe^{4+}	15	38	0

Table 4.2: Summary of energy levels per charge state for the *(top)* nondegenerate and *(bottom)* including degenerate levels.

Chapter 5

Recollision-free multiple tunnel ionization of xenon

This chapter discusses the results obtained from the NIR-pump NIR-probe measurement of tunnel ionization of xenon. The beamline modelling described in Chapter 4 and the nonadiabatic tunnel theory described in Chapter 1 are applied in order to draw comparisons between the measured spatially- and temporally-resolved data.

5.1 NIR beamline overview

Figure 5.1 shows the experimental setup used to study xenon ionization with ultrashort, temporally-shaped pulses. The FemtoLasers CompactPro Ti:S laser system described in Section 2.1.6 produces ~1 mJ, 30 fs NIR pulses, which are spectrally broadened by self-phase modulation in an argon-filled hollow fibre, and recompressed to ~10 fs by a series of chirped mirrors which compensate for the group-delay dispersion (GDD) acquired after propagation through the fibre, as described in Chapter 2. A Mach-Zehnder interferometer then splits the pulse, introducing a variable delay Δt when the two parts are recombined

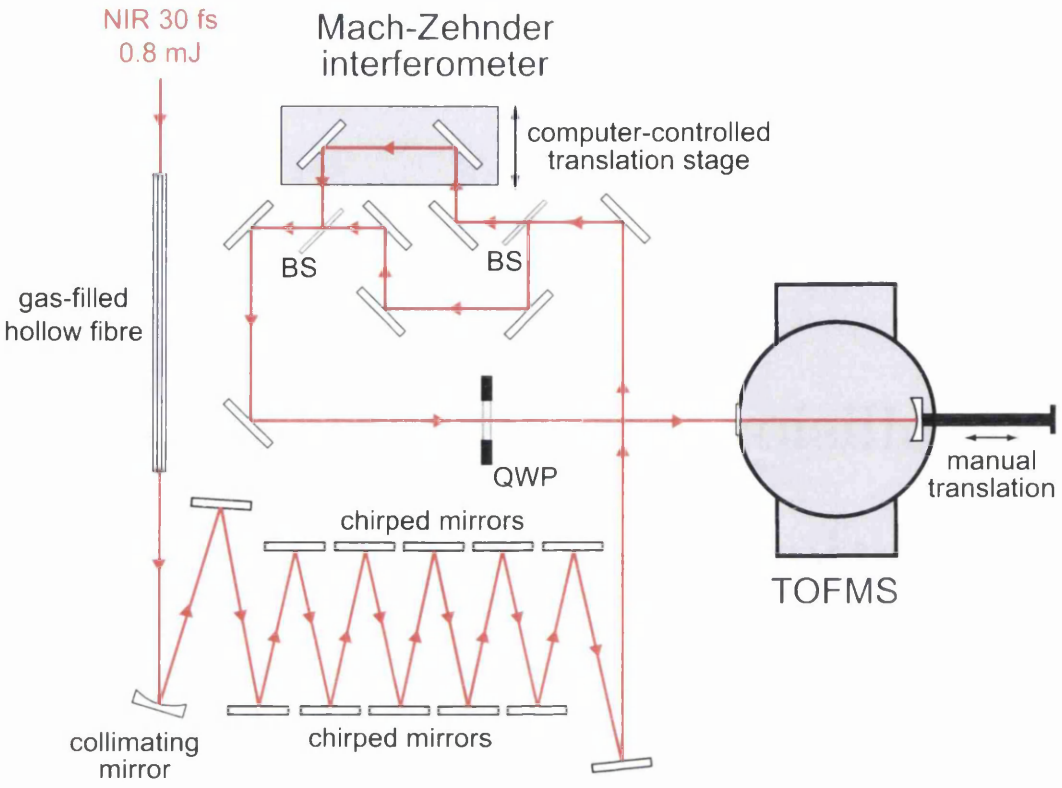

Figure 5.1: Illustration of the NIR beamline. BS = beamsplitter, QWP = quarter-wave plate, TOFMS = ion time-of-flight mass spectrometer.

with an energy ratio of 4:1. $\Delta t = 0$ is defined to be the point at which the pulses are temporally overlapped. A quarter-wave plate converts the pulse from linear to circular polarization. The pulse incurs additional GDD due to the waveplate, as discussed and modelled in Chapter 4. The pulse is reflectively focused ($f = 50$ mm) into an effusive xenon gas jet, generating intensities of 10^{13} – mid-10^{16} W/cm^2 over the focal region. The ions produced are detected using the ion time-of-flight mass spectrometer (TOFMS) described in Section 3.1, with a 250 μm aperture to limit the z-range and therefore the range of intensities over which the ions are detected. The focusing mirror position is varied with 100 μm resolution, translating the laser focus with respect to the aperture in the TOFMS. As a result, ion yield as a function of z and Δt is recorded.

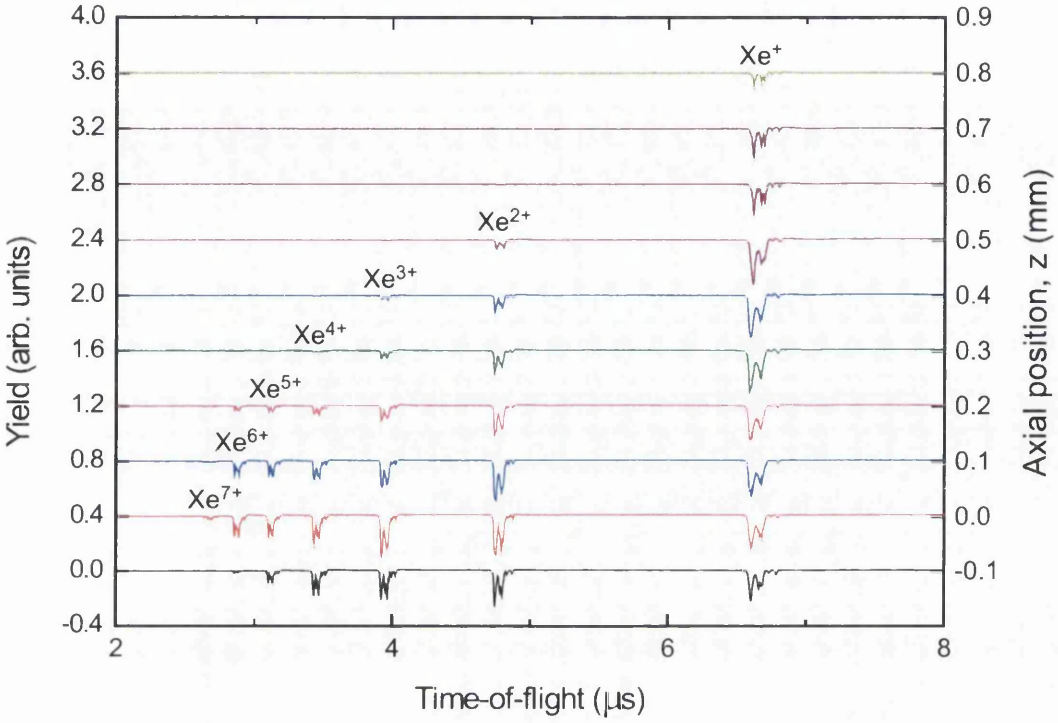

Figure 5.2: Time-of-flight spectra recorded at 100 μm intervals in axial position, z, from the geometric focus. Each spectrum is offset by 0.4 units on the yield axis for clarity.

5.2 Results

A typical time-of-flight spectrum is shown in Figure 3.5 and explained in Chapter 3. The TOFMS is operated in the spatial mode as described in Section 3.1, such that the ions created in the focal region are presumed to travel along straight trajectories to the detector. The TOFMS layout is illustrated, and the applied voltages given in Figure 3.3. Figure 5.2 shows the variation of the xenon time-of-flight spectrum (at $\Delta t = 0$) as a function of z. The highest number of charge states are expected to be detected at the geometric focus where the intensity is highest. This point has been defined as $z = 0$ in the figure, where peaks up to Xe^{6+} are resolved, and Xe^{7+} just detected. As z increases, the number of

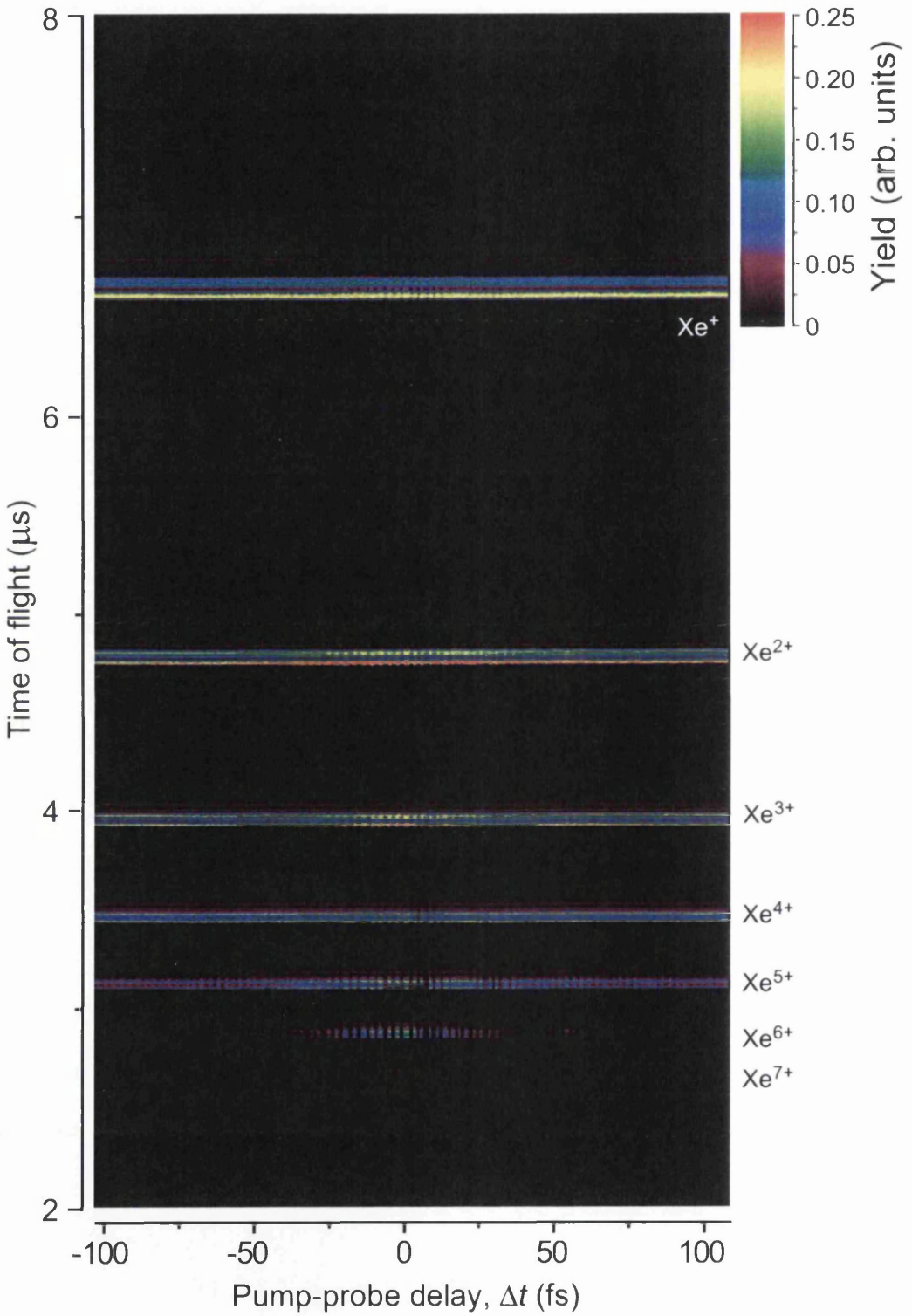

Figure 5.3: Xenon time-of-flight spectra as a function of NIR pump-probe delay, Δt. The structured bands correspond to the structured peaks seen in Figure 5.2. Xe^{7+} is just detected at temporal overlap ($\Delta t = 0$).

charge states detected decreases, with only Xe^+ resolvable at 800 μm. Figure 5.3 shows the variation of the spectrum as a function of Δt, varied in $\frac{2}{3}$fs steps (at $z = 0$ mm), as a colour plot. Each charge state is seen as a distinct band: the structure along the time-of-flight axis within each band corresponds to the different isotopes of each ion (see Figure 3.5 and accompanying text), and the structure in Δt arises from the temporal pulse shaping described in Section 4.3. Since the generation of more highly-charged ions requires higher intensities, the Δt-range over which signal is produced decreases with increasing charge state, peaking at $\Delta t = 0$. The oscillations in the signal are strongest at small Δt and decrease in amplitude away from the temporal overlap, corresponding to the peak intensity variation expected from Figure 4.16. The period of the oscillations is $\sim$8/3 fs over the Δt-range recorded, as expected for a pulse with centre wavelength $\sim$800 nm.

At each Δt and z, a 1000-shot average spectrum is recorded as described in Section 3.2. The background in the immediate vicinity of the signal peaks for each charge state is subtracted, and the signal integrated as a function of time for each charge state. The resulting integrated ion yield, $S_{\text{expt.}}(z, \Delta t)$, is plotted in Figure 5.4. The signal volume decreases in size for increasing charge state, which is seen in the figure as a decrease in the axial extent of the detected signal. The oscillations (period $\sim$8/3 fs) are observed as in Figure 5.3. Additionally, the influence of the temporal pulse shaping (described in Section 4.3) is seen more clearly in the two-dimensional plot, since different intensities are sampled by the detector at each z-position.

5.3 Deconvolution of ionization probabilities

As discussed in Chapter 1, the ability to extract ionization probabilities directly from experimental z-scan measurements greatly enhances the clarity of comparison to theory, particularly when elucidating multielectron behaviour. The orig-

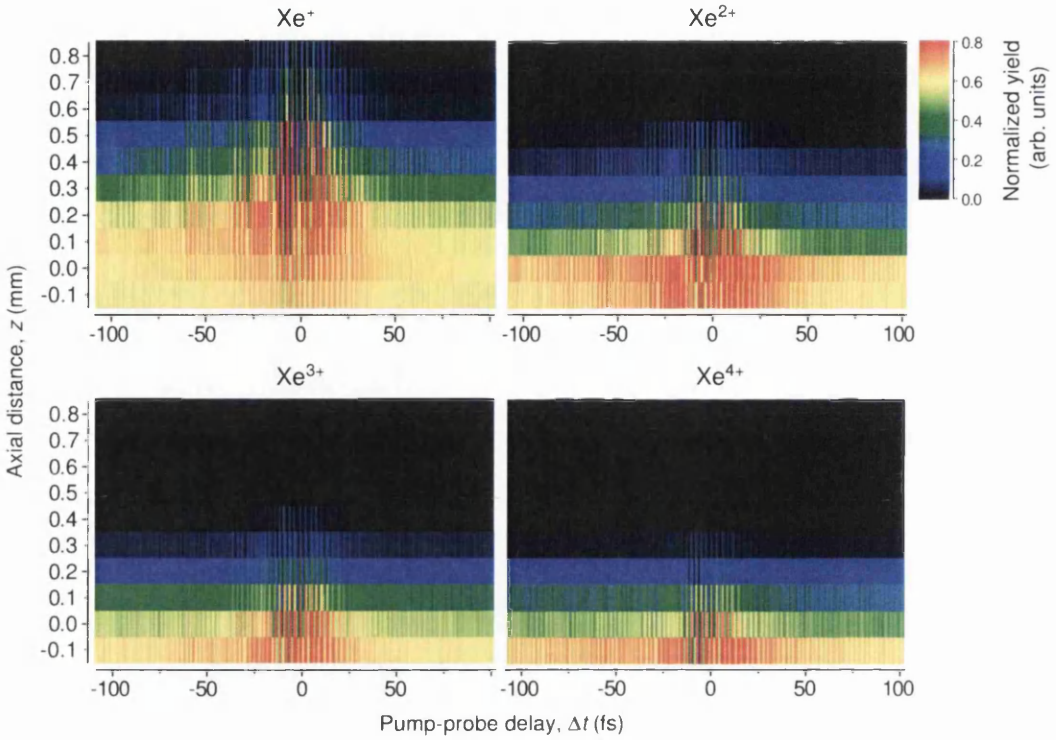

Figure 5.4: Xenon integrated ion yield as a function of delay, Δt, and axial position, z. The yield for each charge state is normalized to the global maximum yield of the dataset. An absolute yield measurement is not possible due to the unknown quantum efficiency of the detector.

inal deconvolution procedure described in Section 1.3 is intended for a slit- or aperture-diameter which is smaller than the Rayleigh range, z_R, of a Gaussian focus. z_R cannot be defined for the focus in the current work, which originates from a propagated diffracted Bessel profile. However, a nondiffracted Gaussian of equivalent diameter before focusing would have $z_R \sim 50$ μm. Comparing to the 250 μm aperture in the TOFMS, this is one-fifth the diameter.

Figure 5.5 shows the recovered ionization probabilities obtained by deconvoluting the z-scans at $\Delta t = -20.7, 0$ and $+18$ fs, where the z-scans refer to the vertical slices extracted from the full dataset shown in Figure 5.4. The data are smoothed using a Savitzky-Golay filter [93,94], then interpolated using the cubic spline method, giving $S(z)$ for the deconvolution routine described in Section 1.3.

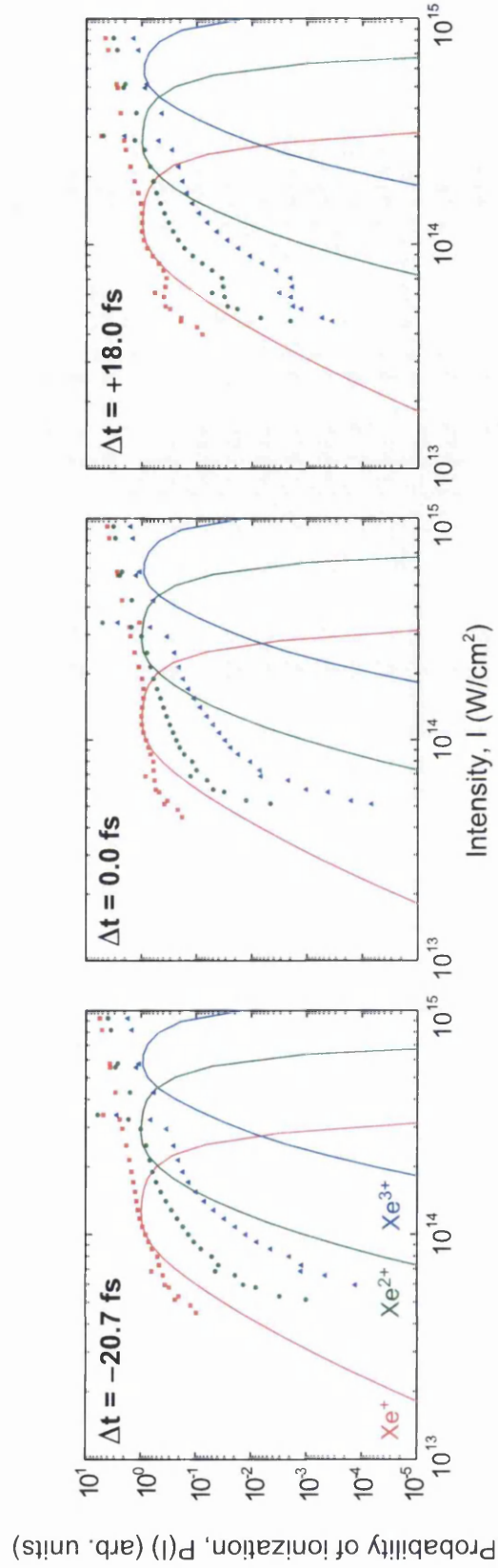

Figure 5.5: Experimentally-recovered ionization probabilities (points) for a peak intensity of 10^{16} W/cm^2, for the z-scans extracted from Figure 5.4 at three selected Δt values, compared to tunnel theory predictions (solid lines) from the modelling described in Section 1.3. Peak intensity refers to the global maximum in the spatial intensity distribution, whereas the intensity axis corresponds to the local on-axis intensity.

The on-axis intensity, $I_{ax}(z)$ is calculated from the beamline model described in Chapter 4. The peak intensity, I_{peak}, is then scaled until a best fit is found between the experimentally-recovered Xe^+ probabilities and the theory. This is because Xe^+ is least-affected by multielectron effects, as only one electron is removed, therefore it is expected to be well-described by the theory. The process by which the theory curves are obtained is described in Chapter 4.

As can be seen from the figure, the Xe^+ data follows the theory curves only over a limited range of intensities near 10^{14} W/cm^2. Below $I_{peak} = 8 \times 10^{14}$ W/cm^2 for each of the Δt values sampled, the Xe^+ data breaks away from the theory. The sudden change in gradient is unexpected, and the fact that it is accompanied by a similar change in gradient in the Xe^{2+} and Xe^{3+} data indicates this is not the result of an atomic process, but a spatial effect.

Since the measured yields are not absolute, due to the unknown quantum efficiency of the detector, a certain amount of arbitrary probability scaling is expected to be required for the remaining charge states. However, this is expected to be no more than a few orders for the highest charge states [67]. In the figure, the Xe^{2+} and Xe^{3+} data are scaled so that they match the theory at saturation. However, this results in a significant recovered probability of ionization below saturation in Xe^{2+} when saturation has not yet been reached in Xe^+, and similarly in Xe^{3+}. This is not self-consistent, since such a large deviation in the Xe^{2+} probability, without an accompanying drop in the Xe^+ probability results in a total probability of ionization greater than unity. Alternatively, a best fit of the data between $I_{peak} = 7 \times 10^{13}$ and 1.3×10^{14} W/cm^2 may be obtained, but this would require a shift in probability of several orders, far more than anticipated due to the compensation for the quantum efficiency [67].

In order to test whether modifications to the deconvolution routine are able to overcome the limit $z_R < \alpha$, where α is the diameter of the aperture in the TOFMS,

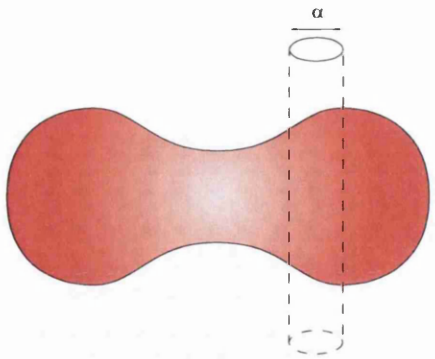

Figure 5.6: The 250 μm diameter aperture in the TOFMS images a cylinder of the signal producing volume with diameter α.

the full three-dimensional focal volume as seen by the detector is modelled using the techniques described in Chapter 4. A significant advantage of the model is that the z-scans can be produced at a much higher resolution than those in the experiment, enabling the deconvolution and any modifications to be tested rigorously.

The modelled z-scans are produced by integrating the signal-producing volume over an α-diameter cylinder at each z position for a range of peak intensities, as illustrated in Figure 5.6.

Figure 5.7 demonstrates the distortion of the z-scan as a function of peak intensity. The effect of the aperture can clearly be seen to dominate the signal at lower peak intensities. However, as the intensity and therefore the extent of the signal in z increases, a large proportion of the signal behaviour is common to both the 10 μm and 250 μm aperture cases. This indicates that at least some of the ionization proabilities may still be recoverable from the aperture-convoluted signal.

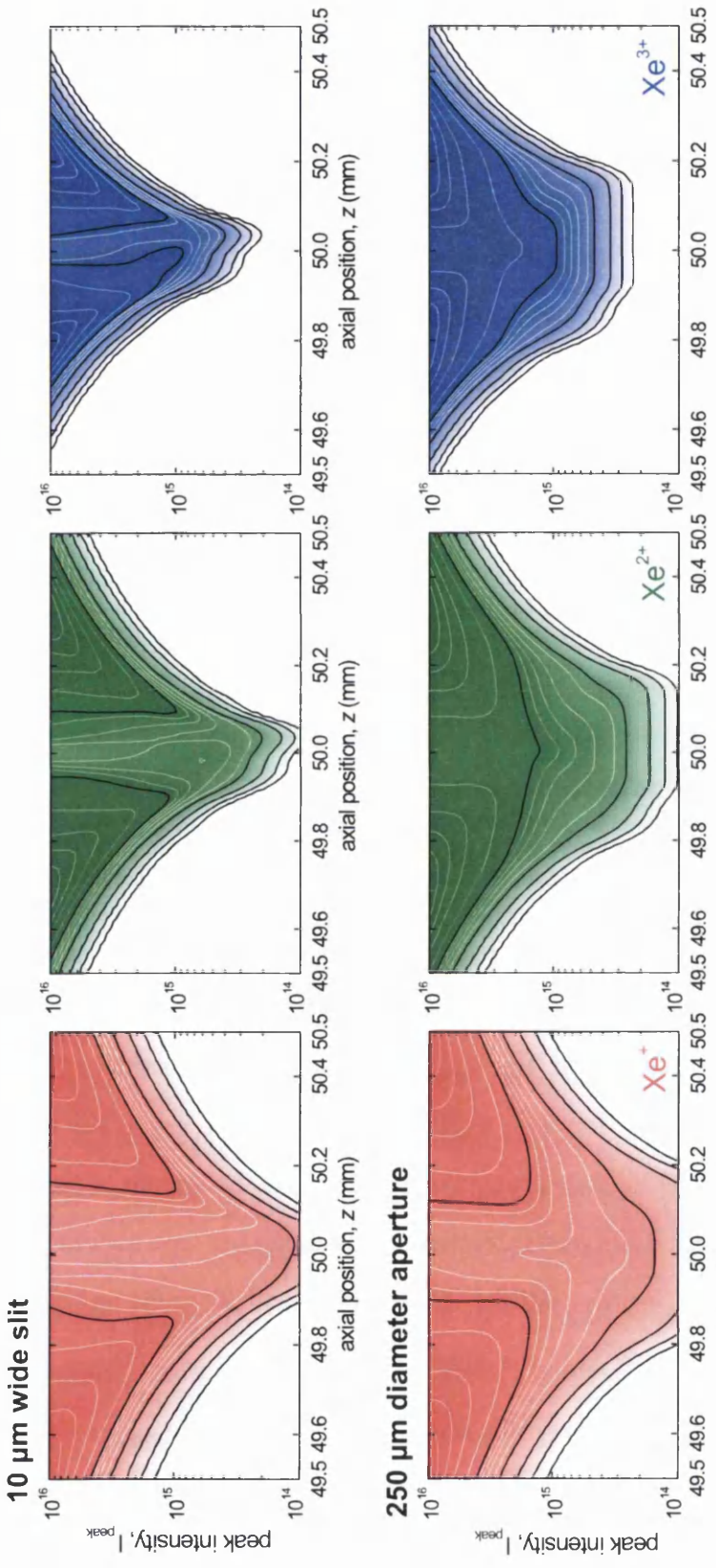

Figure 5.7: Modelled xenon z-scans, $S(z)$, as a function of on-axis peak intensity. $S(z)$ is normalised to 1 for each charge state; each thick contour represents an order of magnitude change, and each thin contour is $\frac{1}{4}$-order. The contour colour change is for clarity only.

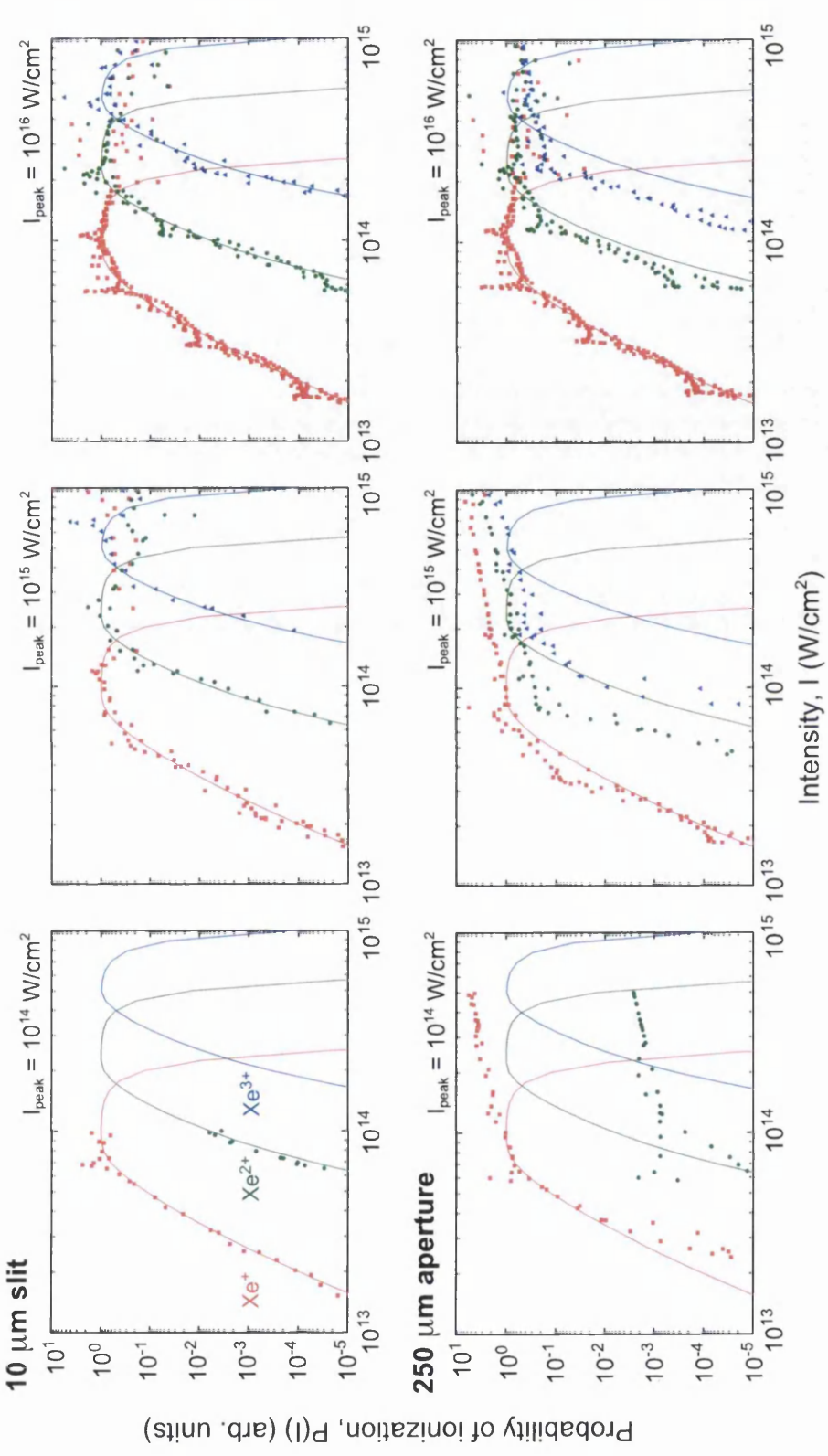

Figure 5.8: Deconvolution testing for *(top)* a 10 μm slit and *(bottom)* a 250 μm aperture. The recovered probabilities from the deconvolution routine (points) should match the input probabilities (solid lines) from the tunnel theory predictions (Section 1.3), but intensity-dependent shifts and changes in shape are observed in the 250 μm case. Peak intensity (I_{peak}) refers to the global maximum in the spatial intensity distribution, whereas the intensity axis corresponds to the local on-axis intensity.

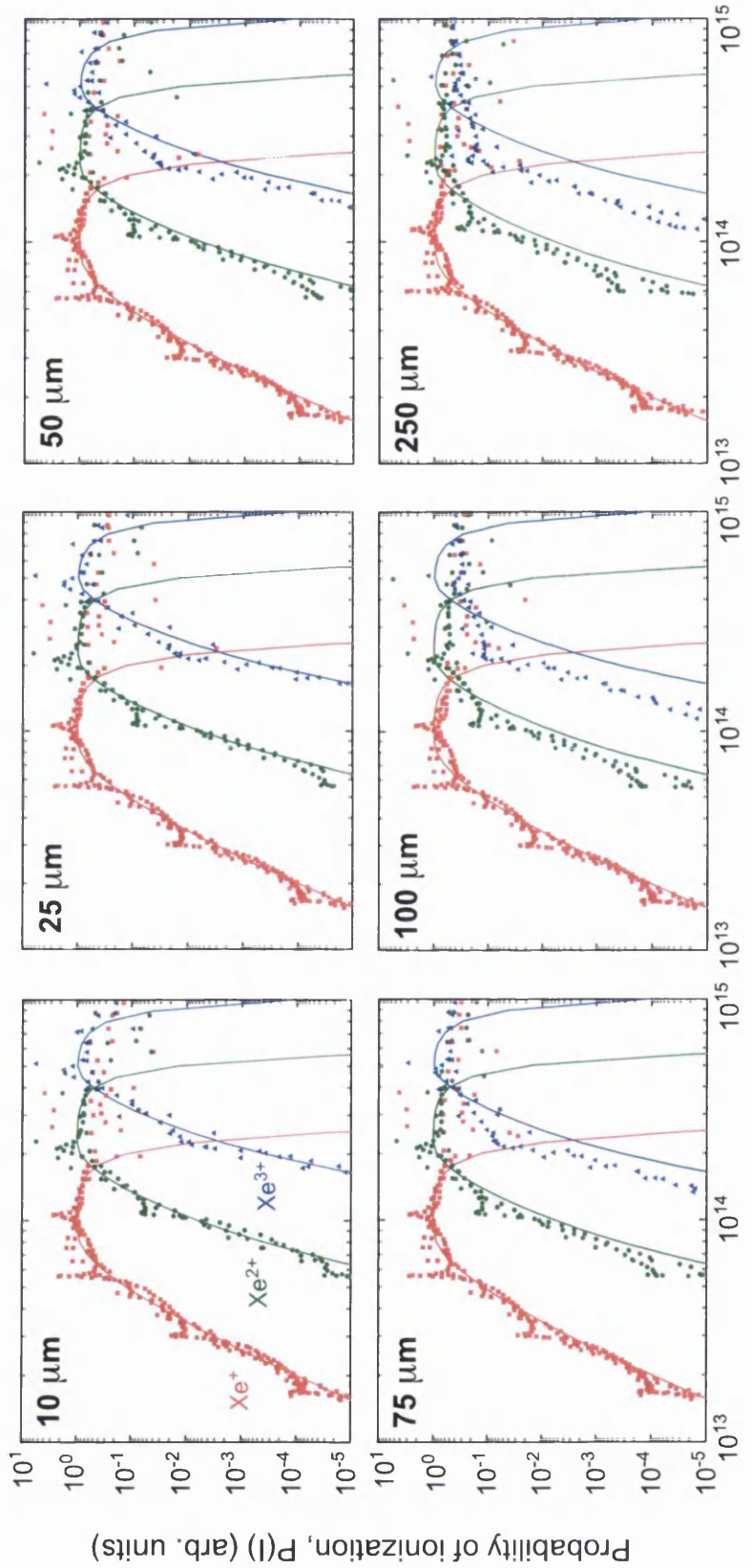

Figure 5.9: Deconvolution testing for $I_{\mathrm{peak}} = 10^{16}$ W/cm^2 and aperture sizes $\alpha = 10, 25, 50, 75, 100$ and 250 μm, as labelled. Recovered ionization probabilities (points) are compared to the input probabilities (solid lines) from the tunnel theory predictions (Section 1.3). Peak intensity (I_{peak}) refers to the global maximum in the spatial intensity distribution, whereas the intensity axis corresponds to the local on-axis intensity.

5.3.1 On-axis deconvolution

The deconvolution in its original form is applied to the modelled z-scans and compared to the inputted theory; the results are shown in Figure 5.8 for three different values of I_{peak}. The recovered probabilities from the deconvolution procedure depend on the gradients of $I_{\text{ax}}(z)$ and $S(z)$ (see Equation (1.8), Section 1.3), and are therefore sensitive to subtle changes in $I_{\text{ax}}(z)$. Diffraction of the propagating beam can result in a beam profile with several points of inflection or local minima, each of which will result in a 'spike' in the deconvoluted probabilities. This is the cause of the significant scatter in Figures 5.8 and 5.9. Despite this, it is expected that the overall shape of the recovered ionization probabilities should match the inputted probabilities very well, since they should be nearly identical to those used to generate the signal-producing volume.

Figure 5.9 shows the results of the deconvolution procedure compared against the probabilities from which they were generated, at $I_{\text{peak}} = 10^{16}$ W/cm^2 for several TOFMS aperture sizes, α. For $\alpha = 10$ μm and 25 μm, the recovered probabilities reproduce the overall behaviour of the input probability curves very well, up to just above saturation. For $\alpha = 50$ μm, however, the Xe^{3+} probabilities begin to depart from the input curves. For $\alpha = 75$ μm, this occurs for Xe^{2+} also. For larger apertures up to 250 μm, there is a significant difference between the recovered and input probabilities for Xe^{2+} and Xe^{3+}, accompanied by a change in shape which makes the saturation point unclear, particularly in the Xe^{3+}.

Figure 5.8 shows the same deconvolution method for a 10 μm slit and a 250 μm aperture, for $I_{\text{peak}} = 10^{14}, 10^{15}$ and 10^{16} W/cm^2. For the 10 μm slit, the input probabilities are well-recovered at each of the intensities. However, as can be seen in the 250 μm case, the shifts and changes in shape apparent in Figure 5.9 become worse at lower intensities.

At $I_{\text{peak}} = 10^{15}$ W/cm^2, the gradient of the recovered Xe^{2+} probabilities up to an intensity of 7×10^{13} W/cm^2 are much steeper than the input probability. For Xe^{3+}, the shift brings the recovered probabilities closer to those expected from Xe^{2+}.

At $I_{\text{peak}} = 10^{14}$ W/cm^2, it becomes difficult to fit even the Xe^{+} to the input probabilities, except for a small range of intensities between 5×10^{13} and 10^{14} W/cm^2. Below this, the recovered probabilities are significantly lower than the inputted probabilities. For Xe^{2+}, the recovered probabilities no longer fit near saturation.

None of the recovered probabilities have been shifted vertically in the figure, nor does the model compensate for any differences in absolute probability for each charge state due to the quantum efficiency of the detector. It is therefore clear that these effects are due to the z-scan not only being a convolution of the ionization probability and the intensity distribution, but also the aperture itself.

Whilst these results indicate that using a smaller aperture improves the success of the deconvolution routine for the model, there is a practical limitation for the experimental case. If a 25 μm aperture had been used for data collection, the reduction in the area would mean that 100 times more laser shots would be required to build up the same TOF spectra at each z and/or Δt, and 625 times more shots would be needed for a 10 μm aperture.

5.3.2 Slit-convolution and volume-averaging

In order to modify the deconvolution, and compensate for the effect of the aperture, two methods have been tested. Assuming $S(z)$ is still dominated by the rapid variation of intensity along the z-axis, the aperture can be considered as a larger-width 250 μm slit. The on-axis intensity distribution in Equation (1.8),

$I_{\text{ax}}(z)$, is then replaced by

$$I_{\text{slit-conv}}(z) = I_{\text{ax}}(z) \otimes T_{\text{ax}}(z) \tag{5.1}$$

i.e. a convolution of the original on-axis intensity distribution with the slit, where

$$T_{\text{ax}}(z) = \begin{cases} 1 & 0 \leq z < \text{slit-width} \\ 0 & z > \text{slit-width} \end{cases} \tag{5.2}$$

is the function describing the extent of the slit in the z-direction.

If the radial variation becomes significant, then the intensity distribution used for deconvolution needs to consist of the most representative intensity for the whole aperture at each z-position. The average intensity over the three-dimensional cylinder (Figure 5.6) imaged by the aperture is not a representative measure, since it takes no account of the significance of each point in the volume. The ionization probability as a function of intensity is highly nonlinear, therefore higher intensity points within the volume are more significant than lower intensities, and therefore should receive a higher weighting in the representative probability for the cylinder. A weighted average is given by the formula $\sum_{i=1}^{n} w_i x_i / \sum_{i=1}^{n} w_i$, where w_i are the weighting factors and x_i the data. The intensities themselves are used as the weighting factors in this case, hence referred to as the intensity-weighted volume average (IWVA).

The validity of using the IWVA is tested with the 10 μm slit, and compared to the non-averaged case in Figure 5.10. For $I_{\text{peak}} = 10^{14}$ W/cm^2, the fit is slightly worse, indicating that the signal at low peak intensity is being generated very near to the axis and would be better represented by the on-axis intensity distribution. However, for $I_{\text{peak}} = 10^{15}$ and 10^{16} W/cm^2, the general behaviour of the recovered probabilities is comparable. The fit is also improved, since the

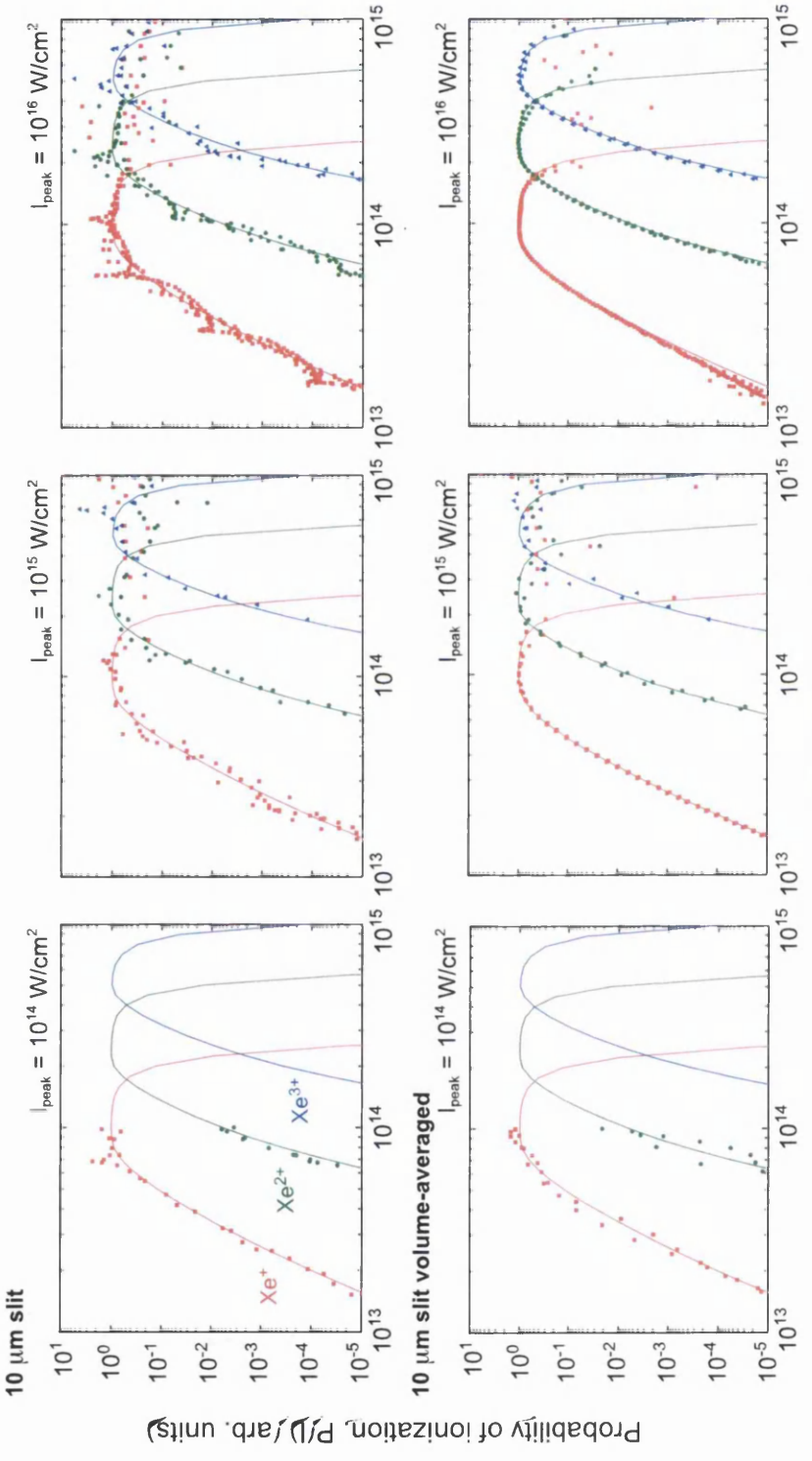

Figure 5.10: Ionization probabilities recovered from the model (points) for a 10 μm slit using *(top)* the on-axis intensity and *(bottom)* the intensity-weighted volume-averaged intensity over the slit at each z, compared with the input probabilities (solid lines) from the tunnel theory predictions (Section 1.3). Peak intensity (I_{peak}) refers to the global maximum in the spatial intensity distribution, whereas the intensity axis corresponds to the local on-axis or intensity-weighted volume-averaged intensity respectively.

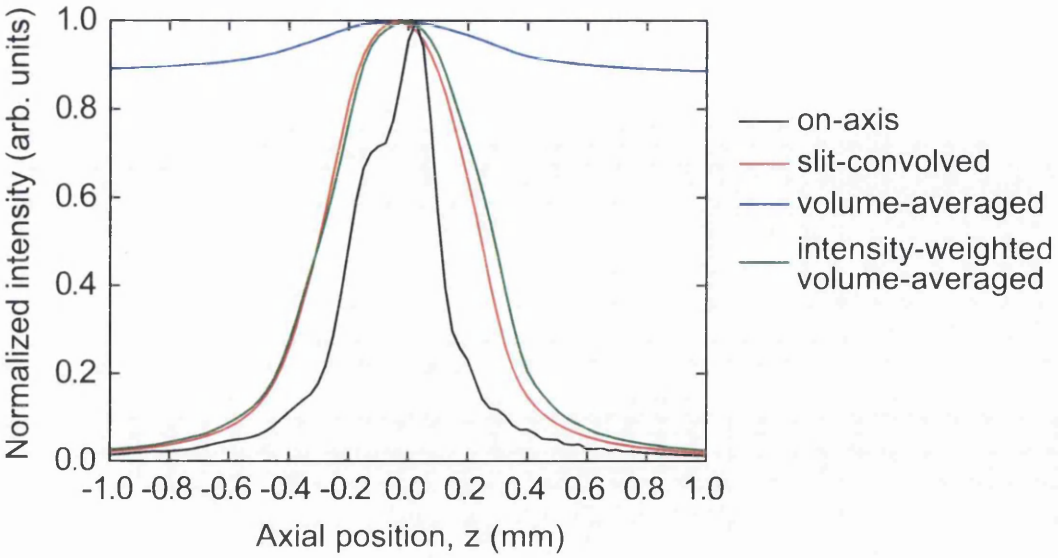

Figure 5.11: One-dimensional intensity distributions used for deconvolution. The slit-convolved distribution (red) is obtained from the on-axis distribution (black) by convolution with a 250μm slit; the volume-averaged (blue) and intensity-weighted volume-averaged (green) distributions are obtained by averaging the intensity over a 250 μm cylinder of the three-dimensional modelled focal volume at each z.

discontinuities caused by the oscillations in the on-axis intensity distribution are smoothed by performing weighted-averaging of the radial and axial intensity distribution at each z-position. The one-dimensional intensity distributions on-axis, slit-convolved, volume-averaged and the IWVA are shown for comparison in Figure 5.11.

The intensity-weighted volume-averaged and slit-convolved deconvolution methods are compared for the 250 μm aperture in Figure 5.12. Both methods almost compensate for the intensity shifting of Xe^{2+} seen in the on-axis deconvolution, but are not so successful with Xe^{3+}. For Xe^{+} and Xe^{2+}, the intensity-weighted volume-averaged $I(z)$ produces the best fit for $I_{\text{peak}} = 10^{16}$ W/cm^2, whereas at $I_{\text{peak}} = 10^{15}$ W/cm^2 the Xe^{2+} fit is comparable, with the slit-convolved $I(z)$ producing a better fit for Xe^{+} at lower intensities.

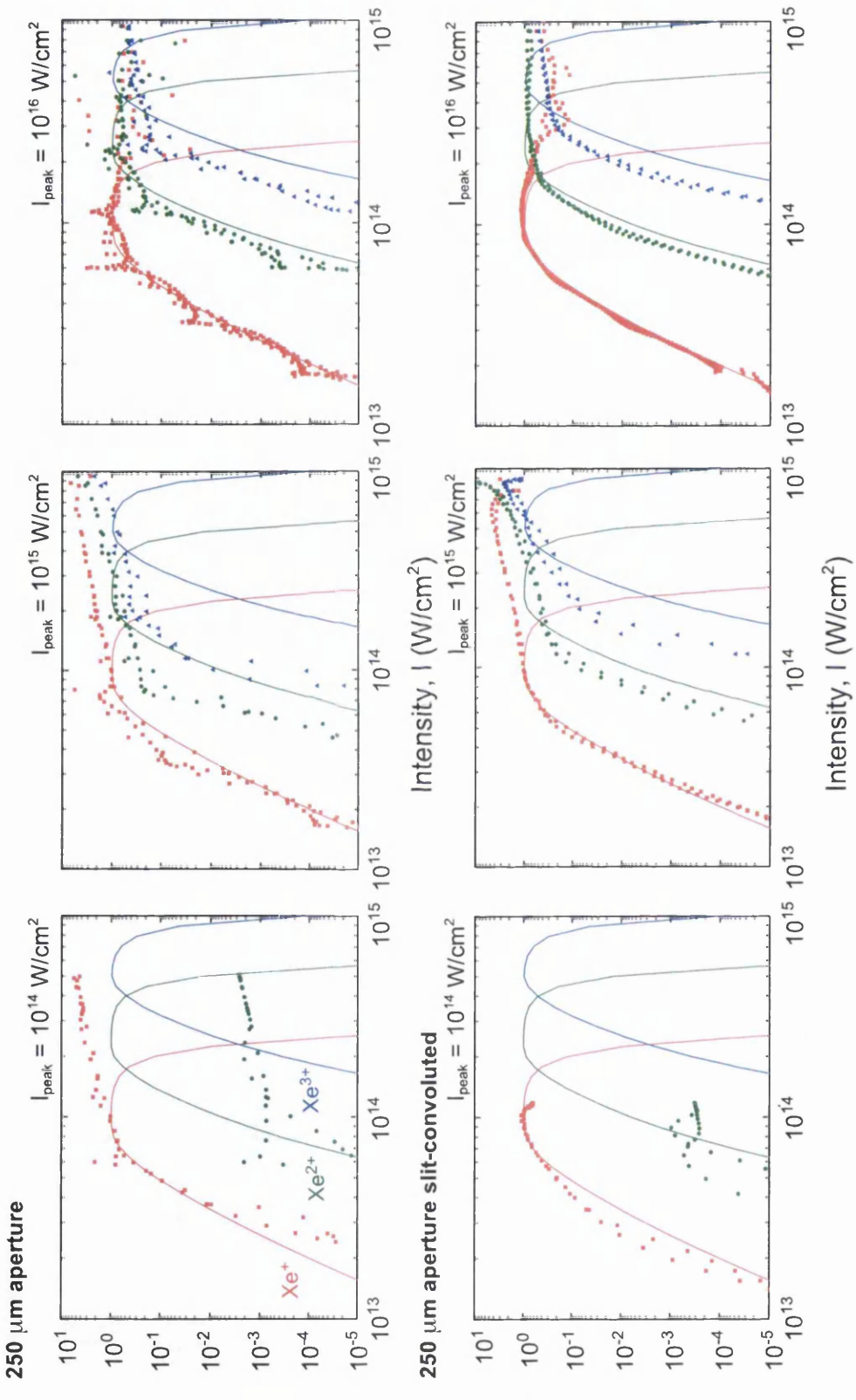
250 μm aperture
250 μm aperture slit-convoluted
I_peak = 10^14 W/cm^2
I_peak = 10^15 W/cm^2
I_peak = 10^16 W/cm^2
Xe+
Xe2+
Xe3+
Probability of ionization, P(I) (arb. units)
Intensity, I (W/cm^2)

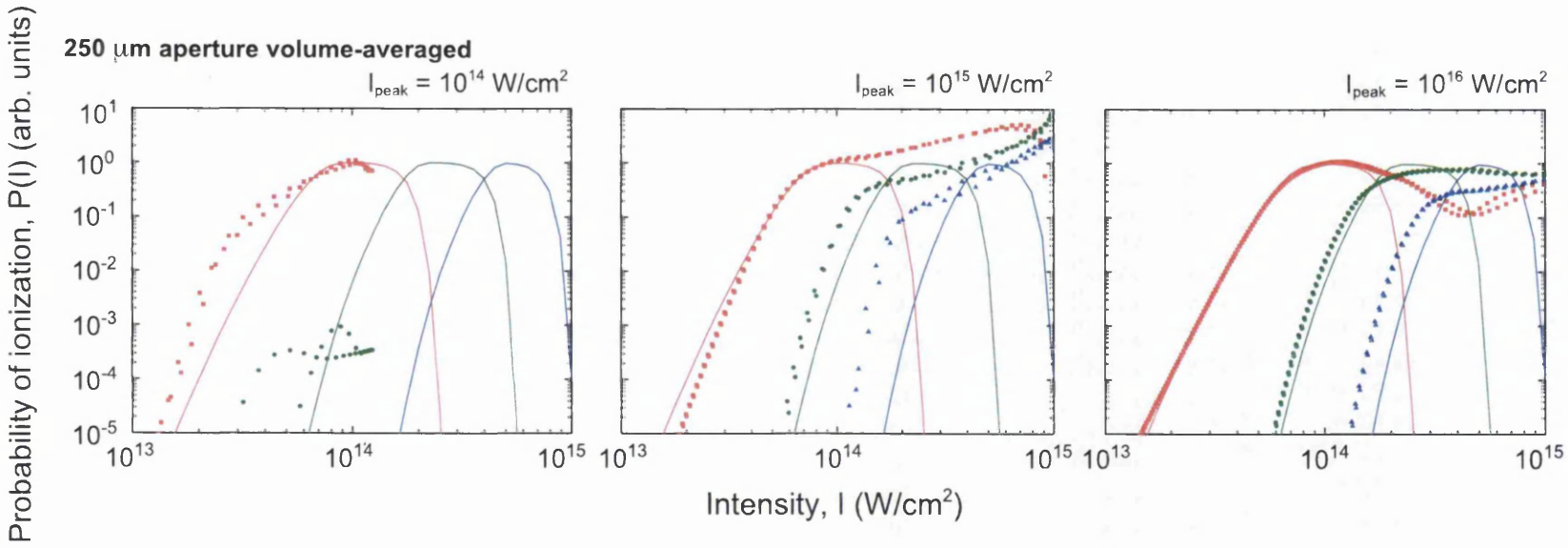

Figure 5.12: Ionization probabilities recovered from the model for a 250 μm aperture using *(top)* the on-axis intensity, *(middle)* slit-convolved and *(bottom)* intensity-weighted volume-averaged intensity over the aperture at each z, compared with the input probabilities (solid lines) from the tunnel theory predictions (Section 1.3). Peak intensity (I_{peak}) refers to the global maximum in the spatial intensity distribution, whereas the intensity axis corresponds to the local on-axis, slit-convoluted or intensity-weighted volume-averaged intensity respectively.

The variation in the quality of fit with peak intensity – in spite of the modifications described – has important implications for the recovered probabilities at different Δt. The signal-producing volume will change in size as the peak intensity varies as a function of Δt. At large Δt, the peak intensity is 0.4 orders lower than the maximum at $\Delta t = 0$, but can be as much as a whole order lower at minimum intensity (Figure 4.16). This means that, for $I_{\text{peak}} \sim 10^{16}$ W/cm^2, the quality of fit for the experimental deconvolution as a function of Δt can vary by an amount comparable to the variation between the $I_{\text{peak}} = 10^{15}$ and 10^{16} W/cm^2 plots shown in Figure 5.8 for the 250 μm aperture.

5.3.3 Genetic algorithm

An iterative approach to finding $I(z)$ could compensate for known and/or unknown geometrical effects in an unbiased fashion. In the case of the model, the input ionization probabilities represent a target state, $P_{\text{target}}(I)$. The recovered probabilities should match these as well as possible, with the ideal limit that they should match exactly. A random variation produces a new, trial $I(z)$, which is used to recover the probability $P_{\text{trial}}(I_{\text{trial}}(z))$ from the modelled $S(z)$. If the fit between P_{trial} and P_{target} is improved, $I_{\text{trial}}(z)$ is accepted, otherwise it is rejected and the previous $I(z)$ accepted. On the next iteration, the accepted intensity distribution is again randomly varied, and this process is repeated until a suitable goodness-of-fit is achieved.

This idea is in principle a simple genetic algorithm, with a goal to maximise the goodness-of-fit by random variation. There are many forms of goodness-of-fit parameter, but in this case the nonlinearity of the ionization probabilities must be taken into account. The Pearson form of the chi-squared test [95] takes the form

$$\sum_i \left(\frac{(P_{\text{target}}(I_i) - P_{\text{trial}}(I_i))^2}{P_{\text{target}}(I_i)} \right) \tag{5.3}$$

and incorporates the weighting of the sum of least-squares by the target probability.

Trial $I(z)$ distributions were constructed using a Fourier series, with initial conditions generated from the initial on-axis, slit-convolved or intensity-weighted volume-averaged $I(z)$ by Fast Fourier Transform (FFT). To avoid unrealistic variations in the amplitude for higher harmonics, each harmonic is weighted by 1/n, where n is the harmonic number.

The genetic algorithm is also allowed to pursue multiple improvements to the fit in parallel, with a number of trial $I(z)$ distributions generated in each iteration, which are individually accepted or rejected based on whether they are an improvement to the fit or not, then the accepted distributions are averaged to give $I(z)$ for the next generation of trials.

Since the genetic algorithm has access to the entire intensity distribution at once, and multiple trial distributions per generation, it converges very quickly. The algorithm produces a comparable $I(z)$ and deconvoluted ionization probabilities to the slit-convolved and IWVA deconvolutions in Figure 5.12 after a runtime of order seconds, with a mixture of slit-convolved at low intensity and IWVA at high intensity being favoured. However, as a result the deconvoluted ionization probabilities still suffer from the problems identified in Section 5.3.2, resulting in a shifting and a change in shape of the recovered curves as a function of peak intensity.

By limiting the intensity and probability ranges over which the genetic algorithm searched for a best fit, the fit could be improved over a runtime of minutes. However, significant improvements were only seen when the limits resulted in each charge state being treated independently. As a result, the genetic algorithm effectively found a different best-fit $I(z)$ for each charge state simultaneously, manifesting as an $I(z)$ with discernible steps in the gradient.

In conclusion, the deconvolution therefore cannot be used to recover the probabilities in its original form, nor using the modifications described, since the change in position and shape of the recovered ionization probabilities indicate that the effects of the focal geometry cannot be completely removed from the data, therefore an intensity-independent comparison of the recovered probabilities at different Δt is impossible.

5.4 Full spatiotemporal analysis

The geometry-independent ionization probabilities could not be recovered using the previously discussed techniques as a function of Δt and z. Therefore, a full spatiotemporal model attempts to reproduce the experimental results using all of the elements described in Chapter 4. The pulse temporal electric field/intensity profile is reconstructed from measured FROG data (Chapter 2), including the temporal shaping introduced by varying Δt using the Mach-Zehnder interferometer, and dispersion due to the quarter-waveplate, as described in Chapter 4. The spatial electric field profile generated at the hollow fibre exit is propagated through a realistic beamline model to generate the three-dimensional intensity distribution over the focal volume, including the effects of diffraction due to hard-edged optics, as also described in Chapter 4. Finally, the predicted tunnel ionization probabilities for each model (ground-state and multiple-state, nondegenerate and degenerate) are calculated for each Δt over a range of peak intensities, and used in conjunction with the beamline model to reconstruct the full three-dimensional signal-producing volume as imaged by the 250 μm aperture in the TOFMS at each z-position, described in Chapter 4. Δt is calculated at the resolution used in the experiment (Δt step size = $\frac{2}{3}$ fs). In order to account for the temporal jitter of the translation stage in the Mach-Zehnder interferometer, the results for an offset of 0 fs and $-\frac{1}{3}$ fs (i.e. half the step size) are averaged.

Figures 5.13 and 5.14 compare the results of the full spatiotemporal models to the experimental data in Figure 5.4. The accuracy of the temporal pulse shaping model (described in Section 4.3) is expected to decrease at large Δt, since the FROG measurements (Section 2.2.2) are known only over a finite t-range. The central 40 fs of the data in Figure 5.4 has therefore been selected, roughly corresponding to the overlap between the highest-intensity parts of the pulse envelopes in each of the interferometer arms (Section 4.3).

In each figure 5.13 & 5.14(a)–(l), the ion yield as a function of axial distance, z and pump-probe delay, Δt is represented as a colour plot. For each charge state, there is expected to be an offset in the global maximum due to the quantum efficiency of the detector. As such, the ground-state only and multiple-state models are scaled by the same factor in order to account for this overall quantitative difference, but the qualitative behaviour of the modelled yield is unaffected. Subtractions are also shown in order to demonstrate the differences between the models. It is expected from the probability plots shown in Figure 4.14, the ground-state and multiple-state models for the nondegenerate case should match almost up to saturation in Xe^+, as should the ground-state and multiple-state degenerate models, because only one electron is removed from the neutral xenon, therefore multielectron effects are minimised. Figures 5.13(m)-(p) and 5.14(m)-(p) confirm this, with the Xe^+ differences being much smaller overall in comparison to Xe^{2+}–Xe^{4+}. The peak intensity has been adjusted in order that the model best represents the data for Xe^+ for both models, which occurs at 3.2×10^{16} W/cm^2 in the nondegenerate case, and 2.8×10^{16} W/cm^2 for the degenerate case. These are higher than the peak intensity expected from the deconvolution (10^{16} W/cm^2), though as discussed in Section 5.3.1, the recovered probabilities are affected by spatial averaging of the recorded z-scans over the 250 μm aperture. The best fit between experimental and modelled Xe^+ yields in Fig-

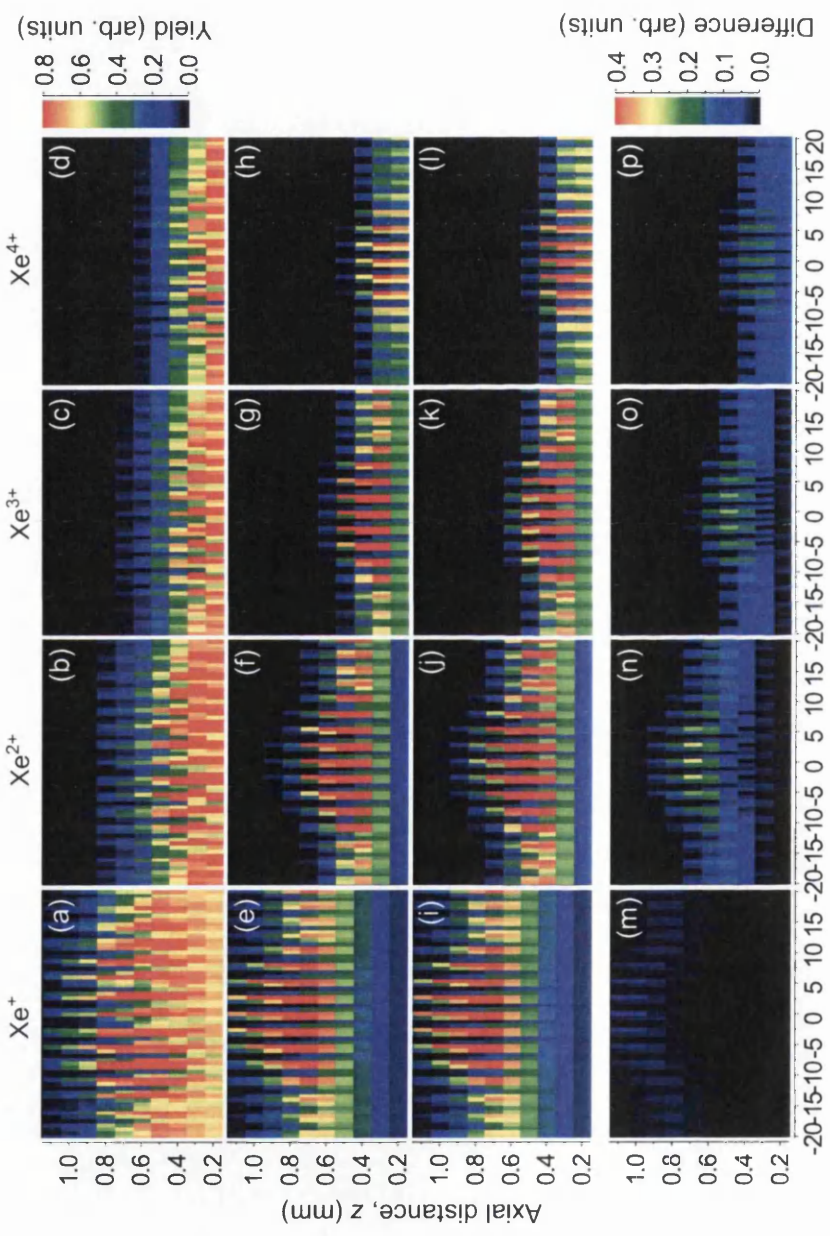

Figure 5.13: Comparison of integrated ion yield data (a)–(d) to the full spatiotemporal nondegenerate ground-state only (e)–(h) and multiple-state (i)–(l) ionization models described in the text, as a function of pump-probe delay, Δt, and axial distance from the focus, z. (m)–(p) Subtraction of the ground-state from the multiple-state models, highlighting differences in the yield.

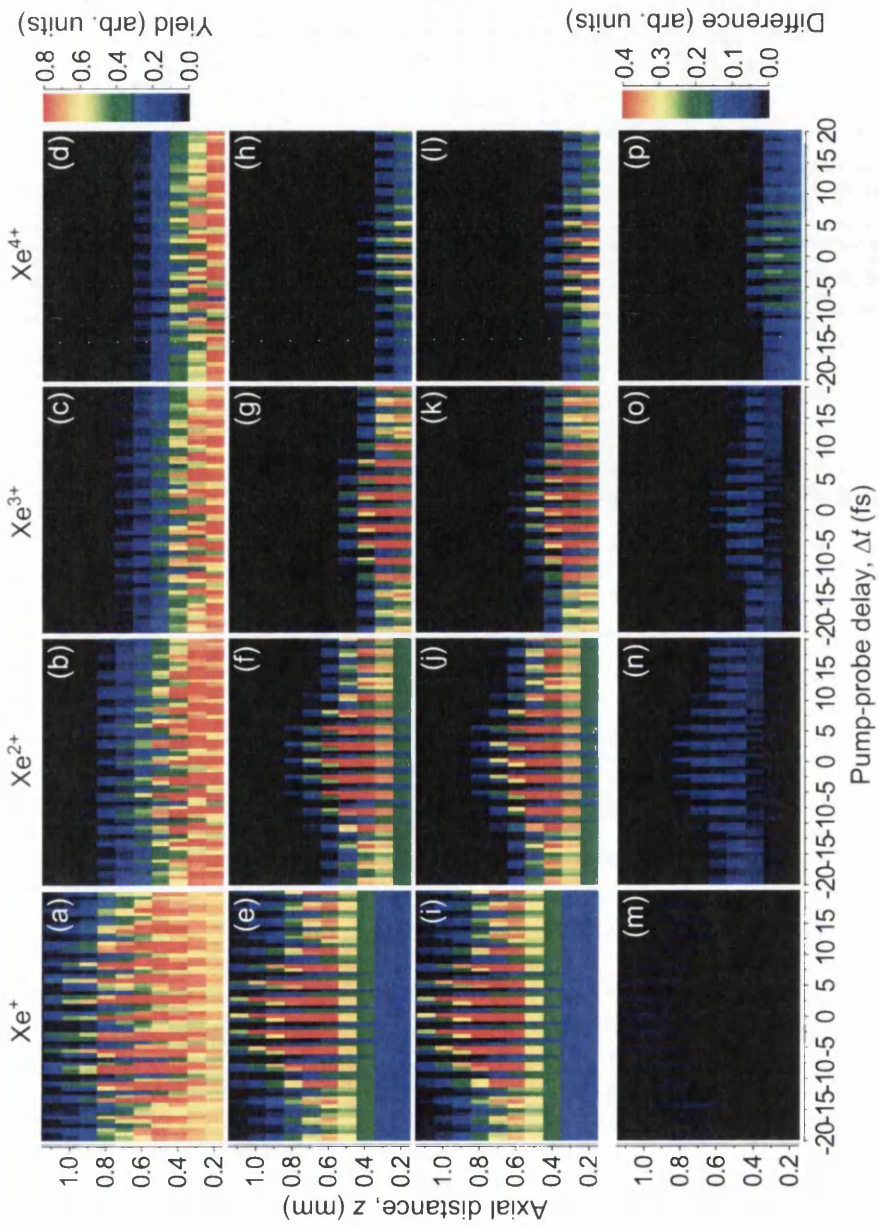

Figure 5.14: Comparison of integrated ion yield data (a)–(d) to the full spatiotemporal degenerate ground-state only (e)–(h) and multiple-state (i)–(l) ionization models described in the text, as a function of pump-probe delay, Δt, and axial distance from the focus, z. (m)–(p) Subtraction of the ground-state from the multiple-state models, highlighting differences in the yield.

ures 5.13 and 5.14 also requires the experimental data to be shifted by 300 μm in the z-direction. As predicted by the beamline modelling described in Chapter 4, there is a 40 μm offset between the peak on-axis intensity and the geometric focus position. The exact position of the on-axis peak intensity falls between the z-positions of the aperture, accounting for as much as a further 50 μm offset. The on-axis and full three-dimensional focus is also asymmetric in z. The shifting of the apparent peak intensity position in z is therefore attributed to these effects, combined with the convolution of the focal volume with the TOFMS aperture.

All models underestimate the signal at small z values for Xe^+–Xe^{3+}, particularly for Xe^+. All ions generated over the focal region are assumed to travel in a straight line when accelerated by the electric field in the TOFMS (between bottom and top plates), and the aperture therefore spatially selects ions produced in a cylinder of the same diameter extending below it. Space charge effects, if present, ensue when the Coulomb repulsion between the ions becomes significant, and causes the ion paths to diverge, causing broadening of the time-of-flight peaks and a spatial spreading of the ions as they travel from the source to the detector.

In order to determine whether space charge effects contribute significantly to the measured signal, Figure 5.15 shows representative TOF spectra from the full dataset, at $\Delta t = -20.7, -3.3, 0, +3.3$ and $+18$ fs. The z-axis values are shifted by 0.2 mm to match Figures 5.13 and 5.14, the reason for which is explained previously.

For Xe^+, the two isotope peaks between 6.65 and 6.70 μs are just resolved from z=0.9 to 1.1 mm across all selected Δt, up to $z = 0.8$ mm for $\Delta t = +18$ and -3.3 fs, and up to $z = 0.7$ mm for $\Delta t = -20.7$ fs. The first sign of a small space charge effect is the merging of these peaks below these z-values. A stronger space charge effect is present when the wings of this merged peak begin to overlap with the wings of the main peak at 6.6 μs. The minimum between the peaks at

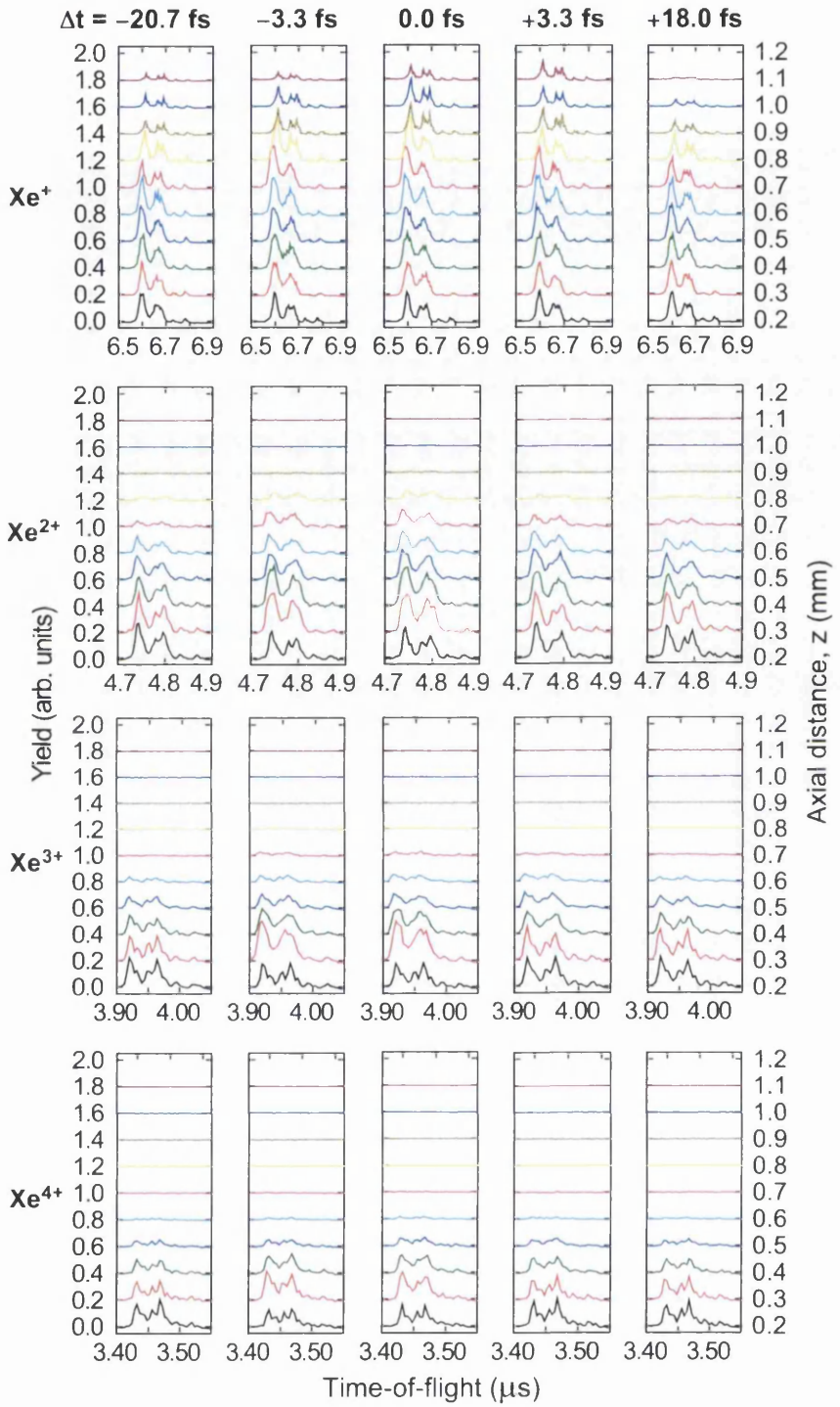

Figure 5.15: TOF spectra for $\Delta t = -20.7, -3.3, 0, +3.3$ and $+18$ fs for Xe^+–Xe^{4+}. The axial distance, z, has been shifted by 300 μm to correspond with Figures 5.13 and 5.14. Spectra are coloured for clarity, with each colour corresponding to the yield recorded at each labelled z-position.

6.63 μs decreases in depth due to this overlap, with the effect being strongest near $\Delta t = 0$ fs between z=0.3 and 0.8 mm.

For Xe^{2+}, the space charge effect is present over a smaller range in z, present between $z = 0.3$ to 0.5 mm for $\Delta t = 0$ and -3.3 fs, and at $z = 0.2$ only for $\Delta t = -20.7, +3.3$ and $+18$ fs. The Xe^{3+} space charge is noticeable only from 0.3–0.4 mm at $\Delta t = 0$ and -3.3 fs. The effect is very small for Xe^{4+}.

Since Xe^{+} has the slowest transit from the interaction region to the detector, a packet of Xe^{+} ions generated at the focus will have the most time to repel and diverge before they reach the aperture. It is in the Xe^{+} signal where the signal, and therefore the ion density is highest that would therefore be the most likely to be affected by any space charge effects, as confirmed by Figure 5.15. As charge state increases, transit times from the interaction region to the aperture also decrease, as does the overall volume of ions produced. The discrepancy between the experimental data and the models at low z therefore appears to be explained by space charge, which also decreases with increasing charge state. Additionally, space charge is not expected to affect the shape of the outer edges of the signals in z (yellow-to-blue regions in the colour plots) for Xe^{+}–Xe^{3+}.

Comparing Figures 5.13(n)–(p) and 5.14(n)–(p) highlights immediately the difference in the way the models behave as a result of including degenerate energy levels. In the nondegenerate case (Figure 5.13), the difference between ground-state only and multiple-state models are most evident in z, with a large difference between the models in (n), slightly smaller in (o) and again in (p), with the Δt extent of the difference very similar in each case. In the degenerate case (Figure 5.14), the differences between the ground-state and multiple-state models in (n) and (o) are much smaller than in the nondegenerate case, followed by a substantial difference in z and Δt predicted yields between the models, as shown in (p). As seen in Figure 4.14, the ground-state degenerate and nondegenerate probabilities

overlap, since (as quoted in Table 4.1) the ground-state degeneracy of Xe^{4+} is 1. More directly, the difference in z and Δt extent between Figures 5.14(g) and (h) is significantly larger than that seen between (k) and (l), between Figures 5.13(g) and (h) or 5.13(k) and (l). Such a large difference is also not seen in the experimental data, indicating that Xe^{4+} in particular is not well-described by the ground-state only degenerate model.

The models predict too much signal at high z. At 0.9 mm in Figure 5.13(b), the experimental Xe^{2+} yield is negligible, yet the ground-state model in (f) predicts a yield contribution peaking at around 0.2 units over a Δt range of -5 to $+5$ fs. The multiple-state model in (j) predicts a higher, more constant yield contribution of ~ 0.2 over a similar Δt range. In fact, in the $z = 0.5$ to 0.9 mm range the overall multiple-state prediction is higher than the ground-state only model, with the ground-state model at $+\Delta t$ producing a better fit to the data particularly around $z = 0.8$ mm. In the degenerate model, the high-z behaviour is better-described in both Figures 5.14(f) and (j), corresponding to the ground-state and multiple-state models respectively, with (f) providing a slightly better description of the data near $\Delta t = 0$. As summarised in Table 4.2, there are 28 energy levels involved in Xe^{2+} ionization in the degenerate case, compared to 9 in the nondegenerate case. This creates a greater density of ionization potentials over the same energy interval, which may be expected to smooth out the intensity-dependent ionization behaviour.

In the Xe^{3+} case, the nondegenerate multiple-state model in Figure 5.13(k) seems to be more descriptive of the data, predicting significant yield consistently at higher z, whereas the ground-state model in (g) seems to predict a much sharper falloff in z. As in Xe^{2+}, including degenerate states results in a much smoother falloff in intensity in both cases. However, differently to Xe^{2+}, the

mulitiple-state degenerate model in Figure 5.14(k) seems to better describe the spatial extent of the signal in (c) for the Xe^{3+}.

The experimental data (Figures 5.13(a)–(d) and 5.14(a)–(d)), there is an overall asymmetry observed, seen most clearly in the leading and trailing edges of the plots. In Xe^{+} (a), the gradient on the $-\Delta t$-side of the overlap (at $\Delta t = 0$) is steeper than on the $+\Delta t$-side. At $-\Delta t$, the strong pulse precedes the weak pulse at the interferometer output, and vice versa at Δt. As described in Section 4.3, the sharpest rising edge exists for the $-\Delta t$-side of the temporal overlap, and therefore the prevalence of nonadiabatic ionization is anticipated to be higher here than on the $+\Delta t$-side.

The nondegenerate model (Figure 5.13) is fairly symmetric overall for Xe^{+} (Figure 5.13(e) and (i)), with a very slight asymmetry developing for subsequent charge states. The deepest signal minima occur for all charge states (Figure 5.13(e)–(l)) between $\Delta t = -5$ and $+5$ fs, with the distribution of minima centred at $\Delta t = 0$, corresponding to the strongest intensity variations expected near temporal overlap as shown in Figure 4.16. In the experimental data however, these occur over a smaller range, centred nearer -8 fs. The reduction in the depth of the minima at $\Delta t = -7$ fs and above is not due to aliasing; if it were, the minima would be expected to follow a regular pattern depending on the step size, becoming deeper again at $+\Delta t$. Neither the ground-state only nor the multiple-state nondegenerate model better reproduces the $-\Delta t$ behaviour below -5 fs, and both models reproduce the behaviour equally well at $+\Delta t$ above $+7$ fs.

In the degenerate case however, whilst the deepest minima are still predicted over a similar range to the nondegenerate case, there is a temporal asymmetry in Xe^{2+} and Xe^{3+} predicted in the multiple-state degenerate model (Figures 5.14(j) and (k)), highlighted by the subtractions (n)–(o). The range of minima is no longer centred at $\Delta t = 0$ but at slight negative $-\Delta t$, over a range ~ -10 to

+5 fs. The asymmetry is possibly present in the multiple-state model for Xe^{4+} also (l), but due to the lower signal yield, the effect on the subtraction (p) is more subtle.

5.5 Conclusions

Spatially- and temporally-resolved measurements of recollision-free xenon ionization using circularly-polarized NIR pulses have been compared to full spatiotemporal models based on modifications to the nonadiabatic tunnel theory of Yudin and Ivanov. The inclusion of direct tunnelling from multiple energy levels has the greatest effect on the spatial distribution of ions; however, some subtle temporal differences are also observed, despite the apparent overall symmetry of the models in Δt. Including all possible degenerate energy levels reveals a more significant temporal asymmetry. The experimental data is visibly asymmetric in Δt.

By comparing experiment and theory in two dimensions (Δt,z) for four charge states, the degenerate multiple-state model appears to be the best description of the experimental data, since it is the best description of the variation of the ion yield in z, and is the only model to begin to explain the temporal asymmetry in the data. With a higher number of energy levels involved in the ionization process, this results in several more ionization channels becoming available, smoothing the intensity-dependence of the process in z, and accentuating the dependence on the temporal shape of the pulse, since the time-ordering of the population of the states becomes more important. However, whilst the degenerate model attempts to be the most complete treatment of all the models, the other models can be better descriptions of localised subtle effects, suggesting the complex variation of the temporal pulse shape with Δt can influence the preference for ionization by specific channels. The degenerate model, for example, assumes that all of the degenerate energy levels have identical ionization probabilities, whereas

Equation (4.10) in Chapter 4 demonstrates that degenerate energy levels will be reached with different probabilities for $m = 1, 0, -1$. The degenerate model may therefore overestimate the ionization rate, whereas the non-degenerate model may underestimate the ionization rate in some cases. A detailed model will require an in-depth look at each accessible level separately, and would therefore become significantly more complex. Additionally, coupling or interference between ionization channels is not considered in the model.

Chapter 6

Two-colour time-resolved ionization of krypton

This chapter briefly reviews single-photon ionization and excitation processes, followed by a detailed discussion of the experimental setup used for the XUV-NIR cross-correlation measurement of krypton ionization. In Chapter 5, strong-field tunnelling in a NIR field results in a time- and intensity-dependent population of multiple electronic energy levels in multiple xenon charge states. In this chapter however, the population of multiple levels in singly-charged krypton occurs instantaneously via weak-field XUV single-photon ionization, with the relative populations of the specific energy levels under investigation depending predominantly on the energy of the XUV photon. The potential for predicting photoionization cross-sections and elucidating electron correlation dynamics from the results is demonstrated by comparing the results to numerical models of the interaction.

6.1 Review

Chapter 1 discusses strong-field ionization and excitation processes requiring the nonlinear absorption of multiple low-energy (typically NIR) photons, resulting in

multiphoton and tunnel ionization with a strong intensity dependence. In weak fields, linear absorption of a single high-energy (typically XUV) photon can cause ionization, and result in the population of excited 'satellite' ionic states which are easily ionized, these processes exhibiting a strong photon energy dependence. In combination, XUV and NIR can therefore be used to control and probe time- and energy-dependent electron dynamics via the satellites.

6.1.1 Weak-field photoionization

Single-photon ionization (SPI) occurs when a photon at or above the ionization threshold is absorbed. For most atoms, a single photon with the required energy to remove an electron would need to be of ultraviolet wavelengths or shorter. For example, the first ionization threshold of krypton is ~14 eV, requiring a ~89 nm (XUV) photon.

The rate of SPI is given by [1]

$$\Gamma_{\mathrm{SPI}} = \sigma(\omega) I \tag{6.1}$$

where I is the laser intensity, and $\sigma(\omega)$ is the photoionization cross-section, which is highly dependent on the photon frequency ω. Figure 6.1 shows the krypton photoionization cross-section modelled by McGuire *et al.* [96], demonstrating a strong peak in the vicinity of the first ionization threshold at ~887 Å (~14 eV). The total photoionization cross-section $\sigma(\omega) = \sum_i \sigma_i(\omega)$, the sum of the partial photoionization cross-sections, σ_i, for each electron orbital [97].

The outgoing electron can cause excitation of the remaining ion via the electron correlation, resulting in the population of satellite states. Several processes may contribute to the population of the satellites: shake-up (SU), configuration interaction (CI) and interchannel coupling (IC). In SU, the sudden change in the

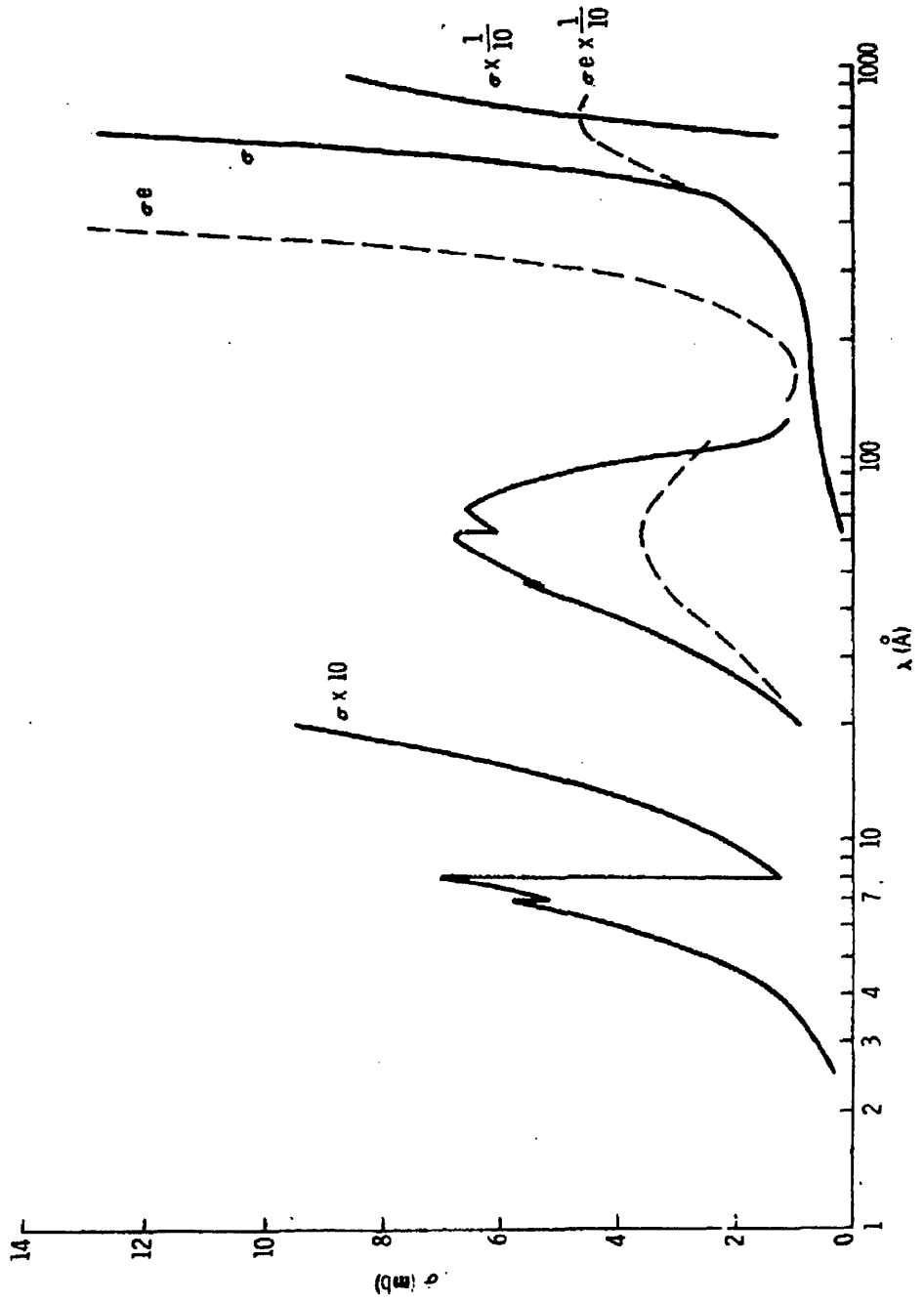

Figure 6.1: Kr photoionization cross-section modelled by McGuire *et al.* Reproduced from [96].

potential from the electron removal results in another electron being excited to a higher energy level, leaving a hole. In CI, there is a strong Coulombic interaction between single-hole and two-hole-one-electron configurations. For example, the $5s5p^6$ singly-ionized state in xenon interacts strongly with the $5s^25p^45d$ and $5s^25p^46s$ states [98, 99].

Shake-up can be separated into two forms, depending on which electron (ejected or excited) removes the majority of the photon energy. Direct shake-up (DSU) sees exchange of energy between the photo- and excited electrons, whereas in conjugate shake-up (CSU) there is an exchange of energy and angular momentum. CSU is dominant at or near threshold as there is a significant overlap between the initial bound and final continuum states, while DSU is strongest when the photon energy is tens or hundreds of eV above threshold.

The satellite states populated during photoionization of krypton by synchrotron radiation have been studied extensively with high resolution photoelectron spectroscopy [97, 99–103]. In these studies, a general agreement on state assignment is reached, however the mechanisms leading to the population of these states is disputed, especially in the vicinity of photoionization thresholds [97, 99, 102, 103].

Figure 6.2 shows the photoelectron spectrum of the $4s$ satellite states in krypton for a photon energy of 68.5 eV, as measured by Caló *et al.* [99]. The intensity variation of some satellite lines follows either the $4s$ or $4p$ photoionization main line as a function of photon energy [97, 99, 103–105], meaning CSU or CI+DSU respectively are expected to dominate. Caló *et al.* measured the partial cross-sections of the satellites over the range 60–88 eV (as shown in Figures 6.3 and 6.4) and used these in combination with the β parameter and total angular momenta to assign and confirm the ionization mechanisms for each state. These $4s$- and

4p-following satellite levels are listed in Table 6.1, and are the levels used in the modelling of the XUV-NIR interaction in Section 6.3.

Peak No. (modelling)	(Caló)	Energy(eV)	State	Mechanism
1	51	35.88	$(^1D)5d(^2G_{9/2})+(^3P)7p$	4p IC, SU
2	46	34.95	$(^1S)5p(^2P_{3/2})$	4p SU
3	30	32.63	$(^1D)5p(^2P_{3/2})$	
			$(^1D)4d(^2D_{3/2})$	4p SU
4	25	31.65	$(^3P)5p(^2S_{1/2})$	4p SU
5	24	31.61	$(^3P)5p(^2D_{3/2})$	4p SU
6	23	31.57	$(^3P)5p(^4S_{3/2})$	4p SU
7	22	31.37	$(^3P)5p(^2P_{3/2})$	4p SU
8	21	31.22	$(^3P)5p(^2P_{1/2})$	4p SU
9	20	31.16	$(^3P)5p(^2S_{1/2})$	4p SU
10	17	30.65	$(^3P)5p(^4D_{3/2})$	4p SU
11	84	39.47	$(^1D)10d(^2D_{3/2})$	4s CI
12	83	39.31	$(^1D)9d(^2D_{3/2})$	4s CI
13	79	38.99	$(^1D)8d(^2S_{1/2})$	4s CI
14	72	38.55	$(^1D)7d(^2S_{1/2})$	4s CI
15	68	37.84	$(^1D)6d(^2S_{1/2})$	4s CI
16	59	36.48	$(^1D)5d(^2S_{1/2})$	4s CI
17	39	34.39	$(^1S)6s(^2S_{1/2})$	4s CI
18	37	34.15	$(^3P)5d(^4D_{1/2})+(^4P_{1/2})$	
		$+(^2F_{7/2})+(^4F_{7/2})$	4s CI	
19	36	34.07	$(^3P)6s(^4P_{1/2})+(^4P_{3/2})$	
		$+(^4D_{3/2})$	4s CI	
20	34	33.94	$(^1D)4d(^2S_{1/2})$	4s CI
21	28	32.08	$(^1S)5s(^2S_{1/2})$	4s CI
22	13	30.23	$(^3P)4d(^4P_{1/2})+(^2P_{1/2})$	4s CI
23	12	30.06	$(^3P)4d(^2P_{1/2})+(^4P_{1/2})$	
		$+(^4F_{5/2})$; $(^1D)4d(^2P_{1/2})$	4s CI	
24	5	28.70	$(^3P)5s(^2P_{3/2})$	4s CI
25	2	28.27	$(^3P)5s(^4P_{3/2})$	4s CI

Table 6.1: Kr^+ satellite energies and states populated following XUV photoionization identified by Caló *et al.* [99] to exhibit a photon energy dependence. The peak numbers from Caló correspond to Figures 6.2–6.4, and the modelling peak numbers correspond to Figures 6.12 and 6.13. State assignments are from [99, 106].

6.1.2 XUV-NIR experiments

Uiberacker *et al.* [107] used a subfemtosecond XUV pulse to populate shake-up satellites in neon and xenon, probed by a NIR few-cycle pulse (FCP) with variable delay between the XUV and NIR. Figure 6.5 demonstrates the ionization

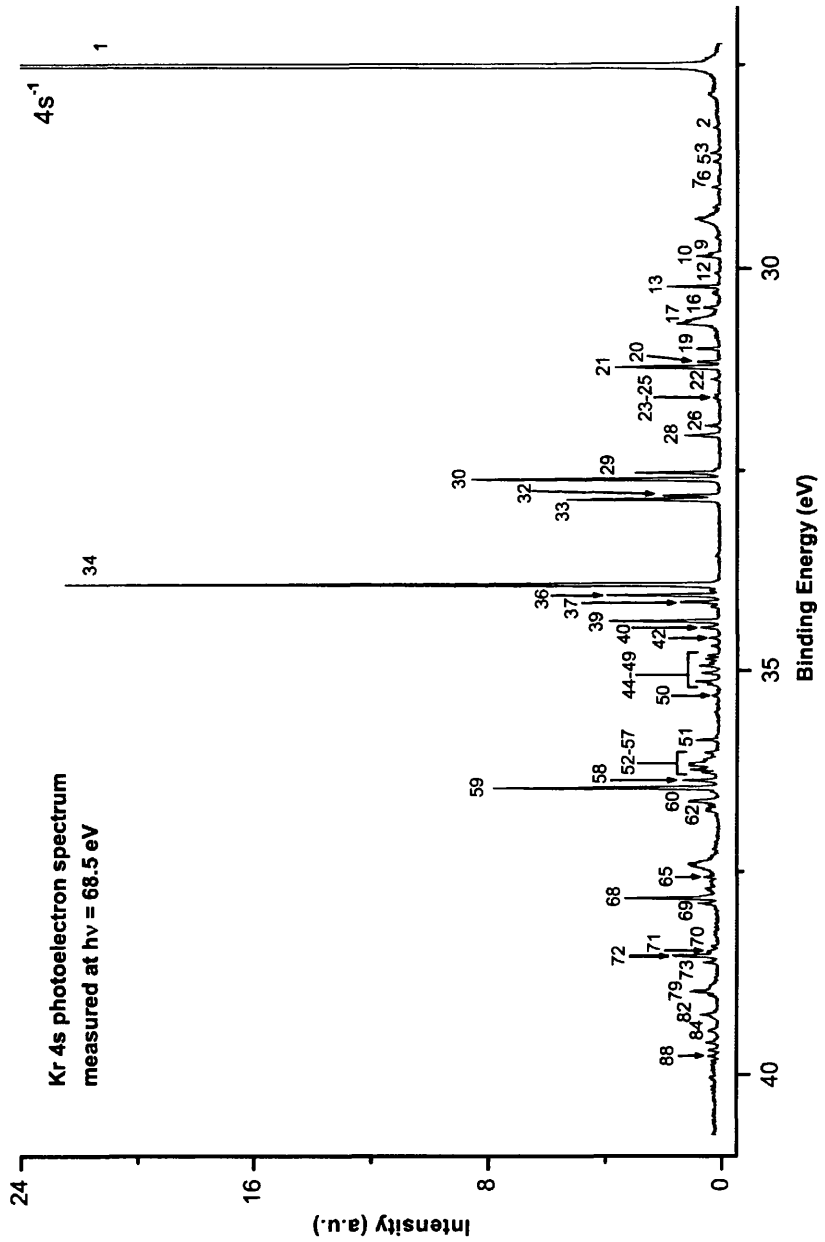

Figure 6.2: High-resolution krypton photoelectron satellite spectrum measured for a photon energy of 68.5 eV. The spectrum is scaled so that the 4s main line is scaled to a peak height of 100. Some of the labelled satellite states are identified in Table 6.1. Reproduced from [99].

routes for one-colour (XUV) and two-colour (XUV+NIR) processes, and shows the relative populations of the satellites and ionization probabilities. Uiberacker *et al.* compare their attosecond XUV pump and femtosecond NIR probe measurements for neon with predictions calculated using the tunnel theory of Yudin and Ivanov (described in Chapter 1) as shown in Figure 6.6. By comparing the measured ion yield as a function of delay to the model, the steps in the yield can be attributed to the onset of distinct satellite contributions at different delays, demonstrating real-time observation of multielectron dynamics.

In contrast, the ability to select XUV pulses of a single wavelength makes it possible to selectively populate energy levels. Synchrotron and XFEL sources can produce highly monochromatic tunable XUV radiation. Meyer *et al.* [108] recently conducted experiments using XFEL XUV and NIR pulses to investigate two-colour above-threshold ionization (ATI) in xenon, neon and helium as a function of pump-probe delay. Figure 6.7(a) illustrates the formation of sidebands in the electron kinetic energy spectrum for XUV photoionization due to the absorption or stimulated emission of NIR photons, and Figure 6.7(b) shows the strong dependence of the measured photoelectron spectra on pump-probe delay.

Unlike separate NIR and XUV sources, high-harmonic generation (HHG) can be used to generate temporally-synchronised collinear NIR and XUV. In a HHG source, the drive NIR causes tunnel ionization of an electron and its subsequent recombination with the parent ion within half a laser cycle. The additional energy gained by the electron due to the driving laser field is released as a high energy photon. The process of HHG is discussed in more detail in Chapter 1). The range of energies gained by the electron, depending on the time at which it is released into the continuum, results in a range of harmonics being produced at odd integer multiples of the NIR, occurring in bursts every half-cycle near the zero crossings of the electric field. As such, the harmonics are automatically synchronized with

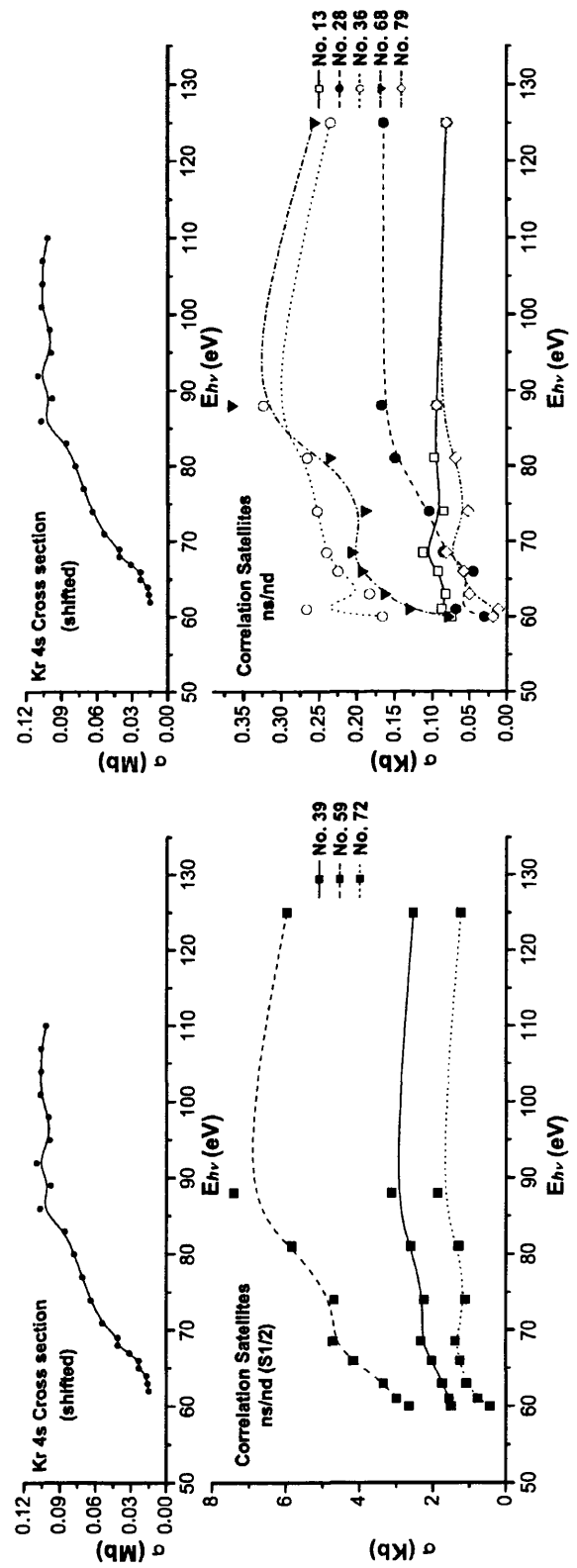

Figure 6.3: Partial cross-sections for selected CI satellites *(bottom)*. The horizontally-shifted 4*s* cross-section is shown for comparison *(top)*. Line numbers correspond to those in Figure 6.2. Curves are shown purely to guide the eye. Reproduced from [99].

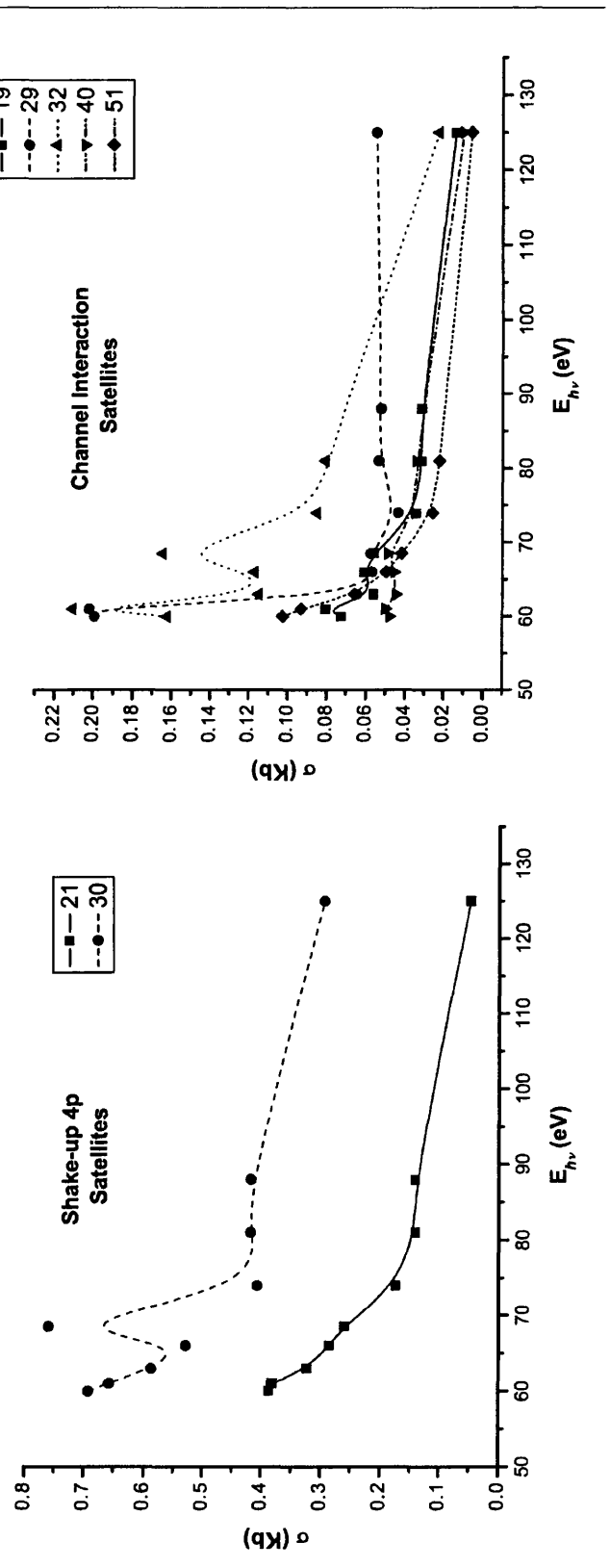

Figure 6.4: Partial cross-sections for selected SU satellites *(left)* and IC satellites *(right)*. Line numbers correspond to those in Figure 6.2. Curves are shown purely to guide the eye. Reproduced from [99].

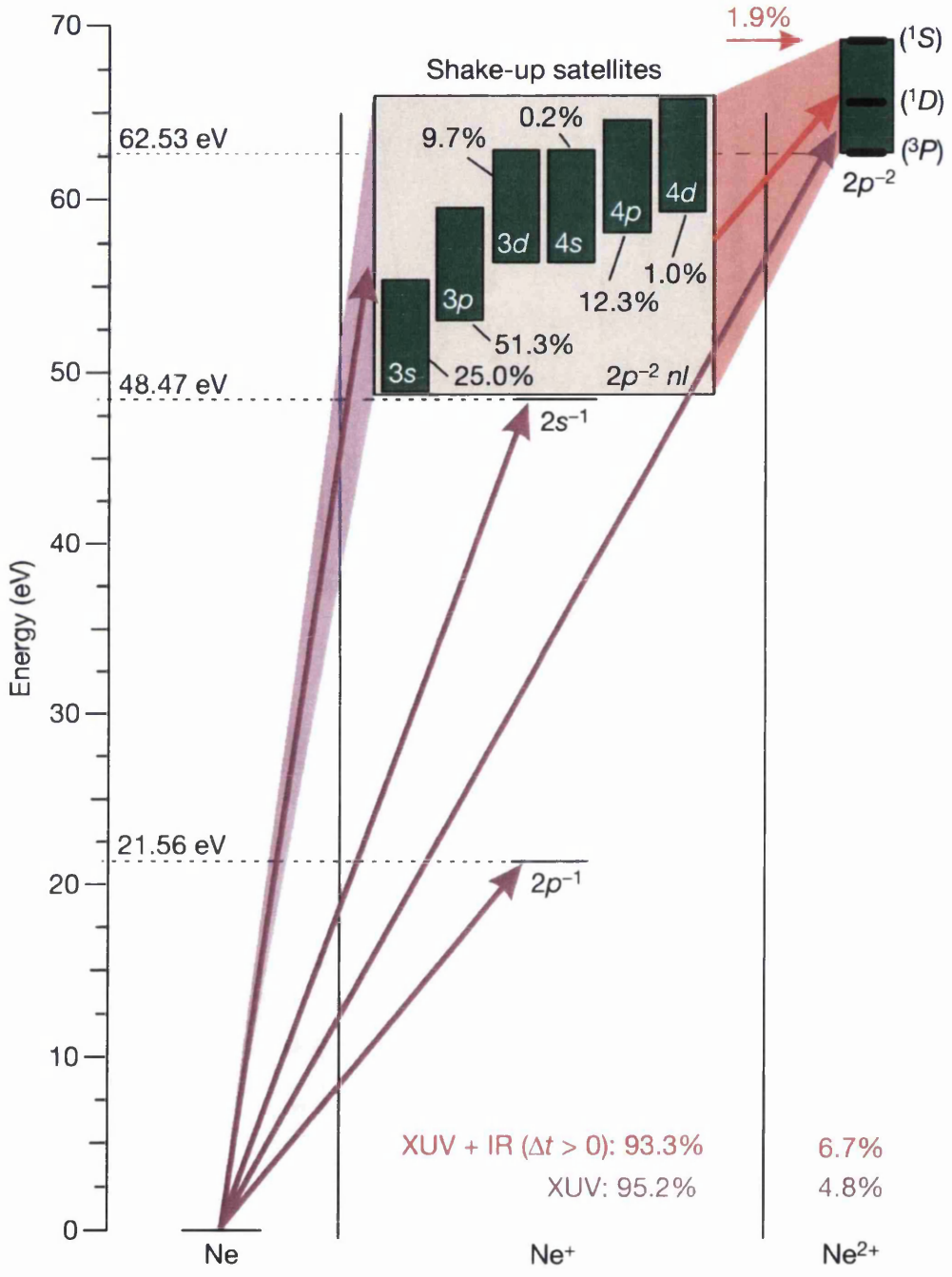

Figure 6.5: Energy levels, transitions and predicted populations in neon considered by Uiberacker *et al.* Reproduced from [107].

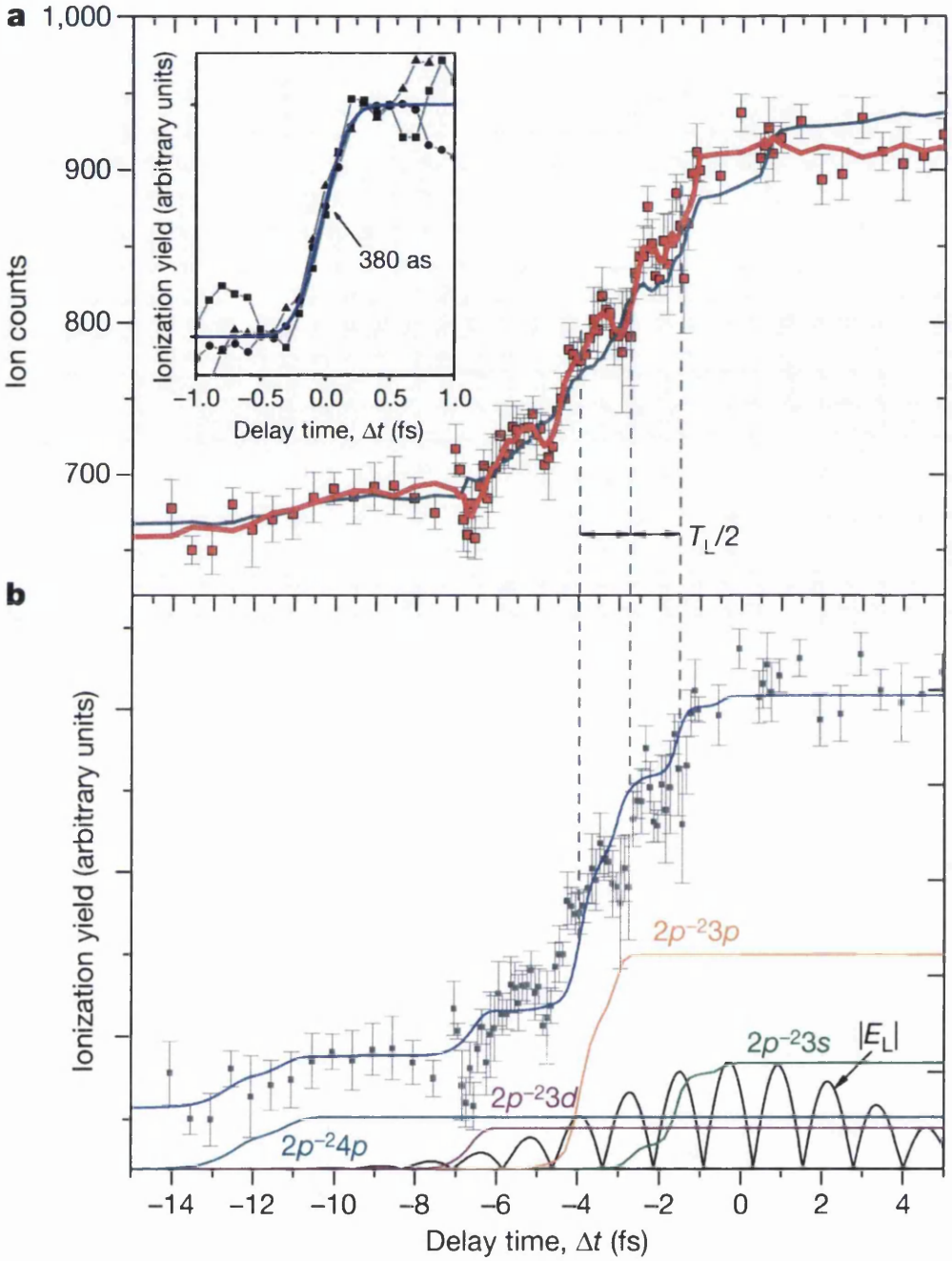

Figure 6.6: Ne^{2+} ion yield versus delay between the subfemtosecond XUV pump and the NIR FCP. The red line *(top)* is a six-point average of the experimental data, and the blue line *(bottom)* is a summation of the remaining thin coloured lines, calculated using nonadiabatic tunnel theory [3] for a 250 attosecond XUV pulse and a 5.5 fs Gaussian NIR pulse. Reproduced from [107].

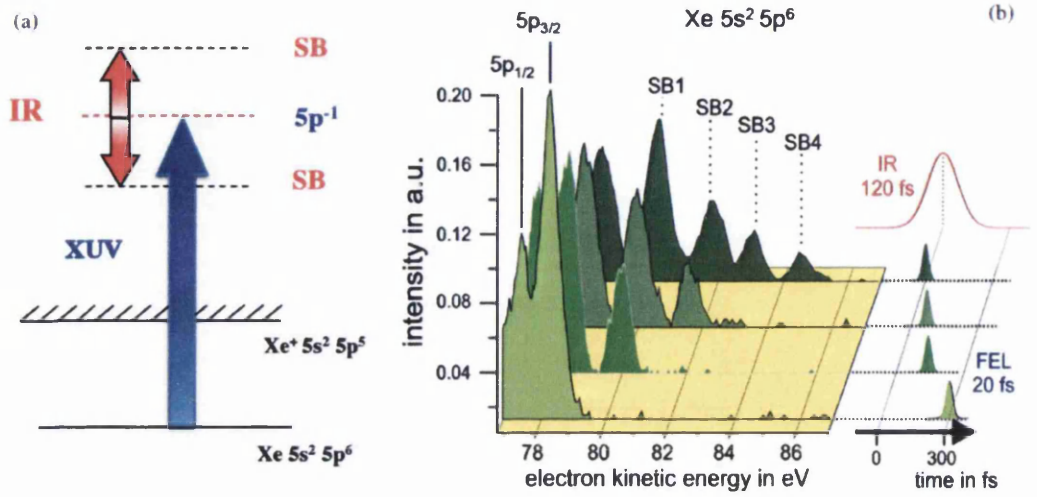

Figure 6.7: (a) Illustration of XUV photoionization and NIR sideband (SB) formation for 5p photoelectrons in Xe, and (b) photoelectron spectra for 90 eV (13.8 nm) XUV and ~1.6 eV (800 nm) NIR for four different XUV-NIR delays. The maximum number of sidebands is generated where the two pulses are at temporal overlap. Reproduced from [108].

the NIR, and the delay between the NIR and harmonic beamlines manipulated using an interferometer setup. Monochromation of the harmonic beam may be achieved using multilayer mirrors [109–111] which selectively reflect a particular harmonic, or a diffraction grating setup [104, 112].

Guyétand *et al.* [109] generate harmonics in a gas cell using 35 fs NIR pulses. A filter reduces the NIR transmitted, and a pair of multilayer mirrors selectively reflects either H19 or H25. The XUV is overlapped with a delayed NIR pulse and focused into an effusive xenon gas jet. The resulting ion and electron momenta and angular distribution are recorded using the COLTRIMS technique described in Chapter 1. The ionization routes considered are illustrated in Figure 6.8. The authors conclude that two-colour sequential ionization processes are generally weaker than nonsequential processes, and sequential processes are dominant for H19+NIR in xenon.

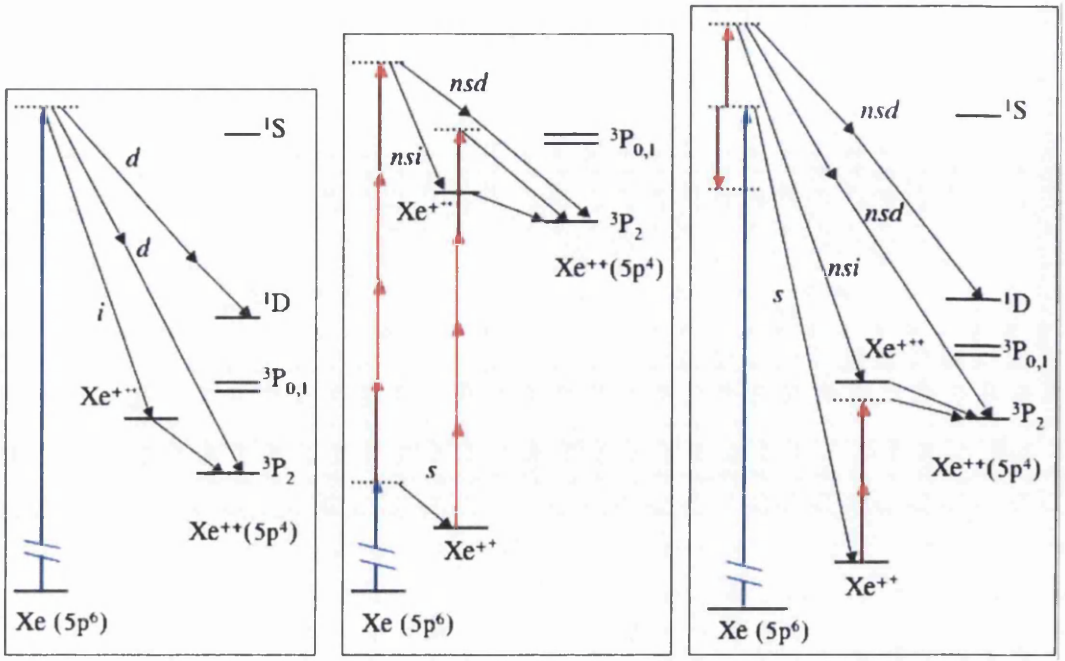

Figure 6.8: Double ionization routes identified by Guyétand *et al.* [109] for *(left)* H25 only, *(middle)* H19+NIR, and *(right)* H25+NIR in xenon, highlighting the additional pathways accessible as a result of a combination of XUV and NIR radiation. In the middle figure, H19 photons only have sufficient energy to singly ionize Xe, but in combination with multiple NIR photons, double ionization occurs via the pathways identified for H25 single-photon ionization (left figure), as well as an additional pathway not accessible to H25 only. In the right-hand figure, NIR in combination with H25 opens several additional ionization pathways via multiphoton processes and sideband formation. s = sequential process, ns = nonsequential process, d = direct, i = indirect. Reproduced from [109].

Ranitovic *et al.* [110] use a combination of NIR and two XUV harmonics, H11 and H13, generated by HHG and separated using filters and multilayer mirrors. Excited states of helium dressed by the NIR are populated by XUV photoabsorption, with the NIR causing ionization. The interference between the two channels is analogous to a double-slit experiment in the frequency domain. The intensity and relative delay between the XUV and NIR are carefully varied to demonstrate controllable modification of the electronic structure to control the interference

between ionization pathways, with complete destructive interference resulting in helium becoming transparent to XUV radiation.

The use of specific-wavelength multilayer mirrors places obvious limits the tunability of a HHG XUV system. Grating monochromators can be used to select harmonics from a large energy range, but at the expense of intensity, and can stretch femtosecond-duration XUV pulses to the order of picoseconds. By using a time-preserving monochromator in the off-plane geometry [104], such as will be described in Section 6.2, pulse stretching is avoided. Additionally, the transmission efficiency may be close to the reflectivity of the mirror coatings used [113].

6.2 Astra Artemis beamline

Figure 6.9 illustrates the experimental setup used for the XUV-NIR cross-correlation measurement. The 1 kHz Ti:S CPA laser described in Section 2.1.7 (KMLabs RedDragon) produces 2.4 mJ, 30 fs pulses at 785 nm, 0.8 mJ of which is focussed by a 25 cm focal length lens into a 1 kHz pulsed effusive argon gas jet controlled by a piezoelectric valve (Attotech, Sweden). High-harmonics are generated over an interaction length of approximately 5 mm, producing XUV radiation by high harmonic generation (HHG) as described in Chapter 1. The beam now consists of a range of harmonics, including XUV harmonics (10–100 nm) mixed with the NIR.

A state-of-the-art XUV monochromator (LUXOR, Padova) [104] is used to select the XUV harmonic transmitted. Four gold-coated diffraction gratings (Richardson Grating, USA) are mounted on a two-axis computer-controlled stage which can be linearly translated in order to select the desired grating, and tilted with respect to the beam propagation direction for wavelength selectivity. A toroidal mirror (Standa, Lithuania) at grazing incidence (TM1) collimates the im-

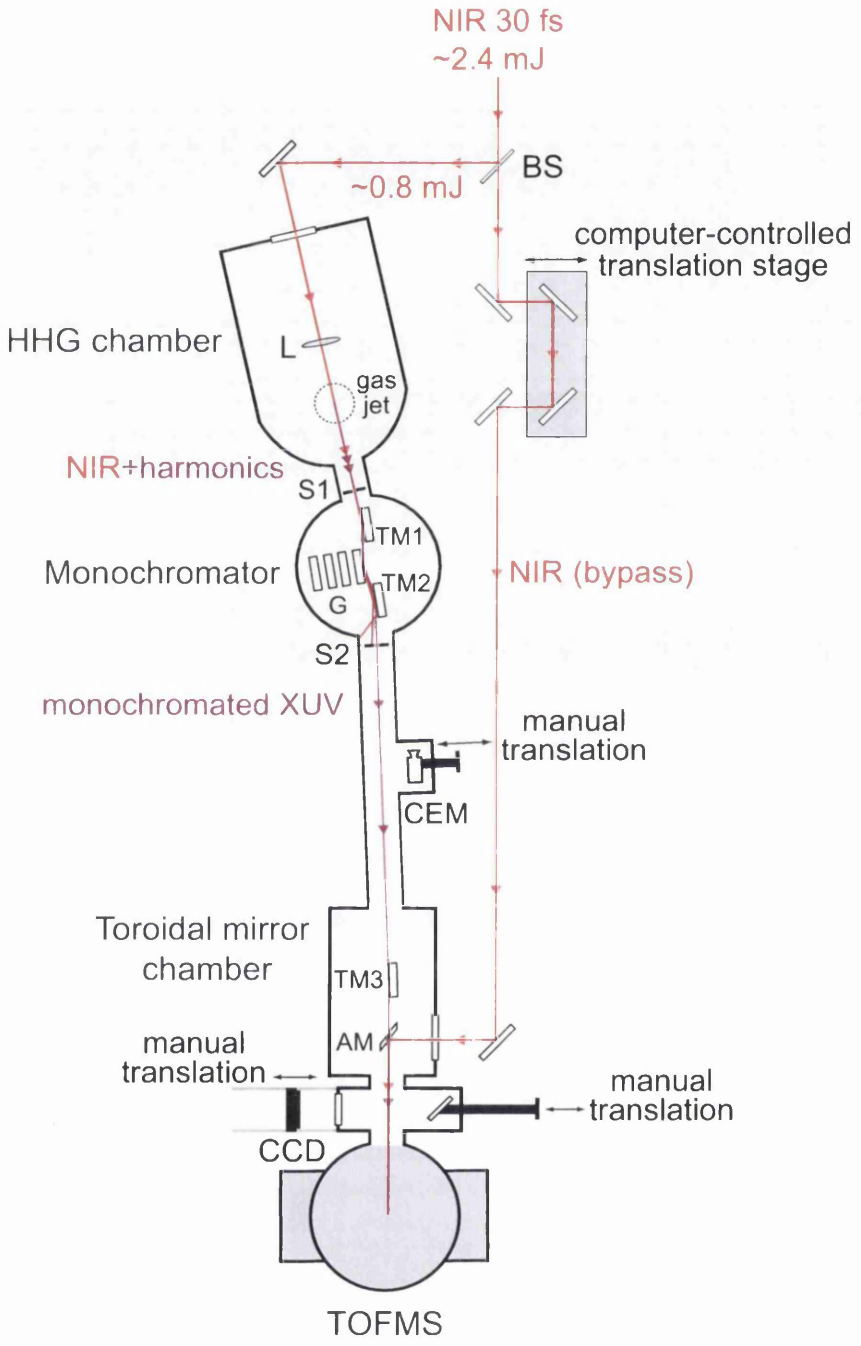

Figure 6.9: Illustration of the Astra Artemis beamline configured for XUV-NIR cross-correlation measurement. BS = beamsplitter (3:1 energy ratio), L = lens, S = slit, TM = toroidal mirror, G = gratings, CEM = channel electron multiplier, AM = annular mirror, TOFMS = ion time-of-flight mass spectrometer.

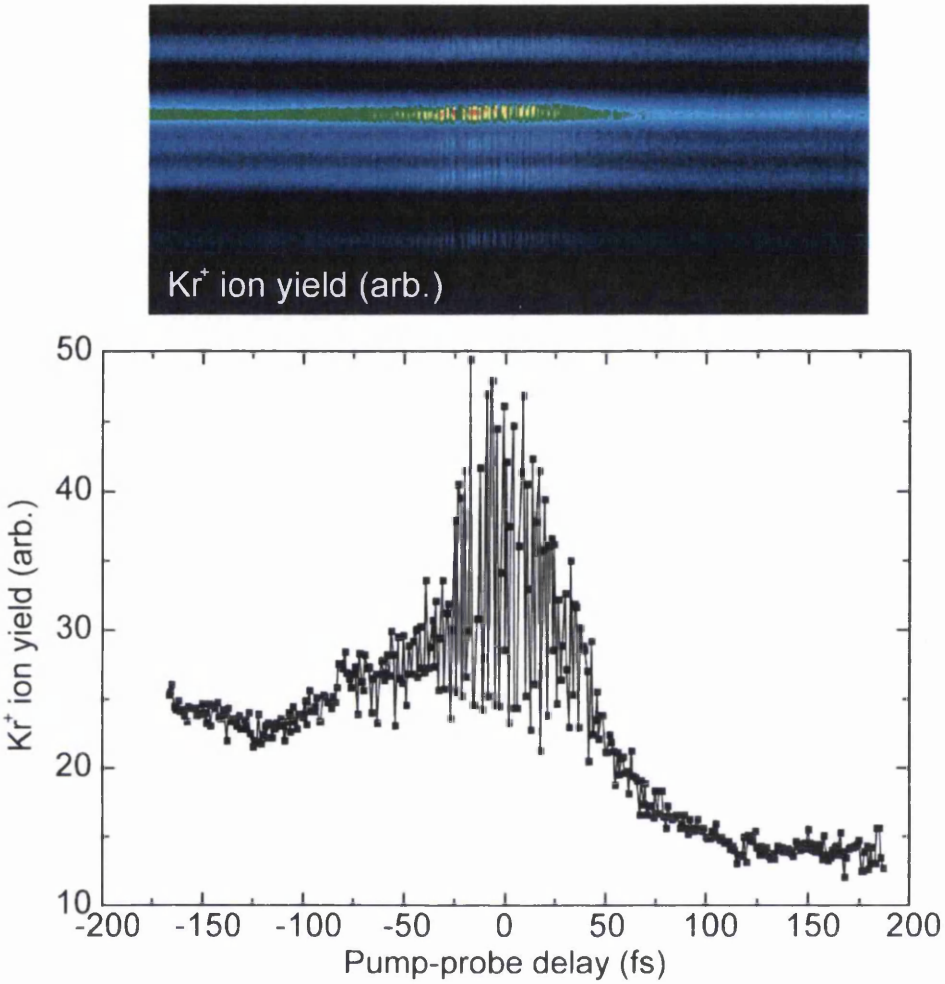

Figure 6.10: Measured Kr^+ yield as a function of the temporal overlap between zero-order (NIR+harmonics) pump and NIR probe, showing interference fringes between the two NIR pulses. The asymmetry in the Kr^+ yield is a consequence of the XUV also transmitted in the zero-order.

age of the entrance slit (S1), which falls onto the selected grating. The diffracted light is focused by a second toroidal mirror (TM2) onto the exit slit of the spectrometer. In this configuration (i.e. diffracted first-order transmission), the NIR hits the toroidal mirror off-axis and is blocked by the chamber wall before the exit slit (S2). Tilting the grating will translate the diffracted XUV spectrum across the exit slit, with the transmitted bandwidth limited by the width of the exit slit.

The transmitted XUV pulse duration depends on the number of grating rulings illuminated and is comparable to, or shorter than, the NIR drive pulse duration.

A third toroidal mirror (TM3) focuses the monochromated XUV into the interaction region of the ion time-of-flight mass spectrometer (TOFMS) described in Section 3.1, where krypton is effusively released to a local density of 2×10^{11} cm^{-3}. En route, the XUV passes through the hole at the centre of an annular mirror (AM).

The remaining 1.6 mJ of the NIR beam bypasses the HHG chamber and monochromator (Figure 6.9) described previously, and is recombined with the monochromated XUV on reflection from the annular mirror (AM). A computer-controlled translation stage in the bypass beamline introduces a sub-cycle temporal delay relative to the XUV. The XUV 'through' and NIR bypass beamlines therefore essentially form an interferometer with arm length ~6 m. The location of temporal overlap was found by configuring the monochromator for zero-order transmission (NIR+harmonics); both beams are then focused into the interaction region of the TOFMS, and the Kr^+ yield recorded as a function of delay, as shown in Figure 6.10. Since the focus produced by the 'through' and 'bypass' beamlines are spatially overlapped, and the NIR present in both beams originate from the same source. Therefore, interference fringes are observed in the Kr^+ yield when the pump-probe delay approaches the pulse duration.

The amplitude variations become larger as the delay approaches zero, or temporal overlap, but is never completely destructive due to the unequal energy splitting between the two NIR pulse copies. The peak in the ion yield locates the translation stage position corresponding to temporal overlap, and the subcycle fringes verify the stability of the system to better than 300 attoseconds.

Due to the nonaxisymmetric beam propagation expected from this beamline, the focal volume modelling techniques described in Chapter 4 have not been used;

instead, the XUV and NIR foci have been characterised experimentally using a CCD for beam profile measurements. The through beam spot size for the zero-order NIR was found to be 130 μm; however, the XUV spot size is not expected to exceed 20 μm due to the size of the source, which should be imaged 1:1 at the output. The NIR bypass beam is larger and more astigmatic (170 μm by 250 μm), with a significant power drop incurred due to the loss of the centre of the beam profile on reflection from the annular mirror. As described in Chapter 7, this can also cause a shift in the focus position with respect to the monochromated XUV or zero-order focus, which is taken into account. Despite these effects, the focused NIR intensity is still expected to be above 10^{13} W/cm^2.

The spatial region in which the XUV and NIR overlap is small; to increase the ion signal, the pressure of the gas target was higher (10^{-6} mbar) compared to the NIR-only experiments (10^{-7} mbar) described in Chapter 5. The aperture in the TOF was also removed, allowing the full interaction volume to be detected.

Using a calibrated channel electron multiplier (CEM) inserted into the beamline after the monochromator slit, the XUV photon flux can be determined from the measurements of CEM current. Changing the angle of the diffraction grating in the monochromator changes the XUV wavelength, and therefore photon energy transmitted, as described previously. By scanning through a range of angles, a spectrum of photon flux vs. photon energy can be plotted, as shown in Figure 6.11(c). A photon flux of 10^4 – 10^6 photons per shot was detected over the harmonic range H13 – H27 (20 – 45 eV).

6.3 Modelling

Figure 6.11(a) illustrates the processes that are to be considered for the XUV-NIR pump-probe setup described in Section 6.2. Over the H21, H23, H25 and H27 photon range (32.8 – 42.1 eV), krypton is either $4p^{-1}$ or $4s^{-1}$ photoionized,

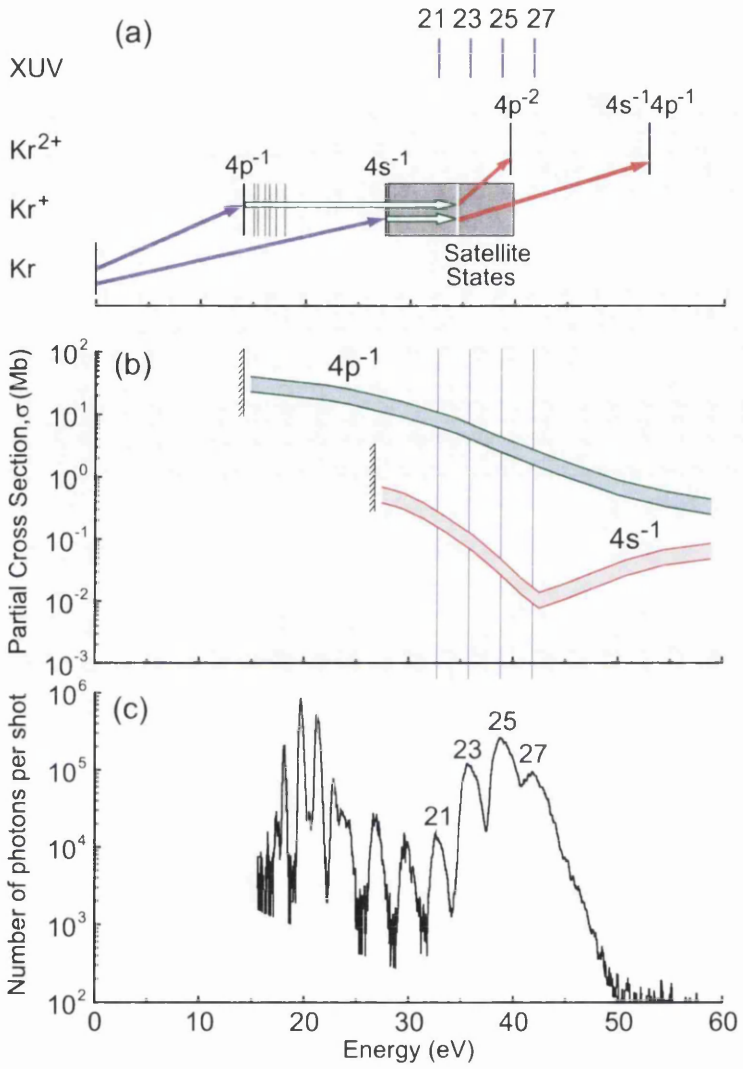

Figure 6.11: (a) Energy level diagram for krypton showing relevant electronic transitions: the XUV harmonics (violet arrows) photoionizes to $4p^{-1}$ or $4s^{-1}$ Kr^+, populating excited satellite states through shake-up or configuration interaction with a bound $4p$ electron (green arrows). The NIR strong field pulse then tunnel ionizes the satellite states (red arrows) leaving the Kr^{2+} ion in the $4p^{-2}$ or $4s^{-1}4p^{-1}$ states. (b) $4s^{-1}$ (red) and $4p^{-1}$ (green) partial photoionization cross sections as a function of photon energy from the respective thresholds of 13.99 and 27.50 eV. The cross-sections are an amalgamation of experimental and theoretical results [97,99–103] with the uncertainty indicated by the shaded area. (c) XUV harmonic spectrum measured on a channel-electron multiplier inserted into the beamline after the monochromator as the photon energy is selected, corrected for CEM sensitivity (electrons per photon) and dispersion as a function of angle.

with the photoionization cross-sections shown in Figure 6.11(b). During photoionization, bound $4p$ electrons have a small probability of being excited into unoccupied orbitals [99,100,102,103] populating satellite states by DSU and CSU as described in Section 6.1.1.

Photoexcitation cross-sections for krypton are unknown at the photon energy range in the present work, therefore the state assignments from Caló *et al.* [99] (as listed in Table 6.1) is employed, assuming the main-line-following behaviour extends to lower photon energy. The model makes no assumptions about the ionization mechanism. The $4s$- and $4p$-following peaks in the photoelectron spectrum from [99] are assumed to be proportional to the $4s$ and $4p$ partial photoabsorption cross-sections σ_{4s} and σ_{4p} respectively; varying these trial cross-sections scales the amplitudes of the corresponding satellite lines, modifying the satellite populations in the model accordingly. The excitation of the satellites could alternatively have been modelled using shifted cross-sections, as used by Caló *et al.* Following $4p^{-1}$ or $4s^{-1}$ ionization, the population of the satellite states occurs under the influence of the XUV photon, resulting in a shift in the electron ejection energy from the $4p^{-2}$nd states. However, this would result in some additional complexity when considering individual states, since individual shifts would also have to be incorporated into the modelling described in Section 6.3, whereas Caló introduce an average shift to aid visual comparison of the $4s$ and the SU, CI and IC satellites.

The harmonic-induced satellite yield is then integrated as a function of time through the XUV pulse; at each time-step (0.02 fs) the tunnel ionization of the cumulative satellite population is then predicted by the established strong-field tunnel ionization theory of Yudin and Ivanov [3], as described in Chapter 1 and used in the modelling in Chapter 5. Importantly, since this theory applies at arbitrary Keldysh parameter, it is valid for all satellite states even in the vicinity of the ionization threshold. Finally, since the focal length is long compared to

the length of the interaction region within the TOFMS, the XUV and NIR foci are approximated by intersecting cylindrical volumes, with radii corresponding to the beam profile measurements given in Section 6.2. Integrating over this volume gives the predicted ion yields for direct comparison with experiment.

The model therefore has only three fitting parameters: the trial partial photoionization cross-sections σ_{4s} and σ_{4p}, and the XUV pulse duration. These are systematically varied to fit the predicted ion yield as a function of pump-probe delay to the experimental results for H21–H27, as will be shown in Section 6.4.

6.4 Results

By varying the harmonic order (i.e. changing the photon energy) and scanning the delay between XUV and NIR, the enhancement of the Kr^{2+} ion yield can be used as an atomic cross-correlation measurement. Figure 6.12 presents the measured Kr^{2+} yields as a function of pump-probe delay for H21–H27, with theoretical predictions modelled as described in Section 6.3. Also shown are the individual predicted satellite populations as a function of pump-probe delay for the levels given in Table 6.1.

If the NIR pulse precedes the XUV pulse, the NIR intensity ($I_{\mathrm{NIR}} < 2 \times 10^{13}$ W/cm^2) is only sufficient to produce Kr^+ in the lowest lying electronic states with a probability of the order 10^{-4} per shot. As a result, subsequent XUV photoionization is essentially negligible as very few Kr^+ ions are generated, so the subsequent Kr^{2+} yield is below the detection limit of the TOFMS. Furthermore, direct tunnel ionization to Kr^{2+} in the NIR is predicted to have a probability around 7 orders of magnitude lower than Kr^+.

There is a clear time-dependent enhancement in the Kr^{2+} yield in the case of XUV-NIR pulse arrival rather than NIR-XUV. As illustrated in Figure 6.11, if

the XUV pulse precedes the NIR, the satellite states populated by the correlated electron dynamics are tunnel ionized by the NIR. As the pulses overlap in time, the satellite states will be depopulated generating either $4s^{-1}4p^{-1}$ or $4p^{-2}$ Kr^{2+}, and the yield and temporal structure is a direct measure of the satellite excitation process.

Despite some statistical noise in the Kr^{2+} yield presented in Figure 6.12, a clear change in the step size from H21 to H27 is seen, which the theoretical treatment reproduces very successfully. Furthermore the changing shape of the rising edge of the step is reproduced: H21 exhibits a sharp gradient change and H23 to H27 exhibit a successively less acute gradient. This is the result of tunnel ionization from the $4s$ satellites occurring later in the NIR pulse (i.e. at higher intensity) and a changing distribution of population with XUV energy.

The XUV photon energy and photoionization cross-sections place limits on the satellite states populated, and, as the harmonic order is varied, the ease with which the NIR pulse can initiate tunnel ionization. This is illustrated in Figure 6.13 where the cumulative Kr^{+} populations are presented for all satellite states following the XUV pulse only, and are equivalent to the photoelectron spectrum expected following the harmonic pulse. For H21, a limited group of low-lying satellite states are energetically permitted; H23 sees this limitation reduced. In H25, only a small number of high-lying $4s$-following states cannot be accessed and for H27, the full range of states are available. The energy considerations of the populated satellite states is approximate; if the XUV photon energy lies below the main line and satellite state, shake-up or configuration interaction are treated as impossible however this is worthy of future theoretical investigation, particularly in light of [110]. The degree of configuration interaction mixing between the $4s^{-1}$, $4p^{-1}$ and satellite states is also of importance.

From the relative $4s$ and $4p$ photoionization cross-sections, it might appear that the photoionization and excitation will be dominated by the $4p$ contribution, however two important factors must be considered. Firstly, there are many more high-lying satellites populated through $4s$ photoionization which will be far more readily tunnel ionized by the NIR. This tips the balance in favour of the $4s$ states, particularly for H25 and H27. Secondly, without the influence of both the $4s$- and $4p$-following states, the best-fit XUV pulse duration would approach 45 fs, as shown in Figure 6.14. The emission harmonic time is principally governed by the time within the pulse that significant tunnel ionization occurs in the argon gas jet. For a 30 fs NIR drive pulse, H21–H27 are caused by tunnelling in the central 12 to 8 fs of the pulse at the dominant intensity in the focal volume. For the plane grating employed in the current work, a full-width temporal response of 10 to 8 fs [112] is expected, calculated by ray-tracing paths from the gas jet to the exit slit through the monochromator. There is a requirement therefore that two processes are occurring: an XUV pulse with a duration of 45 fs would appear unlikely, and the predicted XUV durations of 24 to 28 fs seem much more in line with the ray-tracing predictions.

The σ_{4p} and σ_{4s} satellite photoexcitation cross-sections that produce the best-fit to the Kr^{2+} yields presented in Figure 6.12 are shown in Figure 6.15(a), and compared to the $4s^{-1}$ and $4p^{-1}$ main-line cross-sections. An absolute comparison cannot be performed as normalization to previous observations has not been possible, however relative comparisons reveal the energetic trends which are mediated by the correlation dynamics. The $4p$ satellite follows the energy dependence of the $4p^{-1}$ main line, the result of DSU and CI dominating, as this route is $\simeq$ 20 eV above threshold. This confirms the observations [99,103] at a significantly lower photon energy despite using a radically different experimental configuration. The $4s$ satellite exhibits a distinct divergence from the $4s^{-1}$ cross-section

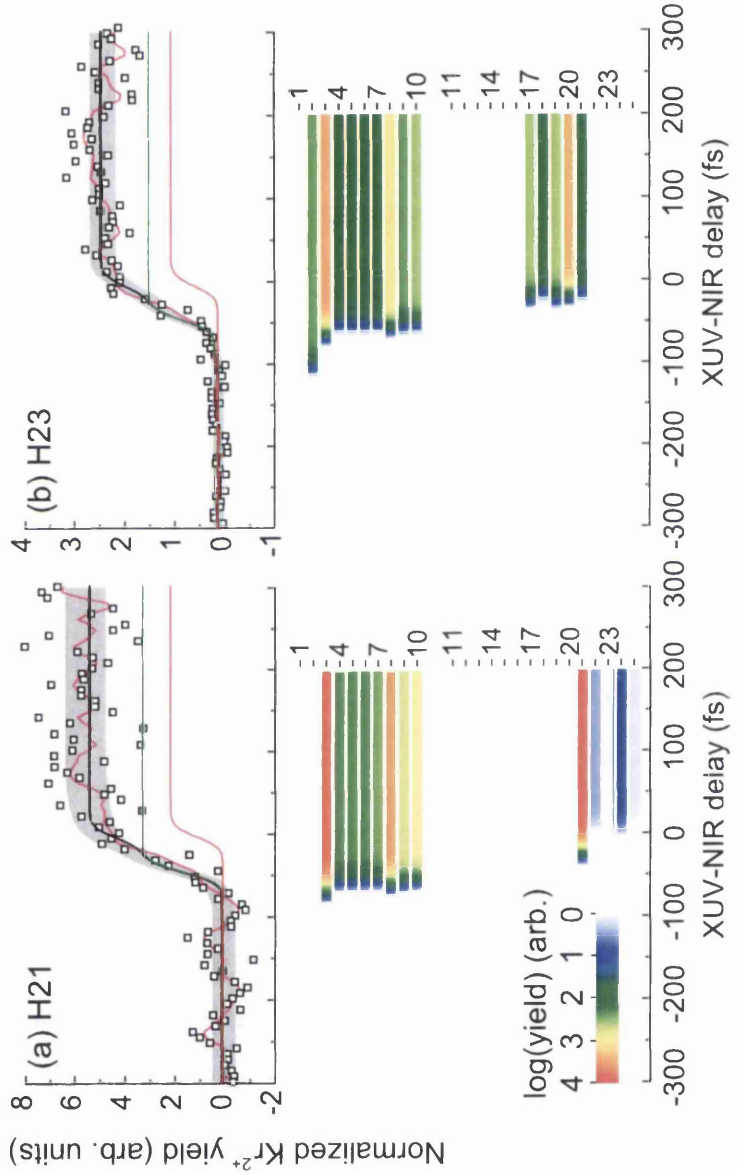
(a) H21
(b) H23
Normalized Kr2+ yield (arb. units)
log(yield) (arb.)
XUV-NIR delay (fs)
XUV-NIR delay (fs)

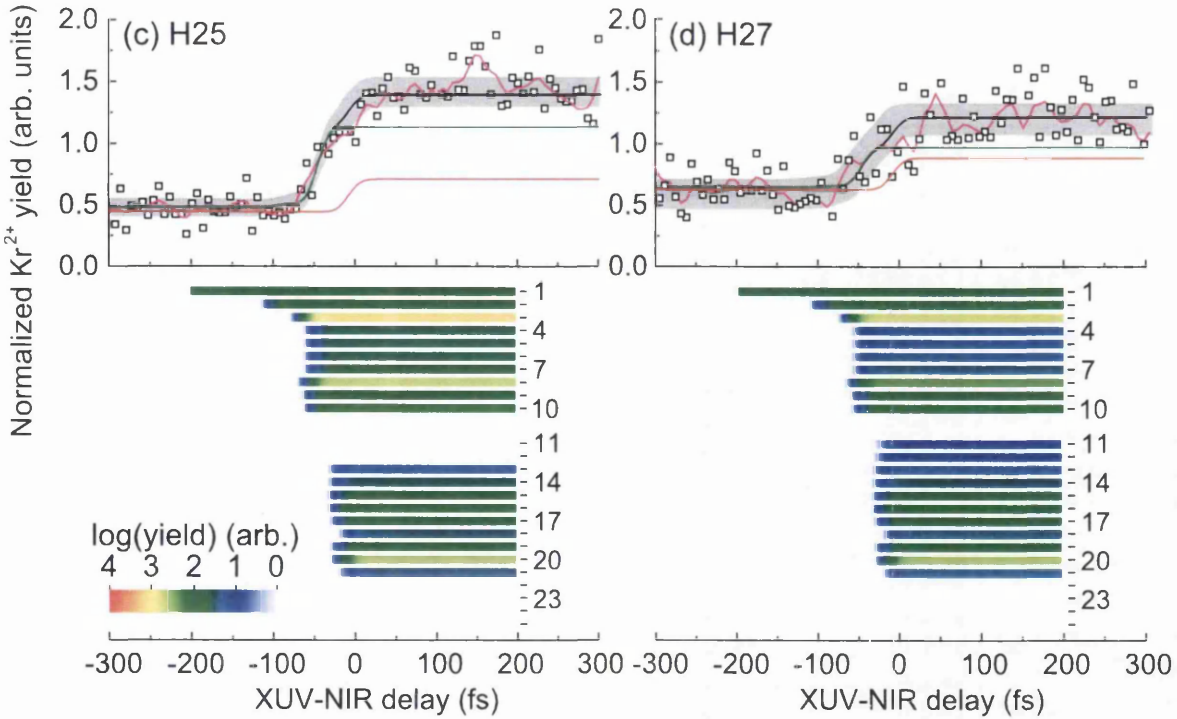

Figure 6.12: Kr^{2+} yield following XUV-pump and NIR-probe as a function of delay and harmonic order. Comparison of measured (squares) and predicted Kr^{2+} yields (black line) for (a) H21 (32.8 eV), (b) H23 (35.9 eV), (c) H25 (39.0 eV) and (d) H27 (42.1 eV) XUV pump with NIR probe at an intensity of 2×10^{13} W/cm^2. Each point is a 2500-shot average, recorded at a laser repetition rate of 1 kHz. A 4-point FWHM Gaussian weighted average is applied to the data (solid magenta) to highlight the underlying variation. The predicted total Kr^{2+} yield (black) is comprised of the 4*s* (red) and 4*p* (green) satellite contributions, and the grey shading represents the uncertainty associated with varying σ_{4s}, σ_{4p} and the XUV duration. For H21–H27, XUV pulse durations of 24, 26, 26 and 28 $\pm$ 2 fs respectively produce the best fit. Below each graph (a)–(d), the bar graphs show the predicted Kr^{2+} tunnel ionization yield as a function of XUV-NIR pulse delay for each of the satellite states considered, with the logarithmic colour scale indicating the yield, and the labels on the vertical axis corresponding to the state numbers as listed in Table 6.1.

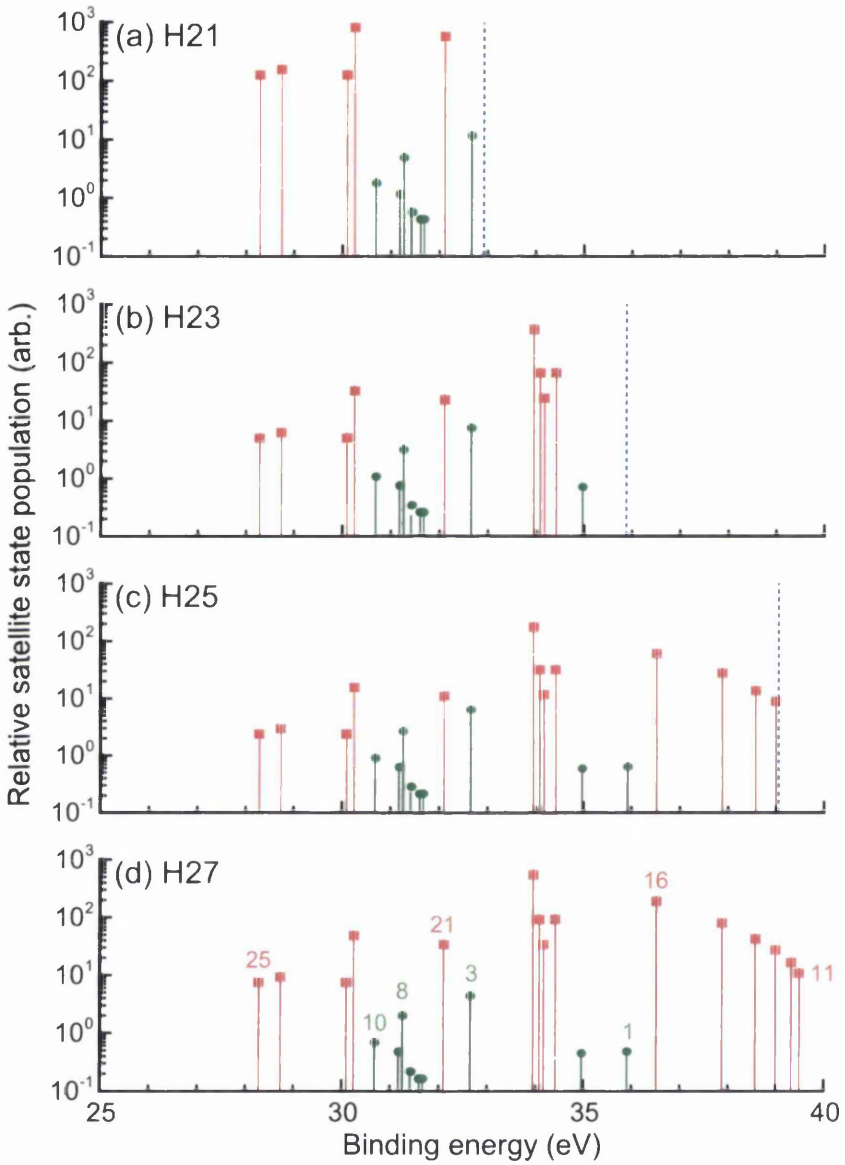

Figure 6.13: Relative populations of satellite states predicted by XUV-NIR modelling following fitting routine. For harmonic orders (a) H21 to (d) H27, the populations of the satellite states identified in Table 6.1 are presented as a function of binding energy. These states are derived from [99] and the populations are predicted by the photoexcitation cross-sections in Figure 6.11 which produces the theoretical yield curve shown in Figure 6.12 following tunnel ionization by the NIR pulse as predicted by [3]. The vertical dashed line represents the photon energy above which excitation is assumed to be energetically forbidden.

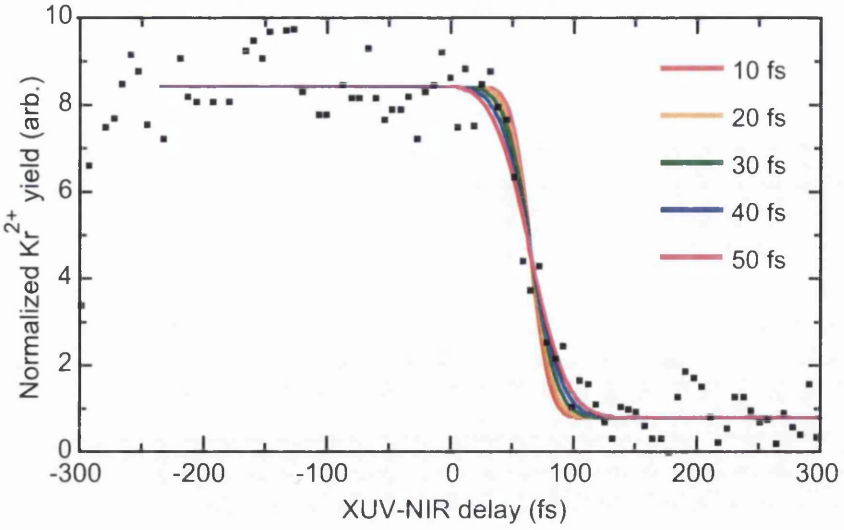

Figure 6.14: Yield of Kr^{2+} (filled squares) as a function of XUV-NIR pump-probe delay (lines) for H23 (35.7 eV). An XUV pulse with a Gaussian temporal profile of ~45 fs gives the best fit to the data.

although a minimum is predicted. The separation between the $4s^{-1}$ and satellite states ranges from 0 to 13 eV hence DSU, CSU and the CI are all possible however CSU is expected to dominate. CSU is the result of multi-electron interactions and is unlikely to be well approximated by the main line.

An interesting by-product of the measurement presented in Figure 6.12 is the first observation of single-photon double-ionization (SPDI) at threshold using a harmonic source, shown in Figure 6.12(b). A single H25 or H27 photon can directly initiate a double $4p$ subshell vacancy, as apparent from Figure 6.11(a). As presented in Figure 6.13, for H21 and H23 the Kr^{2+} yield is zero when the NIR pulse precedes the XUV pulse, however for H25 and H27, there is a clear Kr^{2+} offset that exhibits no time dependence. The XUV intensity is not sufficient to permit two-photon effects, therefore the remaining route is SPDI. This process has an extremely small cross-section, and previous measurements have required a number density orders of magnitude higher and integration times of

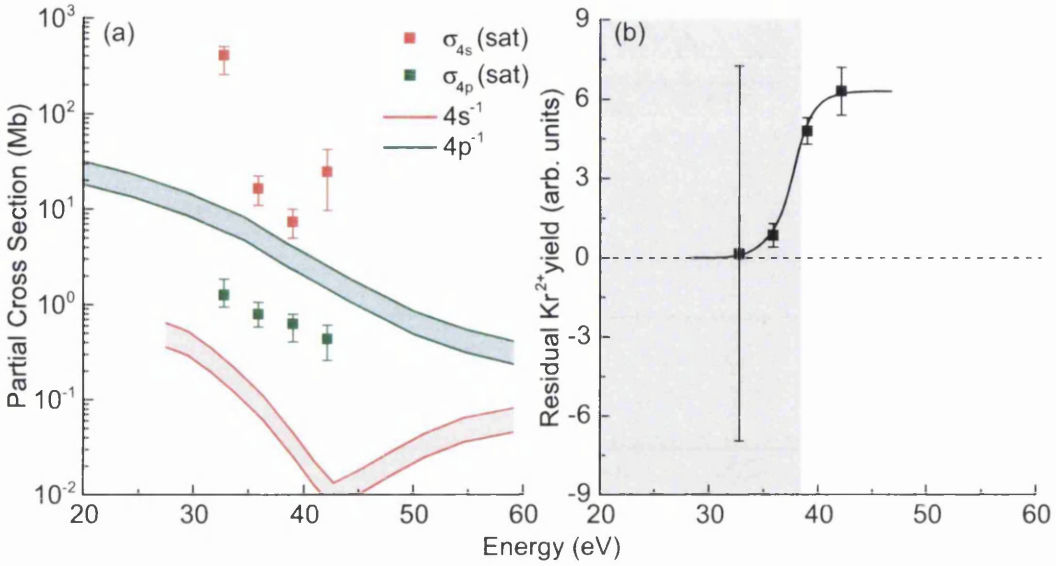

Figure 6.15: (a) Relative photoexcitation cross-sections recovered from time-energy domain XUV-NIR pump-probe initiating photoionization, shake-up and strong-field ionization compared to the $4s^{-1}$ and $4p^{-1}$ photoionization cross sections. The uncertainties are estimated by varying the trial $4s$ and $4p$ photoexcitation cross sections until an appreciable change in the regression fit to the experimental Kr^{2+} yield is found. (b) The non-time-correlated residual Kr^{2+} yield from Figure 6.12 is presented as a function of harmonic order, indicating the onset of direct double ionization for H25 and H27. The shaded region indicates that direct double ionization is energetically unfavorable and the error bars indicates 2 s.d. where the XUV and NIR pulses are well separated in time.

minutes. Contrast this with of the order 10^5 XUV photons per 30 femtosecond shot, repeated for 2500 shots in the present work.

6.5 Conclusion

XUV-NIR cross-correlation measurements reveal a step in the Kr^{2+} ion yield as a function of pump-probe delay. The measured yield is significantly higher when the XUV precedes the NIR, corresponding to the population and subsequent tunnel ionization of satellite states. Single-photon double ionization is also observed as an increase in signal on the lower side of the step for harmonics above the double ionization threshold (H25 and H27). Partial XUV photoionization

cross-sections have been extracted from the data by fitting a model based on nonadiabatic tunnelling theory [3] of satellite states, with relative populations based on photoelectron measurements [99].

Whilst the modelling has reproduced some of the qualitative features of the $4s$ and $4p$ partial photoionization cross-sections (Figure 6.15), future investigations may require the inclusion of processes which are not currently considered, which may account for the quantitative differences. For example, the modelling assumes two-colour double ionization is dominated by sequential processes, and does not include sideband formation [108, 109]. The satellites are assumed to be populated instantaneously by the XUV pulse, whether this is from the $4p$ or $4s$ level. However, as recently discussed in [114], recent experimental results suggest a time delay exists between photoelectron emission from the p and s shells in helium and neon, which the author attributes to elastic scattering and many-electron correlation. Additionally, there is assumed to be zero population in satellite states with energy greater than the XUV photon, which may not be true if the atomic energy levels were significantly shifted in the presence of the NIR field [110].

Chapter 7

Beam-transport diffraction in NIR FCP experiments

In typical few-cycle pulse (FCP) beamlines, material dispersion must be minimised in order to preserve the pulse duration. Air propagation can cause measurable temporal broadening, and few-mm thick optics can broaden the initial few-cycle pulses to tens of fs. In order to control the peak intensity and phase-matching conditions at the focus, hard-edged apertures are therefore often utilised since they introduce no additional material dispersion to the transmitted FCP. As a consequence, however, additional diffraction effects are introduced to the spatial beam profile and the resulting focus.

In this chapter, the methods described in Chapter 4 are applied to a model FCP beamline. The Huygens-Fresnel diffraction integral is used to quantify the distribution of spatial intensity and the shape of the wavefront through the focal volume as the beam propagates and is truncated by finite-diameter optics. Reflection from a spherical annular mirror for a range of annulus and aperture sizes are simulated. Finally, predictions are made of the changes to intensity and

focal position as the aperture is reduced. The model's usefulness as a tool for optimisation of an experimental beamline is therefore highlighted.

7.1 Review of typical FCP beamlines

Generation of a FCP requires the spectrum of the input pulse from a Ti:S laser (Chapter 2) to be broadened to a few hundred nm bandwidth, which is typically achieved by self-phase modulation (SPM) in a gas-filled hollow fibre as described in Section 2.1.8. In an optimally coupled fibre, this imposes a Bessel EH_{11} spatial profile on the divergent beam at the exit of the fibre. The original spatial profile of the laser before the hollow fibre does not propagate. The propagation of the beam profile from the exit of the fibre through diffracting optics can differ significantly from a Gaussian, as discussed in Chapter 4, as modelled by de Nicola [115] for a pure Bessel input beam, and as studied by Nisoli *et al.* [57] with implications to high-harmonic generation (HHG).

State-of-the-art FCP, attosecond and single-harmonic experiments employ minimally- or non-dispersive duration-preserving techniques to vary the intensity of subfemtosecond NIR pulses, separate XUV pulses from the NIR drive pulses in HHG, improve phase matching in HHG and precisely manipulate XUV and NIR pulses spatially and temporally [56, 57, 104, 105, 107–112, 114, 116–118]. Novel solutions include multilayer mirrors, toroidal mirrors, piezoelectrically-manipulated segmented mirrors and composite filters. The latter being a transmission optic, it must be comprised of μm-thickness material in order to ensure minimal dispersion of the NIR, and minimise material absorption of the XUV. Each hard-edge encountered by the NIR beam will result in diffraction, which becomes significant when the optics substantially encroach on the central, highest-intensity part of the beam profile. With the segmented optics previously described, the intensity

profile may be axisymmetrically modified from the centre outwards, as well as from the outer edges inwards using e.g. apertures.

In many pump-probe NIR-XUV experiments, such as the experiment described in Chapter 6, the NIR probe beam is often separated prior to the HHG stage, this however results in a lower intensity pump beam for XUV generation. In 2010, Fieß *et al.* [111] have demonstrated an experimental setup in which the XUV and NIR are successfully separated following HHG. Figure 7.1 is a diagram of the beamline. NIR enters into the first chamber, where it is focused into a gas jet, resulting in HHG. The divergence angle of the harmonics is smaller than that of the drive NIR radiation, enabling them to be spatially separated at the first perforated mirror (PM1). The NIR-only part of the beam is reflected, and the NIR+harmonic beam passes through the hole at the centre of the mirror. Filters reduce the NIR intensity in the harmonic beam, and the multilayer mirror (ML) selectively reflects an XUV harmonic. The intensity of the NIR is controlled using apertures A1 and A2. The beams are then recombined at a second perforated mirror (PM2) before being used in a photoelectron streaking experiment.

In 2011, Magerl *et al.* [116] used the experimental setup illustrated in Figure 7.2. A segmented filter is used to separate the XUV and NIR from a collinear beam, ensuring the separated radiation falls correctly onto the corresponding sections of a coaxial segmented mirror, consisting of a central ~5 mm diameter XUV multilayer mirror and a NIR-reflecting annulus. The filter allows 92% transmission of NIR through a nitrocellulose annulus which completely blocks XUV. The central part of the filter consists of zirconium, which allows transmission of a large fraction of the XUV (~30–50%) whilst reducing the NIR transmission by several orders. The segmented mirror is piezoelectrically manipulated to introduce an XUV-NIR pump-probe delay.

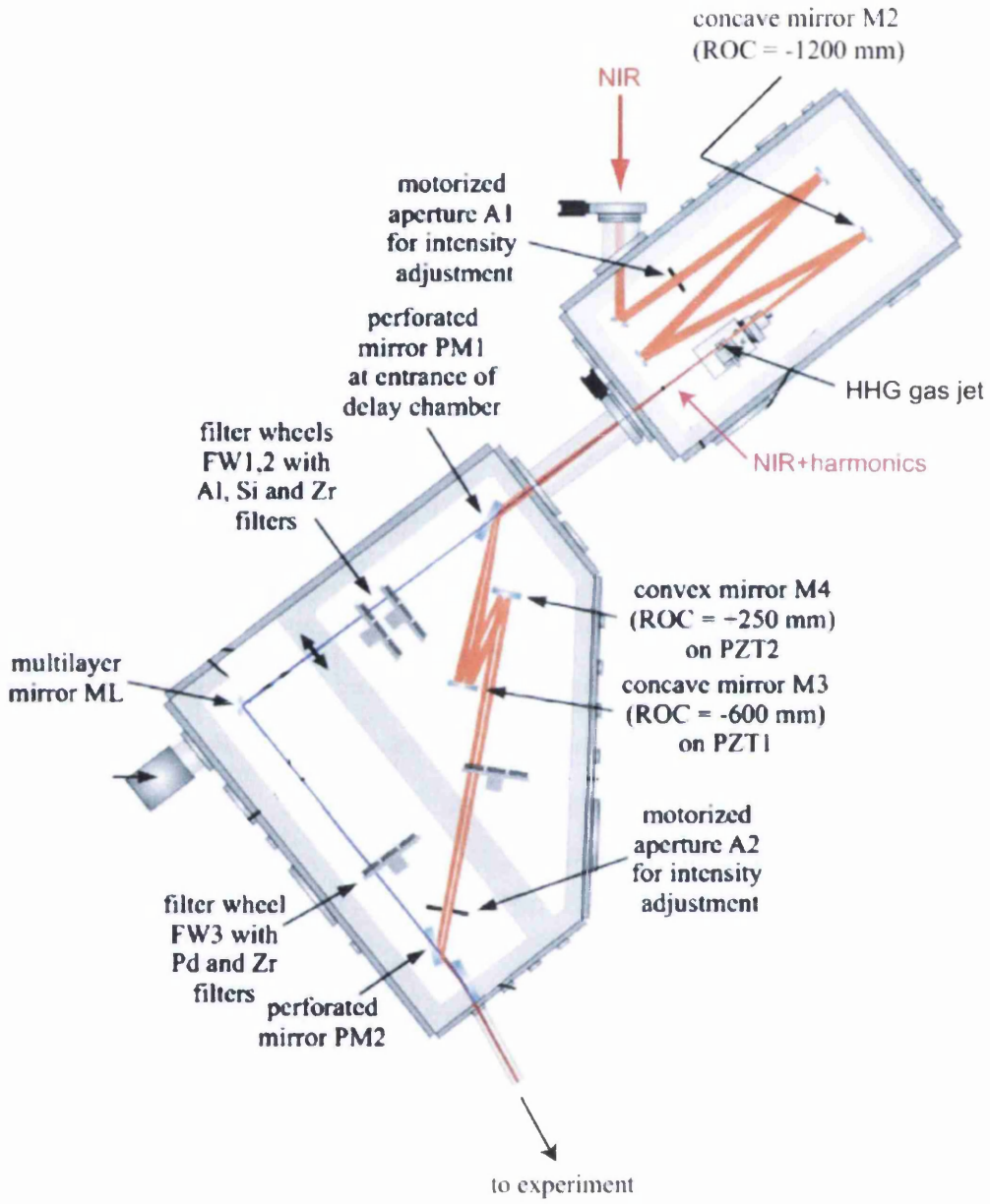

Figure 7.1: Section of the AS-2 attosecond beamline at the MPQ-LMU Joint Laboratory for Attosecond Physics. The first chamber is responsible for HHG, and the second chamber for introducing a delay between the XUV and NIR pulses. The XUV and NIR are separated and recombined using perforated/annular optics, with the NIR intensity varied using apertures, which are used in a photoelectron streaking experiment. Adapted from [111].

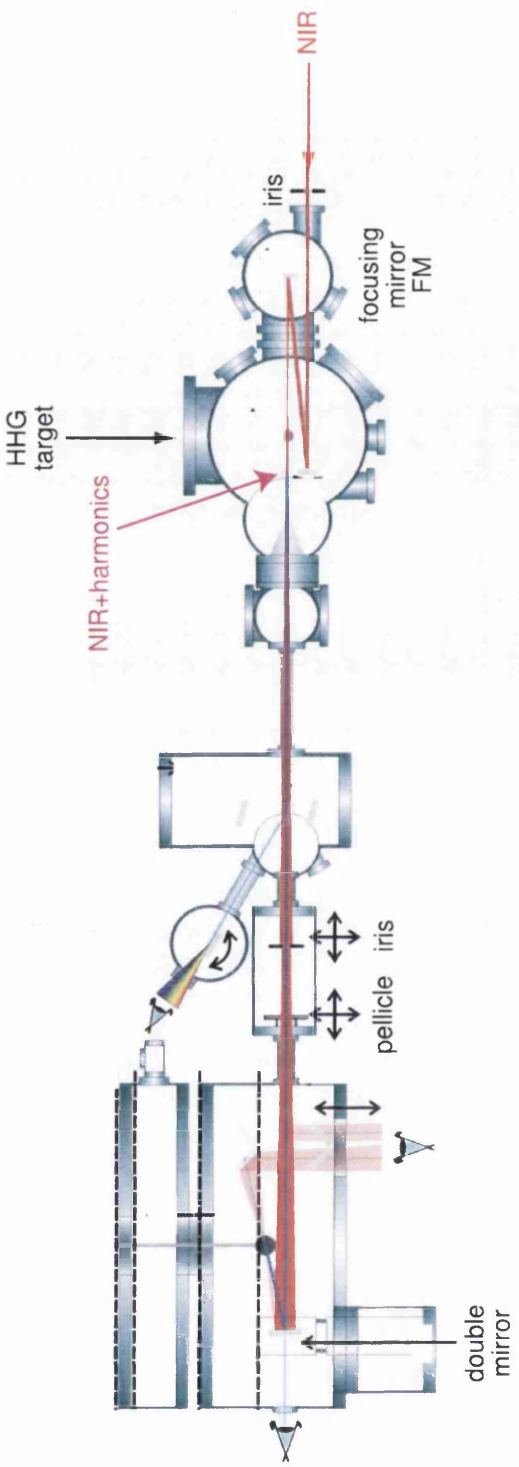

Figure 7.2: AS-3 attosecond beamline at the MPQ-LMU Joint Laboratory for Attosecond Physics. The pellicle (labelled) is a segmented filter, consisting of a nitrocellulose annulus allowing only NIR transmission, and a central section of Zr allowing XUV transmission whilst dramatically reducing the NIR transmitted. Adapted from [116].

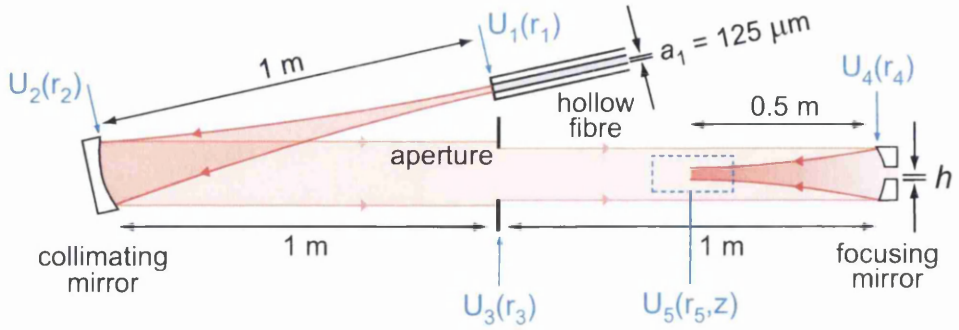

Figure 7.3: Schematic of the optical system considered: a Bessel EH_{11} spatial mode propagates from the input plane at the exit of the hollow fibre (radius a_1 = 125 μm) via a spherical collimating mirror (radius a_2 = 12.7 mm), through an intensity-controlling aperture of variable radius a_3 and focused into the interaction region by a spherical mirror (radius a_4 = 12.7 mm). The annulus is modified by increasing the radius h of the central hole from 0 to 2 mm. The electric field distribution $U_1(r_1)$ is determined by the EH_{11} fibre mode, and is given by Equation (4.6). $U_2(r_2), U_3(r_3), U_4(r_4)$ and $U_5(r_5, z)$ are solutions of the Huygens-Fresnel equation (7.1) after propagation using the matrices described in Equation (7.2), and are plotted in Figure 7.4.

7.2 Model beamline

The beamline in Figure 7.3 is inspired by those described in Section 7.1, and incorporates the salient elements: a hollow-fibre for FCP generation, collimating mirror, intensity-controlling aperture and a perforated/annular focusing mirror. While it does not have the complexity of beamlines AS-2 (Figure 7.1) and AS-3 (Figure 7.2), it is at least illustrative of the optical effects encountered.

On the exit of the fibre, the spatial profile of the pulse electric field is described by an EH_{11} Bessel, the reasons for which are explained in Section 2.1.8. The intensity profile at the hollow fibre exit is shown in Figure 7.4. Following propagation of around 1 m, the fibre output is recollimated on reflection from a spherical mirror, again introducing diffraction from the mirror edge. Temporal compression and beam transport into a vacuum chamber allows the diffraction

from the fibre edge and recollimating mirror to dramatically alter the beam profile.

To facilitate the generation of an XUV pump and NIR femtosecond probe with variable delay, some form of material or spatial beamsplitting and filtering is required. It is assumed at this point that the NIR pulse is split with a thin glass beamsplitter, with one beam reflection-focused into a gas-jet, and the resulting XUV separated from the NIR by metal filters then reflection-focused into the interaction region of a spectrometer without encountering any material.

The Huygens-Fresnel diffraction equation is described in Section 4.1, and is employed to numerically model the beam propagation through the beamline illustrated in Figure 7.3. The case of a spherical mirror followed by an identical treatment for an annular spherical mirror are modelled. It should be noted that only the spatial characteristics of the diffraction process are considered, taking no account for the broadband nature of the temporal pulse or nonlinear processes in the laser focus.

Starting from the generalized form of the Huygens-Fresnel equation for cylindrical coordinates [46, 86, 119] and following the derivation given in Chapter 4, the electric field at the output plane is given by

$$U_2(r_2, z) = -\frac{2\pi i}{\lambda B} \exp(ik(Z' + \frac{Dr_2^2}{2B})) \int_0^a U_1(r_1, z = 0) \exp(Gr_1^2) J_0(Hr_1) r_1 dr_1 \tag{7.1}$$

where $G = ikA/2B$, $H = kr_2/B$, z is the axial coordinate, λ is the wavelength, $k = \frac{2\pi}{\lambda}$ is the wavenumber, and A, B, D are elements of the paraxial system matrix $M = \left(\begin{smallmatrix} A & B \\ C & D \end{smallmatrix}\right)$ describing the optical system between the two planes. The input and output planes are separated by a total axial distance Z', and co-ordinates (r_1, θ) and (r_2, ϕ) define points on the input and output planes respectively.

The ray-tracing matrices describing each section of the beamline between limiting apertures are

$$M_{1\to2} = L_1T_1 = \begin{pmatrix} 1 & d_1 \\ -\frac{1}{f_1} & 1-\frac{d_1}{f_1} \end{pmatrix} \qquad M_{2\to3} = T_2 = \begin{pmatrix} 1 & d_2 \\ 0 & 1 \end{pmatrix}$$
$$M_{3\to4} = T_3 = \begin{pmatrix} 1 & d_3 \\ 0 & 1 \end{pmatrix} \qquad M_{4\to5} = T_4L_2 = \begin{pmatrix} 1-\frac{z}{f_2} & z \\ -\frac{1}{f_2} & 1 \end{pmatrix} \tag{7.2}$$

where $M_{1\to2}$ is the matrix describing the section between the hollow fibre plane, $U_1(r_1)$ on Figure 7.3, and the collimating mirror plane, $U_2(r_2)$; $M_{2\to3}$ the matrix between the collimating mirror and the intensity-controlling aperture plane, $U_3(r_3)$; $M_{3\to4}$ between the aperture plane and the focusing mirror plane $U_4(r_4)$; and $M_{4\to5}$ between the focusing mirror and the plane $U_5(r_5, z)$ within the focal region at a chosen axial position, z. f_1 and f_2 are the focal lengths of the collimating mirror and focusing mirror respectively. In the model described in this chapter, $d_1, d_2, d_3 = 1$ m, $f_1 = 1$ m, and $f_2 = 0.5$ m.

The input plane is defined as the output end of the fibre and the complex electric field distribution at subsequent optics evaluated numerically. Propagation, diffraction and reflection focusing are treated in this representative optical system, however the same treatment can be applied to more complex optical systems provided they are axisymmetric. Clearly the spatial step size defines the computation time required to solve the diffraction integral. Typically, it was sufficient to use a step-size corresponding to 0.1% of the aperture radius. Furthermore, before carrying out the calculations presented here, a convergence test was performed whereby the step size was systematically reduced until a less than 0.01% variation was found. All presented calculations were carried out well within the convergence range.

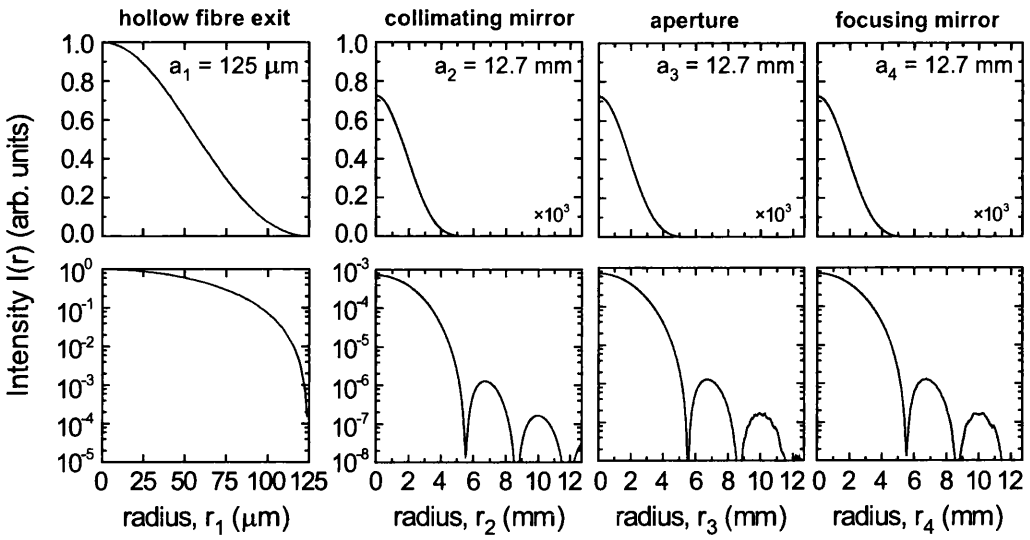

Figure 7.4: Solutions of the Huygens-Fresnel equation at the hollow fibre exit, collimating mirror, aperture and focusing mirror in the optical system illustrated in Figure 7.3, solved for $0 \leq r \leq a$ at planes U_2 to U_5. U_1 is the electric field (EH_{11} mode) at the hollow fibre exit, normalized to 1. $I_i(r) = |U_i^2(r)|$ at each plane i, and are relative to the peak intensity $I_1(0)$ at the fibre exit.

The optical system illustrated in Figure 7.3 is now considered. The complex electric field at the collimating mirror is found by substituting Equation (4.6) for U_1 in Equation (7.1). This is then integrated numerically over the finite aperture of the fibre end. The imaginary component of the electric field contains phase information allowing the wavefront shape to be propagated. This process is then repeated for the collimating mirror which is defined to have a radius of $a_2 = 12.7$ mm, also defining the integration limits of Equation (7.1) at this point, the fully-open intensity-controlling aperture with $a_3 = 12.7$ mm and focusing mirror with $a_4 = 12.7$ mm. The limits a_2, a_3 and a_4 are chosen to represent the hard edges imposed by 25.4 mm (1") diameter beamline optics typically used in experimental beamlines.

Figure 7.4 shows the intensity distribution at the hollow fibre $I_1(r_1)$, and the intensity solutions to the Huygens-Fresnel integral at the collimating mir-

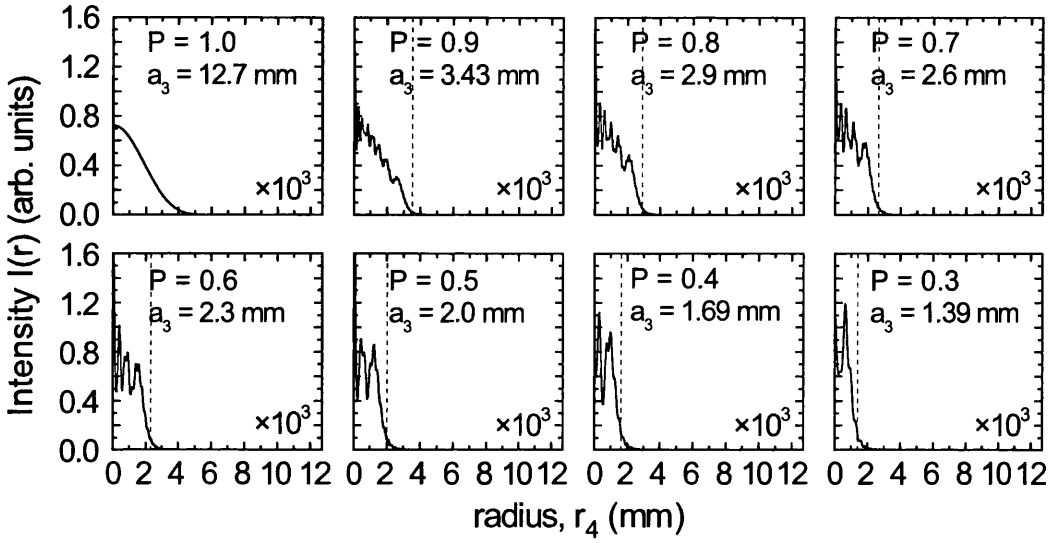

Figure 7.5: Radial intensity distribution at the focusing mirror ($I_4(r_4) = |U_4^2(r_4)|$, where $U_4(r_4)$ is evaluated at the position indicated in Figure 7.3) after propagating 1 m from the intensity-controlling aperture in the optical system illustrated in Figure 7.3. The aperture (radius a_3) truncates the beam and reduces the relative power, P, transmitted. The dotted line shows the position of the aperture edge in relation to the transmitted intensity profile.

ror, $I_2(r_2)$; at the aperture, $I_3(r_3)$; and at the focusing mirror, $I_4(r_4)$, where $I_i(r) = |U_i^2(r)|$, and $U_i(r)$ are labelled in Figure 7.3. Defining the beam radius as the Airy disk radius, i.e. the position of the first intensity minimum, the 125 μm disk at the fibre exit expands to ~5.5 mm at the collimating mirror after 1 m propagation. The diffracted intensity profile is truncated just after the third maximum (at $r_3 \sim 10$ mm), with the second maximum being three orders below the peak intensity (first maximum). The subsequent aperture and optic (12.7 mm radius) have very little effect on the overall intensity profile, with subtle diffraction effects beginning to change the shape of the second maximum.

Figure 7.5 shows the effect of reducing the radius of the intensity-controlling aperture. Since the Airy disk contains 99.2% of the beam power, changes in the aperture size have little effect on the power transmitted for radii between 12.7 mm and 5.5 mm, though the low-intensity features present between these

radii will be truncated and distorted. However, as the hard edge encroaches on the Airy disk, small changes in the transmitted power are immediately accompanied by dramatic changes in the transmitted beam profile. For an aperture radius, $a_3 = 2.9$ mm, corresponding to a relative transmitted power, P = 0.8 compared to $a_3 = 12.7$ mm, the underlying Bessel profile is barely recognisable, dominated by multiple intensity peaks due to diffraction at the intensity-controlling aperture ($U_3(r_3)$ in Figure 7.3).

7.3 Distribution of focused intensity and phase

Figures 7.6 and 7.7 show the spatial intensity distribution and wavefront shape as a function of the optical power transmitted through the aperture after being reflection-focused from a spherical focusing mirror, and an annular spherical focusing mirror respectively. The maximum power corresponds to the aperture being the same radius as the collimating mirror (Figure 7.3).

At the maximum transmitted power (P = 1), where there is negligible diffraction, the spatial distribution of intensity for the non-annular spherical mirror is a good approximation to a Gaussian focus centred at $z = 0.5$ m. As the Airy disk is increasingly truncated by closing the aperture down, diffraction structure becomes immediately apparent at the focus, the contrast of which increases with decreasing aperture radius, as expected from the intensity distributions at the focusing mirror shown in Figure 7.5. Comparing the distribution before and after the focus, it is clear that the distribution of intensity quickly becomes asymmetric due to the truncation. This is also apparent along the axial direction as the frequency of the oscillatory structure increases. Furthermore, as the power drops below P = 0.6 there is a noticeable shift in the maximum intensity position.

The annular mirror has an outer radius of $a_4 = 12.7$ mm and a hole of radius $h = 1$ mm. The integration limits of Equation (7.1) are now h and a_4. As

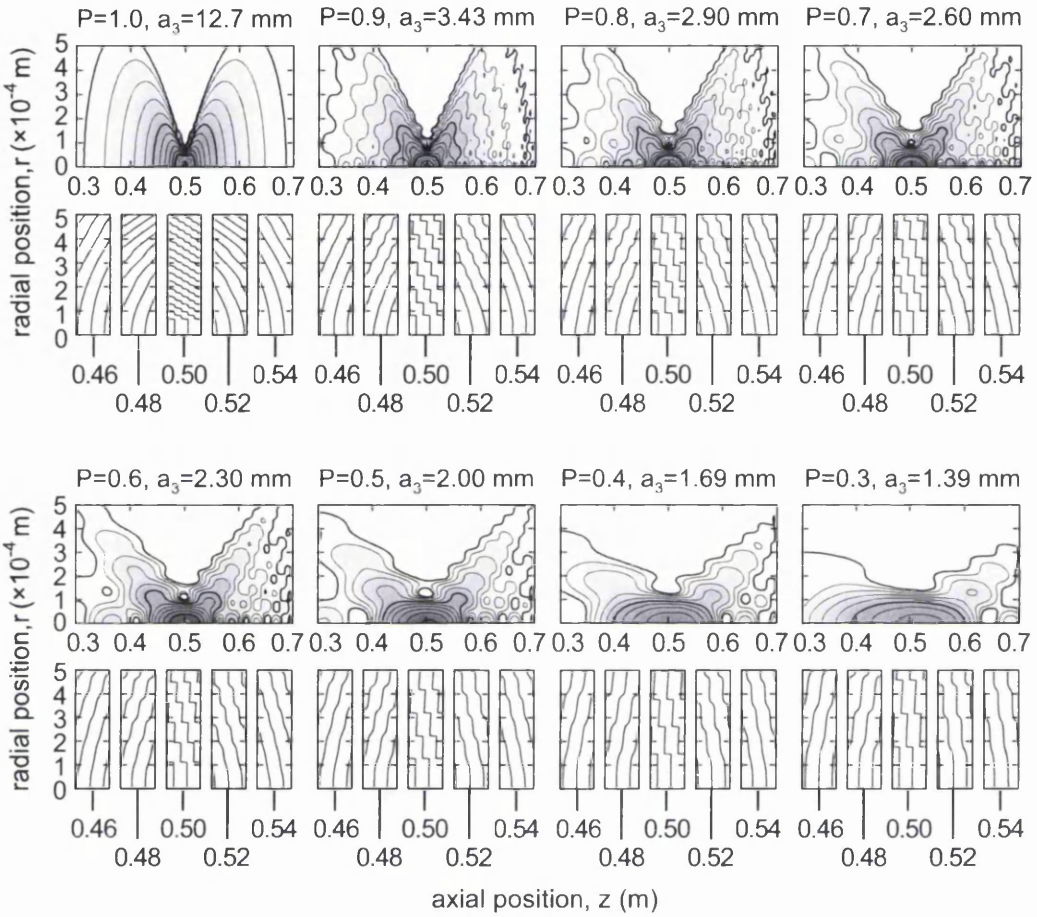

Figure 7.6: Spatial intensity distribution and wavefront shape at the focus of the optical system in Figure 7.3 as a function of relative power, P transmitted by the aperture. Here the focusing mirror is spherical without a hole. The axial position, z is measured with respect to the focusing mirror. Figures 7.4 and 7.5 show the intensity distribution at the focusing mirror at $z = 0$. The lowest relative intensity is 10^{-3} and highest is 10^{0}; each thick contour represents an order of magnitude change, each fine contour is an intensity change of $10^{0.2}$. The power P = 1.0 corresponds to the aperture radius being equal to the collimating mirror radius. Below each intensity plot the wavefront shapes are presented in 2 μm slices; the wavefronts are separated by 2π.

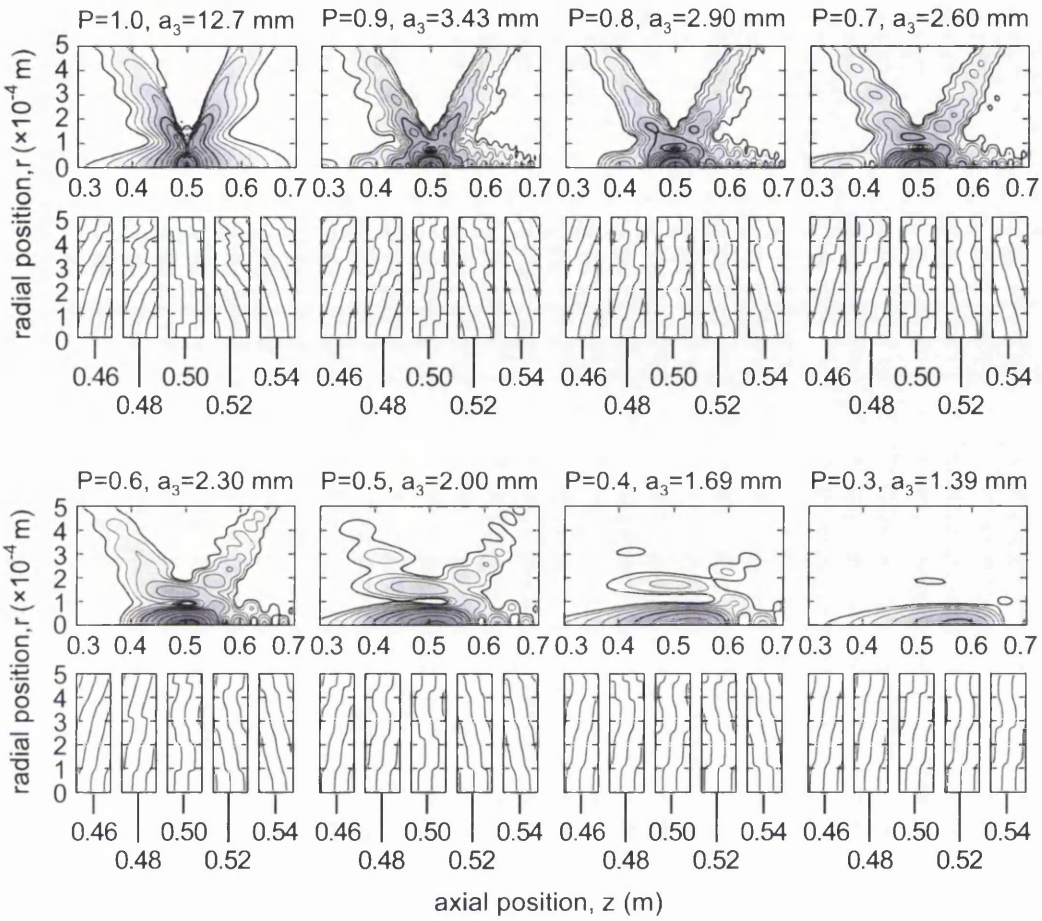

Figure 7.7: Spatial intensity distribution and wavefront shape at the focus of the optical system in Figure 7.3 as a function of relative power, P transmitted by the aperture. Here the spherical focusing mirror has a circular hole at the centre of radius $h = 1$ mm. The axial position, z is measured with respect to the focusing mirror. Figures 7.4 and 7.5 show the intensity distribution at the focusing mirror at $z = 0$. The lowest relative intensity is 10^{-3} and highest is 10^{0}; each thick contour represents an order of magnitude change, each fine contour is an intensity change of $10^{0.2}$. The power P = 1.0 corresponds to the aperture radius being equal to the collimating mirror radius. Below each intensity plot the wavefront shapes are presented in 2 μm slices; the wavefronts are separated by 2π.

is apparent from Figures 7.4, 7.5 and 7.6, propagation from the fibre to the focusing mirror already introduces significant diffraction structure in the beam. A hole in the annular mirror introduces an additional hard edge and removes the highest-intensity section of the beam from the centre to the radius h of the Airy disk, causing additional diffraction effects as well as a reduction in the power transmitted to the focus. The maximum power in Figure 7.7 corresponds to the aperture being the same diameter as the collimating mirror and the relative power transmitted by the aperture agrees with that shown in Figure 7.6. As discussed earlier, this case is comparable to attosecond and XUV-NIR beamlines. Even at the highest power, there are obvious differences between the annular (Figure 7.7) and non-annular spherical mirror (Figure 7.6): cylindrically symmetric intensity lobes are generated on-axis and following the outer edge of the focal cone. As the power is decreased, the structure of the focal volume becomes more pronounced, with the 'V'-shaped distribution dominating. Again, a significant shifting of the peak spatial intensity is observed, to a greater extent than the non-annular case.

Figures 7.6 and 7.7 show the effect of the aperture and the annular mirror on the wavefront shape. In the case of a spherical mirror without a hole, the near-Gaussian profile at $P = 1.0$ (aperture fully open) has the strongest and smoothest wavefront curvature. At $z = 0.5$m, it also has the smallest flat-phase region, extending to $r = 60$ μm, corresponding to an intensity variation of an order of magnitude from the peak. After this point, phase jumps are seen in the plot, but this is less significant since the intensity drops off sharply, and is over three orders lower at $r = 100$ μm. As the aperture radius and the power transmitted decreases, the intensity at the focus becomes shallower, and the regions of flat phase at all selected z extend in r. For $P = 0.7$, the phase is flat to $r = 100$ μm, over two orders of magnitude from the peak. At $P = 0.3$ the peak intensity is reduced by just over an order, but the elongation of the focus results in a region

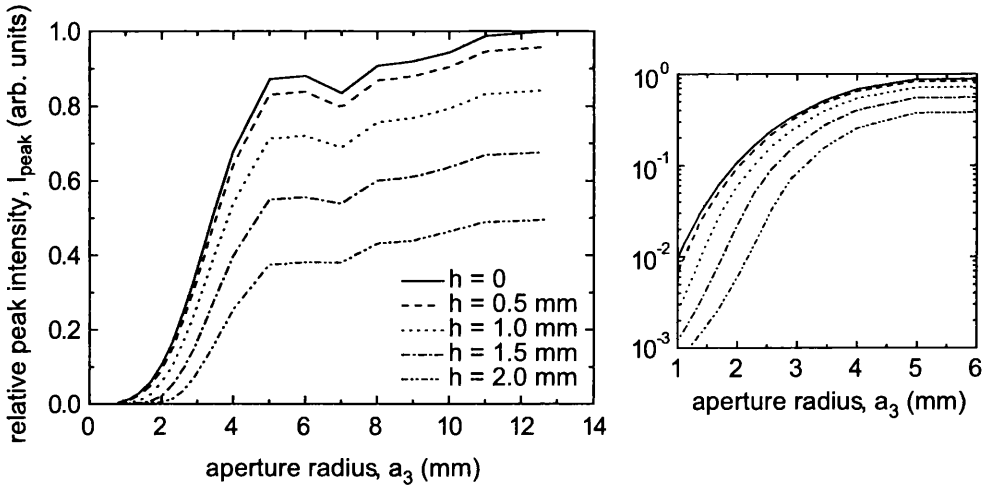

Figure 7.8: Peak spatial intensity in the focal region as function of aperture radius a_3, relative to the peak intensity with the aperture fully open. The minimum in intensity at $a_3 = 7$ mm is due to a splitting of the focus into two peaks, which are symmetric about the geometric focus (average $\Delta f = 0$).

of relatively flat phase over a much larger r and z range, extending to $r \simeq 180$ μm between $z = 0.46$–0.52 m. In the context of HHG, this increases the interaction length over which high harmonics are in phase. Such conditions are qualitatively similar to those experimentally found to maximize the efficiency of HHG by phase matching [57, 120, 121].

The effect of removing a section of the spherical mirror of diameter $h = 1$ mm in the annular mirror case is clearly evident from Figure 7.7 in terms of intensity. In the non-annular case, the wavefront shapes are generally smooth, or incorporate discrete 2π phase jumps. In the annular case shown in the wavefront plots in Figure 7.7, the wavefronts are significantly more complex in structure, following the significant radial and axial structure of the intensity profiles. However, the effect of the aperture is still to extend the flat phase region in r and z, albeit at a lower transmitted intensity due to the loss of the central part of the beam.

Figures 7.6 and 7.7 have been produced from full three-dimensional plots of the focal volume, which require significant computing time to produce at sufficient

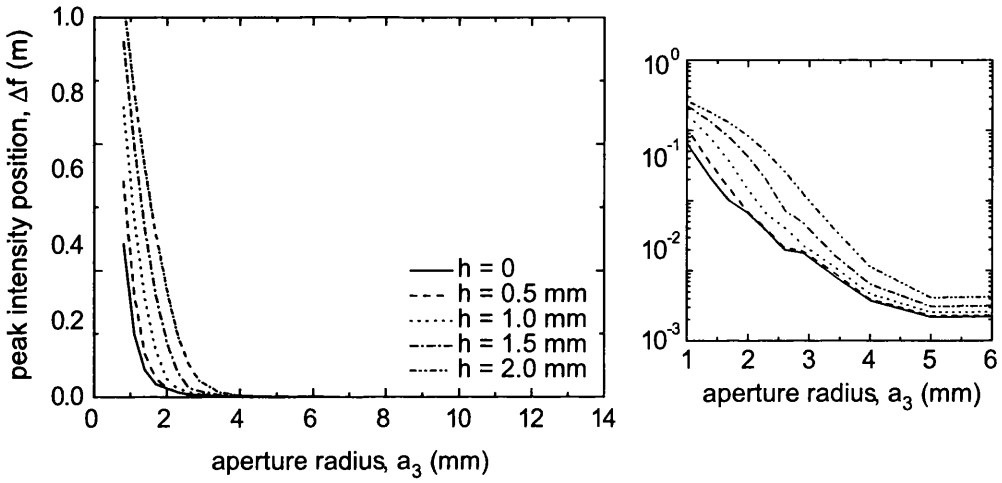

Figure 7.9: Peak intensity position in the focal region as function of aperture radius a_3, relative to the peak position with the aperture fully open ($\Delta f = 0$).

accuracy to be meaningful. However, as can be seen from the figures, despite additional diffraction structure and spreading of the highest-intensity part of the focus, the peak intensity remains on axis. By solving Equation (7.1) at r_2, r_3 and $r_4 = 0$ only, i.e. on axis, the peak intensity and focal shift can be quantified far more quickly and efficiently. Figure 7.8 and 7.9 has been produced in such a manner at representative aperture radii a_3, where the step size in aperture radius is varied with peak power. These plots can be produced in timescales of tens of seconds, meaning this calculation is practicable for quantifying or verifying focal parameters during an experiment.

Figure 7.8 demonstrates how the peak intensity varies as a function of aperture radius, a_3. The spatial intensity depends on the distribution of power through the aperture and the diffractive influence of all other elements in the system. As a result, the peak intensity is expected to be nonlinear with aperture radius.

The increase in aperture size has the largest effect on the peak intensity over the range $a_3 = 0$ to 5 mm. The gradient of the peak intensity increasing rapidly over the first 2 mm. Above $a_3 = 6$ mm, the gradient decreases substantially,

since the aperture is now larger than the Airy disk. The contribution to the intensity now comes from the second maximum in the radial intensity profile between $r \sim 6 - 8$ mm, as shown in Figure 7.4. The second maxima is π phase-shifted relative to the Airy disk, which results in some destructive interference, though the magnitude of the effect will be smeared due to diffraction effects which introduce their own phase modulations across the whole radial profile. Even so, the result is a local minimum in I_{peak} at $a_3 = 7$ mm, where the peak in fact splits into two, separated by a few mm. Between $a_3 = 8 - 11$ mm, the gradient actually increases slightly, where the third radial maximum contributes to I_{peak}.

The effect of an increasing-diameter hole at the centre of an annular mirror on the peak intensity as a function of a_3 is also shown in the figure, for $h = 0$ to 2 mm in 0.5 mm steps. The dominant effect is a drop in the overall intensity as expected, since sections of the Airy disk are being removed from the beam profile. There are also some more subtle effects. The gradient changes more slowly with increasing h over the range $a_3 = 0 - 3$ mm. For $h \geq 1.5$ mm, the lack of significant intensity is visible in the peak intensity plots. In the inset figure (plotted on a log scale), the gradient of $\log(I_{\text{peak}})$ has a point of inflection at $a_3 = h$. The minimum at $a_3 = 7$ mm is also less pronounced as h increases, possibly indicating that removing more of the central part of the Airy disk reduces the destructive interference between it and the second radial maxima over the focal region.

As apparent from Figures 7.6 and 7.7, as the aperture is closed, the maximum spatial intensity is observed to translate along the z-axis by a measurable amount, with clear implications particularly for position-sensitive measurements involving intensity variation. This focal shift is quantified in Figure 7.9 as a function of aperture radius and annular hole radius. For all hole radii, for an aperture radius above 4 mm, the focal shift is less than a millimetre. As the aperture is reduced below 4 mm, a dramatic shift of the focal position is predicted. With a hole radius

of 2 mm and aperture radius of 3 mm (corresponding to a relative intensity of ~0.1), a focal shift of 1 cm is predicted. Such a shift could easily move the useful intensity region of the focal volume outside the source region of a spectrometer.

The model beamline demonstrates several important features of beam propagation. Once the beam profile is defined by the hollow fibre and collimating mirror, hard-edged optics with a much larger diameter than the Airy disk have a minimal effect on the propagating beam. However, even a single intensity-controlling aperture can have a large effect, especially when combined with annular optics which remove central parts of the beam. In the experimental setups reviewed in Section 7.1, several intensity-controlling apertures, annular or segmented reflection optics and filters are common. As a result, the peak intensity variation with aperture radius may be strongly structured compared to the variation shown in Figure 7.8. Focal shift effects may become more pronounced, and for non-axisymmetric beamlines may result in focal shifting in more than one dimension, or the generation of spatially-resolvable multiple foci.

7.4 Conclusion

The numerical modelling of the focal volume, using established methods applied specifically to a typical FCP beamline, reveals significant changes to a focused beam when parameters are modified using typical non-dispersive methods, with clear implications to intensity- and spatially-resolved attosecond and few-cycle pulse experiments. The intensity structure in the focal region can become heavily structured and the peak intensity significantly offset from the geometric focus; these effects have been characterized for a range of conditions. Properly quantified, diffraction can be utilized advantageously to create regions of the focus where the intensity varies smoothly and phase variations are greatly reduced. Full three-dimensional focal volume modelling can be computationally intensive,

but the on-axis intensity distribution can be computed quickly, revealing shifts in the focal position which are not predicted when geometric behaviour is assumed to be dominant. The method relies on a proper characterization of the input beam profile, since the beam propagation and therefore focal volume are strongly dependent on this. The models can therefore be used to guide axisymmetric beamline design and construction, as well as optimisation of focal conditions in FCP beamlines, with application to attosecond pulse production techniques and experiments.

The simplified model gives representative results of the effects of beam propagation for a single wavelength. For sharper foci than those considered, the bandwidth of FCPs may become significant, necessitating modelling over all wavelengths corresponding to the spectrum of the pulse. The model could be expanded, again requiring an increase in computing time proportional to the resolution in wavelength required. If the spectral phase were included, the expansion to the modelling procedures described could yield both spatial and temporal variations across the focal region, enabling a better understanding of spatially-resolved time-dependent ionization experiments.

The assumption has been made in this chapter that diffraction effects are only significant in the NIR beamline. However, the purpose of including the annular mirror in the FCP beamline model is to allow for the copropagation of XUV and NIR pulses. XUV will also be affected by diffraction, albeit less so due to its shorter wavelength. If both the XUV and NIR foci develop the significant structure demonstrated in this chapter for NIR only, this has implications for optimising the spatial overlap between XUV and NIR pulses in pump-probe experiments. Modelling the propagation of XUV along an axisymmetric beamline can be performed simply using the current model. However, typical FCP beamlines involving HHG typically employ grazing-incidence optics such as toroidal

mirrors for XUV beam transport, leading to astigmatic foci. These can still be modelled within the paraxial approximation, but using more complex methods than are employed in this chapter, and resulting in a substantial increase in computing time due to the loss of radial symmetry [122].

Chapter 8

Conclusions and Future Work

8.1 Conclusions

The tunnel ionization of electrons from energy levels higher than the ground state (i.e. more tightly bound) is considered by modifying modern tunnelling theory. In the case of xenon exposed to shaped few-cycle NIR pulses, the direct tunnelling of both $5p$ *and* $5s$ electrons is included and the degeneracy of all states is allowed by introducing additional pathways.

The modified tunnelling models have been employed to numerically predict recollision-free multiple ionization of xenon as a function of laser intensity and pump-probe delay. The laser intensity is controlled by varying the position of the laser focus with respect to an apertured detector, and the 4:1 split pump-probe pulses cause a diversity of structured pulses as a function of the delay.

A deconvolution procedure is attempted, and the limitations of this method qualified in significant detail by the realistic modelling of the spatial propagation of the pulse through the beamline.

The full three-dimensional beamline model is then used in conjunction with the generated probabilities to recreate the signal-producing ion volume as seen

by the detector. Four tunnelling models were considered in total: ground-state only or multiple-state ionization, for the nondegenerate case and considering all degenerate energy levels respectively. There is a subtle difference between the ground-state only and multiple-state nondegenerate models, with neither model being a significantly better fit than the other overall. However, there are two noticeable changes in the output of the degenerate model. The first is a better fit to the experimental data than all other models. The second is the temporal asymmetry, predicted *only* by the multiple-state degenerate model. This model is also the most complete description of the xenon electronic energy levels. Even though the effect of the temporal asymmetry is weaker in the model than in the experimental ion yields, the significance of its appearance in the model with the highest number of energy levels strengthens the evidence for an intensity- and time-dependent multielectron contribution to the overall ion yield.

In contrast to the approach used in the xenon studies, where the population of multiple energy levels by tunnelling is influenced by the pulse shape and varies continuously throughout the pulse duration, the krypton studies focus on the instantaneous population of several energy levels by single photon ionization. The relative populations in singly-charged krypton are therefore independent of the XUV pulse duration and shape, but highly dependent on the photon energy, and are described by extensive synchrotron studies. The time-dependence of subsequent tunnel ionization of the singly-charged krypton is time- and intensity-dependent, but the photon energy distribution of the NIR field does not change. Multiple tunnel ionization of $Kr^+ \rightarrow Kr^{2+}$ is therefore used as a probe of the single photon ionization pathways. A combination of XUV and NIR pulses are used in a pump-probe configuration. If the XUV precedes the NIR, photoionization of $Kr \rightarrow Kr^+$ occurs from the $4s$ or $4p$ valence states, with the excess photon energy resulting in excitation of electrons to satellite states. The weakly-bound

excited electrons are then easily tunnel-ionized by the NIR pulse, creating a significant population of Kr^{2+}. With the pulse order reversed, NIR tunnel-ionizes $Kr \rightarrow Kr^{+}$. For harmonics H21–H23, the XUV photon energy is insufficient to cause double ionization, therefore no significant yield in Kr^{2+} is detected. However, at the higher energies H25–H27, experimental observations of single-photon double ionization are observed.

The step in the ion yield as a function of pump-probe delay gives an estimate of the duration of the XUV pulse. Additionally, the height change in the step as a function of harmonic energy is modelled using satellite population predictions from synchrotron measurements, and the tunnel theory of Yudin and Ivanov described in Chapter 4. By modelling the tunnel ionization rate for multiple energy levels, an estimate of the relative populations in each level, and therefore a photoionization cross-section measurement were possible.

Lastly, the beamline modelling is revisited in the context of a typical few-cycle pulse beamline with XUV generation. The effects of hard-edged optics, including a variable diameter aperture for intensity control and annular optics have been considered. The purpose of the annular optic, with a section removed at its centre, is to allow the XUV pulse to pass through a mirror without being affected by material dispersion, and copropagate with a reflected NIR beam. Despite the significant structure introduced to the focus, the predictions give indications of how the focus might be optimised, with the aperture providing a method by which the highest intensity part of the focus may be elongated and wavefront phase flattened over a significantly larger volume than the unapertured beam. This has particular relevance to HHG or attosecond pulse generation, and spatially- and temporally-resolved experiments such as those discussed previously, where the overlap in both is critical.

8.2 Future Work

The time-dependent processes investigated in the thesis could be improved by a full dynamical picture of the ionization process, including the behaviour of the electrons on leaving the atom, and the effect of the laser field on their trajectory. Such a picture can be obtained using electron-ion coincidence measurements, such as COLTRIMS or velocity map imaging (VMI).

Shorter pulses, of two or three cycles are now achievable for NIR, and would result in a significant increase in the temporal resolution of multielectron ionization processes. This could be combined with a synchronised XUV pulse in a pump-probe configuration. The ability to selectively probe energy levels in the presence of a shaped NIR pulse would provide a measure of the populations in each state as a function of time. The implications of the results would assist in the further development of semiclassical tunnel theory.

A wealth of atomic studies are yet to be carried out. An interesting direction could be the multielectron tunnelling of alkali metals, as they may be cooled to millikelvin temperatures hence far higher momentum measurements are possible, which may further elucidate multielectron ionization dynamics.

The study of ionization is not limited to atoms, but the better understanding of multielectron atomic processes makes an essential contribution to the understanding of processes in more complex systems such as atomic clusters and molecules.

Conferences

Talks

Science Day, Swansea University, U.K., June 2009

QuAMP International Conference on Quantum, Atomic, Molecular and Plasma Physics, University of Leeds, U.K., September 2009

Christmas Meeting of the High Power Laser Science Community, Rutherford Appleton Laboratory, Didcot, U.K., December 2009

Christmas Meeting of the High Power Laser Science Community, Rutherford Appleton Laboratory, Didcot, U.K., December 2010

Poster presentations

Workshop on Advances in Strong Field and Attosecond Physics, University College London, U.K., June 2010

Awards

Professor Dame Jean Thomas Postgraduate Image Award, Swansea University Research Forum (SURF) 'Research As Art' competition, June 2011

Publications

W. A. Bryan, F. Frassetto, C. A. Froud, I. C. E. Turcu, R. B. King, C. R. Calvert, G. R. A. J. Nemeth, P. Villoresi, L. Poletto, and E. Springate. Isolated high-harmonic XUV photon absorption and NIR strong-field tunnel ionization. *New J. Phys.*, 14:013057, 2012

G. R. A. J. Nemeth and W. A. Bryan. Modelling beam-transport diffraction in near-infrared few-cycle strong-field experiments. *J. Mod. Opt.*, 58:1206–1214, 2011

W. A. Bryan, C. R. Calvert, R. B. King, G. R. A. J. Nemeth, J. D. Alexander, J. B. Greenwood, C. A. Froud, I. C. E. Turcu, E. Springate, W. R. Newell, and I. D. Williams. Redistribution of vibrational population in a molecular ion with nonresonant strong-field laser pulses. *Phys. Rev. A*, 83:021406, 2011

W. A. Bryan, C. R. Calvert, R. B. King, G. R. A. J. Nemeth, J. B. Greenwood, I. D. Williams, and W. R. Newell. Quasi-classical model of non-destructive wavepacket manipulation by intense ultrashort nonresonant laser pulses. *New J. Phys.*, 12:073019, 2010

I. C. E. Turcu, E. Springate, C. A. Froud, C. M. Cacho, J. L. Collier, W. A. Bryan, G. R. A. J. Nemeth, J. P. Marangos, J. W. G. Tisch, R. Torres, S. Siegel, L. Brugnera, J. G. Underwood, I. Procino, W. R. Newell, C. Altucci, R. Velotta, R. B. King, J. D. Alexander, C. R. Calvert, O. Kelly, J. B. Greenwood, I. D. Williams, A. Cavalleri, J. C. Petersen, N. Dean, S. S. Dhesi, L. Poletto, P. Villoresi, F. Frassetto, S. Bonora, and M. D. Roper. Ultrafast science and development at the Artemis facility. *Proc. of SPIE*, 7469:746902, 2009

J. D. Alexander, C. R. Calvert, R. B. King, O. Kelly, W. A. Bryan, G. R. A. J. Nemeth, W. R. Newell, C. A. Froud, I. C. E. Turcu, E. Springate, P. A. Orr, J. Pedregosa-Gutierrez, C. W. Walter, R. A. Williams, I. D. Williams, and J. B. Greenwood. Short pulse laser-induced dissociation of vibrationally cold, trapped molecular ions. *J. Phys. B*, 42:154027, 2009

J. D. Alexander, C. R. Calvert, R. B. King, O. Kelly, L. Graham, W. A. Bryan, G. R. A. J. Nemeth, W. R. Newell, C. A. Froud, I. C. E. Turcu, E. Springate, I. D. Williams, and J. B. Greenwood. Photodissociation of D_3^+ in an intense, femtosecond laser field. *J. Phys. B*, 42:141004, 2009

Bibliography

[1] M. Protopapas, C. H. Keitel, and P. L. Knight. Atomic physics with super-high intensity lasers. *Rep. Prog. Phys.*, 60:389–446, 1997.

[2] L. V. Keldysh. Ionization in the field of a strong electromagnetic wave. *Sov. Phys. JETP*, 20:1307, 1965.

[3] Gennady L. Yudin and Misha Yu. Ivanov. Nonadiabatic tunnel ionization: Looking inside a laser cycle. *Phys. Rev. A*, 64(1):013409, Jun 2001.

[4] H. R. Reiss. Unsuitability of the Keldysh parameter for laser fields. *Phys. Rev. A*, 82:023418, 2010.

[5] B. Walker, E. Mevel, B. Yang, P. Breger, J. P Chambaret, A. Antonetti, L. F. DiMauro, and P. Agostini. Double ionization in the perturbative and tunneling regimes. *Phys. Rev. A*, 48:R894–R897, 1993.

[6] W. Gordon. *Z. Phys.*, 40:117, 1926.

[7] D. M. Volkov. *Z. Phys.*, 94:250, 1935.

[8] B. M. Karnakov, V. D. Mur, V. S. Popov, and S. V. Popruzhenko. Ionization of atoms and ions by intense laser radiation. *JETP Lett.*, 93:238–249, 2011.

[9] M. D. Perry, O. L. Landen, A. Szöke, and E. M. Campbell. Multiphoton ionization of the noble gases by an intense 10^{14}-W/cm^2 dye laser. *Phys. Rev. A*, 37:747, 1988.

[10] A. M. Perelomov, V. S. Popov, and M. V. Terent'ev. *Sov. Phys. JETP*, 23:924, 1966.

[11] A. M. Perelomov and V. S. Popov. *Sov. Phys. JETP*, 25:336, 1967.

[12] A. M. Perelomov and V. S. Popov. *Sov. Phys. JETP*, 24:207, 1967.

[13] S. F. J. Larochelle, A. Talebpour, and S. L. Chin. Coulomb effect in multiphoton ionization of rare-gas atoms. *J. Phys. B: At. Mol. Opt. Phys.*, 31:1215–1224, 1998.

[14] M. V. Ammosov, N. B. Delone, and V. P. Krainov. Tunnel ionization of complex atoms and of atomic ions in an alternating electromagnetic field. *Sov. Phys. JETP*, 64:1191, 1986.

[15] V. S. Popov. Tunnel and multiphoton ionization of atoms and ions in a strong laser field (Keldysh theory). *Physics-Uspekhi*, 47:855–885, 2004.

[16] F. A. Ilkov, J. E. Decker, and S. L. Chin. Ionization of atoms in the tunnelling regime with experimental evidence using Hg atoms. *J. Phys. B: At. Mol. Opt. Phys.*, 25:4005–4020, 1992.

[17] S. Larochelle, A. Talebpour, and S. L. Chin. Non-sequential multiple ionization of rare gas atoms in a Ti:Sapphire laser field. *J. Phys. B: At. Mol. Opt. Phys.*, 31:1201–1214, 1998.

[18] B. Walker, B. Sheehy, L. F. DiMauro, P. Agostini, K. J. Schafer, and K. C. Kulander. Precision measurement of strong field double ionization of helium. *Phys. Rev. Lett.*, 73:1227–1230, 1994.

[19] H. R. Reiss. Effect of an intense electromagnetic field on a weakly bound system. *Phys. Rev. A*, 22:1786–1813, 1980.

[20] F. H. M. Faisal. Multiple absorption of laser photons by atoms. *J. Phys. B: At. Mol. Phys.*, 6:L89, 1973.

[21] S. M. Sharifi, A. Talebpour, J. Yang, and S. L. Chin. Quasi-static tunnelling and multiphoton processes in the ionization of Ar and Xe using intense femtosecond laser pulses. *J. Phys. B: At. Mol. Opt. Phys.*, 43:155601, 2010.

[22] T. Auguste, P. Monot, L. A. Lompré, G. Mainfray, and C. Manus. Multiply charged ions produced in noble gases by a 1 ps laser pulse at $\lambda = 1053$ nm. *J. Phys. B: At. Mol. Opt. Phys.*, 25:4181–4194, 1992.

[23] A. Becker and F. H. M. Faisal. Intense-field many-body S-matrix theory. *J. Phys. B: At. Mol. Opt. Phys.*, 38:R1–R56, 2005.

[24] M. A. Lysaght, L. R. Moore, A. A. Nikolopoulos, J. S. Parker, H. W. van der Hart, and K. T. Taylor. *Quantum Dynamic Imaging: Theoretical and Numerical Methods*, pages 107–134. CRM Series in Mathematical Physics. Springer, 2011.

[25] L. R. Moore, M. A. Lysaght, L. A. A. Nikolopoulos, and J. S. Parker. The RMT method for many-electron atomic systems in intense short-pulse laser light. *J. Mod. Opt.*, 58:1132–1140, 2011.

[26] H. W. van der Hart, M. A. Lysaght, and P. G. Burke. Time-dependent multielectron dynamics of Ar in intense short laser pulses. *Phys. Rev. A*, 76:043405, 2007.

[27] A. Zaïr, A. Guandalini, F. Schapper, M. Holler, J. Biegert, L. Gallmann, U. Keller, A. Couairon, M. Franco, and A. Mysyrowicz. Spatio-temporal characterization of few-cycle pulses obtained by filamentation. *Opt. Express*, 15:5394–5404, 2007.

[28] A. Isanin, S. S. Bulanov, F. Kamenets, and F. Pegoraro. Nonlinear generation of ultra-short electromagnetic pulses in plasmas. *Phys. Lett. A*, 337:107–111, 2005.

[29] M. Nisoli, S de Silvestri, O. Svelto, R. Szipöcs, K. Ferencz, Ch. Spielmann, S. Sartania, and F. Krausz. Compression of high-energy laser pulses below 5 fs. *Opt. Lett.*, 22:522–524, 1997.

[30] M. Nisoli, S. Stagira, S. de Silvestri, O Svelto, S. Sartania, Z. Cheng, G. Tempea, C. Spielmann, and F. Krausz. Toward a terawatt-scale sub-10-fs laser technology. *IEEE Journal of Selected Topics in Quantum Electronics*, 4:414–420, 1998.

[31] J. S. Robinson, C. A. Haworth, H. Teng, R. A. Smith, J. P. Marangos, and J. W. G. Tisch. The generation of intense, transform-limited laser pulses with tunable duration from 6 to 30 fs in a differentially pumped hollow fibre. *Appl. Phys. B*, 85:525–529, 2006.

[32] A. Guandalini, P. Eckle, M. Anscombe, P. Schlup, J. Biegert, and U. Keller. 5.1 fs pulses generated by filamentation and carrier envelope phase stability analysis. *J. Phys. B: At. Mol. Opt. Phys.*, 39:S257–S264, 2006.

[33] G. Stibenz, N. Zhavoronkov, and G. Steinmeyer. Self-compression of millijoule pulses to 7.8 fs duration in a white-light filament. *Opt. Lett.*, 31:274–276, 2006.

[34] A. Couairon, M. Franco, A. Mysyrowicz, J. Biegert, and U. Keller. Pulse self-compression to the single-cycle limit by filamentation in a gas with a pressure gradient. *Opt. Lett.*, 30:2657–2659, 2005.

[35] P. B. Corkum. Plasma perspective on strong-field multiphoton ionization. *Phys. Rev. Lett.*, 71:1994–1997, 1993.

[36] T. Brabec and F. Krausz. Intense few-cycle laser fields: Frontiers of nonlinear optics. *Rev. Mod. Phys.*, 72:545–591, 2000.

[37] G. Scoles, editor. *Atomic and Molecular Beam Methods*, volume 1. Oxford University Press, 200 Madison Avenue, New York, New York 10016, 1988.

[38] Th. Weber, H. Giessen, M. Weckenbrock, G. Urbasch, A. Staudte, L. Spielberger, O. Jagutzki, V. Mergel, M. Vollmer, and R. Dörner. Correlated electron emission in multiphoton double ionization. *Nature*, 405:658–661, 2000.

[39] D. N. Fittinghoff, P. R. Bolton, B. Chang, and K. C. Kulander. Observation of nonsequential double ionization of helium with optical tunneling. *Phys. Rev. Lett.*, 69:2642–2645, 1992.

[40] U. Eichmann, M. Dörr, M. Maeda, W. Becker, and W. Sandner. Collective multielectron tunneling ionization in strong fields. *Phys. Rev. Lett.*, 84:3550, 2000.

[41] R. Moshammer, B. Feuerstein, W. Schmitt, A. Dorn, C. D. Schröter, J. Ullrich, H. Rottke, C. Trump, M. Wittman, G. Korn, K. Hoffmann, and W. Sandner. Momentum distributions of Ne^{n+} ions created by an intense ultrashort laser pulse. *Phys. Rev. Lett.*, 84:447–450, 2000.

[42] R. Dörner, Th. Weber, M. Weckenbrock, A. Staudte, M. Hattass, H. Schmidt-Böcking, R. Moshammer, and J. Ullrich. Multiple ionization in strong laser fields. *Adv. Atom. Mol. Opt. Phys.*, 48:1–34, 2002.

[43] Th. Weber, M. Weckenbrock, A. Staudte, L. Spielberger, O. Jagutzki, V. Mergel, F. Afaneh, G. Urbasch, M. Vollmer, H. Giessen, and R. Dörner. Recoil-ion momentum distributions for single and double ionization of helium in strong laser fields. *Phys. Rev. Lett.*, 84:443–446, 2000.

[44] T. Pfeifer, C. Spielmann, and G. Gerber. Femtosecond x-ray science. *Rep. Prog. Phys.*, 69:443–505, 2006.

[45] A. Scrinzi, M. Y. Ivanov, R. Kienberger, and D. M. Villeneuve. Attosecond physics. *J. Phys. B: At. Mol. Opt. Phys.*, 39:R1–R37, 2006.

[46] W. A. Bryan, S. L. Stebbings, E. M. L. English, T. R. J. Goodworth, W. R. Newell, J. McKenna, M. Suresh, B. Srigengan, I. D. Williams, I. C. E. Turcu, J. M. Smith, E. J. Divall, C. J. Hooker, and A. J. Langley. Geometry- and diffraction-independent ionization probabilities in intense laser fields: probing atomic ionization mechanisms with effective intensity matching. *Phys. Rev. A*, 73:013407, 2006.

[47] P. Agostini and L. F. DiMauro. The physics of attosecond light pulses. *Rep. Prog. Phys.*, 67:813–855, 2004.

[48] P. M. Paul, E. S. Toma, P. Breger, G. Mullot, F. Aug, Ph. Balcou, H. G. Muller, and P. Agostini. Observation of a train of attosecond pulses from high harmonic generation. *Science*, 292:1689–1692, 2001.

[49] M. Drescher, M. Hentschel, R. Kienberger, G. Tempea, Ch. Spielmann, G. Reider, P. Corkum, and F. Krausz. X-ray pulses approaching the attosecond frontier. *Science*, 291:1923, 2001.

[50] M. Hentschel, R. Kienberger, Ch. Spielmann, G. A. Reider, N. Milosevic, T. Brabec, P. Corkum, U. Heinzmann, M. Drescher, and F. Krausz. Attosecond metrology. *Nature*, 414:509–513, 2001.

[51] Y. Mairesse, A. de Bohan, L. J. Frasinski, H. Merdji, L. C. Dinu, P. Monchicourt, P. Breger, M. Kovačev, R. Taïeb, B. Carré, H. G. Muller, P. Agostini, and P. Salières. Attosecond synchronization of high-harmonic soft X-rays. *Science*, 302:1540, 2003.

[52] A. Baltuška, M. Uiberacker, E. Goulielmakis, R. Kienberger, V. Yakovlev, Th. Udem, T. W. Hänsch, and F. Krausz. Phase-controlled amplification of few-cycle laser pulses. *IEEE J. Sel. Top. Quantum Electron.*, 9:972–989, 2003.

[53] M. Schultze, E. Goulielmakis, Hofstetter M. Uiberacker, M., J. Kim, D. Kim, F. Krausz, and U. Kleineberg. Powerful 170-attosecond XUV pulses generated with few-cycle laser pulses and broadband multilayer optics. *New J. Phys.*, 9:243, 2007.

[54] F. Ferrari, F. Calegari, M. Lucchini, C. Vozzi, S. Stagira, G. Sansone, and M. Nisoli. High-energy isolated attosecond pulses generated by above-saturation few-cycle fields. *Nature Photonics*, 4:875–879, 2010.

[55] D. Strickland and G. Mourou. Compression of amplified chirped optical pulses. *Opt. Commun.*, 56:219, 1985.

[56] I. C. E. Turcu, E. Springate, C. A. Froud, C. M. Cacho, J. L. Collier, W. A. Bryan, G. R. A. J. Nemeth, J. P. Marangos, J. W. G. Tisch, R. Torres, S. Siegel, L. Brugnera, J. G. Underwood, I. Procino, W. R. Newell, C. Altucci, R. Velotta, R. B. King, J. D. Alexander, C. R. Calvert, O. Kelly, J. B. Greenwood, I. D. Williams, A. Cavalleri, J. C. Petersen, N. Dean,

S. S. Dhesi, L. Poletto, P. Villoresi, F. Frassetto, S. Bonora, and M. D. Roper. Ultrafast science and development at the Artemis facility. *Proc. of SPIE*, 7469:746902, 2009.

[57] M. Nisoli, E. Priori, G. Sansone, S. Stagira, G. Cerullo, S. de Silvestri, C. Altucci, R. Bruzzese, C. de Lisio, P. Villoresi, L. Poletto, M. Pascolini, and G. Tondello. The role of beam profile in high-order harmonic generation by few-optical-cycle pulses. *Appl. Phys. B*, 74:S11–S15, 2002.

[58] G. R. A. J. Nemeth and W. A. Bryan. Modelling beam-transport diffraction in near-infrared few-cycle strong-field experiments. *J. Mod. Opt.*, 58:1206–1214, 2011.

[59] B. A. Zon. *Sov. Phys. JETP*, 89:219, 1999.

[60] A. S. Kornev, E. B. Tulenko, and B. A. Zon. Kinetics of multiple ionization of rare gas atoms in a circularly polarized laser field. *Phys. Rev. A*, 63:043414, 2003.

[61] B. M. Smirnov and M. I. Chibisov. *Sov. Phys. JETP*, 22:585, 1965.

[62] J. Posthumus. *Molecules and clusters in intense laser fields.* Cambridge University Press, Cambridge, U.K., 2001.

[63] P. Hansch, M. A. Walker, and L. D. Van Woerkom. Spatially-dependent multiphoton multiple ionization. *Phys. Rev. A*, 54:R2559–R2562, 1996.

[64] P. Hansch and L. D. Van Woerkom. High-precision intensity-selective observation of multiphoton ionization: a new method of photoelectron spectroscopy. *Opt. Lett.*, 21:1286–1288, 1996.

[65] M. A. Walker, P. Hansch, and L. D. Van Woerkom. Intensity-resolved multiphoton ionization: Circumventing spatial averaging. *Phys. Rev. A*, 57:R701–R704, 1998.

[66] W. A. Bryan, S. L. Stebbings, J. McKenna, E. M. L. English, M. Suresh, J. Wood, B. Srigengan, I. C. E. Turcu, J. M. Smith, E. J. Divall, C. J. Hooker, A. J. Langley, J. L. Collier, I. D. Williams, and W. R. Newell. Atomic excitation during recollision-free ultrafast multi-electron tunnel ionization. *Nat. Phys.*, 2:379–383, 2006.

[67] W. A. Bryan, S. L. Stebbings, J. McKenna, E. M. L. English, M. Suresh, J. Wood, B. Srigengan, I. C. E. Turcu, I. D. Williams, and W. R. Newell. On the recollision-free excitation of krypton during ultrafast multi-electron tunnel ionization. *J. Phys. B: At. Mol. Opt. Phys.*, 39:S349–S356, 2006.

[68] H. Akagi, T. Otobe, A. Staudte, A. Shiner, F. Turner, R. Dörner, D. M. Villeneuve, and P. B. Corkum. Laser tunnel ionization from multiple orbitals in HCl. *Science*, 325:1364, 2009.

[69] A. D. Shiner, B. E. Schmidt, C. Trallero-Herrero, H. J. Wörner, S. Patchkovskii, P. B. Corkum, J-C. Kieffer, F. Légaré, and D. M. Villeneuve. Probing collective multi-electron dynamics in xenon with high-harmonic spectroscopy. *Nat. Phys.*, 7:464–467, 2011.

[70] W. Koechner. *Solid-state laser engineering.* Springer, 2006.

[71] P. F. Moulton. Spectroscopic and laser characteristics of Ti:Al_2O_3. *J. Opt. Soc. Am. B*, 3(1):125–133, 1986.

[72] K. F. Wall and A. Sanchez. The generation of intense, transform-limited laser pulses with tunable duration from 6 to 30 fs in a differentially pumped hollow fibre. *Lincoln Laboratory Journal*, 3:447–462, 1990.

[73] W. Demtröder. *Laser spectroscopy: basic concepts and instrumentation.* Springer-Verlag, Berlin Heidelberg, 3 edition, 2003.

[74] D. E. Spence, P. N. Kean, and W. Sibbett. 60-fsec pulse generation from a self-mode-locked ti:sapphire laser. *Opt. Lett.*, 16(1):42, 1991.

[75] E. Hecht. *Optics (Second Edition).* Addison-Wesley Publishing Company, Reading, Massachusetts (U.S.A.), 1990.

[76] J. Blackwell and E. Thornton. *Mastering Optics - An applications guide to optical engineering.* McGraw-Hill, Cambridge (U.K.), 1996.

[77] F. Graham Smith and Terry A. King. *Optics and Photonics: An Introduction.* John Wiley & Sons, Ltd., Chichester (U.K.), August 2004.

[78] L. Gallmann, D. H. Sutter, N. Matuschek, G. Steinmeyer, and U. Keller. Techniques for the characterization of sub-10-fs optical pulses: a comparison. *Appl. Phys. B*, 70:S67 - S75, 2000.

[79] D. Kane and R. Trebino. *IEEE J. Quantum Electron.*, 29:571, 1993.

[80] M. Guilhaus. Principles and instrumentation in time-of-flight mass spectrometry. *J. Mass Spectrom.*, 30:1519 - 1532, 1995.

[81] S. L. Watson. *Femtosecond Laser Interactions With Dilute Matter.* PhD thesis, University College London, 2005.

[82] E. M. L. English. *Laser Induced Ultrafast Dynamics in Atoms and Molecules.* PhD thesis, University College London, 2007.

[83] W. C. Wiley and I. H. McLaren. Time-of-flight mass spectrometer with improved resolution. *Rev. Sci. Instrum.*, 26:1150, 1955.

[84] C. R. Calvert, W. A. Bryan, W. R. Newell, and I. D. Williams. Time-resolved studies of ultrafast wavepacket dynamics in hydrogen molecules. *Phys. Rep.*, 491:1–28, 2010.

[85] J. Emsley. *Oxford Chemistry Guides.* Oxford University Press, New York, 1995.

[86] S. A. Collins. *J. Acoust. Soc. Am.*, 60:1168, 1970.

[87] J. P. Taché. *Appl. Opt.*, 26:2698, 1987.

[88] E. A. J. Marcatili and R. A. Schmeltzer. Hollow metallic and dielectric waveguides for long distance optical transmission and lasers. *Bell Syst. Tech. J.*, 43:1783–1809, 1964.

[89] J. A. Stratton. *Electromagnetic Theory.* McGraw-Hill, New York, 1941.

[90] *FemtoOptics™ Catalog 2011.*

[91] M. J. Seaton. Quantum defect theory. *Rep. Prog. Phys.*, 46:167–257, 1983.

[92] E. B. Saloman. Energy levels and observed spectral lines of xenon, Xe I through Xe LIV. *J. Phys. Chem. Ref. Data*, 33:765, 2004.

[93] A. Savitzky and M. J. E. Golay. Smoothing and differentiation of data by simplified least squares procedures. *Anal. Chem.*, 36:1627–1639, 1964.

[94] P. A. Gorry. General least-squares smoothing and differentiation by the convolution (Savitzky-Golay) method. *Anal. Chem.*, 62:570–573, 1990.

[95] R. L. Plackett. Karl pearson and the chi-squared test. *International Statistical Review*, 51:59–72, 1983.

[96] E. J. McGuire. Photo-ionization cross sections of the elements helium to xenon. *Phys. Rev.*, 175:20–30, 1968.

[97] U. Becker and D. A. Shirley. *VUV and soft X-ray Photoionization.* Springer, 1996.

[98] H. Aksela, S. Aksela, G. M. Bancroft, and K. H. Tan. $N_{4,5}OO$ resonance Auger spectra of Xe studied with selective excitation by synchrotron radiation. *Phys. Rev. A*, 33:3867–3875, 1986.

[99] A. Caló et al. The Kr valence photoelectron satellite lines in the photon energy region below the $3d$ threshold. *J. Phys. B*, 39:4169, 2006.

[100] R. I. Hall, A. McConkey, K. Ellis, G. Dawber, M. A. MacDonald, and G. C. King. Near-threshold single photon double ionization of neon, argon, krypton and xenon observed by electron-electron coincidence spectroscopy. *J. Phys. B: At. Mol. Opt. Phys.*, 25:799, 1992.

[101] A. E. Slattery, J. P. Wightmans, M. A. MacDonald, S. Cvejanovic, and T. J. Reddish. Threshold photoelectron studies of Kr and Xe. *J. Phys. B: At. Mol. Opt. Phys.*, 33:4833–4848, 2000.

[102] H. Yoshii, T. Aoto, Y. Morioka, and J. Hayaishi. *Electron Spectrosc. Relat. Phenom.*, 144–147:83–85, 2005.

[103] N. Berrah, A. Farhat, B. Langer, B. M. Lagutin, Ph. V. Demekhin, D. Petrov, V. L. Sukhorukov, R. Wehlitz, S. B. Whitfield, J. Viefhaus, and U. Becker. Angle-resolved energy dependence of the $4p^4nd(^2S_{1/2})(n = 4-7)$ correlation satellites in Kr from 38.5 to 250 eV: Experiment and theory. *Phys. Rev. A*, 56:4545–4553, 1997.

[104] L. Poletto and F. Frassetto. Time-preserving grating monochromators for ultrafast extreme-ultraviolet pulses. *Appl. Opt.*, 49:5465–5473, 2010.

[105] G. Kutluk, T. Takaku, M. Kanno, T. Nagata, E. Shigemasa, A. Yigishita, and F. Koike. Ne valence correlation satellites in the photon energy region 80–220 eV. *J. Phys. B*, 27:5637–5646, 1994.

[106] V. L. Sukhorukov, B. M. Lagutin, I. D. Petrov, H. Schmoranzer, A. Ehresmann, and K-H. Schartner. Photoionization of Kr near 4s threshold: II. intermediate-coupling theory. *J. Phys. B: At. Mol. Opt. Phys.*, 27:241–256, 1994.

[107] M. Uiberacker, Th. Uphues, M. Schultze, A. J. Verhoef, V. Yakovlev, M. F. Kling, J. Rauschenberger, N. M. Kabachnik, H. Schröder, M. Lezius, K. L. Kompa, H. G. Muller, M. J. J. Vrakking, S. Hendel, U. Kleineberg, U. Heinzmann, M. Drescher, and F. Krausz. Attosecond real-time observation of electron tunnelling in atoms. *Nature*, 446:627–632, 2007.

[108] M. Meyer, J. T. Costello, S. Düsterer, W. B. Li, and P. Radcliffe. Two-colour experiments in the gas phase. *J. Phys. B: At. Mol. Opt. Phys.*, 43:194006, 2010.

[109] O. Guyétand, M. Gisselbrecht, A. Huetz, P. Agostini, B. Carré, P. Breger, O. Gobert, D. Garzella, J-F. Hergott, O. Tcherbakoff, H. Merdji, M. Bougeard, H. Rottke, M. Böttcher, Z. Ansari, P. Antoine, and L. F. DiMauro. Complete momentum analysis of multi-photon photo-double ionization of xenon by XUV and infrared photons. *J. Phys. B: At. Mol. Opt. Phys.*', 41:065601, 2008.

[110] P. Ranitovic, X. M. Tong, C. W. Hogle, X. Zhou, Y. Liu, N. Toshima, M. M. Murnane, and H. C. Kapteyn. Controlling the XUV transparency of helium

using two-pathway quantum interference. *Phys. Rev. Lett.*, 106:193008, 2011.

[111] M. Fieß, M. Schultze, E. Goulielmakis, B. Dennhardt, J. Gagnon, M. Hofstetter, R. Kienberger, and F. Krausz. Versatile apparatus for attosecond metrology and spectroscopy. *Rev. Sci. Instrum.*, 81:093103, 2010.

[112] F. Frassetto, C. Cacho, C. A. Froud, I. C. E. Turcu, P. Villoresi, W. A. Bryan, E. Springate, and L. Poletto. Single-grating monochromator for extreme-ultraviolet ultrashort pulses. *Opt. Express*, 19:19169–19181, 2011.

[113] R. Petit. *Electromagnetic Theory of Grating.* Springer-Verlag, Berlin, 1980.

[114] A. S. Kheifets and I. A. Ivanov. Delay in atomic photoionization. *Phys. Rev. Lett.*, 105:233002, 2010.

[115] S. De Nicola. On-axis focal shift effects in focused truncated J_0 Bessel beams. *Pure Appl. Opt.*, 5:827–831, 1996.

[116] E. Magerl, S. Neppl, A. L. Cavalieri, E. M. Bothschafter, M. Stanislawski, Th. Uphues, M. Hofstetter, U. Kleineberg, J. V. Barth, D. Menzel, F. Krausz, R. Ernstorfer, R. Kienberger, and P. Feulner. A flexible apparatus for attosecond photoelectron spectroscopy of solids and surfaces. *Rev. Sci. Instrum.*, 82:063104, 2011.

[117] M. Pascolini, S. Bonora, A. Giglia, N. Mahne, S. Nannarone, and L. Poletto. Gratings in the conical diffraction mounting for an euv time-delay compensated monochromator. *Appl. Opt.*, 45:3253–3562, 2006.

[118] W. A. Bryan, F. Frassetto, C. A. Froud, I. C. E. Turcu, R. B. King, C. R. Calvert, G. R. A. J. Nemeth, P. Villoresi, L. Poletto, and E. Springate.

Isolated high-harmonic XUV photon absorption and NIR strong-field tunnel ionization. *New J. Phys.*, 14:013057, 2012.

[119] E. Wolf and M. Born. *Principles of Optics.* Pergamon Press, New York, 5 edition, 1975.

[120] C. Altucci, R. Bruzzese, C. de Lisio, M. Nisoli, E. Priori, S. Stagira, M. Pascolini, L. Poletto, P. Villoresi, and V. *et al.* Tosa. . *Phys. Rev. A*, 68:033806, 2003.

[121] A. Averchi, D. Faccio, R. Berlasso, M. Kolesik, J. V. Moloney, and P. Couairon, A. di Trapani. . *Phys. Rev. A*, 77:021802(R), 2008.

[122] J. B. McManus. Paraxial matrix description of astigmatic and cylindrical mirror resonators with twisted axes for laser spectroscopy. *Appl. Opt.*, 46:472–482, 2007.

[123] W. A. Bryan, C. R. Calvert, R. B. King, G. R. A. J. Nemeth, J. D. Alexander, J. B. Greenwood, C. A. Froud, I. C. E. Turcu, E. Springate, W. R. Newell, and I. D. Williams. Redistribution of vibrational population in a molecular ion with nonresonant strong-field laser pulses. *Phys. Rev. A*, 83:021406, 2011.

[124] W. A. Bryan, C. R. Calvert, R. B. King, G. R. A. J. Nemeth, J. B. Greenwood, I. D. Williams, and W. R. Newell. Quasi-classical model of non-destructive wavepacket manipulation by intense ultrashort nonresonant laser pulses. *New J. Phys.*, 12:073019, 2010.

[125] J. D. Alexander, C. R. Calvert, R. B. King, O. Kelly, W. A. Bryan, G. R. A. J. Nemeth, W. R. Newell, C. A. Froud, I. C. E. Turcu, E. Springate, P. A. Orr, J. Pedregosa-Gutierrez, C. W. Walter, R. A. Williams, I. D.

Williams, and J. B. Greenwood. Short pulse laser-induced dissociation of vibrationally cold, trapped molecular ions. *J. Phys. B*, 42:154027, 2009.

[126] J. D. Alexander, C. R. Calvert, R. B. King, O. Kelly, L. Graham, W. A. Bryan, G. R. A. J. Nemeth, W. R. Newell, C. A. Froud, I. C. E. Turcu, E. Springate, I. D. Williams, and J. B. Greenwood. Photodissociation of D_3^+ in an intense, femtosecond laser field. *J. Phys. B*, 42:141004, 2009.